Search for new resonances in the diphoton final state with the ATLAS detector

Yufeng Wang

SORBONNE UNIVERSITÉ

École doctorale des Sciences de la Terre et de l'environnement et Physique de l'Univers, Paris - ED 560

Laboratoire de Physique Nucléaire et de Hautes Énergies - UMR 7585

Recherche de nouvelles résonances dans l'état final du Diphoton avec le détecteur ATLAS

Présenté par

Yufeng Wang

THÈSE DE DOCTORAT DE PHYSIQUE

Dirigée par Yanwen Liu et Lydia Roos

Presentée et soutenue publiquement le 03/12/2020 devant le jury composé de :

Antonio Baroncelli	USTC	Examinateur
ELi Ben Haim	LPNHE	Examinateur
Lydia Fayard	IJClab	Rapporteuse
Yanwen Liu	USTC	Directeur de thèse
Yajun Mao	PKU	Examinateur
Ioannis Nomidis	LPNHE	Examinateur
Lydia Roos	LPNHE	Directrice de thèse
Lei Zhang	NJU	rapporteur
Antonio Baroncelli		Président

UNIVERSITÉ DE PARIS

École doctorale des Sciences de la Terre et de l'environnement et Physique de l'Univers, Paris (ED 560)

Laboratoire de Physique Nucléaire et de Hautes Énergies (LPNHE)

Search for New Resonances in the Diphoton Final State with the ATLAS Detector

Presented by

Yufeng Wang

Submitted in fulfillment of the requirements for the degree of

DOCTEUR DES SCIENCES SORBONNE UNIVERSITÉ

Supervised by Yanwen Liu and Lydia Roos

Defended on 03/12/2020 in front of the comittee :

Antonio Baroncelli	USTC	Examiner
ELi Ben Haim	LPNHE	Examiner
Lydia Fayard	IJClab	Referee
Yanwen Liu	USTC	Supervisor
Yajun Mao	PKU	Examiner
Ioannis Nomidis	LPNHE	Examiner
Lydia Roos	LPNHE	Supervisor
Lei Zhang	NJU	Referee
Antonio Baroncelli		President

Abstract

This thesis presents the search for new resonances in the diphoton final state with proton-proton collision data collected by the ATLAS detector at the LHC at a centre-of-mass energy of $\sqrt{s} = 13$ TeV. Search for a low-mass spin-0 resonance in the diphoton invariant mass range from 65 to 110 GeV is performed using 80 fb^{-1} data collected in 2015, 2016 and 2017. Selected events are split into three categories depending on the conversion state of the two photons, in order to increase the sensitivity of the search. In the high-mass region above 160 GeV, two kinds of signal are searched for using 139 fb^{-1} data collected in 2015-2018: a spin-0 model-independent resonant state, and a spin-2 graviton excitation state predicted by the Randall-Sundrum model with one warped extra dimension. Analysis selections are optimized and harmonized for both spin-0 and spin-2 searches. Functional decomposition method is applied for the first time in the background modeling procedure, in order to reduce the corresponding systematic uncertainty. For both low-mass and high-mass searches, there is no significant excess observed with respect to the Standard Model expectation. Upper limits are set on the fiducial (total) production cross section times branching ratio as a function of the signal mass for the spin-0 (spin-2) resonances. In addition, a study on the photon-specific energy calibration systematic uncertainty from electromagnetic shower leakage mismodeling is also presented. This uncertainty is quantified as the difference between the lateral energy leakage mismodeling for photons and electrons using $Z \to ee$ events. Results obtained with diphoton events are also shown for the first time as a cross check in a larger kinetic region.

Keywords: LHC, ATLAS, diphoton, beyond Standard Model

Résumé

Cette thèse présente la recherche de nouvelles résonances se désintégrant en deux photons, dans les données de collisions proton-proton collectées par le détecteur ATLAS au LHC, à une énergie dans le centre de masse de $\sqrt{s} = 13$ TeV. La recherche d'une résonance de spin 0 dans une gamme de masse allant de 65 à 110 GeV est effectuée à l'aide de 80 fb^{-1} de données collectées en 2015, 2016 et 2017. Les événements sélectionnés sont divisés en trois catégories en fonction de l'état de conversion des deux photons, afin d'augmenter la sensibilité de la recherche. Dans la région de masse au-dessus de 160 GeV, deux types de signaux sont recherchés à l'aide de 139 fb^{-1} données collectées de 2015 à 2018 : un état résonnant de spin 0 sans se référer à un modèle théorique spéfcifique, et un état d'excitation du graviton, de spin 2, prédit par le modèle Randall-Sundrum avec une dimension supplémentaire déformée. La sélection des événements est optimisée et harmonisée entre les deux recherches. La méthode de décomposition fonctionnelle est appliquée pour la première fois dans la procédure de modélisation du bruit de fond, afin de réduire l'incertitude systématique correspondante. Tant pour les recherches à basse masse qu'à haute masse, aucun excès significatif n'est observé par rapport aux prédictions du modèle standard. Des limites supérieures sont établies sur le produit de la section efficace de production fiducielle (totale) et du rapport d'embranchement, en fonction de la masse du signal, pour les résonances de spin-0 (spin-2). En outre, une étude de l'incertitude systématique sur l'étalonnage de l'énergie des photons due à la mauvaise modélisation de la fraction d'énergie de la gerbe électromagnétique perdue latéralement est également présentée. Cette incertitude est quantifiée comme la différence entre la perte d'énergie pour les photons et les électrons en utilisant les événements $Z \to ee$. Les résultats obtenus avec les événements diphotons sont également présentés pour la première fois comme contrôle dans une région cinématique plus grande.

Mots clés: LHC, ATLAS, diphoton, au-delà du modèle standard

Contents

Introduction

With decades of efforts throughout the second half of the 20th century, the Standard Model (SM) of the elementary particles was finalized in the mid-1970s. Currently, it is our best description of the fundamental building blocks of the matter in our universe, and the basic laws that govern their interactions. The Standard Model is so far self-consistent, and its validity has been successfully confirmed by several experimental results. The most famous prediction of the Standard Model as well as its last missing piece, the Higgs boson, is the explanation how the massive elementary particles acquire their masses at the beginning. It motivated generations of experimental physicists, and to prove the existence of the Standard Model Higgs boson was one of the main purpose of the Large Hadron Collider (LHC), the world's largest and most powerful particle collider. For a long time, people were expecting evidence to show up from ATLAS (A Toroidal LHC ApparatuS) and CMS (Compact Muon Solenoid), the two general-purpose particle detectors.

After a 40-year long quest, a particle of properties consistent with those of the Standard Model Higgs boson was eventually discovered in 2012 by the ATLAS and the CMS collaborations at the LHC. Since its discovery, the study of the Higgs sector has become an important objective of the ATLAS program. One aspect of this program is to study the properties of the new boson, and to investigate its role in the mechanism of Electroweak symmetry breaking and the generation of the SM particles masses. Detailed studies performed in the past years has shown a good consistency with the SM predictions. On the other hand, although the Standard Model is now complete, unanswered questions still remain and indicate that the Standard Model might just be part of a more fundamental theory. Therefore, another equally important objective is to investigate the physics beyond the Standard Model, such as the possibility of extended Higgs sectors with additional states predicted by many extensions of the Standard Model.

This manuscript presents the search for new resonances decaying to two photons. The diphoton decay channel played an important role in the discovery of the Standard Model Higgs at 125 GeV, thanks to the excellent mass resolution provided by the electromagnetic calorimeter and the moderate and easy-to-measure background. For the same reasons, this channel might offer further discovery potential, for either resonances below 125 GeV or for higher-mass states. The search was divided into two

analyses: one searches for a spin-0 resonance in the diphoton invariant mass range from 65 to 110 GeV ("low-mass search"); the other searches for a spin-0 model-independent resonance with mass above 160 GeV, or a spin-2 Randall-Sundrum graviton resonance with mass above 500 GeV ("high-mass search"). The low-mass search uses the Run 2 pp collision data collected at $\sqrt{s} = 13$ TeV with the ATLAS detector in 2015-2017, corresponding to an integrated luminosity of 80 fb^{-1}. The result was presented at the International Conference on High Energy Physics (ICHEP) in 2018. After that, the high-mass search was initiated and inherited the experiences and analysis framework, using the full Run 2 data (2015-2018) corresponding to an integrated luminosity of 139 fb^{-1}. Results were presented at ICHEP 2020, while a paper is under preparation. I joined the analysis team in 2017 to start working with the low-mass search, and was mostly involved in the high-mass search. I will describe my contributions to the two analyses in more detail, while trying to give an overall introduction to the strategy of such classic resonance search.

A study on the photon-specific energy calibration systematic uncertainties from electromagnetic shower leakage mismodeling is also presented. The energy loss due to shower leakage mismodeling is corrected by the in-situ energy calibration performed with $Z \to ee$ events. However the corrections for electrons of certain transverse energy might not hold for photons or for other transverse energies due to the imperfect simulation of the shower shape. This study was my qualification task in order to become an ATLAS author, and was recorded in the electron and photon energy calibration paper that was published in Journal of Instrumentation (JINST) in 2018.

This manuscript is formed by five chapters, organised as follows.

Chapter 1 presents an overview of the Standard Model. Gauge theory and spontaneous symmetry breaking are briefly introduced, followed by the different production and decay modes of the Higgs boson as these models might also be assumed for a potential new resonance. Two models, the two-Higgs doublet models (2HDM) and the Randall-Sundrum (RS) model are also introduced as examples of the models of beyond the Standard Model (BSM) physics.

Chapter 2 presents a general description of the LHC and the ATLAS detector. This chapter begins with the overview of the LHC accelerator complex and its performance. Then the ATLAS detector is described, the structures as well as the design parameters of its sub-detectors are introduced.

Chapter 3 presents the reconstruction, calibration and identification of the photons in the ATLAS experiment, which is the most relevant object of the physics analyses of this thesis. The necessary procedures and their performance to reconstruct and identify a photon candidate are described in detail.

Chapter 4 presents my contribution to the electron and photon calibration, which is a study on the photon-specific uncertainty from electromagnetic shower leakage mismodeling. Variables used to quantify this uncertainty are constructed and measured

with $Z \to ee$ and $Z \to \mu\mu\gamma$ samples, while diphoton sample is also used as a cross-check for the first time.

Chapter 5 presents the search for new resonances in the diphoton final state. Two analyses are performed separately in the low-mass and high-mass regions, while the basic analysis strategy and the methods of signal and background modeling are common.

Chapter 1

Theory

Throughout the human history, scientists have been trying to figure out the ultimate answer to "everything": the basic constituent of matter, and the fundamental laws of the universe. After the discovery of quite a big number of elementary particles up to the 1960s, the corresponding theories that put them all under one self-consistent framework became the famous Standard Model (SM). So far, most of its predictions are successfully confirmed by many experiments. In 2012, the Higgs boson was discovered at the LHC, which is the last particle predicted by the Standard Model. However the journey to the unknown continues, as people are still searching for physics beyond the Standard Model. In this chapter, a brief introduction of the Standard Model is given in Sec. 1.1, including the basic concepts of the gauge principle, the Standard Model Lagrangian, the spontaneous symmetry breaking and a brief review of the Higgs mechanism and properties. In Sec. 1.2, two particular models are introduced as examples of the extension of the current Standard Model of particle physics.

1.1 The Standard Model of particle physics

The elementary particles in the Standard Model are illustrated in Fig. 1.1, along with their basic properties. The elementary fermions with spin 1/2 consist all the matter in the universe, classified as quarks and leptons.[1] The interactions between these particles are carried by the elementary bosons with integral spin. The Standard Model describes three of four fundamental forces: electromagnetic, weak and strong forces. The bosons, photon, $W^{\pm}/Z^0$ bosons and gluons are the carrier of the three fundamental forces respectively. The fourth force, gravity is not included in the Standard Model, since the attempt of describing gravity with quantum field theory leads to renormalization problems[1]. However if the carrier of gravity (graviton) exists, it must be a spin-2 boson[2]. Finally, the Higgs boson has spin 0, and the massive particles acquire masses through their interactions with the Higgs field.

[1] More precisely, muons and taus can only be produced in high energy collisions, such as particle accelerators and cosmic rays.

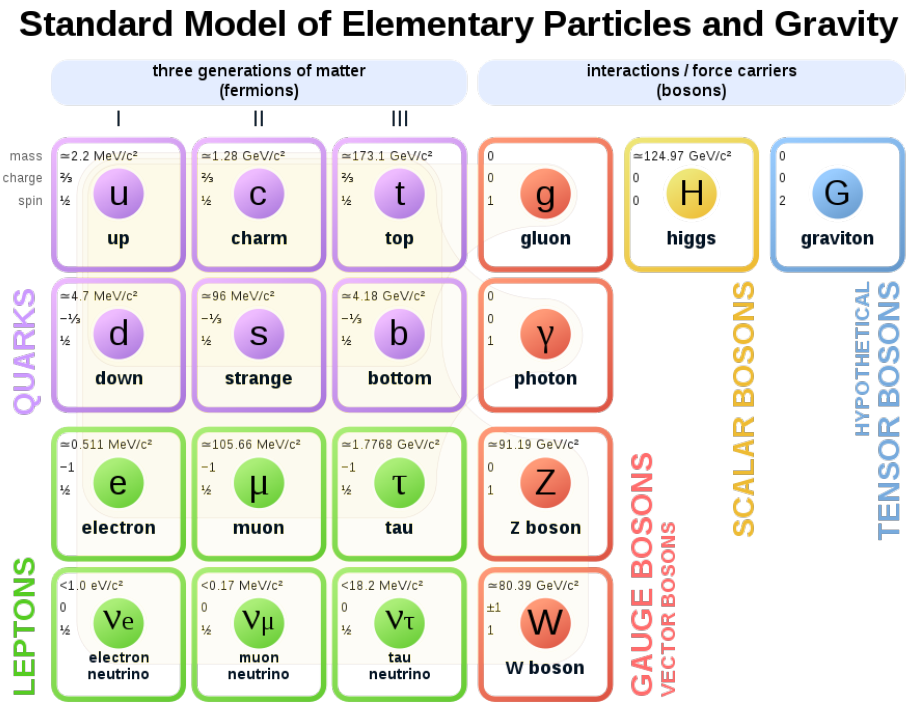

Figure 1.1 – The elementary ingredients of the Standard Model.

Considering all the particles in the Standard Model with different properties, we have 36 quarks, 12 leptons and 12 mediators of the forces, each of them are already "elementary". In addition, there is one scalar Higgs boson, giving us a total of 61 particles. Although this number is large, these particles are interrelated and follow clear rules. As illustrated, there are three generations of leptons and quarks with significantly different masses. The type of charge they possess decides the kind of fundamental interaction they can participate. For example, a neutrino ($q = 0$) interacts only via the weak force and gravity. A charged lepton ($q = \pm 1$) could participate in the electromagnetic interaction as well. The six flavours of quarks ($q = 2/3$ or $q = -1/3$) also have a "color" charge (conventionally named as red, green and blue), allowing them to participate in the strong interaction. The eight gluons also have colors in order to carry the strong interaction, and they are completely identical except for the color charge.

1.1.1 The gauge theory

In order to explain the content of the Standard Model, the first thing we should look into is symmetry. As the Noether's Theorem states, every symmetry of nature yields a conservation law, and conversely every conservation law reflects an underlying symmetry. The Standard Model is built on the gauge principle, which means that the complete Lagrangian that corresponds to the interactions between the elementary

particles is invariant under local phase transformations. To illustrate this idea, one can consider the Dirac Lagrangian (for example, a free electron or positron):

$$\mathcal{L}_{free} = i\bar{\psi}\gamma^{\mu}\partial_{\mu}\psi - m\bar{\psi}\psi \tag{1.1}$$

where ψ is a massive Dirac field with mass m, γ^{μ} are the Dirac matrices[3]. This Lagrangian is invariant under the following global phase transformation:

$$\psi \rightarrow e^{iq\theta}\psi \tag{1.2}$$

where q is the electric charge of the particle, and the phase factor θ can be any real number that is independent of space or time. However, this holds no more when it comes to local transformation:

$$\psi \rightarrow e^{iq\theta(x)}\psi \tag{1.3}$$

Because the derivative of $\theta(x)$ gives an extra term. In order to restore the invariance, one can introduce a new massless vector field A_{μ} to soak up the extra term, by replacing:

$$\partial_{\mu} \rightarrow \partial_{\mu} + iqA_{\mu} \tag{1.4}$$

where $D_{\mu} = \partial_{\mu} + iqA_{\mu}$ is called "covariant derivative". The new field A_{μ} itself changes under the local transformation as:

$$A_{\mu} \rightarrow A_{\mu} - \partial_{\mu}\theta(x) \tag{1.5}$$

Now, after requiring local invariance and introducing the vector field A_{μ}, the complete Lagrangian becomes:

$$\mathcal{L} = i\bar{\psi}\gamma^{\mu}\partial_{\mu}\psi - m\bar{\psi}\psi - \frac{1}{16\pi}F^{\mu\nu}F_{\mu\nu} - (q\bar{\psi}\gamma^{\mu}\psi)A_{\mu} \tag{1.6}$$

where $F_{\mu\nu} = (\partial^{\mu}A^{\nu} - \partial^{\nu}A^{\mu})$, γ^{μ} are the Dirac matrices mentioned above. Equation 1.6 can be written as:

$$\mathcal{L} = \mathcal{L}_{free} - qJ^{\mu}A_{\mu} \tag{1.7}$$

where $J^{\mu} = \bar{\psi}\gamma^{\mu}\psi$ is the electromagnetic current density, and the introduced vector field A_{μ} is known as the photon field.

It is convenient to use the group theory to study symmetries. The transformation above could be considered as multiplication of ψ by a unitary matrix (in this case, $U = e^{i\theta}$):

$$\psi \to U\psi, U^{\dagger}U = 1 \tag{1.8}$$

The group of all such matrices is $U(1)$. The full gauge symmetry group of the Standard Model is $SU(3)_C \otimes SU(2)_L \otimes U(1)_Y$: the strong force is described by the Quantum Chromo-Dynamics (QCD), which is a gauge theory with $SU(3)_C$ symmetry, based on the conservation of the color charge (C). The electromagnetic and weak interactions are unified, together described by the Glashow-Weinberg-Salam (GWS) electroweak theory based on the conservation of left-handed isospin (L) and hypercharge (Y). The corresponding gauge symmetry group is $SU(2)_L \otimes U(1)_Y$.

1.1.2 The Standard Model Lagrangian

As introduced above, the Standard Model Lagrangian is invariant under the local gauge transformations. It can be divided into four parts:

$$\mathcal{L}_{SM} = \mathcal{L}_{fermions} + \mathcal{L}_{gauge} + \mathcal{L}_{Higgs} + \mathcal{L}_{Yukawa} \tag{1.9}$$

The first two components describe the kinetic energies and interactions of the fermion and gauge bosons. The rest, Higgs sector ($\mathcal{L}_{Higgs} + \mathcal{L}_{Yukawa}$), is the key for the massive particles to acquire mass. This subsection focuses on the fermion and gauge fields, introducing their kinetic terms and their couplings.

The fermion and gauge boson fields

Any free particle in the SM can be described by a relativistic field. The SM fermions are all Dirac fermions except for the neutrinos.[2] The kinetic term of a Dirac fermion ψ is given by:

$$i\bar{\psi}\gamma^{\mu}\partial_{\mu}\psi \tag{1.10}$$

Note that the left-handed and right-handed fermion fields are not mixed in the SM as a consequence of the $SU(2)_L$ symmetry. By absorbing the matrix $(1-\gamma^5)$ where $\gamma^5 = i\gamma^0\gamma^1\gamma^2\gamma^3$, the left-handed fermion fields are treated as $SU(2)_L$ doublets:

[2] It is not determined yet wether the neutrinos are Dirac fermions or Majorana fermions (each particle is also its own anti-particle).

$$f_L = \frac{1-\gamma^5}{2} f \tag{1.11}$$

and the right-handed fields are treated as singlets:

$$f_L = \frac{1+\gamma^5}{2} f \tag{1.12}$$

In addition, considering the $U(1)_Y$ symmetry, the left-handed and right-handed fermions also have different weak hypercharges Y. The relation of the hypercharge, the electric charge (Q) and the third component of isospin (I^3, or "weak isospin") is given by the Gell-Mann-Nishijima formula:

$$Q = I^3 + \frac{1}{2}Y \tag{1.13}$$

Then, the kinetic term and self-interactions of the gauge boson fields is given by:

$$\mathcal{L}_{gauge} = -\frac{1}{4}G^a_{\mu\nu}G^{\mu\nu}_a - \frac{1}{4}W^a_{\mu\nu}W^{\mu\nu}_a - \frac{1}{4}B_{\mu\nu}B^{\mu\nu} \tag{1.14}$$

The three gauge fields, G, W and B correspond to the generators of each of the sub-groups of $SU(3)_C \otimes SU(2)_L \otimes U(1)_Y$. $G^a_{\mu\nu}$ is the gluon tensor where index a labels elements of the eight generators of $SU(3)_C$. Similarly, $W^a_{\mu\nu}$ is the gauge field tensor of $SU(2)_L$, where index a runs over its three generators. Gauge field B_μ corresponds to generator of $U(1)_Y$ group, and the gauge field tensor is denoted by $B_{\mu\nu}$. The three field strength tensors are defined as:

$$G^a_{\mu\nu} = \partial_\mu G^a_\nu - \partial_\nu G^a_\mu + g_s f^{abc} G^b_\mu G^c_\nu \tag{1.15}$$

$$W^a_{\mu\nu} = \partial_\mu W^a_\nu - \partial_\nu W^a_\mu + g_2 \varepsilon^{abc} G^b_\mu G^c_\nu \tag{1.16}$$

$$B_{\mu\nu} = \partial_\mu B_\nu - \partial_\nu B_\mu \tag{1.17}$$

where g_s and g_2 (or named as g_w) are the strong and weak coupling constants respectively, f^{abc} and ε^{abc} are tensors that serve different symmetry group: for the $SU(3)$ group, the generators λ^a (Gell-Mann matrices) follow the communication relation $[\lambda^a, \lambda^b] = i f^{abc} \lambda^c$, where f^{abc} (a, b, c = 1, 2, ...8) is the structure constant of $SU(3)$; similarly, the generators T^a of $SU(2)$ follow the communication relation $[T^a, T^b] = i\varepsilon^{abc} T^c$, where ε^{abc} is called the Levi-Civita symbol (also named as permutation symbol, antisymmetric symbol, or alternating symbol). In the case of $U(1)$ group, the generators do commute and follow $[Y^a, Y^b] = 0$, which is different from the other two non-abelian group. It means that the G and W fields can self-interact while the B cannot, as seen in Eq. 1.15. Furthermore, to determine the couplings between the fermions and gauge bosons, the quantum chromodynamics theory and the electroweak theory are briefly introduced below.

Quantum chromodynamics

Quantum chromodynamics (QCD) describes the strong interactions between the colored particles, i.e. the quarks and the gluons. The strong coupling constant, which determines the strength of the chromodynamic force is given by:

$$g_s = \sqrt{4\pi\alpha_s} \tag{1.18}$$

or equivalently $\alpha_s = g_s^2/4\pi$. The strong coupling constant can be thought as the fundamental unit of color charge. Furthermore, it becomes asymptotically weaker as the energy scale increases and the corresponding length scale decreases, known as *asymptotic freedom*. The coupling decreases approximately logarithmically as:

$$\alpha_s = \frac{g_s^2(k^2)}{4\pi} \approx \frac{1}{\beta_0 \ln \frac{k^2}{\Lambda^2}} \ (k^2 \gg \Lambda^2) \tag{1.19}$$

where k is a renormalization scale of the given physical process; $\beta_0 = (11n - 2f)/12\pi$ is a constant, with n and f denotes the number of the colors (3 in the SM) and flavors of the quarks (6 in the SM); Λ is the QCD scale.

The specification of a quark state requires its momentum, spin and the color. A three element column vector c gives the color of a quark in QCD:

$$c = \begin{pmatrix}1\\0\\0\end{pmatrix} \text{ for red}, \quad \begin{pmatrix}0\\1\\0\end{pmatrix} \text{ for blue}, \quad \begin{pmatrix}0\\0\\1\end{pmatrix} \text{ for green}$$

At a quark-gluon vertex, the quark color changes and the difference before and after the interaction is carried by the gluon. Each gluon carries one unit of color and one unit of anticolor, resulting in nine different color states. Practically, the gluons are the linear combinations of these color states. The nine states constitute a "color octet":

$$(r\bar{b} + b\bar{r})/\sqrt{2} \tag{1.20}$$
$$-i(r\bar{b} - b\bar{r})/\sqrt{2} \tag{1.21}$$
$$(r\bar{g} + g\bar{r})/\sqrt{2} \tag{1.22}$$
$$-i(r\bar{g} - g\bar{r})/\sqrt{2} \tag{1.23}$$
$$(b\bar{g} + g\bar{b})/\sqrt{2} \tag{1.24}$$
$$-i(b\bar{g} - g\bar{b})/\sqrt{2} \tag{1.25}$$
$$(r\bar{r} - b\bar{b})/\sqrt{2} \tag{1.26}$$
$$(r\bar{r} + b\bar{b} - 2g\bar{g})/\sqrt{6} \tag{1.27}$$

and a "color singlet":

$$(r\bar{r}+b\bar{b}+g\bar{g})/\sqrt{3} \tag{1.28}$$

In our universe, there are only eight gluons. This fact involves another important feature of the QCD theory, *quark confinement*, which requires all the naturally occuring particles to be color singlets. The octet gluons as free particles are therefore forbidden, while the singlet gluons are allowed to be free particles as a mediator of long-range force[3] between two color singlets. However, the strong force observed in our universe is practically of quite short range. The singlet gluon is absent, which also indicates that the symmetry of QCD theory is $SU(3)$, not $U(3)$ that requires all the nine gluons. As a consequence of quark confinement, the quarks exist with the form of colorless mesons ($q\bar{q}$) and baryons (qqq). When two quarks are separated to a certain extent, the potential energy due to separation would be large enough to produce a new quark-antiquark pair. This process is called "hadronization", which is the reason we see jets instead of single quarks in the accelerators.

In the end, the QCD Lagrangian with quark field q_f with flavor f is given by:

$$\mathcal{L}_{QCD} = -\frac{1}{4}G^a_{\mu\nu}G^{\mu\nu}_a + \sum_f \bar{q_f}(i(\gamma^\mu D_\mu) - m_f)q_f \tag{1.29}$$

with the covariant derivative D_μ replacing ∂_μ:

$$D_\mu = \partial_\mu + i\frac{g_s\lambda_a}{2}G^a_\mu \tag{1.30}$$

where G is the gluon field strength tensor, λ_a are the Gell-Mann matrices mentioned before.

The electroweak theory

The electromagnetic and weak interactions are unified by the electroweak theory (also named as Glashow-Weinberg-Salam theory). The couplings between fermions and electroweak bosons can be determined using the following covariant derivative to replace ∂_μ:

$$D_\mu = \partial_\mu - ig_2T_aW^a_\mu - ig_1\frac{Y}{2}B_\mu \tag{1.31}$$

where g_1 and g_2 are the coupling constants of $SU(2)$ and $SU(1)$, T_a is the $SU(2)$ generator mentioned before, Y is the hypercharge. Remember the left-handed fermion

[3] Similarly to the electrodynamics, the gluons mediate a force of infinite range as they are massless.

fields are $SU(2)$ doublets and right-handed fields are singlets, denote as (take electron, the first lepton generation as an example[4]):

$$L = \begin{pmatrix} \nu_e \\ e^- \end{pmatrix}_L, \; R = e_R^-$$

and the Lagrangian of the electroweak interactions is hence given by:

$$\mathcal{L}_{EW} = \frac{g_2}{2}[\bar{\nu_L}\gamma^\mu \nu_L W_\mu^3 - \sqrt{2}\bar{\nu_L}\gamma^\mu e_L W_\mu^+ - \sqrt{2}\bar{e_L}\gamma^\mu \nu_L W_\mu^- - \bar{e_L}\gamma^\mu e_L W_\mu^3] \tag{1.32}$$

$$-\frac{g_1}{2}[Y_L(\bar{\nu_L}\gamma^\mu \nu_L) - Y_R \bar{e_R}\gamma^\mu e_R]b_\mu \tag{1.33}$$

where $W_\mu^\pm$ are physical fields of charged W bosons. In the electroweak theory, the physical weak boson fields (charged $W_\mu^\pm$, neutral Z_μ) and photon field (A_μ) are determined through linear combinations of the W and B fields:

$$W_\mu^\pm = \frac{1}{\sqrt{2}}(W_\mu^1 \mp i W_\mu^2) \tag{1.34}$$

$$Z_\mu = \frac{-g_1 B_\mu + g_2 W_\mu^0}{\sqrt{g_1^2 + g_2^2}} \tag{1.35}$$

$$A_\mu = \frac{g_2 B_\mu + g_1 W_\mu^0}{\sqrt{g_1^2 + g_2^2}} \tag{1.36}$$

For convenience, one can define the weak mixing angle (Weinberg angle):

$$\sin\theta_W = \frac{g_1}{\sqrt{g_1^2 + g_2^2}} \tag{1.37}$$

Note that so far the mass term is not included in the Lagrangian, since it breaks the local gauge symmetry. We need the Higgs sector term $\mathcal{L}_{Higgs} + \mathcal{L}_{Yukawa}$ to complete our SM Lagrangian, which is introduced in the next section.

1.1.3 Spontaneous symmetry breaking and the Higgs mechanism

The idea of spontaneous symmetry breaking is quite subtle. The calculation of quantum field theory is a perturbation procedure, which means we always start from the ground state ("vacuum") and have the fields fluctuate around the ground state. Although the Lagrangian is invariant under the gauge transformation, however the vacuum may not share the symmetry of the Lagrangian, as the vacuum state is not necessarily zero. Since no external action is responsible in this case, we call it "spontaneous" symmetry breaking.

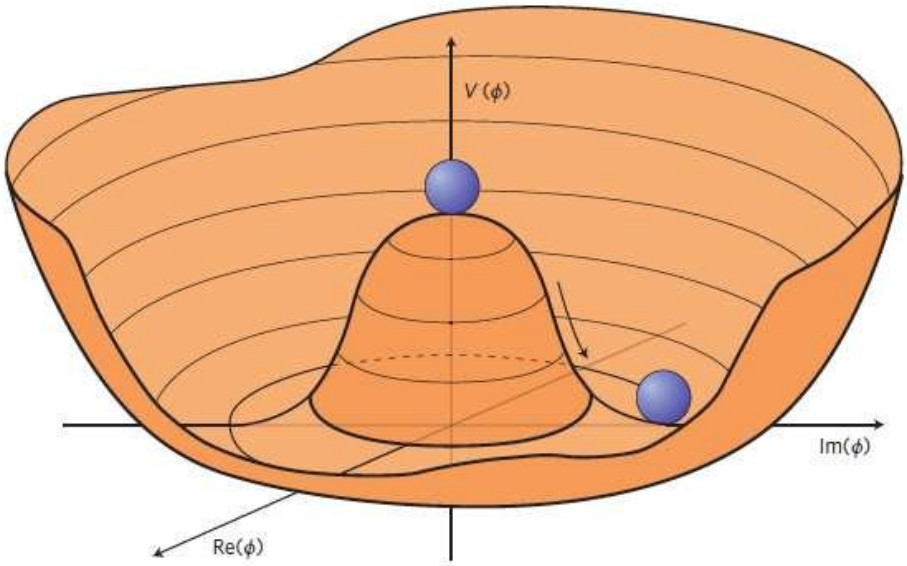

Figure 1.2 – The potential $V(\phi)$ for a complex scalar field with $\mu^2 < 0$.[5]

A simple scenario could be used to illustrate spontaneous symmetry breaking and how the mass term of the given particle appears as a consequence. Consider the following Lagrangian of a simple complex scalar field $\phi = (\phi_1 + i\phi_2)/\sqrt{2}$:

$$\mathcal{L} = \partial_\mu \phi^\dagger \partial^\mu \phi - V(\phi) \tag{1.38}$$

with potential energy density $V(\phi) = \mu^2 \phi^\dagger \phi + \lambda(\phi^\dagger \phi)^2$. For $\mu^2 > 0$ and $\lambda > 0$, it is easy to find that the minimum of $V(\phi)$ corresponds to $\phi_1 = \phi_2 = 0$. However, for $\mu^2 < 0$ and $\lambda > 0$, the shape of $V(\phi)$ becomes a "Mexican hat", as illustrated in Fig. 1.2. The minimum of $V(\phi)$ is now a continuous set on the $(\phi_1,\ \phi_2)$ plane:

$$\sqrt{\phi_1^2 + \phi_2^2} = \sqrt{\frac{-\mu^2}{\lambda}} = v \tag{1.39}$$

To expand around a particular vacuum state, we could choose $\phi_1 = v$, $\phi_2 = 0$, and introduce the following new fields:

$$\eta = \phi_1 - v, \quad \xi = \phi_2 \tag{1.40}$$

which are the fluctuations around the selected vacuum state. Therefore, the Lagrangian (Eq. 1.38) can be rewritten as (higher order terms of η and ξ are not shown):

$$\mathcal{L} = [\frac{1}{2}(\partial_\mu \eta)(\partial^\mu \eta) - (\lambda v^2)\eta^2] + [\frac{1}{2}(\partial_\mu \xi)(\partial^\mu \xi) + 0 \times \xi^2] + ... \tag{1.41}$$

It can be seen from the last line that two particles are generated from the spontaneous symmetry breaking. The first term is a free Klein-Gordon Lagrangian corresponding to a massive field η with mass $m_\eta = \sqrt{-2\mu^2}$; the second term is a free Lagrangian corresponding to a massless field ξ.

Then, then Higgs mechanism is nothing but the spontaneous breaking of the electroweak symmetry $SU(2)_L \otimes U(1)_Y$. Simply replace ϕ with a complex $SU(2)$ doublet scalar field Φ:

$$\Phi = \begin{pmatrix} \phi^+ \\ \phi^0 \end{pmatrix} = \frac{1}{\sqrt{2}} \begin{pmatrix} \phi_3 + i\phi_4 \\ \phi_1 + i\phi_2 \end{pmatrix}$$

The corresponding Lagrangian and potential energy density are given by:

$$\mathcal{L}_{Higgs} = (D^\mu \Phi)^\dagger (D_\mu \Phi) - V(\Phi), \quad V(\Phi) = \mu^2 \Phi^\dagger \Phi + \lambda (\Phi^\dagger \Phi)^2 \tag{1.42}$$

where D^μ is the covariant derivative, given in Eq. 1.31. In the case $\mu^2 < 0$, we also have the "Mexican-hat" shaped potential, meaning the electroweak symmetry is broken. To expand the Lagrangian around the vacuum state, we have:

$$\Phi = \frac{1}{\sqrt{2}} \begin{pmatrix} 0 \\ v + h \end{pmatrix}$$

where h is the introduced Higgs field. Hence, the first term of the Lagrangian (1.42) gives:

$$(D^\mu \Phi)^\dagger (D_\mu \Phi) = \frac{1}{2} \partial_\mu h \partial^\mu h + \frac{(v+h)^2}{8} (2 g_1^2 W_\mu W^\mu + (g_1^2 + g_2^2) Z_\mu Z^\mu) \tag{1.43}$$

The mass terms of the three vector bosons can then be extracted, assigning masses to the $W^\pm$, Z bosons and the photon:

$$m_W^2 = \frac{1}{4} g_1^2 v^2, \quad m_Z^2 = \tfrac{1}{4}(g_1^2 + g_2^2) v^2, \quad m_A = 0 \tag{1.44}$$

Note that the $U(1)$ symmetry actually remains unbroken and the photon is therefore massless. In addition, one can also find the following relation between the W and Z masses:

$$\frac{m_W}{m_Z} = \frac{g_1}{\sqrt{g_1^2 + g_2^2}} = \cos(\theta_w) \tag{1.45}$$

The mass of W boson is related to the Fermi coupling constant $G_F = 1.166 \times 10^{-5}$ GeV^{-2}[6], which means we can measure the vacuum expectation v via G_F:

$$m_W = \frac{g_1}{2\sqrt{\sqrt{2}G_F}}, \quad v = \sqrt{\frac{1}{\sqrt{2}G_F}} \tag{1.46}$$

The measured value of v through the measurement of the life time of muons[7] is around 246 GeV.

Finally, the mass term of the fermions is introduced by including the gauge invariant Yukawa interaction term between the fermion fields ψ and scalar (Higgs) fields Φ, with form $\mathcal{L} = -g\bar{\psi}\Phi\psi$ (g is the coupling constant). Taking electrons as an example: after the spontaneous symmetry breaking (i.e. replacing the Higgs field as an fluctuation around the vacuum expectation value v), the full Yukawa Lagrangian with electron field e and Higgs field H becomes:

$$\mathcal{L}_{Yukawa} = -\frac{1}{\sqrt{2}}\lambda_e(v+H)\bar{e_L}e_R \tag{1.47}$$

from which the electron mass is given by $m_e = \lambda_e v/\sqrt{2}$, and the coupling between electron and Higgs boson is given by $\lambda_e/\sqrt{2}$, which is proportional to m_e.

1.1.4 The production and decay of Higgs boson

The properties of the Higgs boson, especially its production and decay at the Large Hadron Collider (LHC) are briefly summarized in this section. Driven from Eq. 1.42, the mass and kinetic terms of the Higgs boson itself is given by:

$$\mathcal{L}_{Higgs} = \frac{1}{2}(\partial^\mu h)^2 - \lambda v^2 h^2 - \lambda v h^3 - \frac{1}{4}\lambda h^4 \tag{1.48}$$

Therefore the mass of Higgs boson is $m_h = \sqrt{2\lambda v^2}$. The Higgs mass is not predicted in the Standard Model since λ is a free parameter of the Standard Model. Experimentally, the measured SM Higgs mass is around 125 GeV[8]. Equation 1.48 also indicates the existence of the self-interaction of the Higgs boson.

Figure 1.3 shows the lowest-order Feynman diagrams of five Higgs production processes with the largest cross section at the LHC:

- gluon-gluon fusion ($gg \to H$);
- vector boson fusion ($qq \to Hqq$ via W^+W^- or $ZZ \to H$);
- associated production with vector (W or Z) boson ($q\bar{q} \to VH$);
- associated production with $t\bar{t}$ pair (gg, $q\bar{q} \to t\bar{t}H$).

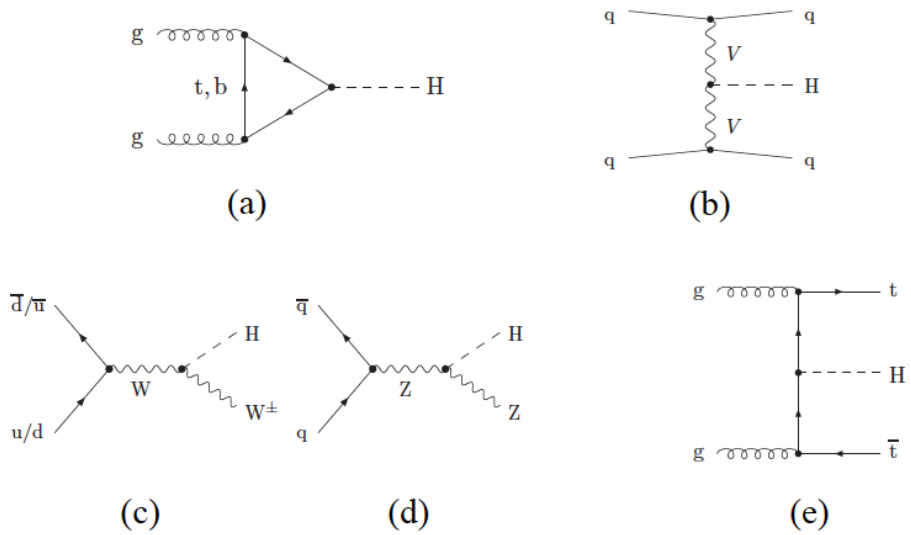

Figure 1.3 – The lowest-order Feynman diagrams for the five different Higgs boson production processes: (a) gluon-gluon fusion; (b) vector-boson fusion; associated production with W (c) or Z (d) vector boson; (e) associated production with $t\bar{t}$ pair.

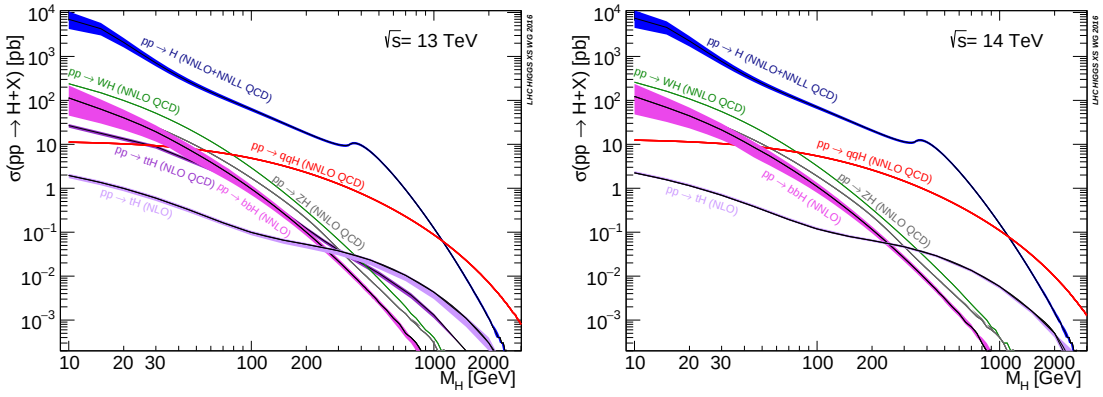

Figure 1.4 – The Higgs boson production cross sections as a function of Higgs mass (SM-like coupling, narrow-width assumption, no electroweak corrections applied) measured at $\sqrt{s} = 13$ (left) and 14 TeV (right).

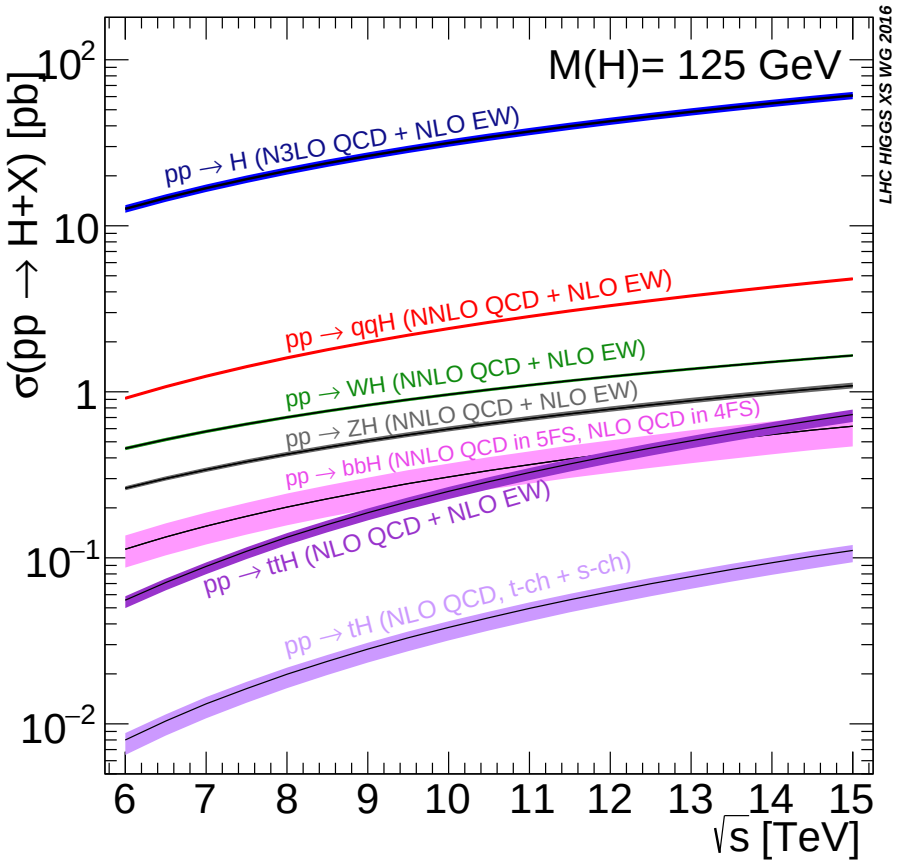

Figure 1.5 – The Higgs boson production cross sections as a function of centre-of-mass-energies for $m_H = 125$ GeV. The tH production cross section accounts for t-channel and s-channel computations only.

The evolution of the SM Higgs production cross section as a function of the Higgs mass for different production modes is shown in Fig. 1.4, at centre-of-mass collision energies of $\sqrt{s} = 13$ and 14 TeV. In addition, the cross section as a function of the centre-of-mass-energies is shown in Fig. 1.5 for a 125 GeV Higgs boson. It can be seen that the gluon-gluon fusion (ggF) through a heavy quark loop is the dominant production mode at the LHC, coming from the huge gluon-gluon statistics after the hadron collision. The production mode with second-largest cross section is vector boson fusion (VBF). The contributions from associate production with vector bosons (WH, ZH) or $t\bar{t}$ ($t\bar{t}H$) events are relatively small.

The masses of fermions and massive bosons comes from their coupling to the Higgs boson. Following the calculation from previous section, the Higgs boson coupling to the fermions and vector gauge bosons after the spontaneous symmetry breaking is given by:

$$g_{Hff} \propto \frac{m_f}{v}, \quad g_{HVV} \propto \frac{m_V^2}{v}, \quad g_{HHVV} \propto \frac{m_V^2}{v^2} \tag{1.49}$$

The Higgs boson is unstable and can decay to various pair of particles. Its partial decay widths are proportional to the Higgs couplings to the final state fermions or bosons given by Eq. 1.49, which means that the Higgs boson tends to decay to the heaviest particle allowed kinematically. Figure 1.6 shows the SM Higgs boson branching ratios of the main decay modes as well as the total decay width as a function of Higgs boson mass. In addition, the branching ratios as a function of Higgs mass in a smaller mass range near 125 GeV are shown in Fig. 1.7. It can be clearly seen that for the 125 GeV Higgs, the dominant decay mode is $H \to b\bar{b}$ since the b quark is the heaviest particle allowed in this case. The second-largest branching ratio is the WW^* decay mode, with one of the W boson produced off-shell. The branching ratios of the SM Higgs with mass of 125 GeV for different decay modes are summarized in Tab. 1.1.

A decay channel with high sensitivity does not necessary have high branching ratio. For example, the branching ratio of $H \to \gamma\gamma$ decay is quite low (0.23%), yet it was still one of the "golden channel" for the discovery of the SM Higgs boson thanks to the clean experimental signature and the excellent diphoton invariant mass resolution of the detectors. Figure 1.8 shows the leading-order Feynman diagrams of loop-induced decays to $\gamma\gamma$ or $Z\gamma$ events. Such processes are usually generated by loops via massive particles like W (dominant) and fermions in the diagrams.

1.1.5 Non-resonant diphoton production

Searches for the $\gamma\gamma$ final states suffer from the background coming from the non-resonant diphoton production, which will be discussed later in the analysis chapter. Figure 1.9 shows the leading-order Feynman diagrams of the different processes with non-resonant diphoton productions. The main contribution of diphoton events comes

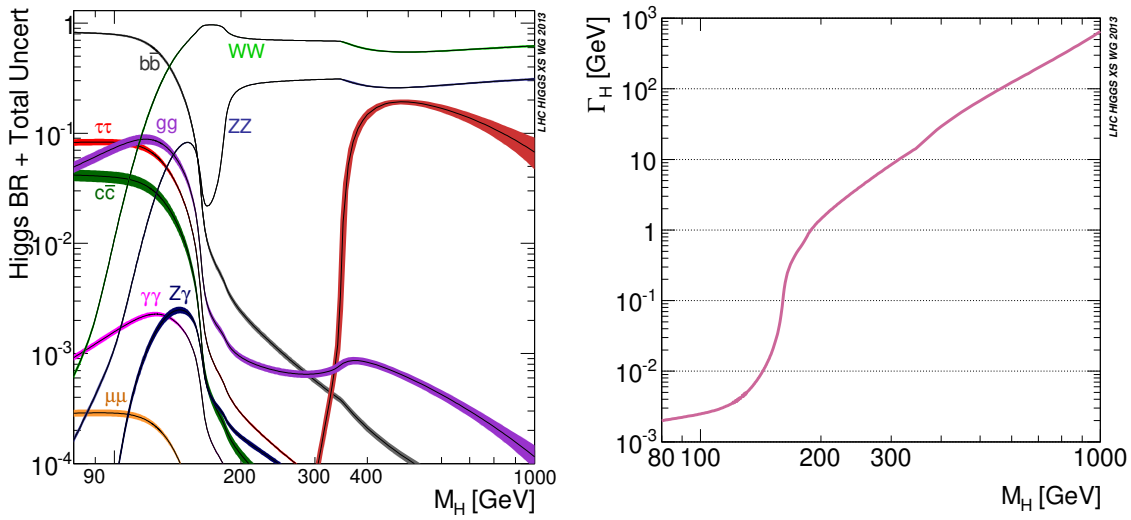

Figure 1.6 – The Standard Model Higgs boson decay branching ratio (left) and total width (right), as a function of the Higgs boson mass in a wide mass range.

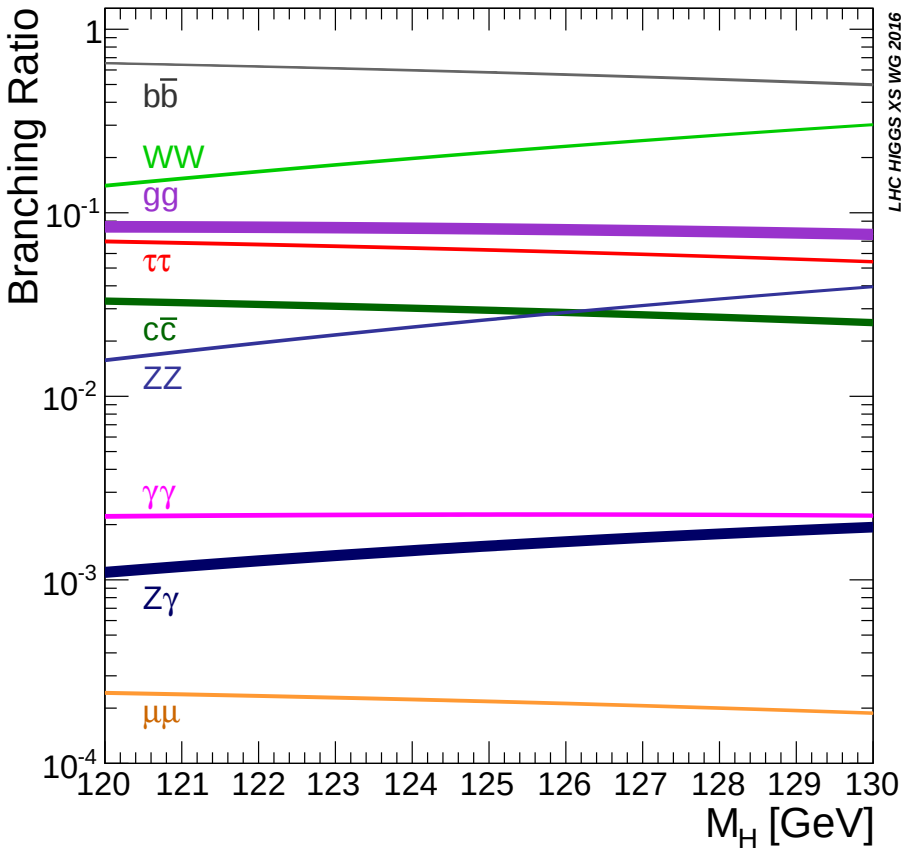

Figure 1.7 – The Standard Model Higgs boson decay branching ratio as a function of the Higgs boson mass, in the mass range from 120 to 130 GeV.

Decay modes	Branching ratio (%)
$H \to b\bar{b}$	58.24
$H \to WW^*$	21.37
$H \to \tau\tau$	6.27
$H \to ZZ^*$	2.62
$H \to \gamma\gamma$	0.23
$H \to Z\gamma$	0.15
$H \to \mu\mu$	0.02
others	11.10

Table 1.1 – The branching ratios of SM Higgs with mass of 125 GeV, provided by the Handbook of LHC Higgs Cross Sections.[9]

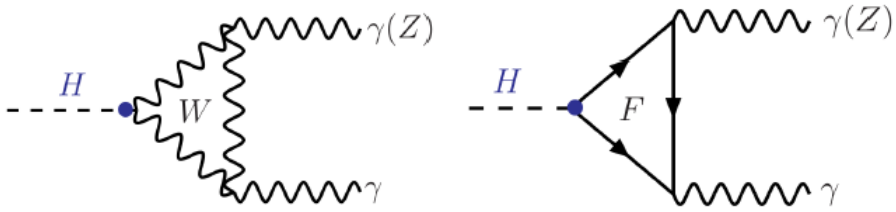

Figure 1.8 – The leading-order Feynman diagram of the $H \to \gamma\gamma$ ($H \to Z\gamma$) decay.

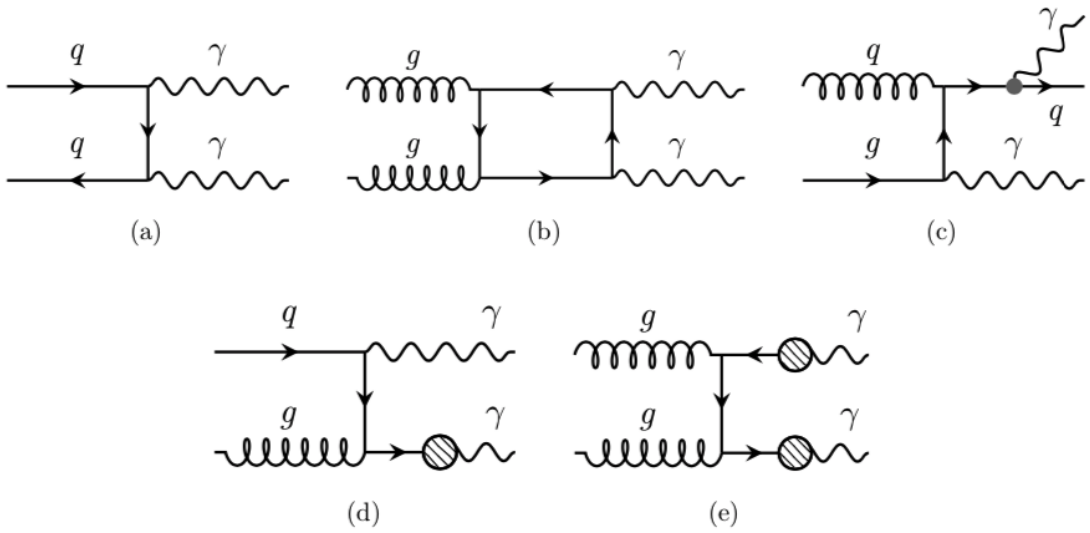

Figure 1.9 – The leading-order Feynman diagrams of (a) the Born process $qq \to \gamma\gamma$, (b) the box process $gg \to \gamma\gamma$, (c) the bremsstrahlung process $qg \to q\gamma\gamma$, the leading-order fragmentation process with one (d) or (e) two partons fragment into high-transverse momentum photons.

from direct production: the Born process ($qq \to \gamma\gamma$), the box process ($gg \to \gamma\gamma$), and the bremsstrahlung process ($qg \to q\gamma\gamma$). The photon in the $\gamma\gamma$ final state might also coming from the fragmentation process of a gluon or a quark. Another important background component comes from the photon-jet and multi-jet productions, since there is a chance that jets might be mis-identified as photons during the physical analysis. The cross section of such jet enriched production is very high, however its contribution is not as significant as the prompt $\gamma\gamma$ thanks to the strong suppression from the photon identification. In addition, the invariant mass spectrum of these processes has a smoothly falling shape, which is relatively easy to model.

1.2 Beyond the Standard Model

So far, the Standard Model is our most successful theory of particle physics. Most of its predictions have been confirmed by many experiments, and almost all the observed phenomena in the particle colliders all over the world are well explained. However, the standard Model is not a perfect, or complete theory. The SM fails to provide dark matter candidates or convincing explanations to the dark energy, massive neutrino or matter-antimatter asymmetry in our universe. Physicists are also expecting mechanism that breaks the CP symmetry in the strong interaction, however such violation has not been observed experimentally yet. Moreover, some problems of the SM always exist within its mathematical framework, e.g. the SM is not compatible with the general relativity, and therefore cannot explain the forth fundamental interaction, gravity. The hierarchy problem is also unsolved: some quantum corrections (e.g. on the Higgs mass) are so much larger than the effective value itself, and the fine tuning on this seems unnatural. In addition, there are a few experimental results that deviate a lot from the SM expectation, such as the famous anomalous magnetic dipole moment of muon. Answering to this kind of problem requires more precise and careful experiments as well.

Fortunately, solving the existing problems of the SM does not mean that we need to reject the whole theory. A lot of excellent ideas are raised by physicists known as "Beyond the Standard Model" (BSM), which are modifications of the SM in a subtle way so that the new models would still be consistent with the current data and observations. Two models are briefly introduced in this section as examples, and both of them predict new resonances in the diphoton final state. They can be seen as the physical motivation of the analysis part of this thesis.

1.2.1 The Two-Higgs-Doublet Models

As discussed in Sec. 1.1.3, the Standard Model assumes a simple scalar structure with only one $SU(2)$ doublet, while experimentally the existence of extended scalar

sectors is still allowed. The Two-Higgs-Doublet Models (2HDM)[10] are some of the simplest extension of the SM, which extend the SM Higgs sector into two scalar doublets. An additional Higgs doublet might be an elegant solution to many problems. For example, the 2HDMs are able to generate baryon asymmetry of the universe while the SM cannot[11]; an additional Higgs doublet is needed for cancellation of anomalies in supersymmetry[12]; with two Higgs doublets, it is also possible to imposing a global $U(1)$ symmetry, which is needed to deal with a CP-violating term in the QCD Lagrangian in the Peccei-Quinn model[13][14].

The 2HDMs are categorized according to the way the Higgs doublets couple to the quarks and leptons. There are four types of 2HDMs: Type-I, Type-II, $lepton-specific$ and $flipped$ models. A serious potential problem of general 2HDMs is the existence of tree-level flavour-changing neutral currents (FCNC), which are excluded by the data. A solution to circumvent this problem is to impose discrete symmetries. The four types of 2HDMs mentioned above are all free from the flavour-changing neutral current, although models with tree-level FCNCs also exist, such as the Type-III model listed in Tab. 1.2, together with the coupling of the two doublets Φ_1 and Φ_2 with the fermions.

Type	u_R^i	d_R^i	e_R^i
Type-I[4]	Φ_2	Φ_2	Φ_2
Type-II	Φ_2	Φ_1	Φ_1
Lepton-specific	Φ_2	Φ_2	Φ_1
Flipped	Φ_2	Φ_2	Φ_1
Type-III	Φ_1, Φ_2	Φ_1, Φ_2	Φ_1, Φ_2

Table 1.2 – The five types of Two-Higgs-doublet models and the couplings of the scalar doublets to different fermions: right-handed up quarks, right-handed down quarks and charged right-handed leptons. The superscript i is a generation index. By convention, the right-handed up quark u_R^i always couple to Φ_2.

One can rewrite the Higgs potential in Eq. 1.42 for two complex scalar doublets under some necessary assumptions (e.g. CP conservation in the Higgs sector). After symmetry breaking, minimization of this potential ends up in eight fields, among which three are used to generate mass for the $W^{\pm}$ and Z bosons; the five remaining fields are physical states. There is one neutral CP-odd pseudoscalar A, two charged Higgs $H^{\pm}$, and two neutral CP-even Higgs H and h with different masses. The free parameters of 2HDM are: the four Higgs masses m_h, m_H, m_A and $m_{H^{\pm}}$, the ratio between the two vacuum expectation values ($tan\beta = \frac{v_2}{v_1}$), and the mixing angle α of the neutral CP-even 2HDM Higgs bosons. With these parameters, we can express the 2HDM couplings in terms of the SM couplings.For example, the light CP-even Higgs

boson h coupling to WW^* or ZZ^* is given by the SM coupling multiplied by a factor of $sin(\beta-\alpha)$, and the coupling of the heavier Higgs H is given by the SM coupling multiplied by $cos(\beta-\alpha)$[10].[5] Assuming the SM Higgs discovered in 2012 with mass of 125 GeV being the neutral Higgs boson H or h, we might be able to discover the other one as well in the lower- or higher-mass region.

1.2.2 The Randall-Sundrum model

A new spin-2 resonance is predicted by the Randall-Sundrum (RS) model[15][16]. This mechanism was proposed for solving the hierarchy problem, where the electroweak scale ($M_{EW} \sim 10^{10}$ GeV) is much lower than the Planck mass scale ($M_{pl} \sim 10^{19}$ GeV).

To illustrate the RS model, we need to start with the central idea of the brane cosmology, *brane* and *bulk*. Our visible, three-dimensional universe is restricted to a "brane" inside a higher-dimensional space, called the "bulk" (or "hyperspace"). At least some of the extra dimensions of the bulk are extensive, so that other branes may be moving through this bulk. Assuming the simplest case: the higher dimensional spacetime is approximately a product of a 4-dimensional spacetime with a n-dimensional compact space. Then, the effective four-dimensional (reduced) Planck scale $\bar{M_{pl}}$ ($\bar{M_{pl}} = M_{pl}/\sqrt{8\pi}$) can be determined by the fundamental $(4+n)$-dimensional Planck scale M_*, and the geometry of the extra dimensions:

$$\bar{M_{pl}^2} = M_*^{n+2} V_n \tag{1.50}$$

where V_n is the n-dimensional volume of the compact space. By taking the compact space to be very large, the hierarchy between the weak scale and Planck scale may be eliminated.[17]

Particularly, the RS models describe our universe as a 5-dimensional warped-geometry[18] universe. There were two models with one extra dimension proposed in 1999 by Lisa Randall and Raman Sundrum: one is called RS1 model, which has a finite size of extra dimensions with two branes, one as each end; the other is called RS2 model, which has only one brane left since the other brane is placed infinitely far away. The following discussion is based on RS1 model. As illustrated in Fig. 1.10, it involves a finite 5-dimensional bulk that is extremely warped and contains two branes: the Planck brane (also called "gravity brane" where gravity is a relatively strong) and the TeV brane (also called "weak brane"). The trick is that all the SM particles and forces are confined to a 4-dimensional subspace (TeV brane), while gravity is free to propagate in the full spacetime (bulk). The exponential drop of the probability

[5] The coupling of the neutral Higgs bosons to the W and Z are the same for all the 2HDMs. The couplings to the charged Higgs are given by the 2HDM Yukawa Lagrangian, and are different in each model. The coupling of the pseudoscalar to vector bosons vanishes.

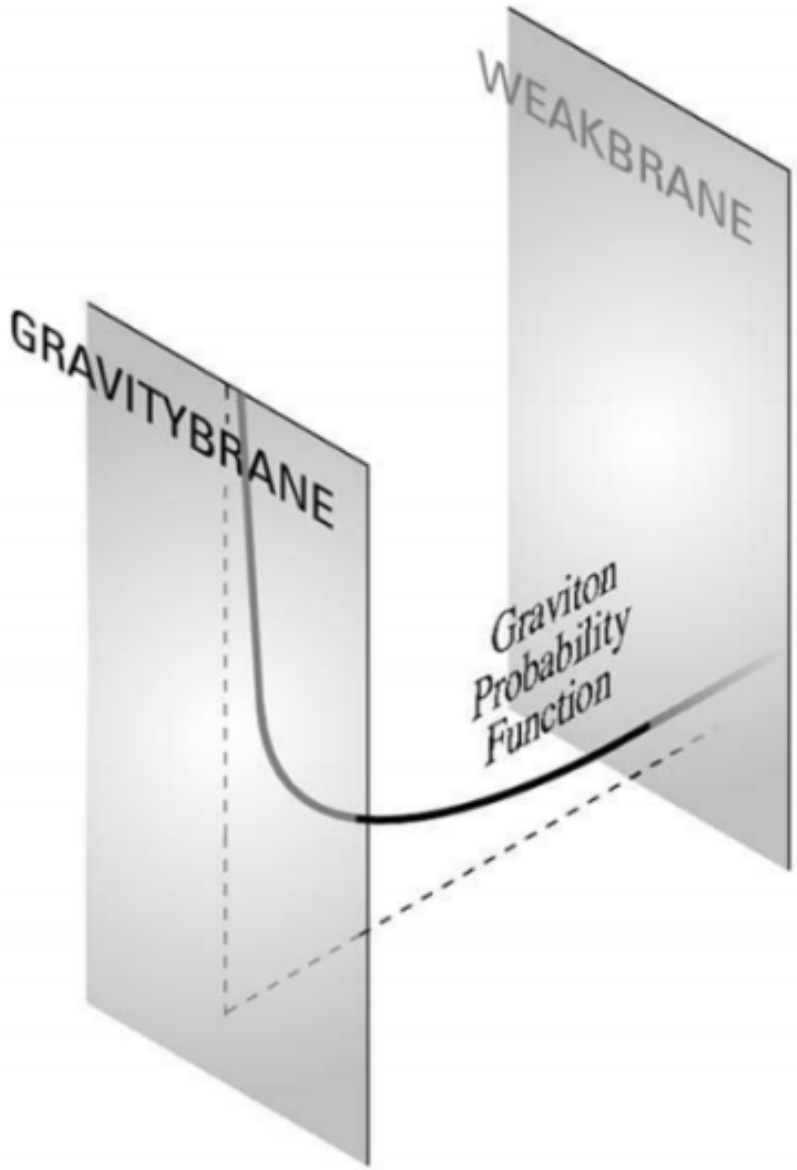

Figure 1.10 – Scheme of dimensions on RS1 theory. The Planck (Plank) and TeV branes are the 4-dimensional boundaries of the extra dimension.

function of the graviton indicates that the gravity would be much weaker on the TeV brane than on the Planck brane.

The resulting 5-dimensional metric is non-factorizable, given by:

$$ds^2 = e^{-2kr_c\phi}\eta_{\mu\nu}dx^\mu dx^\nu + r_c^2 d\phi^2 \tag{1.51}$$

where k and r_c are the curvature and compactification radius of the extra dimension; η is the Minkowski metric; x^μ are the traditional coordinates for the four dimensions; ϕ is the coordinate for the extra dimension, in the range $0 < \phi < \pi$. With reasonable kr_c (e.g. $kr_c \sim 12$), the hierarchy problem can be eliminated.

With the spacetime configured above, the TeV scale is related to the Planck scale, given by:

$$\Lambda_\pi = \bar{M}_{pl}\exp(-kr_c\pi) \tag{1.52}$$

When the graviton travels freely in the bulk, a series of massive graviton excitations come out as a consequence. This set of possible graviton mass values are called a Kaluza-Klein (KK) tower[19]. They are visible on the TeV brane, meaning that we could observe the KK gravitons just like other SM particles. The KK gravitons have spin 2, and a universal dimensionless coupling to the SM fields of $k/\bar{M}_{pl}$. Its mass m_{G^*} is splitted between the different KK levels on the TeV scale.

Chapter 2

The Large Hadron Collider and the ATLAS detector

2.1 The Large Hadron Collider

The world's largest and most powerful particle accelerator, the Large Hadron Collider (LHC) [12], is located beneath the France-Switzerland border near Geneva. It lies in the former Large Electron-Positron collider (LEP) [20][21] tunnel, which is 27 km in circumference, around 100 m underground.

The LHC is a two-ring-superconducting-hadron accelerator, designed to collide proton and heavy ion beams with a centre-of-mass energy up to 14 TeV. In December 1994, the approval of the LHC project was given by the European Organization for Nuclear Research (CERN). The construction of the LHC started in 1998. After the LEP was closed to liberate its tunnel in 2000, the LHC was finished in 2008 under the cooperation of many scientists, universities and laboratories across the world. Seven detectors, each designed for different purposes, are positioned at the four crossing points of the collider. There are four main experiments: ATLAS[22], CMS[23], LHCb[24] and ALICE[25]. The two high luminosity experiments, ATLAS (A Toroidal LHC ApparatuS) and CMS (Compact Muon Solenoid) are general-purpose detectors, both designed to operate at a peak luminosity of $L = 10^{34}$ cm^{-2}s^{-1} for proton operation. The low luminosity experiment LHCb (Large Hadron Collider beauty) is designed for B-physics, capable of data-taking at a peak luminosity of $L = 10^{32}$ cm^{-2}s^{-1}. The dedicated heavy ion experiment ALICE (A Large Ion Collider Experiment) is designed to study of the physics of strongly interacting matter at extreme energy densities, aiming at a peak luminosity of $L = 10^{27}$ cm^{-2}s^{-1} for nominal lead-lead ion operation.

On 10 September 2008, the first beam was circulated through the LHC. Nine days later, however, a magnet quench occurred and the collider had to be stopped. After one year of repairs and reviews from the consequential damages, the first operation run (Run 1) started on 20 November 2009. The proton beam energy was 3.5 TeV (corresponding to centre-of-mass energy of 7 TeV) in 2010, and increased to 4 TeV

($\sqrt{s} = 8$ TeV) in 2012. On 13 February 2013, the LHC was shut down for a two-year upgrade, enabling collisions at its designed energy and enhancing the detectors and pre-accelerators. After the Long Shutdown 1 (LS1), the second operation run (Run 2) started on 5 April 2015 with collision energy of 13 TeV. On 10 December 2018, the Long Shutdown 2 (LS2) started for the purposes of maintaining and upgrading of the LHC and ATLAS complex. After which, Run 3 is planned to start in February 2022. The implementation of the High Luminosity Large Hadron Collider (HL-LHC) project has been preparing since LS2, aiming to be used in Run 4 in the future. The beam parameters and hardware configuration are designed for the HL-LHC to reach a peak luminosity of 5×10^{34} cm^{-2}s^{-1}, allowing an integrated luminosity of 250 fb^{-1} per year[26].

2.1.1 The LHC injection chain

In order to accelerate protons and heavy ions to the required energy, a chain of accelerators is used as shown in Fig. 2.1. The LHC injection chain for protons is Linac 2 — Proton Synchrotron Booster (PSB) — Proton Synchrotron (PS) — Super Proton Synchrotron (SPS). The protons are first stripped of the hydrogen gas by an electric field. Then, the protons are injected into a linear accelerator Linac 2, and accelerated to a beam energy of 50 MeV before being injected into the PSB. The PSB accelerates the beam to 1.4 GeV, followed by the PS which accelerates the beam to 25 GeV. The protons are then injected to the SPS, and the beam energy increases to 450 GeV before they are finally transferred into the two beam pipes of the LHC.

The beams are guided to circulate in opposite directions in the accelerator ring of the LHC by the magnet system. 1232 dipole magnets are used to bend the beams, and 392 quadrupoles are used to focus them. The nominal dipole field is 8.33 T, corresponding to a beam energy of 7 TeV. However, the actual field attainable depends on the heat load and temperature margins inside the magnets, therefore a distribution system of liquid helium is designed to keep an operating temperature of 1.9 K for the magnets. In the rings of LHC, the proton beam energy are accelerated to a maximum of 7 TeV by the electric field in the radio frequency (RF) cavities, and then kept as a constant at this value. At the designed instantaneous luminosity of $L = 10^{34}$ cm^{-2}s^{-1}, $\sqrt{s} = 14$ TeV (7 TeV per beam), bunches containing up to 10^{11} protons will collide 40 million times per second.

2.1.2 Luminosity and performance

Figure 2.2 shows the cross sections of several processes of interest as a function of the centre-of-mass energy of proton-(anti)proton collisions. For a given the physics process with cross section σ_{process}, the event rate is $L \cdot \sigma_{event}$, where L is the instantaneous luminosity. The instantaneous luminosity reflects the characteristics of a certain

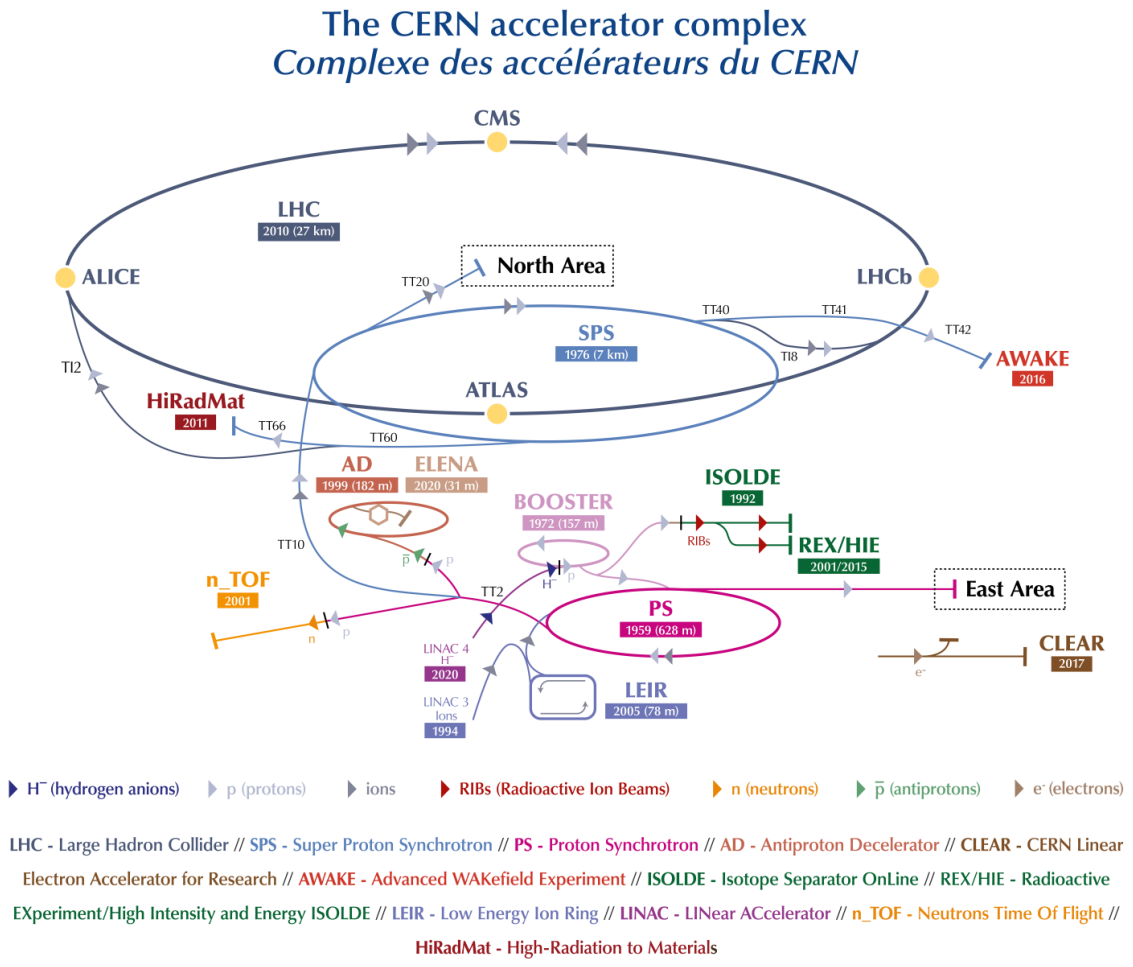

Figure 2.1 – The CERN accelerator complex.

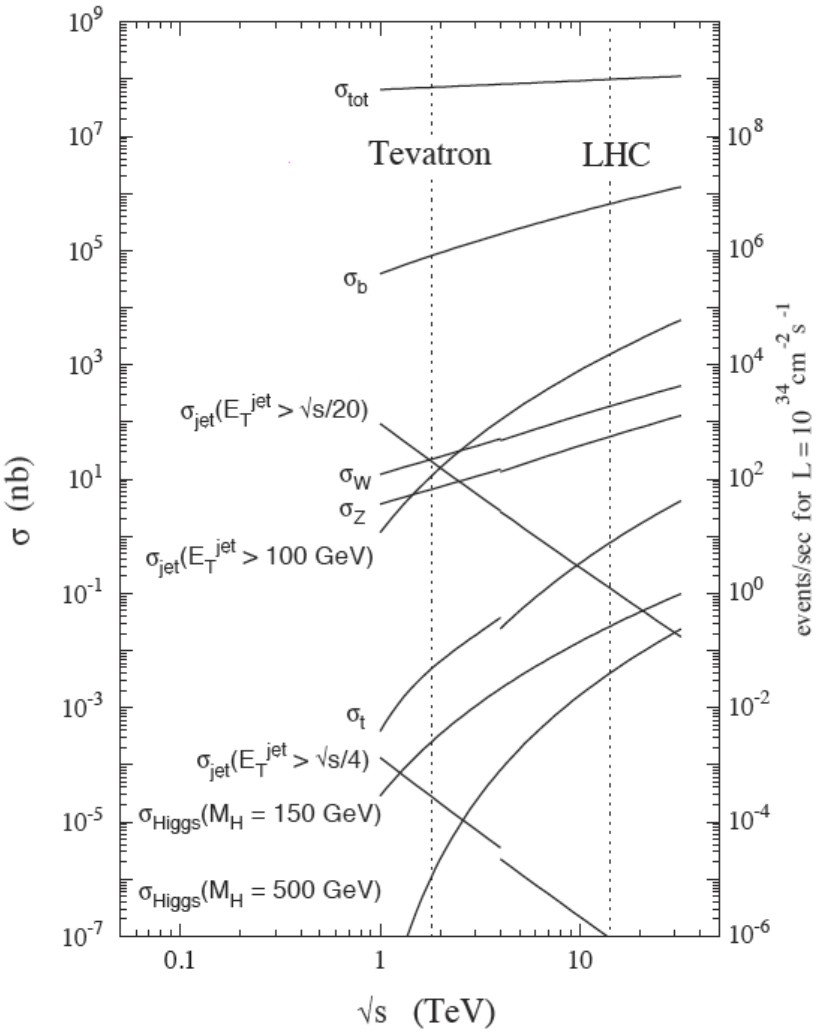

Figure 2.2 – Expected cross sections for specific physics processes as a function of the centre-of-mass energy $\sqrt{s}$. The dotted lines show the energies of two hadron collider (the proton-antiproton collider Tevatron at 1.96 TeV, and the LHC at 14 TeV).

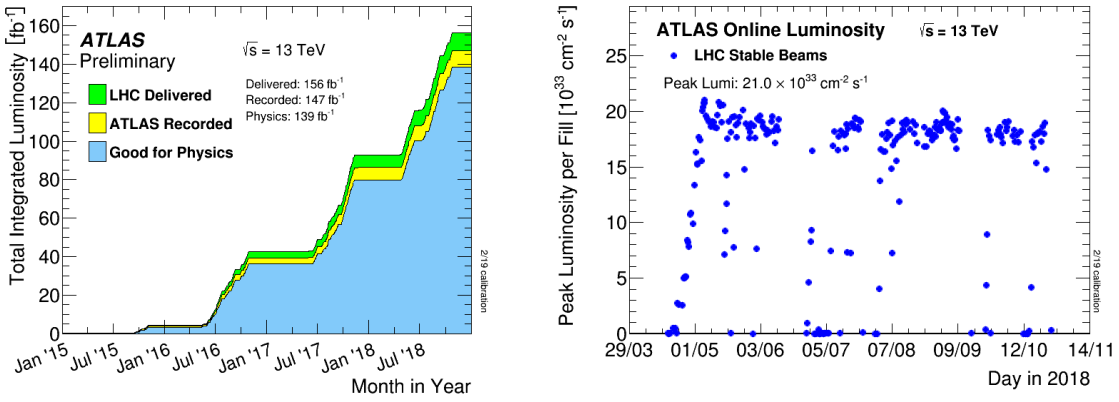

(a) (b)

Figure 2.3 – (a) Integrated luminosity versus time delivered to ATLAS (green), recorded by ATLAS (yellow), and certified to be good quality data (blue) during stable beams for pp collisions at 13 TeV centre-of-mass energy since 2015 to 2018. (b) The peak instantaneous luminosity delivered to ATLAS during stable beams for pp collisions at 13 TeV centre-of-mass energy is shown for each LHC fill as a function of time in 2018.

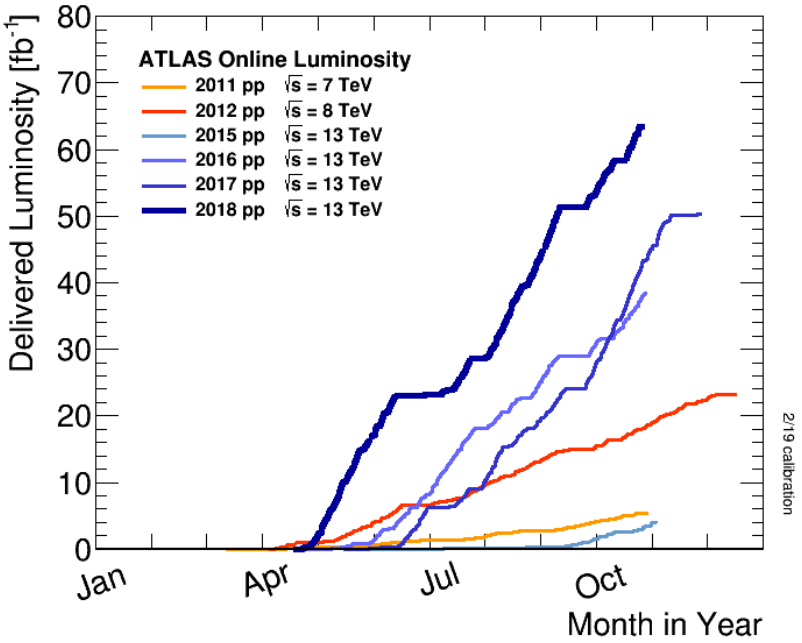

Figure 2.4 – Integrated luminosity versus day delivered to ATLAS during stable beams (p-p collisions only).

accelerator as it is given by:

$$L = \frac{N_b^2 n_b f \gamma}{4\pi\sigma_x\sigma_y} F, \tag{2.1}$$

where N_b is the number of particles per bunch, n_b is the number of bunches per beam, γ is the relativistic factor of the accelerated particles, f is the revolution frequency (11.2kHz for the LHC), $\sigma_{x,y}$ are the horizontal and vertical beam size (around 2.5 μm for the LHC), F is a geometrical correction factor from the crossing-angle of the two beams at the interaction point.

In order to maximize the physics reach of the LHC, the aim of the operation of the accelerator is to provide the highest integrated luminosity possible, calculated as $\mathcal{L} = \int L dt$. Figure 2.3 shows the total integrated luminosity and data quality in 2015-2018 (Run 2) and the peak luminosity per fill in 2018. So far, the LHC has reached its designed luminosity. The peak instantaneous luminosity gradually increased since Run 1, and even exceeded the designed value, reaching 2.1×10^{34} cm^{2}s^1 in 2018. During the whole Run 2, 156 fb^{-1} was delivered by the LHC. The ATLAS detector collected 147 fb^{-1} of pp (proton-proton) collisions, about 95% of the dataset is good for physics studies. The integrated luminosity delivered to ATLAS as a function of time for the year 2011 to 2018 is shown in Fig. 2.4.

As a result of the high instantaneous luminosity, the pileup, namely the additional pp collisions accompanying the hard scattering pp interactions of interest, becomes more significant and must be taken into account in the data analysis. There are two types of pileup:

- In-time pileup, occurring in the same bunch-crossing of the collision of interest.
- Out-of-time pileup, occurring in the previous or the following bunch-crossings of the collision of interest.

In order to quantify the pileup, the average number of interactions per bunch crossing, $< \mu >$, is usually calculated. This number is shown in Fig. 2.5 for each year in Run 2. For the whole Run 2, the average number of $\langle\mu\rangle$ is 33.7. The high pile-up condition has effects on the calibration and identification of the physics objects, requiring dedicated correction procedures.

2.2 The ATLAS detector

The largest general-purpose particle detector ever constructed, the ATLAS (A Toroidal LHC ApparatuS) detector, is installed in its experimental cavern at point 1 at CERN, as shown in 2.1. With the unprecedented energy and luminosity achieved by the LHC, the ATLAS detector was designed to search for new phenomena that involve highly massive particles which were not observed before with the former accelerators, and to measure the known physics processes with higher precision. Among which, the

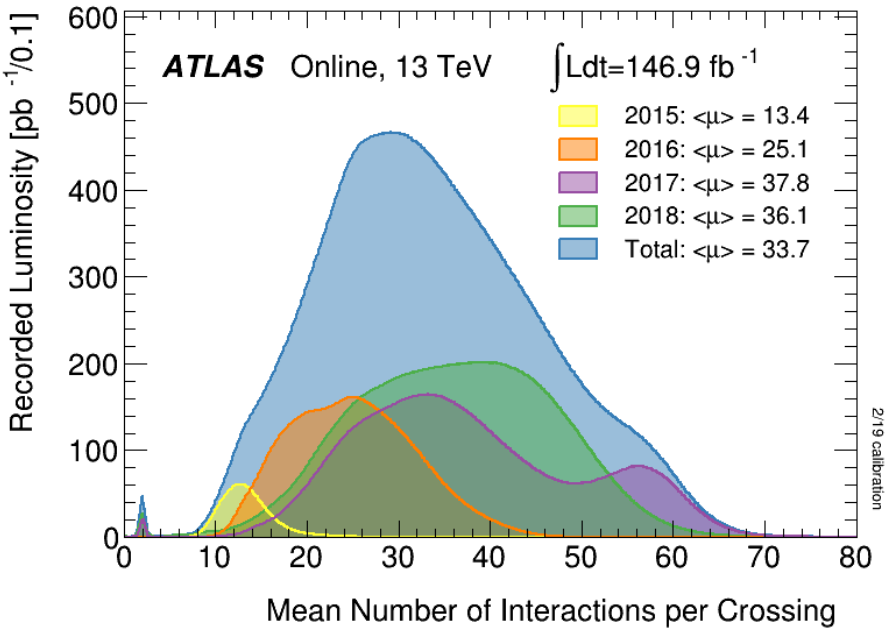

Figure 2.5 – Mean number of interactions per bunch crossing per year in Run 2.

most strong physical motivation is to search for the Higgs boson. In July 2012, the discovery of the Higgs boson was made by the ATLAS. The CMS collaboration has independently discovered the particle and announced the discovery at the same time.

The overall ATLAS detector layout is illustrated in Fig. 2.6. The detector is 44 meters long, 25 meters high, 25 meters in diameter and has a total weight of about 7,000 tons. The ATLAS detector is composed of three subsystems. From the inside out, there are the Inner Detector (ID), the Calorimeters, and the Muon Spectrometer (MS). The detector is forward-backward symmetric, each subsystem has multiple layers, and consists of a series of concentric cylinders (barrel) around the interaction point. For the purpose of a larger coverage, there are also disc-shaped components (end-cap) set along the beam direction. Functions of each detector complement each other: the Inner Detector provides a precise measurement of the trajectories and vertices of the charged particles, the Calorimeters provide the energy and position information of the stopped particles, and additional measurements of muons are given by the Muon Spectrometer. For charged particles, their tracks are bent by the magnet system and left in the ID and the MS. Considering the huge event rates coming from the *pp* collisions, a trigger system is installed in order to select the events of interest. The main performance goals are listed in Tab. 2.1.

The following right-handed Cartesian coordinate system is used by the ATLAS detector: the origin of the coordinate system is defined as the nominal interaction point of the proton beams, which is also the geometrical centre of the detector. The z-axis is defined as the beam direction that runs clock-wise, and the x-y plane is orthogonal to it. The positive x-axis is defined as pointing from the interaction point to the centre

of the LHC ring, while the positive y-axis points upwards. In the transverse plane x-y, the cylindrical coordinates are also used: the azimuthal angle Φ is defined around the beam axis, and the polar angle θ is defined with respect to the z-axis. The more commonly used value, pseudorapidity, is defined as $\eta = -\ln\tan(\theta/2)$.

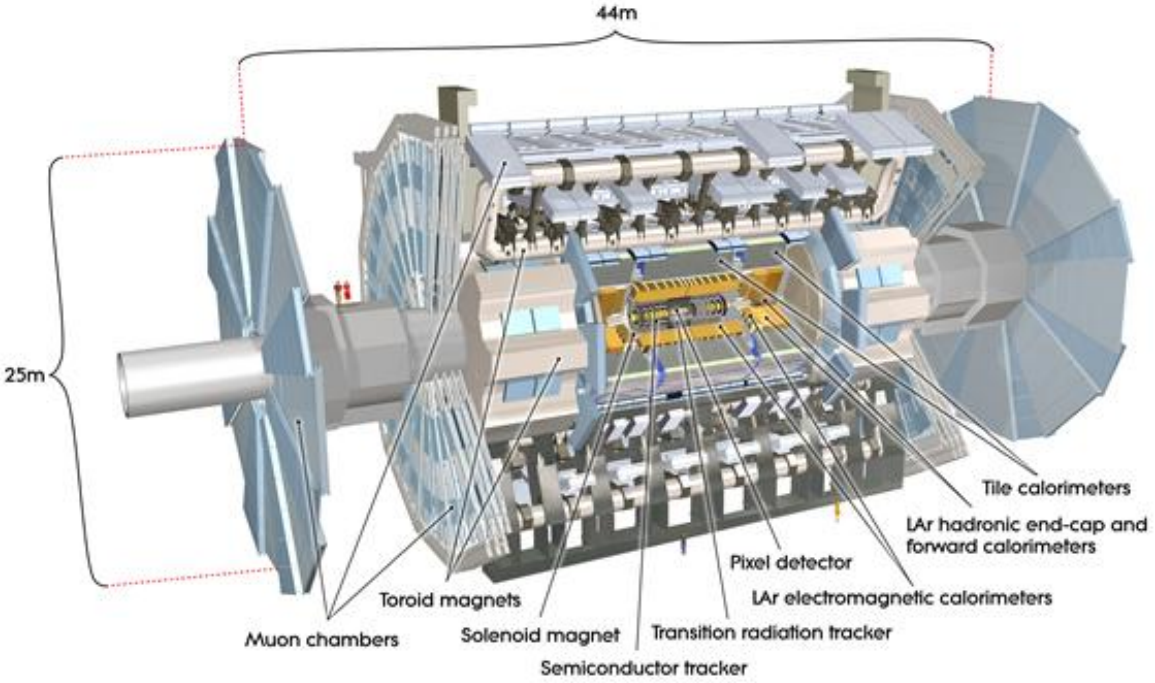

Figure 2.6 – The cut-away view of the ATLAS detector.

Detector component	Required resolution	η coverage	
		Measurement	Trigger
Tracking	$\sigma_{p_T}/p_T = 0.05\% p_T \oplus 1\%$	± 2.5	
Electromagnetic calorimetry	$\sigma_E/E = 10\%/\sqrt{E} \oplus 0.7\%$	± 3.2	± 2.5
Hadronic calorimetry (jet)			
barrel and end-cap	$\sigma_E/E = 50\%/\sqrt{E} \oplus 3\%$	± 3.2	± 3.2
forward	$\sigma_E/E = 100\%/\sqrt{E} \oplus 10\%$	$3.1 < \lvert\eta\rvert < 4.9$	$3.1 < \lvert\eta\rvert < 4.9$
Muon spectrometer	$\sigma_{p_T}/p_T = 10\%$ at $p_T = 1$ TeV	± 2.7	± 2.4

Table 2.1 – General performance goals of the ATLAS detector. The units for E and p_T are in GeV.

2.2.1 Inner detector

The Inner Detector is designed for an excellent momentum and position resolution. A general scheme of the ID and a sketch showing the detailed structures are shown

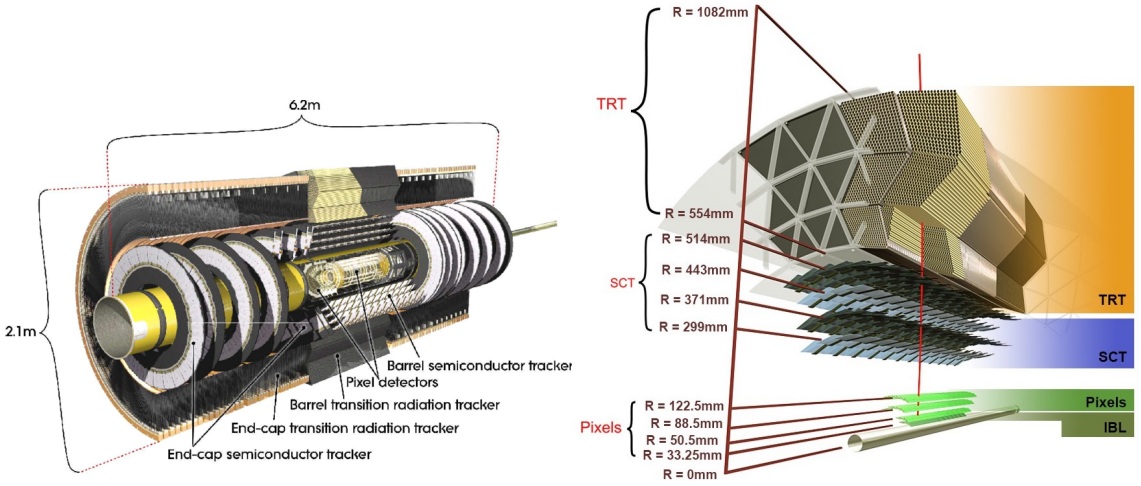

(a) (b)

Figure 2.7 – (a) The cut-away view of the ATLAS Inner Detector. (b) Sketch of the ID showing all its subsystems, including the new IBL.

in Fig. 2.7. The diameter of the Inner detector is about 2.1 meters, and the total length along the direction of the proton beam is 6.2 meters. The ID is placed in a 2 T axial magnetic field, provided by a surrounding superconducting solenoid. The motion of charged particles is tracked by detecting their interaction with the materials at various positions of the detector. From the inside out, the ID is composed of four sub-detectors: the Insertable B-Layer (IBL), the Pixel detector, the Semiconductor Tracker (SCT) and the Transition Radiation Tracker (TRT).

The Insertable B-Layer (IBL)

The Pixel detector is designed for an instantaneous luminosity of 1×10^{34} cm^{-2}s^{-1}, and is exposed to high radiation level. In order to cope with the high hit rate in Run 2, the IBL was installed in May 2014, right between the existing Pixel detector and a new, smaller beam pipe at a radius of 3.3 cm. It consists of 14 carbon fibre staves (2 cm in width and 64 cm in length), each tilted by 14° in ϕ surrounding the beam-pipe, covering $|\eta| < 3$. Two new sensor technologies are adopted: the pixel planar sensors and 3D sensors. The pixel size is only 60% of the one used for the Pixel detector. The performance of b-jet tagging significantly benefits from the additional hit information at the closest position to the collision point. For instance, the light jet rejection in $t\bar{t}$ event for 60% b tagging efficiency almost doubled with the IBL information[27].

The Pixel detector

The Pixel detector[28] is designed to provide precise trajectories and vertex measurements with a coverage of $|\eta| < 2.5$. It consists of three coaxial cylinders around the proton beam, and three disks perpendicular to it at each end-cap region. There are

1,744 identical pixel sensors on the cylinders and the disks, each contains 47,268 pixels and can measure an area of 2.44 cm × 6.34 cm. The minimum detection unit is 1 pixel, each corresponding to one read out channel. The resolution of the charged particle position is 10 μm $(R-\Phi)\times$ 115 μm(z). In order to reduce the radiation damage, the working temperature of the Pixel detector must be kept at about $-6°$C.

The Semiconductor Tracker (SCT)

The Semiconductor Tracker[29] is designed to provide high-resolution pattern recognition capabilities using discrete space-points. It consists of four concentric cylinders, and nine disks at each end-cap region with silicon microstrip. There are 2,122 modules on the cylinders, and 1,976 modules on the disks, embedded with 6.2 million read out channels in total. The total measurable area is 61 m^2. For each track, the SCT can give precisely at least four additional space points, resulting in a resolution of 17 μm $(R-\Phi)\times$ 580 μm(z).

The Transition Radiation Tracker (TRT)

The TRT[30] is the outmost part of the Inner Detector. It is a transition radiation detector that uses gas ionization to track the charged particles. The TRT is composed of straw-tubes with a diameter of 4 mm and length of 144(37) cm in the cylindrical(end-cap) layer. The straw-tubes are filled with a mixture of Xenon gas, which is operated at a voltage of -1500 V. When charged particles pass by and ionize the gas, the anions move towards the wire located in the centre of the straw, generating a current pulse signal. The precision of the measurements performed by the TRT is merely 170 mm per straw-tube, however this lack of precision can be compensated by large number of hits. In addition, transition radiation is emitted when charged particles with moving speed close to the speed of light pass the interface of material with different refractive indices (polyethylene fibres and air). For a given momentum, the energy of the photons generated by electrons will be much higher for electrons than for pions and muons, as it is proportional to the relativistic factor $(\gamma = E/m)$ of the incident particle. This difference can be used to distinguish electrons from pions.

2.2.2 Calorimetry

The calorimeters measure the energy of the incident particles: the incident particles interact with the material of the calorimeters, producing new particles with less energy; each of the secondary particles repeat the same interaction until a large number of particles are produced (which is called electromagnetic or hadronic shower, depending on the type of incident particles), and finally stopped in the material and fully absorbed. The deposited energy will converted into measurable signal.

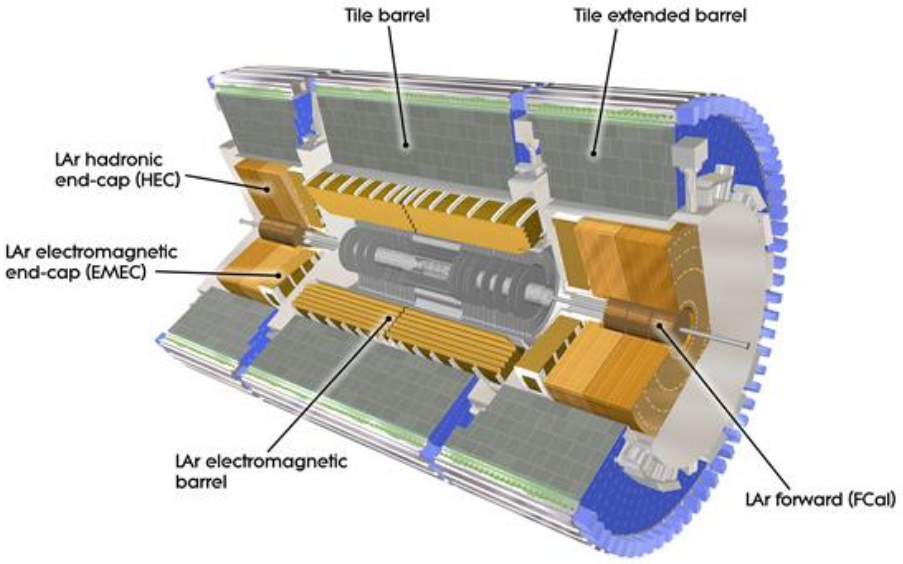

Figure 2.8 – Cut-away view of the ATLAS calorimeter system.

The ATLAS calorimeters are illustrated in Fig. 2.8. All of the calorimeters of ATLAS are sampling calorimeters, which only sample part of the energy of the incident particles. A sampling calorimeter consists of alternating layers of absorber (in which the particle shower develops) and sampler (which gives detectable signal). The absorber (dense material) usually has a low radiation length[1], while the sampler (active material) has large radiation length. For all the ATLAS calorimeter, the liquid argon (LAr) is chosen as the sampler for its intrinsic linear behaviour, its intrinsic radiation-hardness and its stability of response over time. The following calorimeters are included by the ATLAS experiment:

- the electromagnetic calorimeter with coverage up to $|\eta| = 3.2$. It is divided into a barrel part (EMB) for $|\eta| < 1.475$ and two end-cap parts (EMEC) for $1.375 < |\eta| < 3.2$.

- the hadronic calorimeter, divided into a tile calorimeter in the barrel (one covering $|\eta| < 1$ and two extended barrels covering $0.8 < |\eta| < 1.7$), a liquid argon hadronic end-cap calorimeter (HEC) covering $|\eta| < 3.9$ and a liquid-argon forward calorimeter (FCal) extending the coverage to $3.1 < |\eta| < 4.9$.

LAr electromagnetic calorimeter

The ATLAS electromagnetic calorimeter is a lead-LAr sampling detector. The electromagnetic showers are mainly developing in the lead layers. Liquid Argon is

[1] X_0, A characteristic of certain material, related to the energy loss of high energy particles electromagnetically interacting with it.

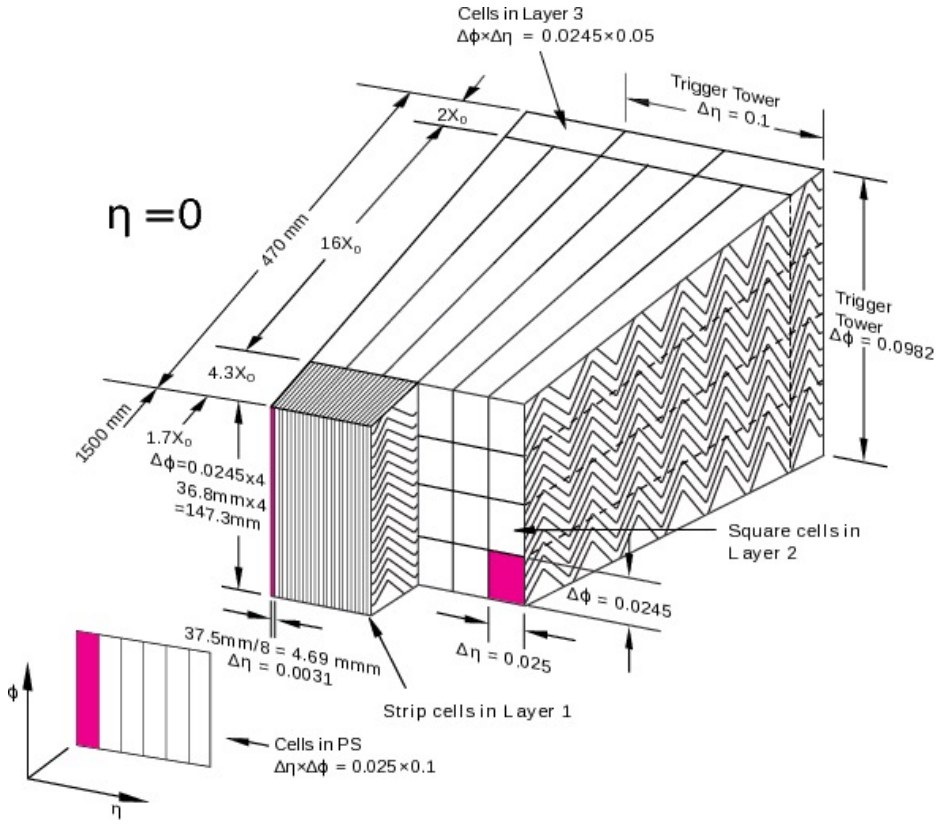

Figure 2.9 – Scheme of the ATLAS liquid argon electromagnetic calorimeter.

filled in between, used as the sampler. The lead absorbers and the electrodes have an accordion geometry, which ensures a full coverage in Φ without any cracks and a fast extraction of the signal.

As shown in Fig. 2.9, the EM calorimeter has three longitudinal layers, allowing a more precise measurement of the longitudinal development of the EM shower. The first layer (strips layer) has the thickness of around 4.4 X_0. The high granularity of this layer is important for the photon identification based on the transverse shower profiles. The background from the neutral mesons, such as π^0 decaying to multiple photons can be significantly reduced. The middle layer has a thickness up to 22 X_0. Most of the energy of the electromagnetic showers are deposited in this layer. The third layer has the thickness of about 2 X_0, which collects the energy of the tail of the showers and measures the energy leakage to the hadronic calorimeter outside.

Hadronic calorimeters

Tile calorimeter

The tile calorimeter is a sampling hadronic calorimeter using steel as the absorber and scintillating tiles as the sampler. Ultraviolet scintillation light is produced when a charged particle crosses the active material, and collected by wavelength-shifting optical fibre. As an output of the fibre, the ultraviolet light is converted into visible light

and passed to a photon-multiplier, producing measurable signal. The tile calorimeter is segmented in depth into three layers, and divided azimuthally into 64 modules as shown in Fig. 2.10.

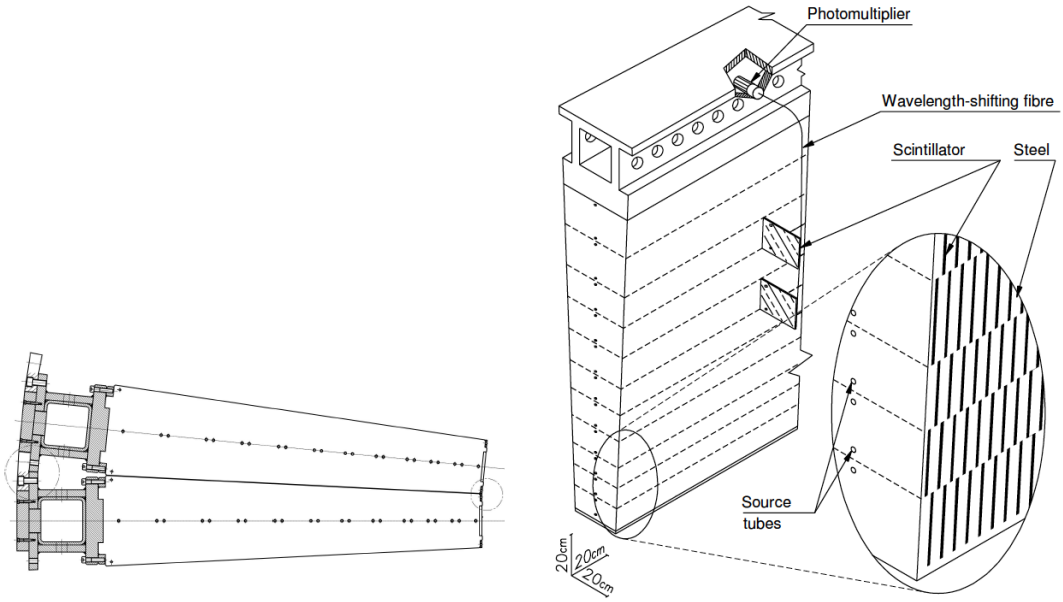

(a) (b)

Figure 2.10 – (a) Schematic showing how the mechanical assembly and the optical readout of the tile calorimeter are integrated together. (b) Azimuthal view of the tile calorimeter module-to-module interface.

LAr hadronic end-cap calorimeter

The hadronic end-cap calorimeter (HEC) is a sampling hadronic calorimeter using copper plates as absorbers and LAr as sampler. It has two independent wheels per end-cap (front wheel HEC1 and rear wheel HEC2), sharing the same LAr cryostats as the electromagnetic end-cap calorimeter (EMEC). Each wheel is divided into two segmentations in depth, and has 32 identical wedge-shaped modules.

LAr forward calorimeter

The forward calorimeter (FCal) is designed to extend the acceptance of the calorimeter up to $|\eta| = 4.9$. The FCal is a sampling hadronic calorimeter using LAr as sampler. In each end-cap, the FCal consists of three individual modules. the first layer uses copper as absorber and is optimised for measuring the electromagnetic objects. The other two layers use tungsten as absorbers, meant to measure the hadronic interactions.

2.2.3 Muon spectrometer

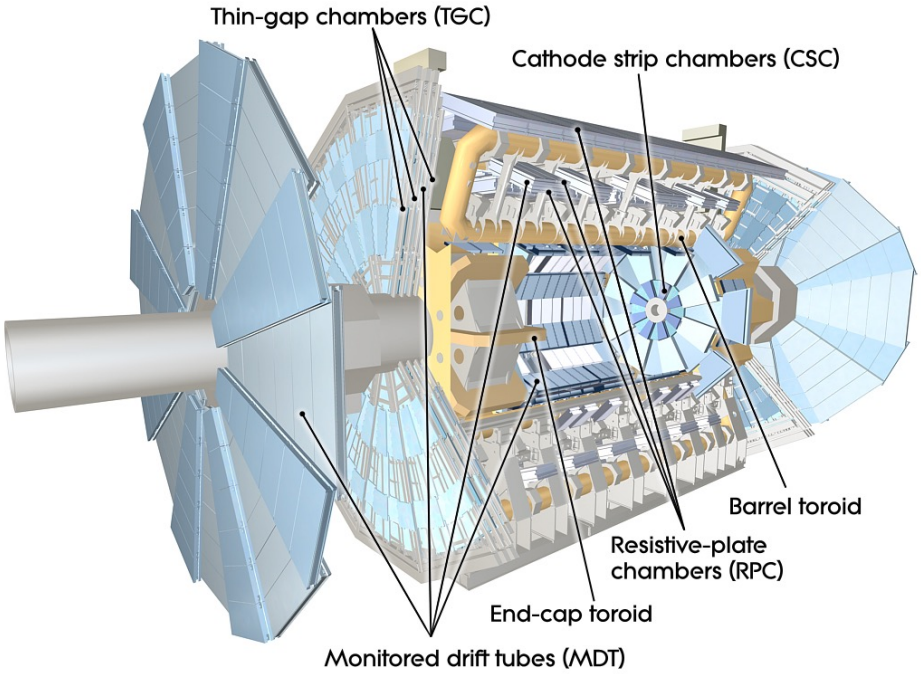

Figure 2.11 – Scheme of the ATLAS muon spectrometer.

As illustrated in Fig. 2.11, the Muon Spectrometer (MS) is the outermost part of the ATLAS detector, surrounding the hadronic calorimeter. The coverage of the Muon Spectrometer is $|\eta| < 2.7$. It is designed to detect the charged particles exiting the calorimeters and to measure their momentum. For $|\eta| < 2.4$, the MS can also provide the trigger capability, since the precision-tracking chambers can deliver the track information within a few tens nanoseconds once a charged particle pass by. Four different gaseous chambers are adopted in the MS depending on the usage and position: the Monitored Drift Tubes (MDTs), the Cathode Strip Chambers (CSCs), the Resistive Plate Chambers (RPCs) and the Thin Gap Chambers (TGCs). MDTs provide precise measurement of the momentum up to $|\eta| = 2$. For $2 < |\eta| < 2.7$, the CSC are used in the innermost tracking layer for higher rate capability and better time resolution. In different $|\eta|$ coverage, the RPCs ($|\eta| < 1.05$) and the TGCs ($1.05 < |\eta| < 2.4$) are used separately by the trigger system.

2.2.4 Magnet system

ATLAS is equipped with the unique hybrid system of four large superconducting magnets. The trajectories of the charged particles are bent in the magnetic field, therefore the momenta can be measured by the detector. The magnetic system is 26 m long and 22 m in diameter, with a stored energy of 1.6 GJ. The system consists of:

- **a solenoid:** the central solenoid aligned on the beam axis, providing a 2 T axial magnetic field for the Inner Detector.

- **a toroid:** there is one barrel toroid and two end-cap toroids, providing about 0.5 T (barrel) and 1 T (end-cap) toroidal magnetic field for the Muon Detectors.

2.2.5 Forward detectors

In addition of the ATLAS main detectors, four smaller sets of detectors are built in the region $|\eta| > 5$ in order to provide good coverage in the very forward region. The forward detectors are:

- **LUCID:** the Luminosity measurement using Cherenkov Integrating Detector (LUCID) is dedicated to online monitoring of the LHC luminosity. Two detector modules of LUCID are installed in both end-cap regions of the ATLAS detector, 17 m away from the interaction point. The coverage of LUCID is $5.5 < |\eta| < 5.9$. Each module consists of 1.5 m long tubes that are filled with C_4F_{10} gas at a constant pressure, providing a Cherenkov threshold of 10 MeV for electrons and 2.8 GeV for pions.

- **ZDC:** the Zero Degree Calorimeter (ZDC) is dedicated to the detection of the forward neutrons with $|\eta| > 8.3$ in heavy-ion collisions, and to measure the centrality of such collisions. The ZDCs are located $\pm$140 m away from the interaction point, where the straight section of the beam pipe is divided back into two independent beam pipes. Four modules (one electromagnetic, three hadronic) are installed in each arm.

- **ALFA:** the Absolute Luminosity For ATLAS (ALFA) detector determines the absolute luminosity for the ATLAS using the elastic-scattering amplitude at small angles (around 3 μrad). ATLAS adopted the Roman-pot technique[31] for the measurements very close to circulating beams. The ATLAS Roman-pots are located $\pm$240 m away from the interaction point, two Roman-pot stations separated by four meters on each side.

- **AFP:** the ATLAS Forward Proton (AFP) detector is dedicated to tagging and measuring the momentum and emission angle of very forward protons (around 100 μrad), in order to extend the physics reach of ATLAS. The AFP detector was installed in 2017, $\pm$200m from the interaction point.

2.2.6 Trigger system

Limited by the reaction time, readout bandwidth, storage space, etc, it is impossible and redundant to store all the data collected by the ATLAS detector given such a

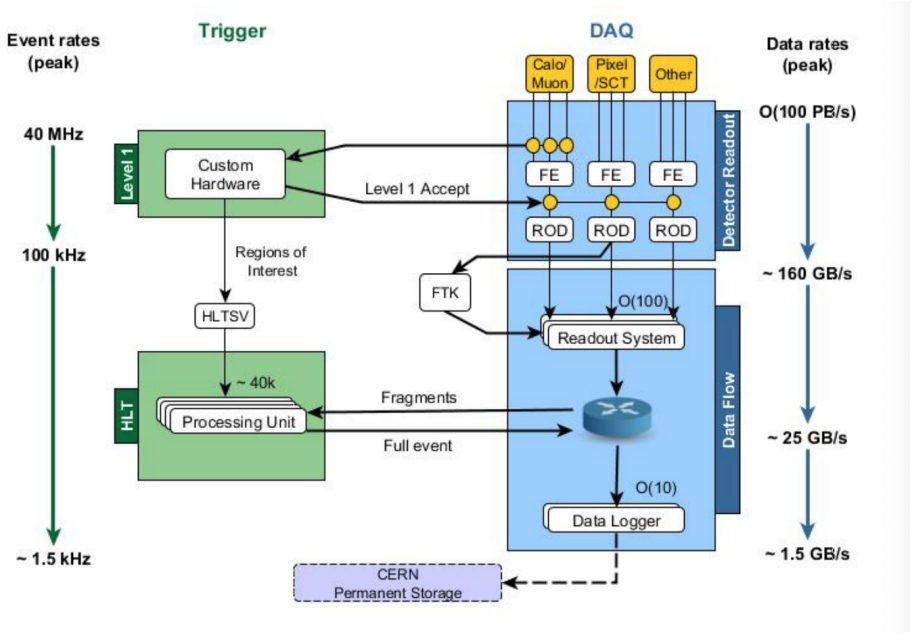

Figure 2.12 – The ATLAS Trigger and Data Acquisition (DAQ) System in LHC Run 2[32].

high designed luminosity. Therefore, ATLAS uses a trigger system to select only the interesting events for offline analyses. The ATLAS trigger system can be divided into three levels of event selection: Level-1 (L1), Level-2 (L2) and the event filter. Each level only processes the events that already passed the previous level of selection. The trigger system operates within the framework called the Data Acquisition (DAQ) system, which receives and buffers the data from the readout electronics. An overview of the ATLAS trigger and DAQ system during Run 2 is shown in Fig. 2.12.

- **Level-1 trigger:** the L1 is implemented using custom-made fast electronics, using only the information from the calorimeters and the Muon Spectrometer. It selects muons with high transverse momentum, electrons, photons, jets, τ leptons decaying into hadrons and large missing transverse energy ($E_T^{missing}$). One or more Regions of Interest (RoI) is defined by the L1, in which exist the potentially interesting signatures. The RoIs are later passed to the next levels of trigger system. L1 reduces the event rate from 40 MHz to around 100 kHz.

- **High-level trigger:** the High-Level Trigger (HLT) is formed by the L2 and the event filter. The software-based HLT system has access to the full detector information within the RoI, and further reduces the event rate to around 1 kHz. Once an event is accepted by the HLT, it is sent to the CERN permanent storage via the Data Logger.

Chapter 3

Photon reconstruction and performance

The ATLAS detector provides a precise measurement of photons that benefits a lot of physics analyses. This chapter will discuss all the necessary steps to reconstruct and identify a photon: the reconstruction and energy calibration procedure are introduced in Sec. 3.1 and Sec. 3.2 separately. The photon identification procedure, aiming to select prompt photon, which is defined as the photons produced from the hard scattering, in contrast to those produced from the decays of the hadrons, is described in Sec. 3.3. The photon isolation criteria aiming to further suppress the background contribution from hadronic decay is described in Sec. 3.4.

3.1 Photon reconstruction

Information from ATLAS Calorimeters is Inner Detectors are essential for photon reconstruction. As discussed in Sec. 2.2.1 and Sec. 2.2.2, photon candidates in ATLAS detector are reconstructed through:

- interactions with the electromagnetic (EM) calorimeters. Photons (and electrons) develop EM showers in the absorber in the LAr EM calorimeter, deposit their energy in a region of the detector containing multiple cells, which are reconstructed as clusters.
- interactions upstream of the calorimeter. Photon conversions ($\gamma \to e^+e^-$) might happen in the inner detector, leaving tracks that may be matched to EM clusters.

3.1.1 Energy reconstruction

Signal readout

The readout electronics of the ATLAS calorimetry is designed to measure the energy in each calorimeter cell, and provide the L1 trigger system with the deposited energy.

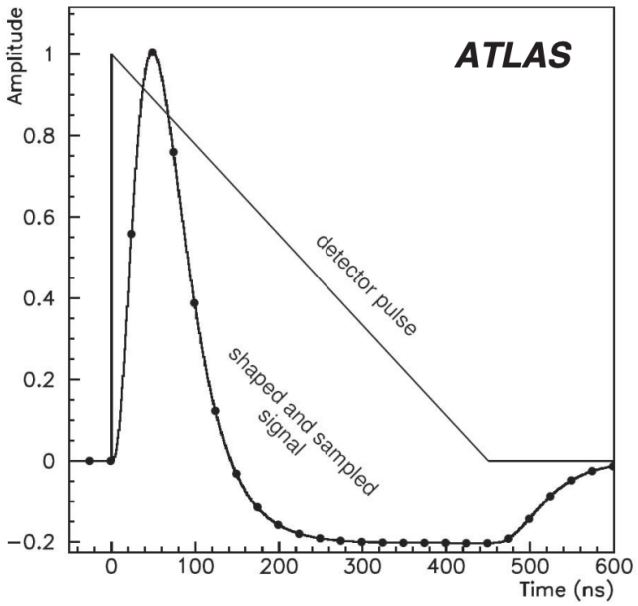

Figure 3.1 – Shapes of the LAr calorimeter current pulse in the detector and of the signal output from the shaper chip. The dots indicate an ideal position of samples separated by 25 ns.[33]

The signal readout begins when the electromagnetic showers ionize the LAr in the EM calorimeter, resulting in drifting electrons which induce a triangular current pulse on the copper electrodes. The amplitude of the triangular signal is proportional to the deposited energy. The signal is then amplified, shaped and digitalized to optimise the signal-to-noise ratio. The triangular input current pulse and the shaped output pulse from the FEB are shown in Fig. 3.1.

The signals are then sampled at the LHC bunch crossing frequency of 40 MHz, and temporarily stored here during the L1 trigger latency. Once the events are accepted, the samples are read out and digitized by a 12-bit Analog to Digital Converter (ADC). A Gain Selector chips (GSEL) is used to choose the most suitable gain for each channel in each event, in order to optimize the precision of the energy measurement. In the end, The digitized samples with the chosen gain are transmitted to the corresponding readout drivers (ROD). Equation 3.1 shows the conversion of the reconstructed pulse amplitude A to the deposited energy (E) in MeV.

$$E = F_{\mu A \to MeV} \times F_{DAC \to \mu A} \times \frac{1}{\frac{M_{phys}}{M_{cali}}} \times G \times \sum_{j=1}^{N_{samples}} a_j (s_j - p) \tag{3.1}$$

The factor $F_{\mu A \to MeV}$ converts the ionization current in the calorimeter to the energy deposited. $F_{DAC \to \mu A}$ converts the Digital-to-Analog Converter (DAC) counts set of the calibration board to the injected current in μA. G is the gain of the channel, and $\frac{M_{phys}}{M_{cali}}$ is a correction factor of G where M_{phys} is the ionization pulse response, M_{cali} is the calibration pulse corresponding to the same input current, to adapt to

physics-induced signals. For the selected electronic gain, s_j are the samples of the shaped signal. a_j are the optimal filtering coefficients (OFC), calculated according to an optimal filtering algorithm for better energy and timing resolution. p denotes the pedestal value, namely the mean value of the samples when no signal is present.

Clustering algorithm

After the energy is measured using Eq. 3.1, the calorimeter cells are clustered via different clustering algorithms.

The first algorithm is called Sliding-window algorithm[34]. The calorimeter cells are divided into towers of size $S_{tower} = \Delta\eta \times \Delta\phi = 0.025 \times 0.025$, each tower sums up all the energy of the cells on the longitudinal layer. Then a fixed-size window scan of 3×5 towers is performed. A cell with total transverse energy above 2.5 GeV is selected as the seed, around which the cluster is built by summing the energy of all cells within a 3×7 (5×5) $\Delta\eta \times \Delta\phi$ window in the barrel (end-cap) region. The cluster reconstruction efficiency is given by the number of reconstructed EM clusters divided by the number of produced particles. The efficiency varies as a function of E_T and $|\eta|$, and can reach above 99% for $E_T > 15$ GeV.

The second algorithm is called Dynamical topological cell clustering algorithm[35]. This new clustering algorithm was implemented since 2017, with which one can easily recover low-energy deposits from bremsstrahlung photons and associate them to the electron cluster, together form a so-called "supercluster" as shown in Fig. 3.2.

The main idea of the topological cell clustering algorithm is to choose an initial seed, and add the neighboring cells under certain rules. One important observable that governs the seeding and growth of a topo-cluster, cell significance, is given by:

$$\zeta_{cell}^{EM} = |\frac{E_{cell}^{EM}}{\sigma_{noise,cell}^{EM}}| \tag{3.2}$$

where E_{cell}^{EM} is the cell energy, $\sigma_{noise,cell}^{EM}$ is the expected cell noise.

The initial seed is chosen with $\zeta_{cell}^{EM} \geq 4$, around which all the immediate neighboring cells with $\zeta_{cell}^{EM} \geq 2$ are added. Then, all the cells which are immediate neighbors of the first added ones are added. Finally, All cells that are immediate neighbors of those added previously are added, regardless of the ζ_{cell}^{EM} value. Following this procedure, the constructed clusters are called EM topoclusters. From a seed topocluster, a supercluster is built after satellite cluster candidates around the seed candidate are resolved. There is no upper E_T threshold on the satellites, a cluster of cells is accepted as a satellite only if it falls within a window of $\Delta\eta \times \Delta\phi = 0.075 \times 0.125$ around the seed cluster barycentre. An identified satellite can not be used for other clusters. The whole satellite finding procedure is summarized in Fig. 3.3.

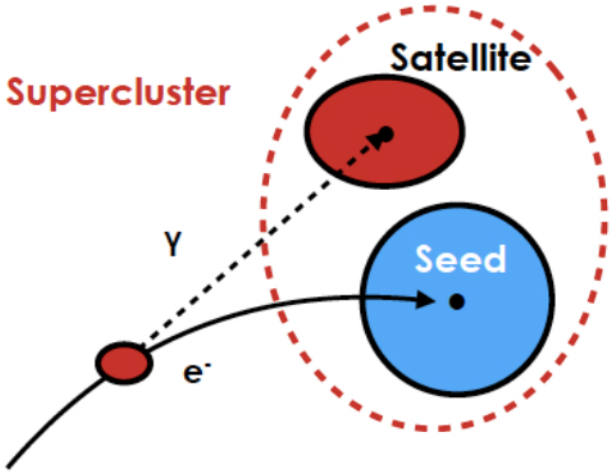

Figure 3.2 – Diagram of an example supercluster showing a seed electron cluster and a satellite photon cluster.

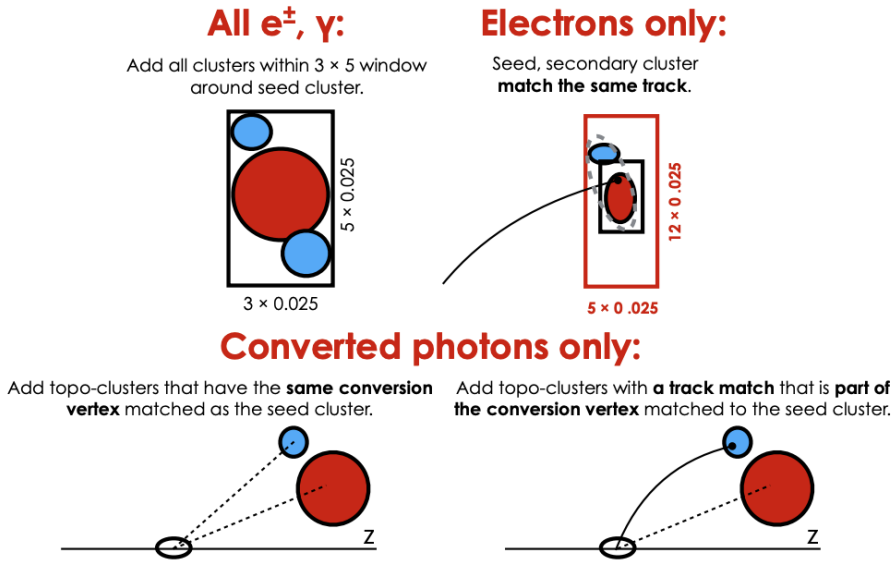

Figure 3.3 – Diagram of the dynamical topological cell clustering algorithm for electrons and photons.

The search region of the detector is not limited by the topo-cluster algorithm, which means that cells from both the LAr and Tile calorimeters may be included in a single topo-cluster. Another important value, the EM fraction is defined as:

$$f_{EM} = \frac{E_{L1} + E_{L2} + E_{L3} + w\dot{(}E_{E4} + E_{PS})}{E_{cluster}}, w = \begin{cases} 1, 1.37 < |\eta| < 1.63 \\ 0, otherwise \end{cases} \tag{3.3}$$

E_{Lx} is the cluster energy in layer x, the term $(E_{E4} + E_{PS})$ only considered for clusters within the transition region $1.37 < |\eta| < 1.63$, where the energy deposition is non-negligible in the pre-sampler and E4 scintillators. Only the topo-clusters with $f_{EM} > 0.5$ and $E_T > 400$ MeV are accepted.

3.1.2 Track matching

The electrons, unconverted and converted photons are characterized depending on the number of reconstructed tracks and the matching situations: the electrons are reconstructed with clusters matched to ID track from a vertex in the interaction region. The converted photons are reconstructed with clusters matched to the track (tracks) originating from a conversion vertex. Unconverted photons are reconstructed with clusters without matching tracks. Figure 3.4 illustrates the path of an electron through the detector [36].

The standard track-pattern reconstruction [37] is first performed everywhere in the inner detector. A silicon track seed is searched within a certain region of interest, which is a set of silicon detector hits used to start a track. If the standard pattern recognition fails, a modified pattern recognition algorithm using a Kalman filter [38] is used, up to 30% energy loss at each material intersection is allowed. Track candidates are then fitted with the global χ^2 fitter [39], allowing for additional energy loss when the standard track fit fails. To improve track parameter estimation, the tracks with silicon hits loosely matched to clusters are re-fitted using a Gaussian Sum Filter (GSF) algorithm[40]: the loosely matched, re-fitted tracks are then matched with the seeded EM clusters by extrapolating the track from the perigee to the second layer of the calorimeter, using either the measured track momentum or rescaling the magnitude of the momentum to match the cluster energy. A track is considered as matched if, with either measured or rescaled momentum, $|\eta| < 0.05$ and $-0.10 < q \cdot (\phi_{track} - \phi_{cluster}) < 0.05$ (q represents the sign of the reconstructed charge of the track). In case more than one tracks are matched to the same cluster, tracks with hits in pixel detector are preferred, then tracks with hits in the SCT only. For converted photons, both tracks with silicon hits (Si tracks) and tracks reconstructed only in the TRT (TRT tracks) are used for the conversion reconstruction. Two-track conversion vertices are reconstructed from two opposite-charge tracks forming a vertex consistent with that of a massless particle.

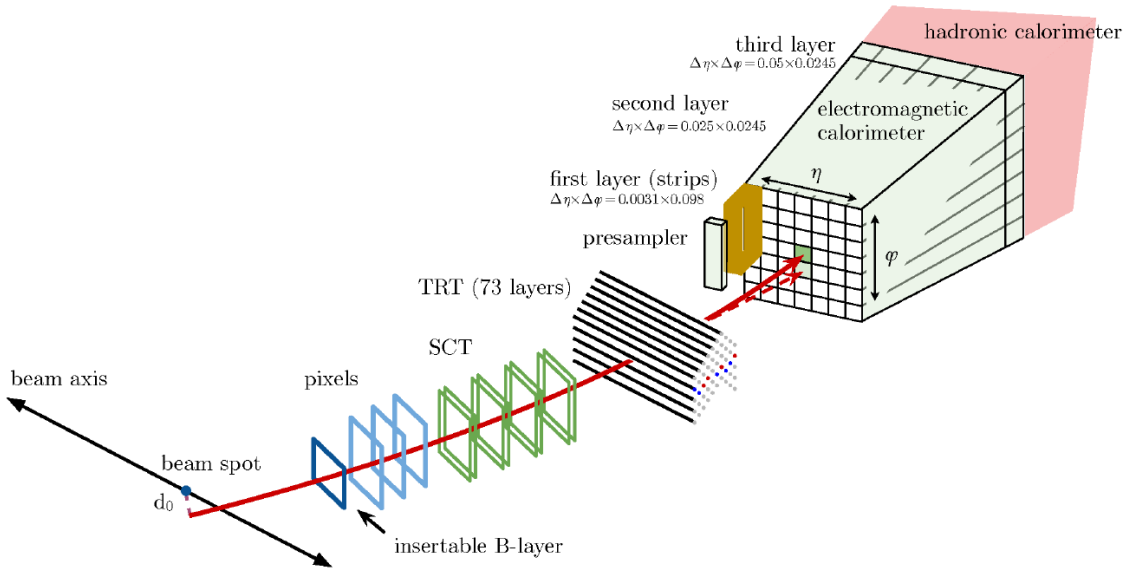

Figure 3.4 – A schematic illustration of the path of an electron through the detector. The red trajectory shows the hypothetical path of an electron, which first traverses the tracking system (pixel detectors, then silicon-strip detectors and lastly the TRT) and then enters the electromagnetic calorimeter. The dashed red trajectory indicates the path of a photon produced by the interaction of the electron with the material in the tracking system.

Single-track vertices are reconstructed from tracks without hits in the innermost sensitive layers.

3.2 Energy calibration

After summing up the energy of all the cells of the three layers of the EM calorimeter and the pre-sampler, the photon energy is corrected by a dedicated calibration procedure. In general, the cluster energy is calibrated to the original electron or photon energy, and an absolute energy scale is obtained using data-driven method to correct for the data-MC difference using $Z \to ee$ samples. Photon specific uncertainties are applied due to the difference of the shower shape between electrons and photons. As shown in Fig. 3.5, the calibration proceeds as follows:

The first step is the training of MC-based e/γ calibration. A multivariate (MVA) regression algorithm is trained based on Monte-Carlo (MC) simulation of the detector, in order to calibrate the EM cluster properties to the original electron and photon energy. The calibration constants are determined using the MVA, and its optimization is performed separately for electrons, converted and unconverted photons.

The following variables are used as an input to the MVA algorithm:

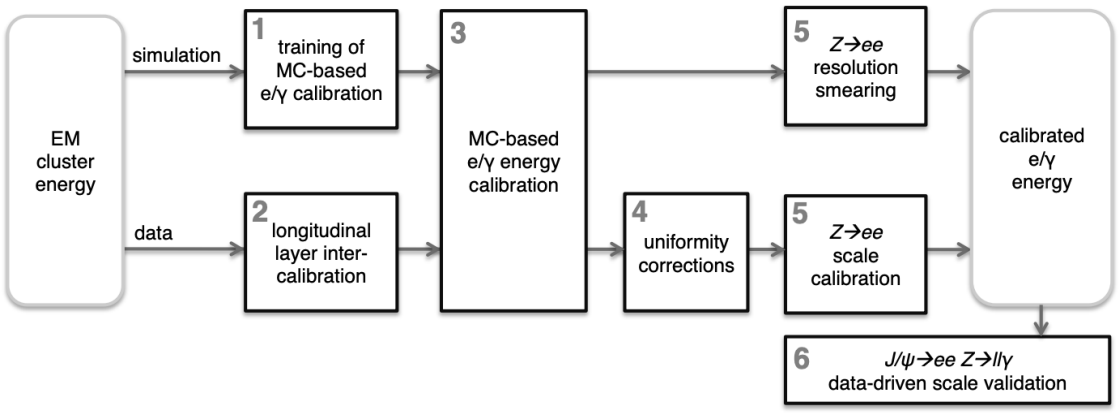

Figure 3.5 – Schematic overview of the procedure used to calibrate the energy response of electrons and photons in ATLAS.[41]

- total energy in the accordion, $E_{acc} = E_1^{raw} + E_2^{raw} + E_3^{raw}$, where E_x^{raw} is the uncalibrated energy of each layer.
- ratio of the energy in the pre-sampler to the energy in the accordion, E_0/E_{acc}, only used for the clusters within the geometric range of the pre-sampler $|\eta| < 1.8$.
- ratio of the energy in the first layer to the energy in the second layer, E_1^{raw}/E_2^{raw}, which provides the information of the longitudinal shower depth.
- pseudorapidity $\eta_{cluster}$ in the ATLAS frame.
- cell index, an integer number defined as the integer part of $\eta_{calo}/\Delta\eta$, where η_{calo} is the pseudorapidity of the cluster in the calorimeter frame, and $\Delta\eta = 0.025$ is the size of one cell in the middle layer. This variable is sensitive to the non-uniformities of the calorimeter.
- η with respect to the cell edge.
- ϕ with respect to the lead absorbers.

Additional variables are used for converted photons:

- radius of the conversion R, used only for converted photon with p_T^{conv} larger than 3 GeV, where p_T^{conv} is the sum of the transverse momentum of the conversion tracks.
- ratio of the conversion transverse energy to the transverse momentum in the accordion E_T^{acc}/p_T^{conv}, where $E_T^{acc} = E_{acc}/\cosh(\eta_{cluster})$.
- fraction of the conversion p_T carried by the highest-p_T conversion track.

An essential requirement is that the detector geometry and interactions of particles with matter are accurately described in the MC simulation. Measuring E_1/E_2 in data

allows a precise determination of the amount of material upstream of the calorimeters, based on which the modifications of the detector material settings in simulation are made.

Figure 3.6 illustrates the energy resolution $\sigma_{E_{calib}/E_{gen}}$, where E_{calib} is the reconstructed energy after the algorithm is applied, and E_{gen} is the true energy. The resolution is defined as the interquartile range of $\sigma_{E_{calib}/E_{gen}}$, i.e. the interval excluding the first and last quartiles of the $\sigma E_{calib}/E_{gen}$ distribution in each bin, divided by 1.35 in order to convert to the equivalent standard deviation of a Gaussian distribution.

The second step is the longitudinal layer inter-calibration. Since the EM calorimeter is longitudinally segmented into three layers, the scales of the different longitudinal layers should be equalised in data with respect to simulation before the determination of the overall energy scale, in order to ensure the correct extrapolation of the response in the full p_T range. Any mismatch between data and the simulation of the relative energy response of the different layers could bias the calibrated energy.

Muons from $Z \to \mu\mu$ decays are used to study the relative calibration of the first and second layers, since its deposited energy is insensitive to the amount of passive material upstream of the calorimeters. The observed muon energy distribution in each layer can be described by a convolution of a Landau distribution (energy deposit) and a noise distribution. The relative calibration is calculated as $\alpha_{1/2} = (\langle E_1 \rangle^{data} / \langle E_1 \rangle^{MC})/(\langle E_2 \rangle^{data} / \langle E_2 \rangle^{MC})$, where $\langle E_1 \rangle$ ($\langle E_2 \rangle$) is the most probable value (MPV) in the first (second) layer. MPV of the deposited energy can be obtained with two method: fit the muon energy distribution ("fit method"), or compute the mean of energy over a restricted window to minimize the sensitivity to the tails of the distribution ("truncated-mean method"). Figure 3.7 shows the $\alpha_{1/2}$ obtained with the two methods.

The third step is the MC-based e/γ energy calibration. After training and optimization, the MC-based e/γ response calibration is applied to the cluster energies in both data and simulated samples.

The fourth step is the uniformity corrections. The corrections are aimed to account for energy response variations not included in the simulation due to some specific reasons, for instance, non-optimal high voltage, geometric effects, or biases associated with the LAr calorimeter electronic calibration.

The fifth step is $Z \to ee$ scale calibration and resolution smearing. The overall electron response in data is calibrated so that it agrees with the expectation from simulation, using a large sample of electrons from Z boson decays. Per-electron scale factors are extracted, and applied to both electron and photon candidates in data. The resolution in data is slightly worse than that in simulation, therefore the energy in MC simulation is smeared to match the data.

The difference in energy scale between data and simulation after all the corrections on data mentioned above is defined as α_i, where i corresponds to different region in

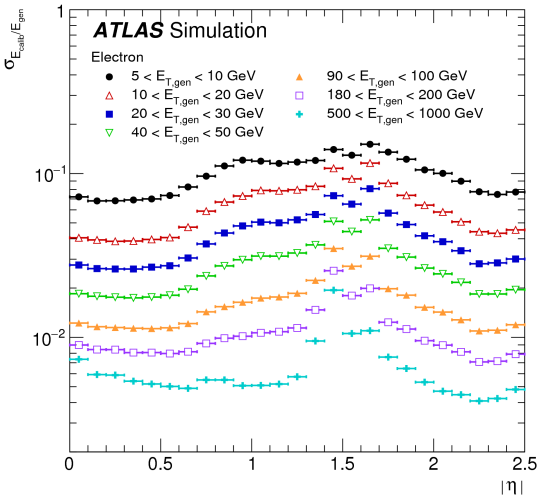

(a)

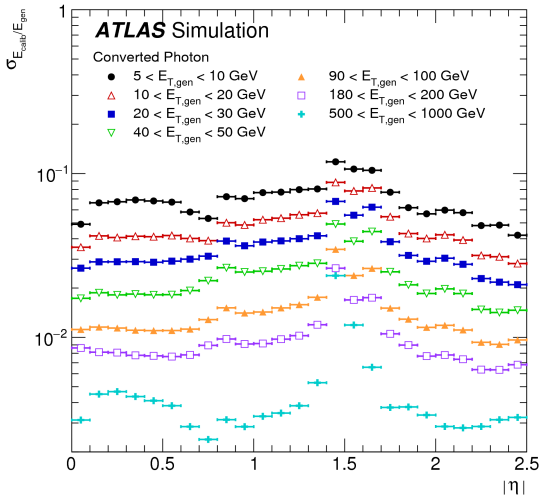

(b)

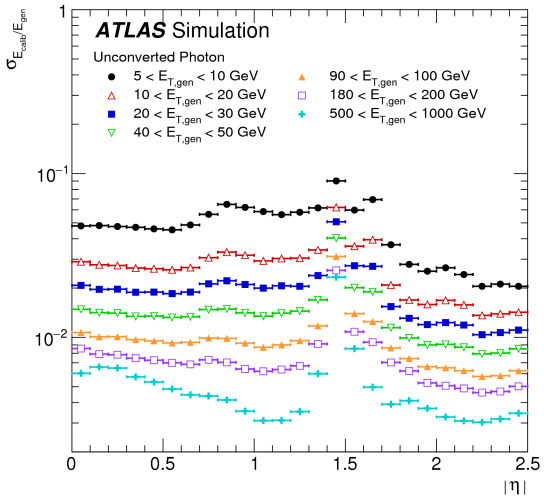

(c)

Figure 3.6 – Energy resolution, $\sigma_{E_{calib}/E_{gen}}$, estimated from the interquartile range of $\sigma E_{calib}/E_{gen}$ as a function of $|\eta|$ for (a) electrons, (b) converted photons and (c) unconverted photons, for different E_T ranges.[42]

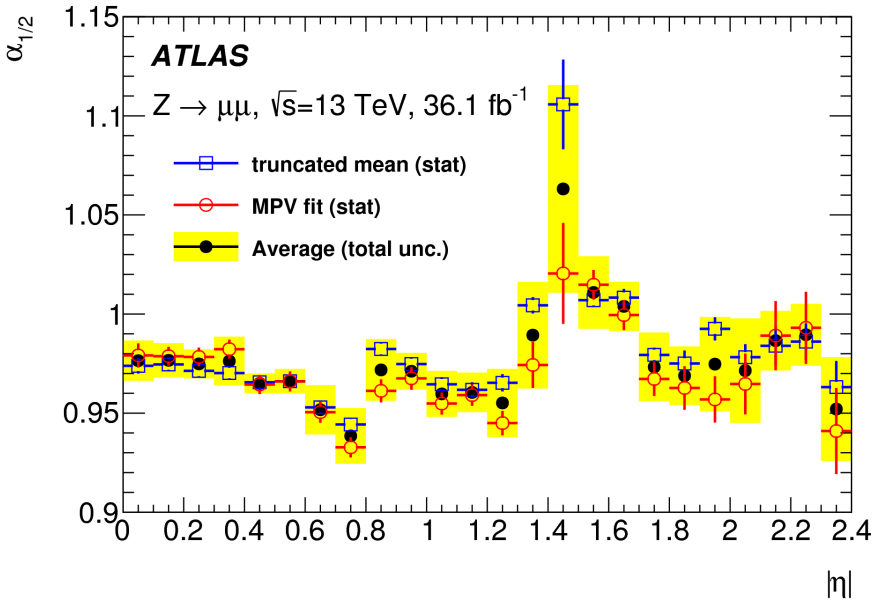

Figure 3.7 – Ratio $\alpha_{1/2} = (\langle E_1 \rangle^{data} / \langle E_1 \rangle^{MC}) / (\langle E_2 \rangle^{data} / \langle E_2 \rangle^{MC})$ as a function of $|\eta|$, as obtained from the study of the muon energy deposits in the first two layers of the calorimeters. The results from the two methods are shown with their statistical uncertainties. The final average measurement is shown with its total uncertainty including the statistical and systematic uncertainties.[42]

η. The difference in energy resolution between data and simulation is defined as an additional constant term c_i in the energy resolution, also depending on η:

$$E^{data}_{scale} = E^{MC}_{scale}(1+\alpha_i), (\frac{\sigma_E}{E})^{data} = (\frac{\sigma_E}{E})^{MC} \oplus c_i \tag{3.4}$$

where i represents bins of pseudorapidity, and $\oplus$ denotes a sum in quadrature. For $Z \to ee$ decays with the two electrons falling in regions i and j in $|\eta|$, the difference in average di-electron invariant mass and in mass resolution is given by:

$$m^{data}_{ij} = m^{MC}_{ij}(1+\alpha_{ij}) \tag{3.5}$$

$$(\frac{\sigma_m}{m})^{data}_{ij} = (\frac{\sigma_m}{m})^{MC}_{ij} \oplus c_{ij} \tag{3.6}$$

where $\alpha_{ij} = (\alpha_i + \alpha_j)/2$, $c_{ij} = (c_i \oplus c_j)/2$, obtained from comparison between the shape of the invariant mass distributions in data and in simulation, separately for each (i,j) region. Two methods are considered as cross-checks of each other: shift the mass scale in simulation distributions by α_{ij} and apply an extra resolution contribution of c_{ij}, where the best estimation of the two values are obtained by minimizing the χ^2 of the difference between data and simulation templates ("template fit method"), or fit both data and simulated invariant mass distribution in each bin by an analytic

fuction, extract the parameters from a simultaneous fit of all $i-j$ regions ("lineshape method").

Figure 3.8 shows the energy scale and resolution corrections measured with 2015-2016 data. The energy scale corrections are about -3% to 2% depending on pseudorapidity, the uncertainty is about 0.02% to 1%. The additional constant term of the resolution c_i is typically smaller than 1% in the barrel region, and is up to 2% in end-cap region. Figure 3.9 shows the $Z \to ee$ invariant mass distribution of data and simulations after applying the energy scale and resolution corrections. The stability of the reconstructed peak position as a function of the average number of interactions per bunch crossing is also presented.

The sources uncertainty are listed below, computed separately in each η interval:

- accuracy of the main method (template fit method). Pseudo-data samples generated from the simulation samples are used to validate the procedure of estimation of α_i and c_i. The residual bias of the method in the estimation is computed, comparing the values used to generate the pseudo-data samples with the extracted values. The bias is assigned as a systematic uncertainty.

- method comparison. The difference between the results of the two methods is assigned as a systematic uncertainty.

- mass range used to perform the comparison between data and simulation. Mass range is changed from 80-100 GeV (nominal) to 87-94.5 GeV, and the difference is assigned as a systematic uncertainty.

- region selection. The choice of the invariant mass range of the two electrons can introduce bias if non-Gaussian tails of the energy resolution are not correctly modeled. An η-dependent invariant mass range selection is applied to remove such biased $i-j$ region. The difference obtained by varying this criteria is assigned as a systematic uncertainty.

- background with prompt electrons. The small contributions of backgrounds from $Z \to \tau\tau$, diboson pair production and top-quark production is neglected in the parameter extraction. The difference between including and neglecting them is assigned as a systematic uncertainty.

- with/without election isolation requirement, as described in Sec. 3.4.

- Tight/Medium election identification, as described in Sec. 3.3.

- electron bremsstrahlung probability. Before reaching the calorimeter, electrons can lose a significant fraction of energy by bremsstrahlung. Electrons with higher momentum loss due to bremsstrahlung have worse resolution. The fraction of momentum loss through bremsstrahlung is defined as $f_{brem} = 1 - \frac{(q/p)^{IP}}{(q/p)^{outofID}}$.

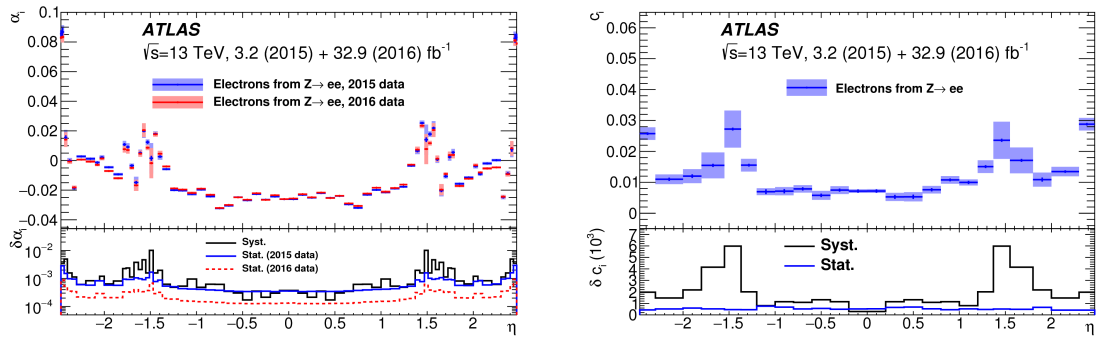

(a) (b)

Figure 3.8 – Measured (a) energy scale and (b) resolution corrections as a function of η using $Z \to ee$ events in 2015 and 2016 data. The systematic and statistical uncertainties are shown separately in the bottom panels.

The ratio q/p is estimated from the tracking algorithm, where q is the charge of the particle and p is the momentum at the interaction point (IP) and when the particle is leaving the inner detector (out of ID). The additional requirement $f_{brem} < 0.5$ is performed on electrons, and the difference in results obtained with/without the requirement is assigned as uncertainty.

- corrections on the electron reconstruction, trigger, identification and isolation efficiencies, which can slightly change the shape of the invariant mass distribution predicted by the simulation.

The sixth step is data-driven scale validation of the extrapolation of the calibration to low-E_T electrons using $J/\Psi \to ee$ events, and to photons using $Z \to ll\gamma$ events in data. The electron-to-photon extrapolation is performed assuming that the energy scale corrections obtained from $Z \to ee$ are also valid for photons within the uncertainties. As an additional correction, the residual photon energy scale difference correction factor $\Delta\alpha$ is parameterized and then applied to photon energy. The residual corrections are shown in Fig. 3.10 as function of the photon energy. The additional sources of uncertainty for the photon energy scale are listed below. They will be explained in details in the next chapter, which describes the work I performed at the beginning of my Ph.D. in order to qualify as an ATLAS author.

- photon conversion classification. The MVA algorithm is trained separately for electrons, converted and unconverted photons. Misclassification of the conversion type may bias the calibration, typically result in uncertainties of about 0.05% at $E_T = 60$ GeV.

- modeling of the lateral shower shape. The difference of lateral energy leakage outside of the cluster between electron and photon is taken as an uncertainty,

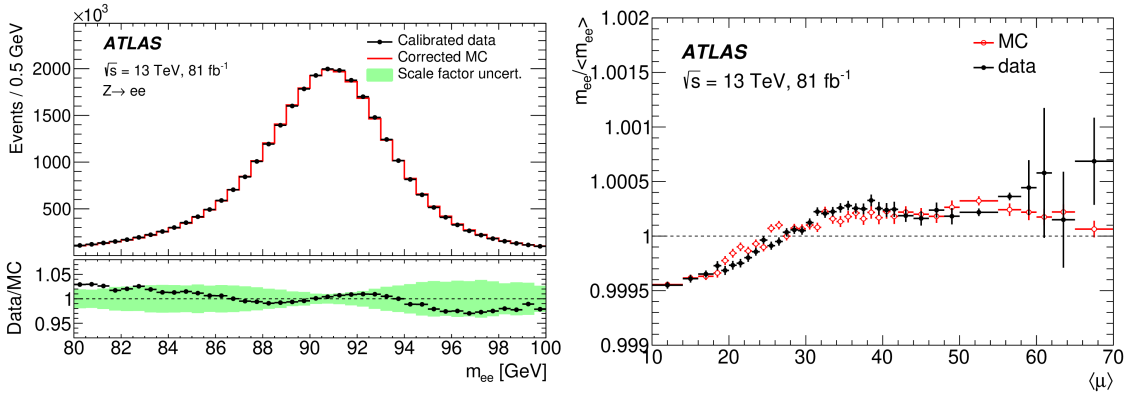

(a) (b)

Figure 3.9 – (a) Comparison between data and simulation of the invariant mass distribution of the two electrons in the selected $Z \to ee$ candidates, after the calibration and resolution corrections are applied. The total number of events in the simulation is normalized to the data. The uncertainty band of the bottom plot represents the impact of the uncertainties in the calibration and resolution correction factors. (b) Relative variation of the peak position of the reconstructed di-electron mass distribution in $Z \to ee$ events as a function of the average number of interactions per bunch crossing. The error bars represent the statistical uncertainties.[43]

coming from the difference between electron and photon showers related to the interaction probabilities with the material upstream of the calorimeter.

3.3 Photon identification

After the reconstruction, the sample of photon candidates contains a significant number of background candidates ("fake" photons from jets). It is important to distinguish prompt photons (produced in hard scattering process) from the faked ones, originating from the neutral hadrons decays (mostly $\pi^0 \to \gamma\gamma$) or QCD jets depositing a large energy fraction in the EM calorimeter. As shown in Fig. 3.11, prompt photons deposit narrower showers in the EM calorimeter and leak less in the hadron calorimeter. Therefore, a set of discriminating variables (DVs) that characterize the lateral and longitudinal electromagnetic shower development in the EM calorimeter and the leakage fraction of showers in the hadron calorimeter is defined, listed in Tab. 3.1 and Fig. 3.12. The photon identification is constructed from one-dimensional selection criteria (cut-based selection) applied on the discriminating variables.

There are three photon identification working points: the primary identification selection is labelled as Tight, and the Medium and Loose selections are less restrictive ones mainly used for the trigger system. In 2015 and 2016, Loose selection was the main

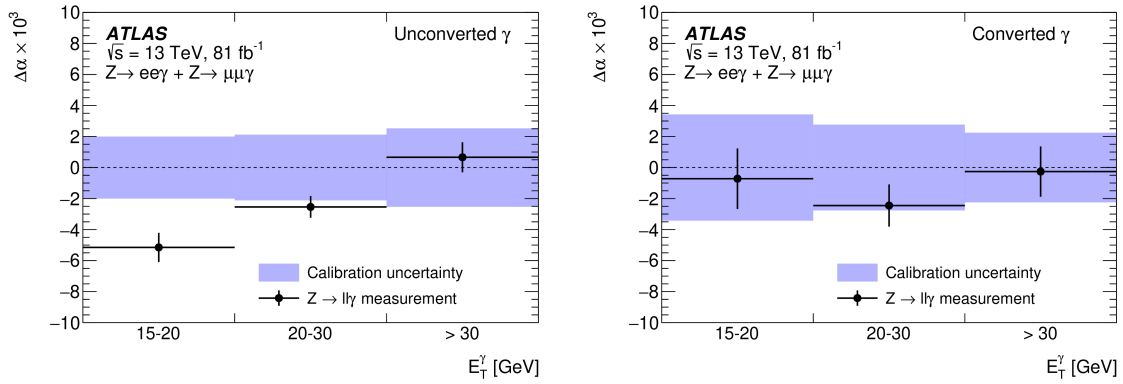

(a) (b)

Figure 3.10 – Residual photon energy scale factors, $\Delta\alpha$, for (a) unconverted and (b) converted photons as a function of the photon transverse energy E_T^γ, respectively. The points show the measurement with its total uncertainty and the band represents the full energy calibration uncertainty for photons from $Z \to ll\gamma$ decays.[43]

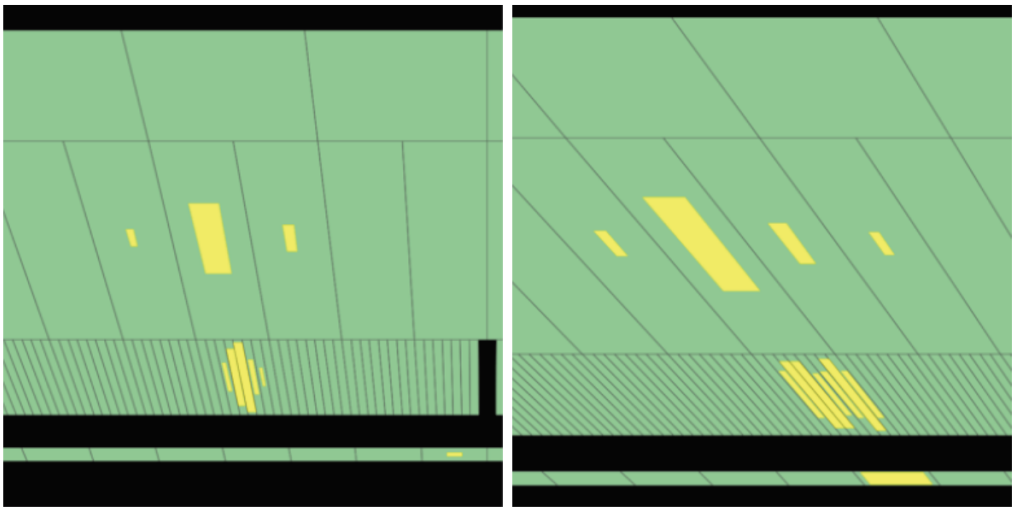

Figure 3.11 – Event display of a prompt photon candidate (left) and of a fake photon candidate (right).

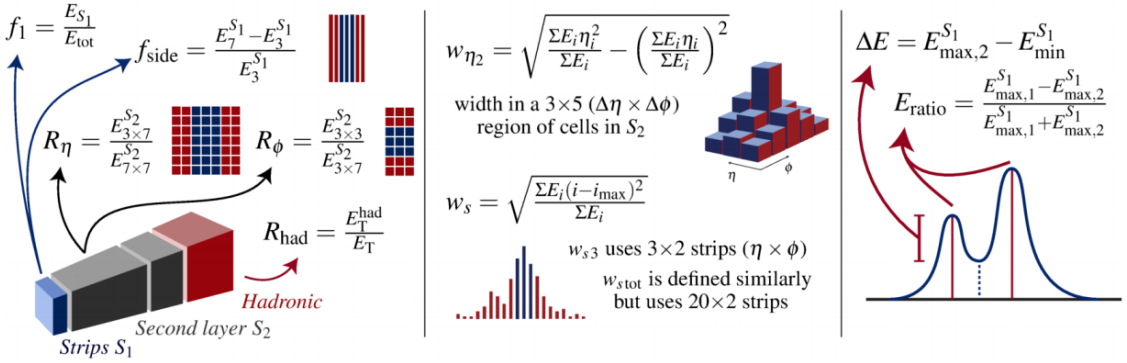

Figure 3.12 – Schematic representation of the photon identification discriminating variables, from Ref. [8]. $E_C^{S_N}$ denotes the electromagnetic energy collected in the $N-th$ longitudinal layer of the electromagnetic calorimeter in a cluster of properties C, identifying the number and/or properties of selected cells. E_i is the energy in the $i-th$ cell, η_i is the pseudorapidity centre of that cell.

selection for photon and di-photon event events triggering, using only R_{had}, R_{had1}, R_η and $w_{\eta 2}$ variables. Since 2017[43], the Medium selection, which adds a loose cut on E_{ratio}, became the main trigger selection in order to maintain an acceptable trigger rate. The Loose and Medium selections are the same for converted and unconverted photons. The Tight identification criteria are optimized separately for converted and unconverted photons using the TMVA algorithm[1], since the shower shape of them are different due to the opening angle of e^+e^- conversion pairs which is amplified by the magnetic field.

The efficiency of the photon identification is measured in both data and simulation using three methods: a directly measurement using photons from radiative Z boson decays, a matrix method based on inclusive photon production, and measurement using $Z \to ee$ decays with the shower shape of electrons modified to resemble photons. The final estimation of photon identification efficiency is the combination of the three methods. The difference between data and simulation is used as a correction factor for simulation. Generally, the photon identification efficiency is better than 90% for photons with $E_T > 40$ GeV, varying with respect to η and E_T of the photon candidate. Figure 3.13 shows the Tight identification efficiencies efficiencies for unconverted and converted photons (in region $0.6 < |\eta| < 1.37$) as measured with the three efficiency methods.

[1]The Toolkit for Multivariate Data Analysis with ROOT (TMVA) is a ROOT-integrated project providing a machine learning environment for the processing and evaluation of multivariate classification, both binary and multi class, and regression techniques targeting applications in high-energy physics.

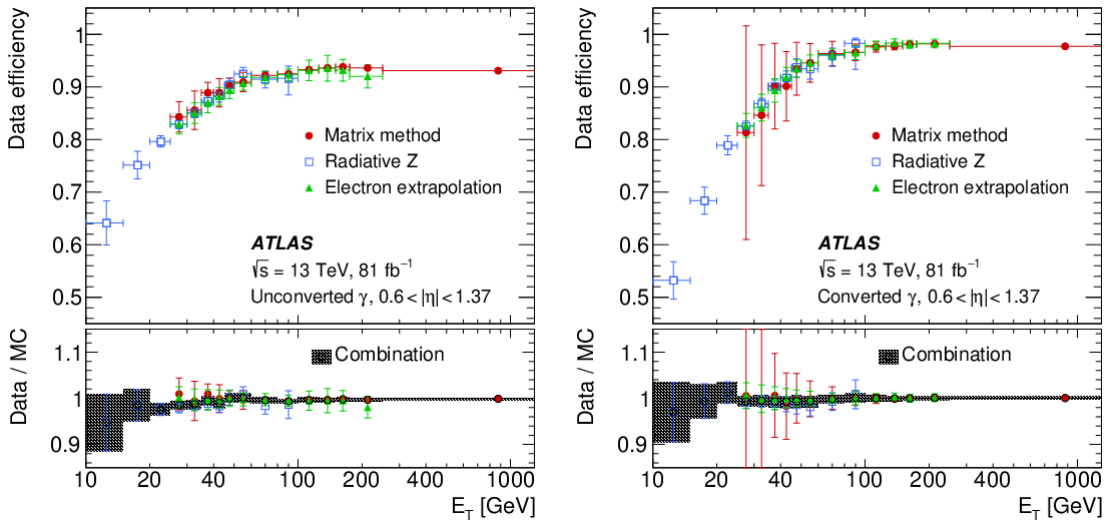

(a) (b)

Figure 3.13 – The photon identification efficiency, and the ratio of data to MC efficiencies, for (a) unconverted photons and (b) converted photons with a Loose isolation requirement applied as preselection, as a function of E_T. The combined scale factor, obtained using a weighted average of scale factors from the individual measurements, is also presented; the band represents the total uncertainty.[44]

3.4 Photon isolation

One signature of the prompt photons is that they are usually isolated with little energy activity around them. Therefore, to further suppress the background from hadronic decay, the isolation criteria is often required. Two kinds of isolation variables are built to construct the isolation criteria: the calorimeter isolation variable E_T^{coneXX} and the track isolation variable p_T^{coneXX}. The variables are defined as the sum of the calorimeter cell E_T or track p_T inside a cone (namely isolation cone) of a given radius around the electron or photon cluster barycentre, where XX refers to the size of the cone (e.g, $XX = 40$ for a cone size of 0.4). The detailed definition will be given later.

In order to compute the calorimeter isolation variable, a raw isolation transverse energy, $E_{T,raw}^{isol}$ is first computed by summing the transverse energy of positive-energy topological clusters whose barycentre falls within the isolation cone. Figure 3.14 is a scheme of the isolation cone with the core contribution shown in yellow, which is the raw EM particle energy that needs to be subtracted from the sum. The subtraction is made by simply removing the energy of the cells contained in a 5×7 (in units of middle layer cell sizes) rectangular cluster around the barycentre of the EM particle cluster. An additional leakage correction is needed to correct for the energy leakage outside of the 5×7 window into the isolation cone. The leakage is parameterized as a function of E_T and $|\eta|$ using single particle simulated samples without pile-up. The

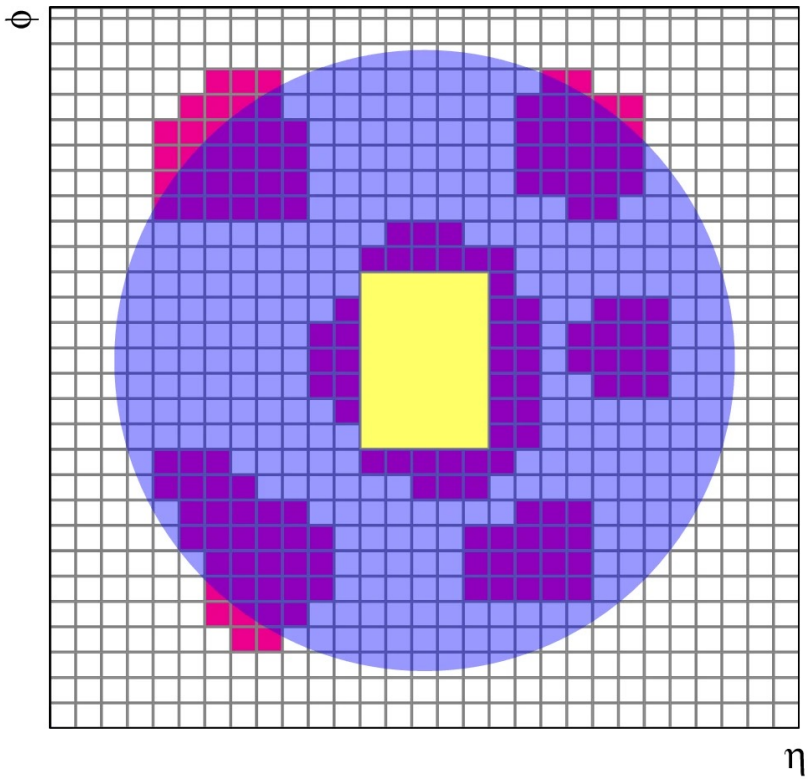

Figure 3.14 – Schema of the calorimeter isolation method: the grid represents the second-layer calorimeter cells in the η and ϕ directions. The candidate electron is located in the centre of the purple circle representing the isolation cone. All topological clusters, represented in red, for which the barycentres fall within the isolation cone are included in the computation of the isolation variable. The 5×7 cells (which cover an area of $\Delta\eta \times \Delta\phi = 0.125 \times 0.175$) represented by the yellow rectangle correspond to the subtracted cells in the core subtraction method.

contribution from pile-up and underlying-event is estimated and subtracted as well. The final calorimeter isolation variable is given by:

$$E_T^{coneXX} = E_{T,raw}^{isolXX} - E_{T,core} - E_{T,leakage}(E_T, \eta, \Delta R) - E_{T,pileup}(\eta, \Delta R) \tag{3.7}$$

where $\Delta R = XX/100$. Both cone size $\Delta R = 0.2$ and 0.4 are used for photon isolation working points.

The track isolation variable p_T^{coneXX} is computed by summing the transverse momentum of the selected tracks within a cone centred around the electron or the photon cluster direction, excluding the tracks matched to the EM cluster. Only tracks that have $p_T > 1$ GeV, $|\eta| < 2.5$, at least seven silicon (Pixel+SCT) hits, at most one shared hit (defined as $n_{Pixel}^{sh} + n_{SCT}^{sh}/2$, where n are the numbers of hits assigned to tracks in the Pixel and SCT detectors), at most two silicon holes (missing hits in the pixel and SCT detectors) and at most one pixel hole are considered. The cone size varies with respect to the transverse momentum of the electron or photon candidate, since the other decay products tend to be very close to the candidate direction in the boosted case. The cone size is defined as:

$$\Delta R = min(\frac{10}{p_T\,[GeV]}, \Delta R_{max}) \tag{3.8}$$

where ΔR_{max} is the maximum cone size, typically 0.2.

Three working points of the photon isolation selection are summarized in Tab. 3.2, each has different efficiency and rejection ability. The efficiency of the photon isolation is measured using photons from $Z \to ll\gamma$ events ($10 < E_T < 100$ GeV) and inclusive photons ($25 < E_T < 1500$ GeV). In general, isolation efficiency is higher for photons with higher transverse momentum. With increasing pile-up activity, the decrease of efficiency is observed (about 10% when increasing $\langle\mu\rangle$ from 15 to 60). There is a slight disagreement (about 5%) of the measured efficiencies in data and simulation, due to the mismodelling of the lateral profile development of the EM showers in simulation. Data-driven shifts are therefore applied to the calorimeter isolation variables in simulation, computed from the difference in the fitted peak values of the calorimeter isolation variable distributions between data and simulation. The isolation efficiencies for unconverted and converted photons as function of η and E_T are illustrated in Fig. 3.15 and Fig. 3.16. In both barrel and end-cap regions of the detector, the isolation efficiencies tend to increase with $|\eta|$ due to an imperfect pile-up correction. The efficiencies also increase with E_T in general as we have less fake photons (e.g. π^0 decays) in high-E_T region. Figure 3.17 shows the decrease of efficiency with increasing pile-up activity.

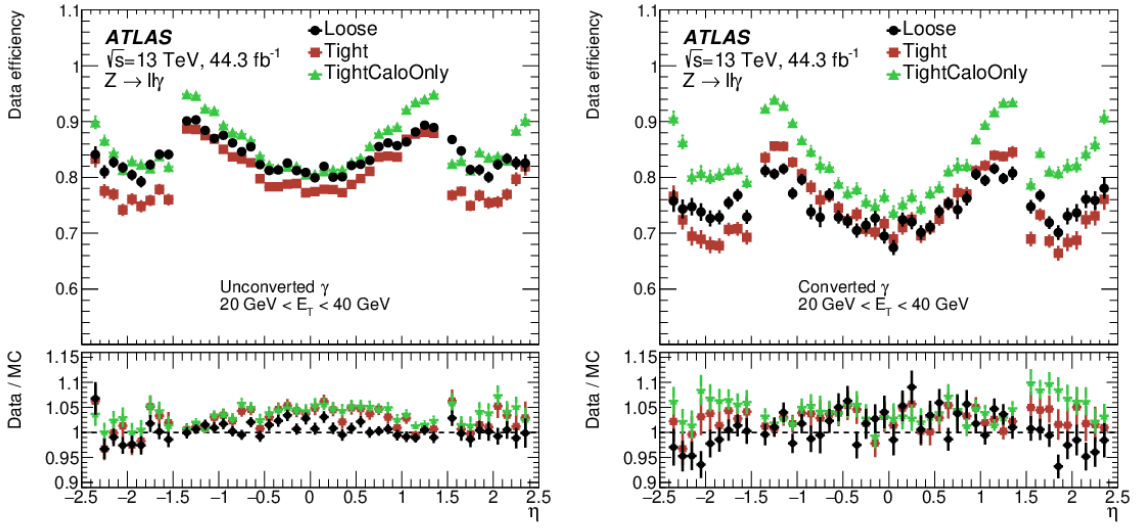

(a) (b)

Figure 3.15 – Efficiency of the isolation working points defined in Tab. 3.2, using $Z \to ll\gamma$ events, for (a) unconverted and (b) converted photons as a function of photon η. The lower panel shows the ratio of the efficiencies measured in data and in simulation. The total uncertainties are shown, including the statistical and systematic components[44].

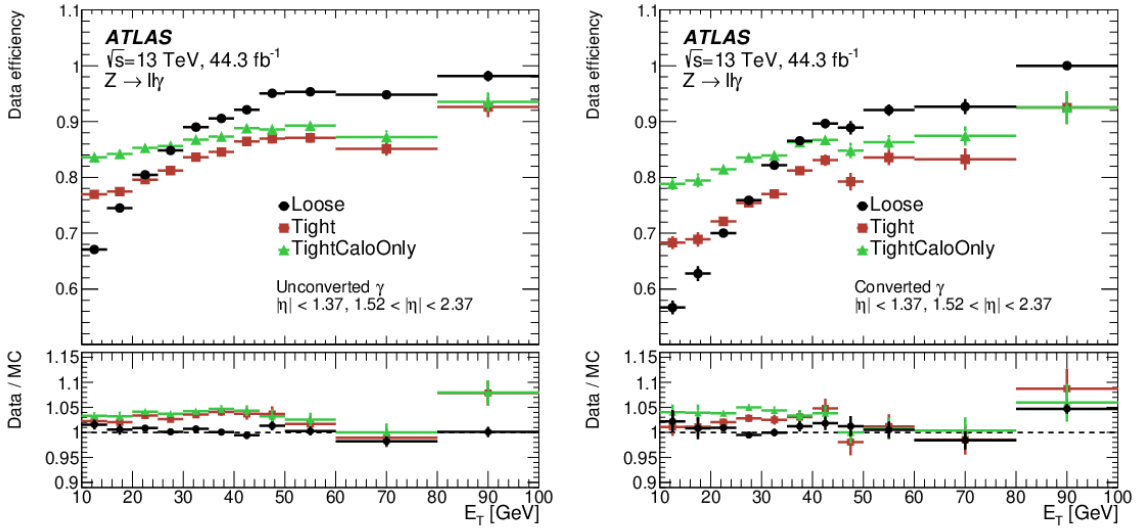

(a) (b)

Figure 3.16 – Efficiency of the isolation working points defined in Tab. 3.2, using $Z \to ll\gamma$ events, for (a) unconverted and (b) converted photons as a function of photon E_T. The lower panel shows the ratio of the efficiencies measured in data and in simulation. The total uncertainties are shown, including the statistical and systematic components[44].

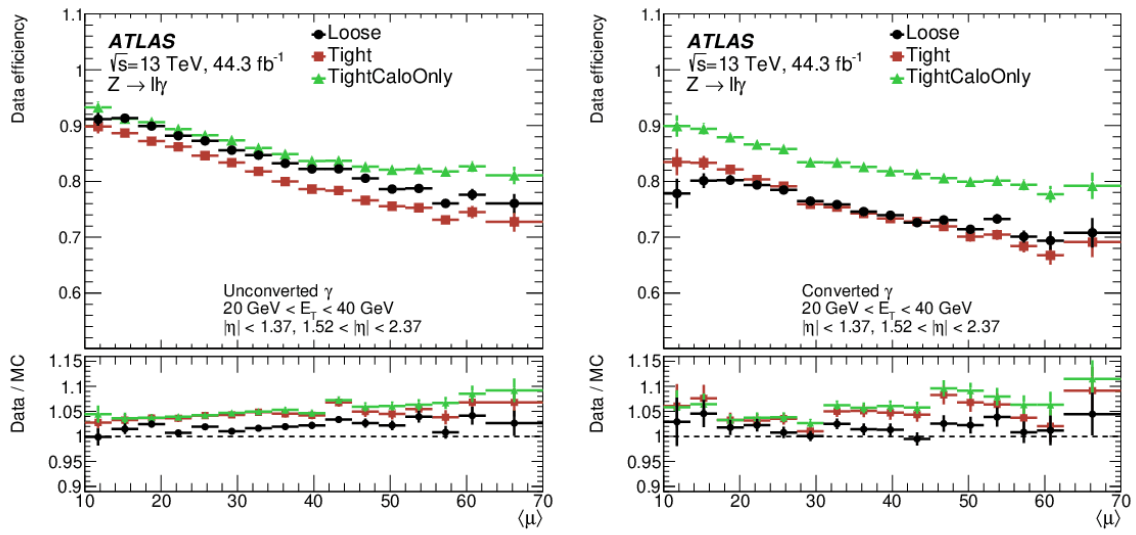

(a) (b)

Figure 3.17 – Efficiency of the isolation working points defined in Tab. 3.2, using $Z \to ll\gamma$ events, for unconverted (left) and converted (right) photons as a function of $\langle\mu\rangle$. The lower panel shows the ratio of the efficiencies measured in data and in simulation. The total uncertainties are shown, including the statistical and systematic components[44].

Category	Description	Name	*loose*	*tight*
Acceptance	$\|\eta\| < 2.37$, with $1.37 < \|\eta\| < 1.52$ excluded	-	✓	✓
Hadronic leakage	Ratio of E_T in the first sampling layer of the hadronic calorimeter to E_T of the EM cluster (used over the range $\|\eta\| < 0.8$ or $\|\eta\| > 1.52$)	R_{had1}	✓	✓
	Ratio of E_T in the hadronic calorimeter to E_T of the EM cluster (used over the range $0.8 < \|\eta\| < 1.37$)	R_{had1}	✓	✓
EM middle layer	Ratio of the energy in 3×7 $\eta \times \phi$ cells over the energy in 7×7 cells centered around the photon cluster position	R_η	✓	✓
	Lateral shower width, $\sqrt{(\sum E_i \eta_i^2)/(\sum E_i) - ((\sum E_i \eta_i^2)/(\sum E_i))^2}$, where E_i is the energy and η_i is the pseudorapidity of cell i and the sum is calculated within a window of 3×5 cells	w_{η_2}	✓	✓
	Ratio of the energy in 3×3 $\eta \times \phi$ cells over the energy of 3×7 cells centered around the photon cluster position	R_ϕ		✓
EM strip layer	Lateral shower width, $\sqrt{(\sum E_i (i - i_{max})^2)/(\sum E_i)}$, where i runs over all strips in a window of 3×2 $\eta \times \phi$ strips, and i_{max} is the index of the highest-energy strip calculated from three strips around the strip with maximum energy deposit	w_{s3}		✓
	Total lateral shower width, $\sqrt{(\sum E_i (i - i_{max})^2)/(\sum E_i)}$, where i runs over all strips in a window of 20×2 $\eta \times \phi$ strips, and i_{max} is the index of the highest-energy strip measured in the strip layer	w_{tot}		✓
	Energy outside the core of the three central strips but within seven strips divided by energy within the three central strips	f_{side}		✓
	Difference between the energy associated with the second maximum in the strip layer and the energy reconstructed in the strip with the minimum value found between the first and second maxima	ΔE_s		✓
	Ratio of the energy difference between the maximum energy deposit and the energy deposit in the secondary maximum in the cluster to the sum of these energies	E_{ratio}		✓
	Ratio of the energy in the first layer to the to the total energy of the EM cluster	f_1		✓

Table 3.1 – Discriminating variables used for loose and tight photon identification.

Working point	Calorimeter isolation	Track isolation
Loose	$E_T^{cone20} < 0.065 \times E_T$	$p_T^{come20}/E_T < 0.05$
Tight	$E_T^{cone40} < 0.022 \times E_T + 2.45GeV$	$p_T^{come20}/E_T < 0.05$
TightCaloOnly	$E_T^{cone40} < 0.022 \times E_T + 2.45GeV$	-

Table 3.2 – Definition of the photon isolation working points.

Chapter 4

Photon energy calibration uncertainties from shower leakage mismodeling

Studies described in this chapter were my qualification task in order to become an ATLAS author. In this chapter, one of the photon-specific systematic uncertainties on the energy calibration is discussed. The shower shape in EM calorimeter is mismodeled [45] by the simulation.This mismodeling can slightly bias the energy estimation, as it is possible that the energy leaking outside of an electromagnetic cluster is different between electrons and photons, or varies with respect to p_T. For electrons of certain E_T, the loss of energy is corrected by the in-situ energy scales. However, the correction might not hold for other transverse energies or photons anymore.

To study the electron to photon leakage mismodeling, the photons are selected from the $Z \to \mu\mu\gamma$ and diphoton samples, and the electrons are selected from the $Z \to ee$ samples. To be consistent with the energy calibration procedure, the results obtained with photons from the radiative Z decay channel are used to quantify the photon-specific systematic uncertainty, while the results obtained with photons in diphoton samples are used as a cross-check in the high p_T region. In addition, single particle MC samples are used to study the impact of detector material and conversion reconstruction mismodeling. Section 4.1 introduces the method and the data and simulated samples used in the analysis. The measured variables are presented in Sec. 4.2, and some further studies are discussed in Sec. 4.3. Finally, two important corrections and the final results of this analysis are summarized in Sec. 4.4.

4.1 Method

This study is based on clusters reconstructed by the sliding-window algorithm described in Sec. 3.1.1. In the electromagnetic calorimeter, the cluster energy is first

reconstructed using the hits in the second layer, where cells within a certain window around the cell with the highest energy are clustered together. For other layers, all cells intersecting the geometrical projection of this window are included. In practice, energy collected within a 7×11 window in $\eta \times \phi$ in the middle layer is taken as the reference energy. Once this 7×11-cell cluster and its centre have been found, it is possible to build clusters of arbitrary sizes, as long as they are smaller.

The variables used to describe the energy leaking outside a given cluster are defined in Sec. 4.1.1. The data and simulated samples are discussed in Sec. 4.1.2. Particularly, the background component (jet faking photons) needs to be removed when using the diphoton samples. A dedicated subtraction method is described in Sec. 4.1.3.

4.1.1 Definition of leakage variables

Two main quantities are studied in this analysis. The first one is the fraction of energy leaking outside a given cluster (namely l):

$$l = \frac{E_{\mathrm{s2}}(7 \times 11) - E_{\mathrm{s2}}(size)}{E_{\mathrm{s2}}(size)} \tag{4.1}$$

where E_{s2} represents the energy collected in layer 2 for a given cluster size. The size might depend on the type of particle (electron or photon) and its position in the detector (barrel or end-cap). However, in Run 2, the size is identical for electrons, converted photons and unconverted photons and is 3×7 in the barrel and is 5×5 in the end-cap region.

Next, in order to quantify the difference between data and MC, electrons and photons, the "double difference" is defined as:

$$\Delta((e-\gamma)^{\mathrm{data}} - (e-\gamma)^{\mathrm{MC}}) = (l^{\mathrm{el}} - l^{\mathrm{ph}})^{\mathrm{data}} - (l^{\mathrm{el}} - l^{\mathrm{ph}})^{\mathrm{MC}} \tag{4.2}$$

where l is the energy leakage as defined in Eq. 4.1, and the superscripts indicate the sample it is estimated from (electrons or photons, in data or MC).The absolute value of double difference is used as a photon-specific systematic uncertainty, as the result of the subtractions in Eq. 4.2 could be positive or negative.

In addition, two other variables are calculated to study the lateral energy leakage along η and ϕ directions:

$$l_{\eta} = \frac{E_{\mathrm{s2}}(7 \times 7) - E_{\mathrm{s2}}(3 \times 7)}{E_{\mathrm{s2}}(size)} \tag{4.3}$$

$$l_{\phi} = \frac{E_{\mathrm{s2}}(7 \times 11) - E_{\mathrm{s2}}(7 \times 7)}{E_{\mathrm{s2}}(size)} \tag{4.4}$$

The energy leaking outside a given cluster is calculated separately for electrons, converted photons and unconverted photons. Since the thickness of absorbers changes in the calorimeter at $|\eta| = 0.8$, three η bins are set: $|\eta| < 0.8$ (namely "inner barrel region"), $0.8 < |\eta| < 1.37$ ("outer barrel region") and $1.52 < |\eta| < 2.37$ ("end-cap region"). The double difference may also depend on the p_T of the candidates or on pile-up conditions. In order to check the dependence, the data-MC simple differences for photons and electrons are calculated separately in selected p_T bins, while the double differences are calculated only in the common bins. As for pile-up, the double differences are calculated in different bins of number of interactions per bunch crossing.

4.1.2 Data and simulated samples

Radiative Z decaying to a lepton pair and one photon provides a photon sample of high purity, although it is limited in statistics and the available kinematic range. In this study, the lateral leakage for electrons is extracted from a sample of $Z \to ee$ events. To avoid the electron to photon ambiguity, the $Z \to ee\gamma$ channel is not used, while a $Z \to \mu\mu\gamma$ event selection is applied to provide low-p_T photon samples. Photons with higher p_T coming from QCD production of photon pairs are also studied as a cross-check and an extension.

By the time the study was done, the data taking of Run 2 was not finished and only a dataset of 33 fb^{-1} collected in 2016 is used in the analysis (the results may still be referred as "Run 2 results" when they are compared with Run 1 results). For both $Z \to \mu\mu\gamma$ and $Z \to ee$ processes, the simulated samples are generated and showered with Powheg, Pythia8, EvtGen and Photospp generators. The diphoton events are generated with the Sherpa generator. The simulation is performed in slices of the diphoton invariant mass $M_{\gamma\gamma}$, therefore the samples for all slices are then merged with the proper normalization to match the luminosity corresponding to the one in the data.

When the Monte Carlo samples are produced, one can only put a best-guess of the data pile-up conditions as they are generated during (or even before) the data-taking period. The pile-up condition might have significant impact especially when the luminosity is high. Therefore, the MC pile-up condition needs to be reweighted to what is found in data. This weight is usually computed using the distributions of the average number of pile-up interactions for a given dataset and for MC as inputs.

The $Z \to \mu\mu\gamma$ candidate events must pass the double muon trigger requirement (the events must contain two muons with $p_T^\mu > 10$ GeV) and at least one single muon trigger requirement (loosest ones require a muon with $p_T^\mu > 40$ GeV, or a muon with $p_T^\mu > 20$ GeV which passes loose identification). Similarly, the $Z \to ee$ candidates must pass the double electron trigger requirement (two electrons with $p_T^e > 15$ GeV, both

pass loose identification[1]) or at least one single electron trigger requirements (loosest ones require a electron with $p_T^e > 24$ GeV which passes tight identification, or electron with $p_T^e > 60$ GeV which passes medium identification). The diphoton candidates must pass one of the following diphoton trigger requirements:

- $p_T^{leading} > 35$ GeV, $p_T^{sub-leading} > 25$ GeV, both leading (the photon with higher p_T) and sub-leading photons pass the loose identification requirement.
- $p_T^{leading,sub-leading} > 50$ GeV, both leading and sub-leading photons pass the loose identification requirement.
- $p_T^{leading,sub-leading} > 20$ GeV, both leading and sub-leading photons pass the tight identification requirement.

The criteria used to select the objects and the events for the energy leakage measurement are listed below:

$Z \to e^+e^-$**:** the electrons are required to have $p_T > 18$ GeV and $|\eta| < 2.47$, excluding the crack region ($1.37 < |\eta| < 1.52$). They are also required to pass the likelihood-based LHMedium identification criteria, and a gradient[2] isolation requirement.

$Z \to \mu^+\mu^-\gamma$**:** the muons are required to have $p_T > 10$ GeV and $|\eta| < 2.4$. They are also required to have a reconstructed track with small impact parameter with respect to the primary vertex, $|d_0|/\sigma_{d_0} < 10$ and $|z_{pv}| < 10$ mm[3].

The photons are required to have $p_T > 10$ GeV and $|\eta| < 2.37$, excluding the crack region ($1.37 < |\eta| < 1.52$). They are required to pass the tight photon identification requirement and the Tight isolation requirement, as defined in Tab. 3.2.

diphotons: photons are required to have $p_T > 25$ GeV and $|\eta| < 2.37$, excluding the crack region ($1.37 < |\eta| < 1.52$). The tight photon identification requirement and the tight isolation requirement are also applied.

[1]The baseline electron identification algorithm used in Run 2 is the likelihood-based (LH) method. When making a selection decision, several properties of the electron candidates are evaluated simultaneously. Three levels of identification working points (loose, medium, tight with increasing the background rejection ability) are provided. Each of them uses the same variables to define the LH discriminant while the selection on the discriminant is different. The online selections are kept as close as possible to the offline ones, except for some important differences on variables such as the impact parameter, $\Delta p/p$, E/p, etc.

[2]The gradient working point is a set of requirements on E_T^{cone20} and p_T^{cone20} (defined similarly as in Sec. 3.4), designed to give a fixed value of efficiency of 90% at $p_T = 25$ GeV and 99% at $p_T = 60$ GeV, uniform in η.[44]

[3]The transverse impact parameter, d_0, is defined as the shortest distance between a track and the beam line in the transverse plane. The significance of the transverse impact parameter is defined as the ratio of d_0 to its uncertainty. The longitudinal impact parameter, z_{pv}, is defined as the distance in z between the primary vertex and the point on the track used to evaluate d_0.

For the Z decay events, the following event-level selection is applied:

- exactly two electrons or two muons, passing the object selection criteria described above. Exactly one additional photon is required for the $Z \to \mu^+\mu^-\gamma$ channel;
- the two leptons are required to have opposite charges;
- the two leptons must match the objects, on which the trigger decision was made;
- for the $Z \to \mu^+\mu^-\gamma$ channel, the invariant mass must lie within the following ranges: 40 GeV $< M_{\mu\mu} <$ 83 GeV and 83 GeV $< M_{\mu\mu\gamma} <$ 100 GeV.
- for the $Z \to e^+e^-$ channel, the mass window should be 75 GeV$< M_{ee} <$ 105 GeV.

Figure 4.1 shows the p_T distributions for photons from the $Z \to \mu^+\mu^-\gamma$ channel and electrons from the $Z \to e^+e^-$ channel. After all the selection requirements, the p_T spectrum for electrons is peaked around 45 GeV while for photons it is much softer. The η distributions are shown in Fig. 4.2. Figure 4.3 shows the transverse momentum distribution of both leading$-p_T$ and sub-leading$-p_T$ photons.

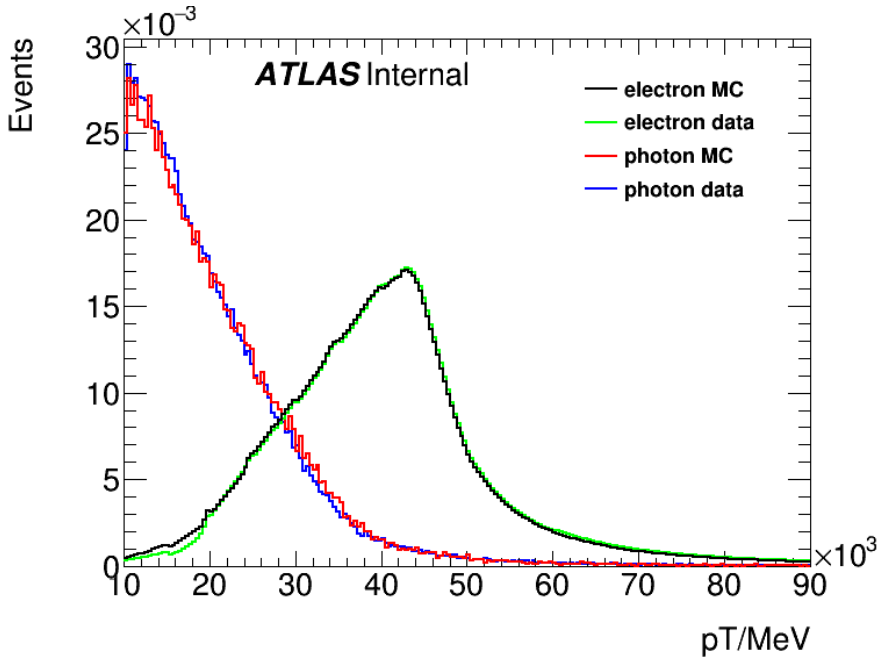

Figure 4.1 – The distributions of p_T for electrons in MC (black), electrons in data (green), photons in MC (red) and photons in MC sample (blue line). The distributions from MC samples are scaled to the same normalization as the distributions in data.

In order to check the contamination from fake photons and fake electrons, the background contamination of the selected samples is estimated. For $Z \to \mu\mu\gamma$ events, the $M_{\mu\mu\gamma}$ distribution is fitted in the range [45 GeV, 125 GeV] and the signal region is defined as [83 GeV, 100 GeV]. The signal is modeled with the convolution of a

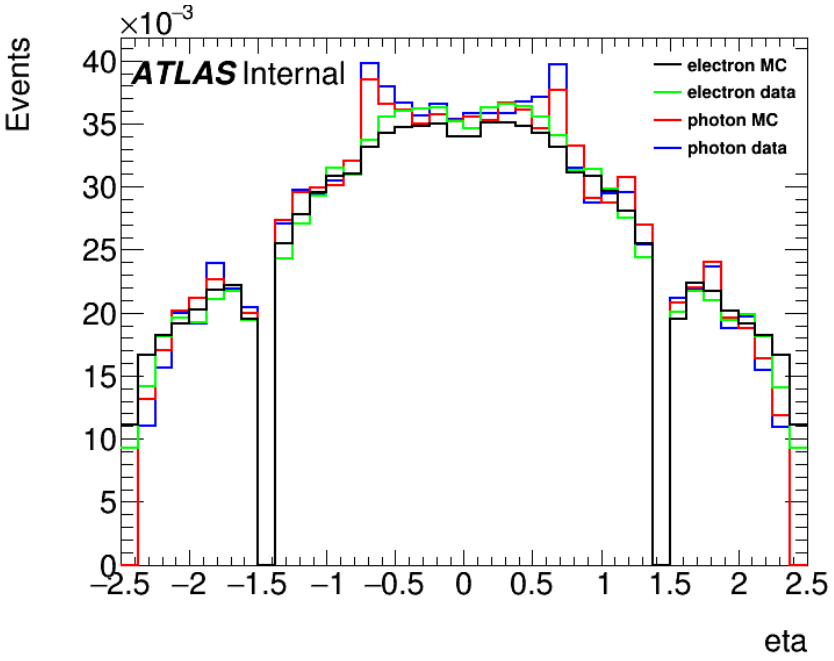

Figure 4.2 – The distributions of η for electrons in MC sample (black line), electrons in data sample (green line), photons in MC sample (red line) and photons in MC sample (blue line). The distributions from MC samples are scaled to the same normalization as the distributions in data.

Breit-Wigner function and a Crystal Ball function while a polynomial is used to describe the background. For $Z \to ee$ events, the M_{ee} distribution is fitted in the range [66 GeV, 116 GeV] and the signal region is defined as [75 GeV, 105 GeV]. The signal is modeled with a Voigt function while a polynomial is used to describe the background. The results are shown in Fig. 4.4. The fraction of background in the signal region is estimated to 1.96% in the $Z \to \mu\mu\gamma$ channel and 0.08% in the $Z \to ee$ channel. Since the sample purities are high, the background is neglected in the following.

In the diphoton channel however, one cannot simply neglect the background contamination. As an example, distributions of energy leakage of leading converted photon falling into the inner barrel region are shown in Fig. 4.5 for two p_T regions. After normalization to the luminosity in data, the number of events in data is about twice as much as in $\gamma\gamma$ simulated samples. In addition, energy leakage distributions in data tend to have longer tails and larger central values, most likely due to background from jets faking photons, which are more likely to have larger leakage in the second layer of the calorimeter. One can also see in Fig. 4.5 that the purity of the photons sample increases with respect to p_T. For photons with p_T larger than about 100 GeV, the background contribution is negligible. However in the low p_T region, the background contamination must be subtracted.

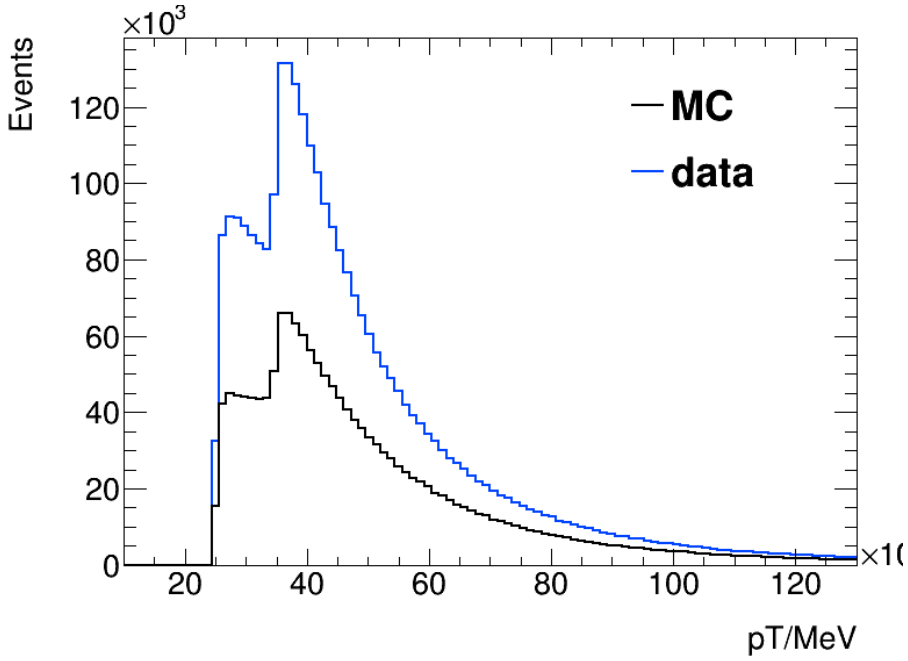

Figure 4.3 – The distributions of p_T for photons after normalization in MC (black) and in data (blue).

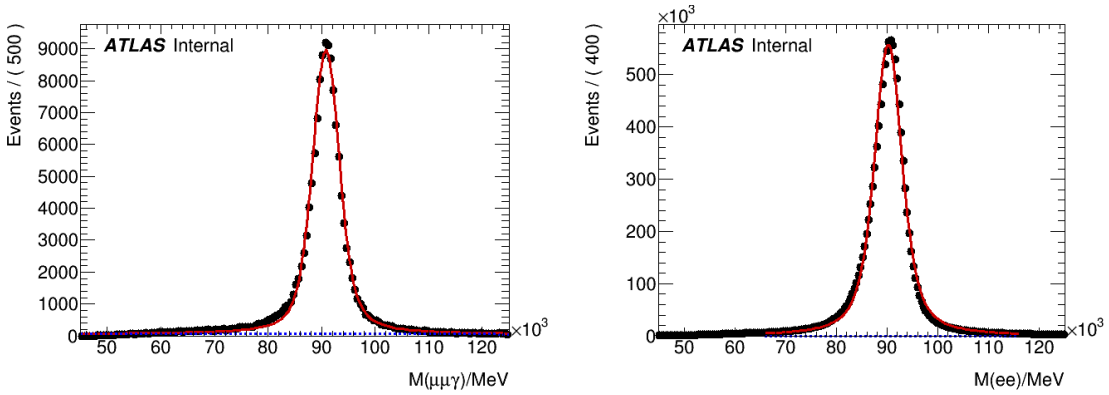

(a) (b)

Figure 4.4 – Invariant mass distribution for (a) the $Z \to \mu\mu\gamma$ sample and (b) the $Z \to ee$ sample. The black dots represent the distributions from the data samples. The red line is the result of the signal+background fit described in the text.

4.1.3 Background subtraction in the diphoton sample

There are four components in the diphoton data sample: the signal component ($\gamma\gamma$), and three background components: photon-jet pairs (γjet, $jet\gamma$) and jet pairs ($jetjet$). A standard method to extract the fraction of each component is to fit the distributions of the isolation variables. In this study, however, a fit to the boolean variable indicating

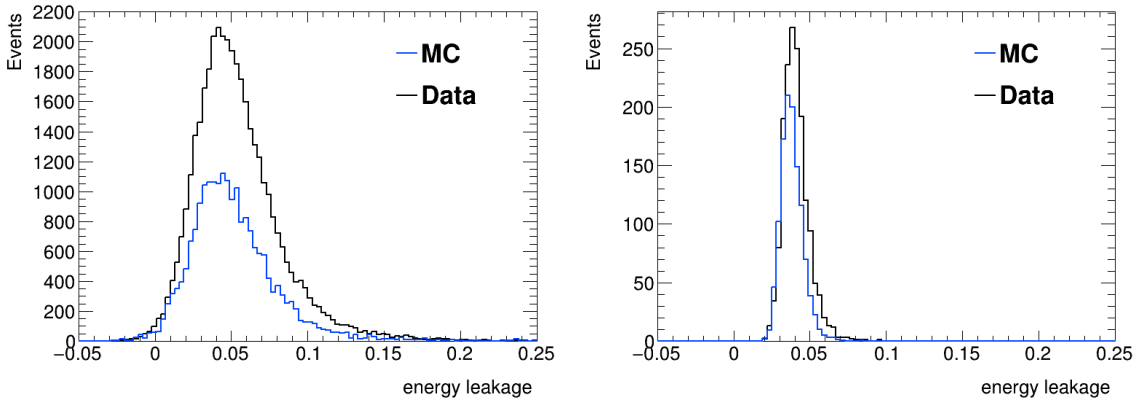

(a) (b)

Figure 4.5 – Energy leakage distribution of leading converted photon with $|\eta| < 0.8$, (a) $35<p_T<45$ GeV and (b) $150<p_T<200$ GeV.

if the candidate photon passes or not the isolation criteria is preferred in order to reduce the impact of the correlation between isolation and leakage.

It was not possible to directly use γjet simulation samples to build the fitting templates for two reasons: it was seen in the past that the jet-to-photon fake rate is not modeled accurately in the simulation, and the amount of simulated events is not enough, especially after applying the tight photon identification and isolation criteria. A control region (CR) from data is therefore used. It is defined by reverting at least one criterion on two shower shape variables (so-called "Loose'2" selection): the second maximum difference (ΔE) and the maximum relative ratio (E_{ratio}), as illustrated in Fig. 3.12. The signal template is built from $\gamma\gamma$ MC samples, applying the selection described in Sec. 4.1.2. Definitions of signal and control regions are summarized in Tab. 4.1. Note that the fit is performed on the isolation status of the leading photons, while the isolation criteria is still applied on the sub-leading photons in order to reduce the background.

Region	Candidate	photon ID
Signal	Leading	Tight
	Sub-leading	Tight
Background	Leading	Loose'2
	Sub-leading	Loose

Table 4.1 – Definition of the control and signal regions.

The boolean variable "PassIsolation" is set to 1 (0) if the leading candidate passes (fails) the tight isolation requirement as mentioned before. The two-bin histograms of

PassIsolation obtained from signal MC and background CR are then used as signal and background templates to fit the data. Then, the fraction of background f_{bkg} (or conversely, the purity) in the PassIsolation=1 bin is extracted. The purity of the diphoton sample is shown in Fig. 4.6. The purity increases with respect to photon p_T as expected, and is slightly higher for unconverted photons (except for the inner barrel region). For photons with p_T larger than 100 GeV, the purity is above 95%, therefore the background is neglected in such case. The fractions obtained from the fit are used to normalize the energy leakage of the background, which is later subtracted from data.

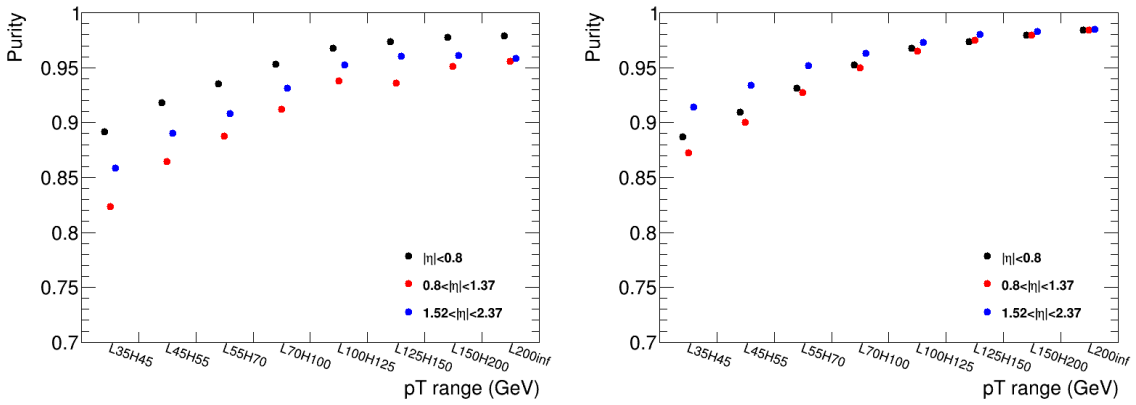

(a) (b)

Figure 4.6 – Purity for samples with (a) converted and (b) unconverted leading photon. The black dots represent $|\eta| < 0.8$, red corresponds to $0.8 < |\eta| < 1.37$, and blue to $1.52 < |\eta| < 2.37$. The statistical uncertainty is negligible.

4.2 Measurement of the lateral leakage and double difference

4.2.1 Measurement of the lateral leakage

Since the p_T distributions are quite different for electrons and photons, the photon sample from the Z decays is split according to two p_T bins: $15 < p_T < 25$ GeV and $p_T > 25$ GeV in order to better compare with electrons. The distributions of the energy leakage for converted, unconverted photons and electrons are shown in Fig. 4.7, Fig. 4.8 and Fig. 4.9 respectively. One can see that the profiles of electrons are narrower, while for photons with low p_T, the profiles are wide especially in the barrel region.

For the high-p_T diphoton sample, more p_T bins are defined: 35-45, 45-55, 55-70, 70-100, 100-125, 125-150, 150-200, >200 GeV. Similarly to the photons and electrons

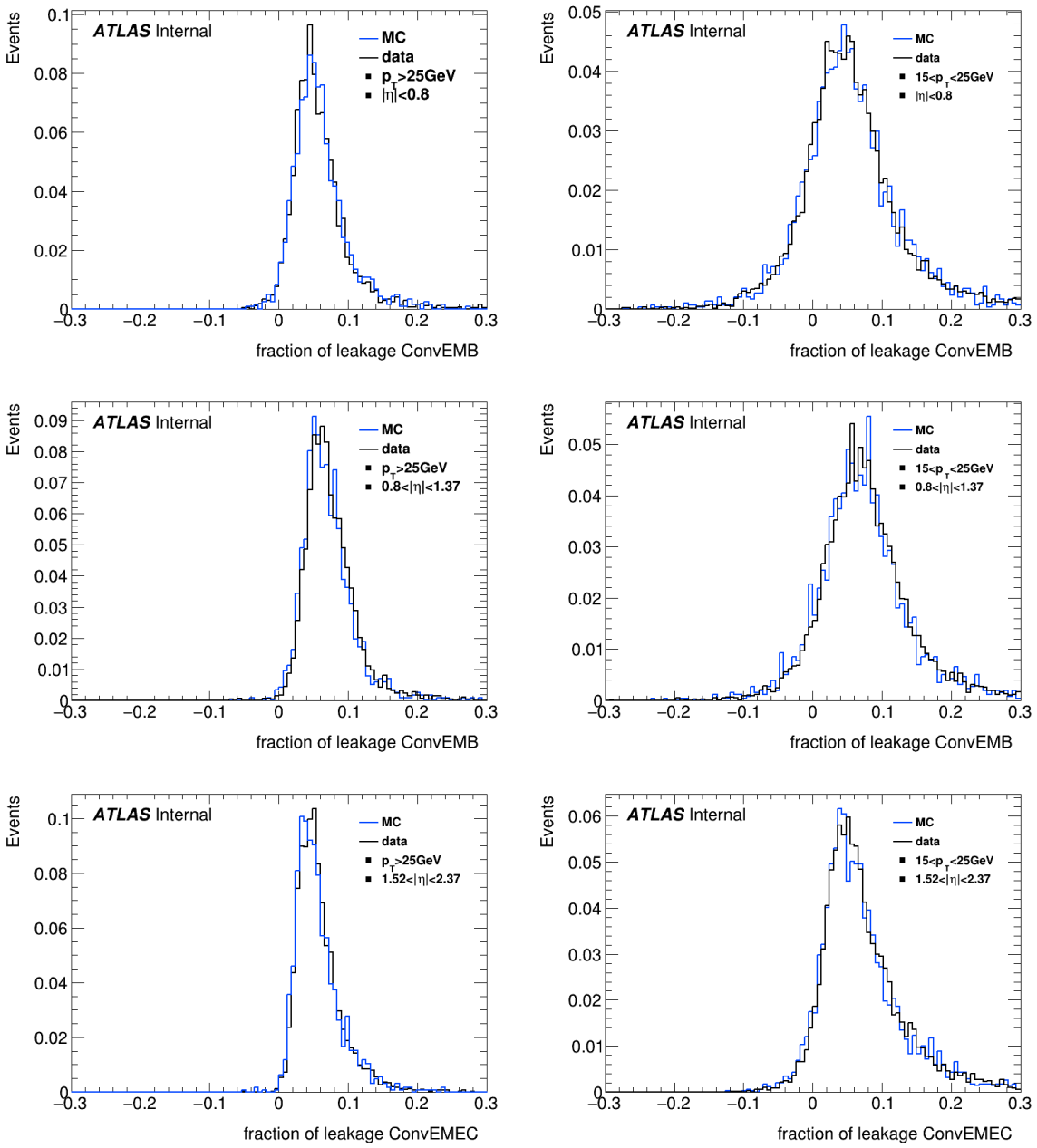

Figure 4.7 – Distributions of the shower leakage for converted photons in $|\eta| < 0.8$ (top row), $0.8 < |\eta| < 1.37$ (middle) and $1.52 < |\eta| < 2.37$ (bottom), for photon candidates with $p_T > 25$ GeV (left) and $15 < p_T < 25$ GeV (right). Data and MC distributions are shown in black and blue respectively.

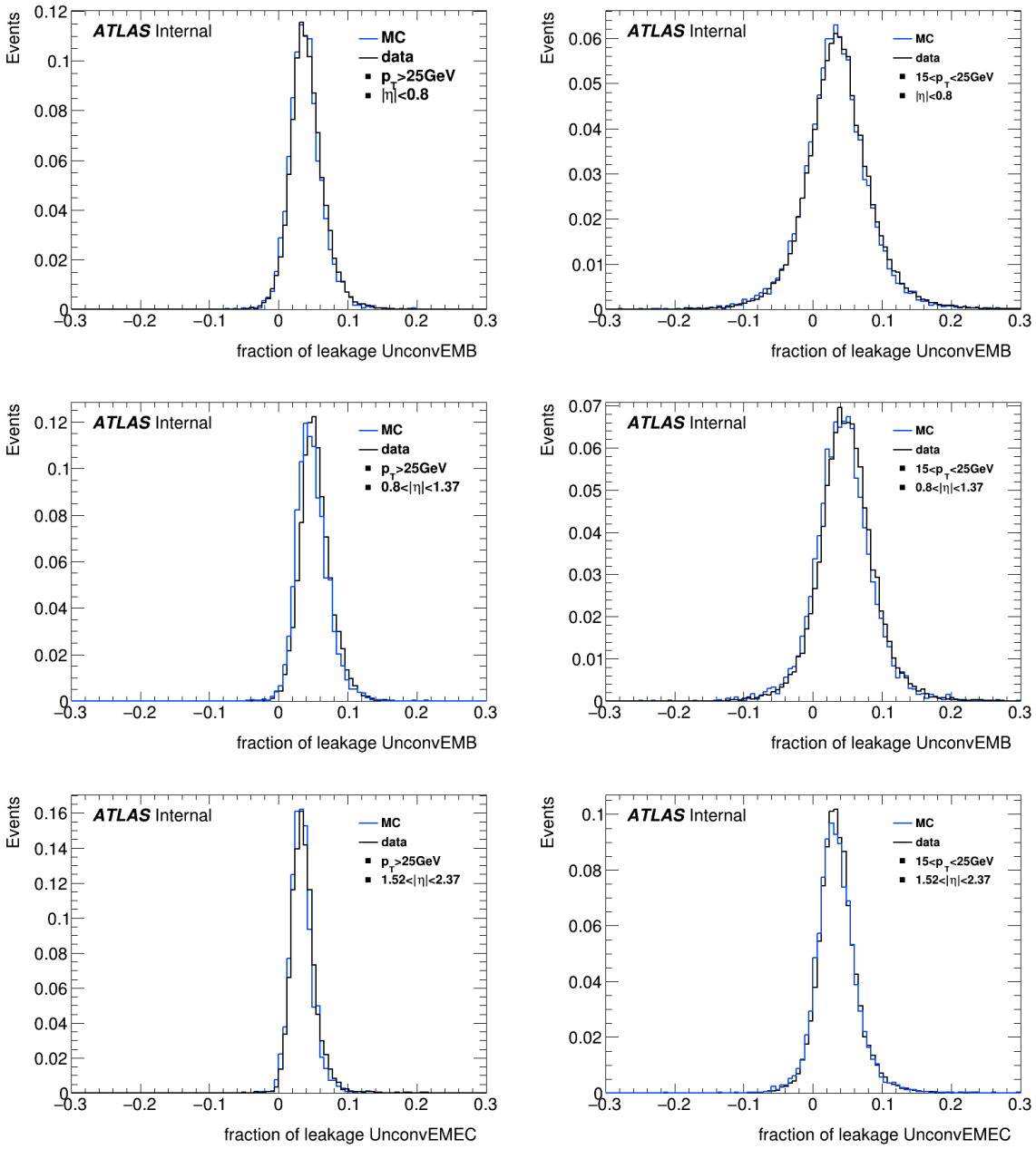

Figure 4.8 – Distributions of the shower leakage for unconverted photons in $|\eta| < 0.8$ (top row), $0.8 < |\eta| < 1.37$ (middle) and $1.52 < |\eta| < 2.37$ (bottom), when the photon candidates has $p_T > 25$ GeV (left) or $p_T < 25$ GeV (right). Data and MC distributions are shown in black and blue respectively.

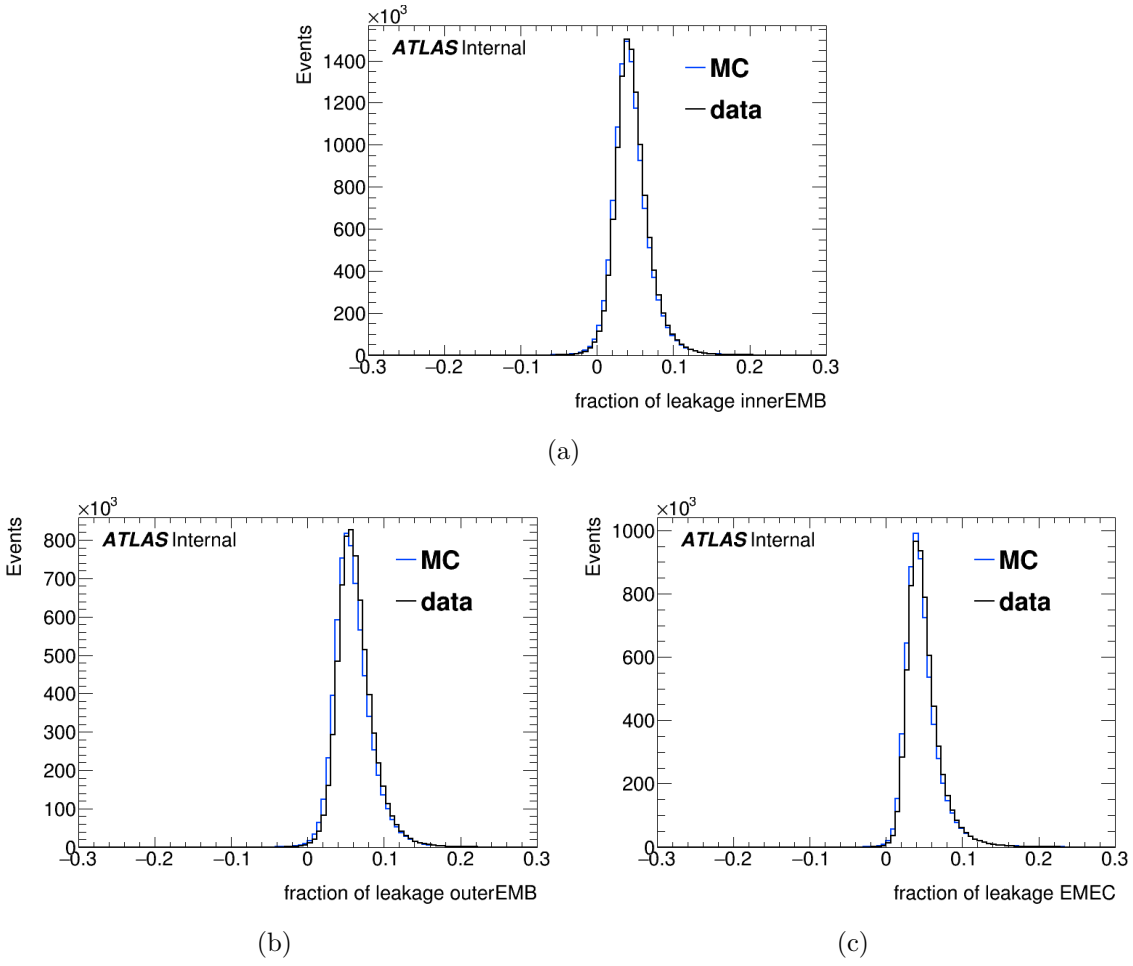

(a)

(b)

(c)

Figure 4.9 – Distributions of the shower leakage for electrons in (a) $|\eta| < 0.8$, (b) $0.8 < |\eta| < 1.37$ and (c) $1.52 < |\eta| < 2.37$. The blue histogram represents the MC samples and the black histogram represents data.

from the Z decay, mean and spread of the energy leakage decreases as p_T increases. As an example, the distributions of energy leakage in MC and data in the region $35 < p_T < 45$ GeV are shown in Fig.4.10, after the subtraction procedure described in Sec. 4.1.3. Comparing to Fig.4.5, one can see that the background is efficiently suppressed by the dedicated method.

4.2.2 Measurement of the double difference

The mean values of the leakage distributions in Sec. 4.2.1 are used to calculate the double difference using Eq. 4.2. Figure 4.11 shows the results without any correction, obtained with photons from radiative Z decays in three η bins: $|\eta| < 0.8$, $0.8 < |\eta| < 1.37$, $1.52 < |\eta| < 2.37$. Here all electrons have $p_T > 25$ GeV and all photons have $p_T > 15$ GeV. The Run 1 results are also plotted for comparison. Generally, the double difference is smaller than 0.2% with large statistical uncertainties. The mean value and statistical uncertainties of the double difference are listed in Tab. 4.2.

Double difference(%)	$\|\eta\| < 0.8$	$0.8 < \|\eta\| < 1.37$	$1.52 < \|\eta\| < 2.37$
El - Conv, $p_T^\gamma > 25$GeV	0.273 ± 0.095	-0.056 ± 0.089	-0.014 ± 0.080
El - Unconv, $p_T^\gamma > 25$GeV	-0.072 ± 0.033	-0.164 ± 0.040	-0.092 ± 0.035
El - Conv, $15 < p_T^\gamma < 25$ GeV	0.196 ± 0.114	-0.031 ± 0.112	-0.138 ± 0.093
El - Unconv, $15 < p_T^\gamma < 25$ GeV	-0.158 ± 0.038	-0.087 ± 0.046	-0.026 ± 0.037

Table 4.2 – Double difference measured for converted and unconverted photons from Z decay. Electrons have $p_T > 25$ GeV.

As a cross check, the double difference calculated using the energy leakage of photons from diphoton channel is shown in Fig. 4.12. Results are also shown in three η regions separately. Before background subtraction, the double difference tends to be negative due to the large value of energy leakage of fake photons. This effect is obvious in the low p_T region due to lower photon purity. In the high p_T region, the background contamination is negligible. After background subtraction, the double difference is generally around zero. Only statistical uncertainty is shown here, which is much smaller compared to the results obtained with Z decay photons. However non-negligible systematic uncertainty coming from the background subtraction must be considered, introduced later in Sec. 4.4.2.

4.3 Studies on the double difference

In order to further understand the results in Sec. 4.2.2 and to study potential biases, a few checks on the double difference are performed and described in this section.

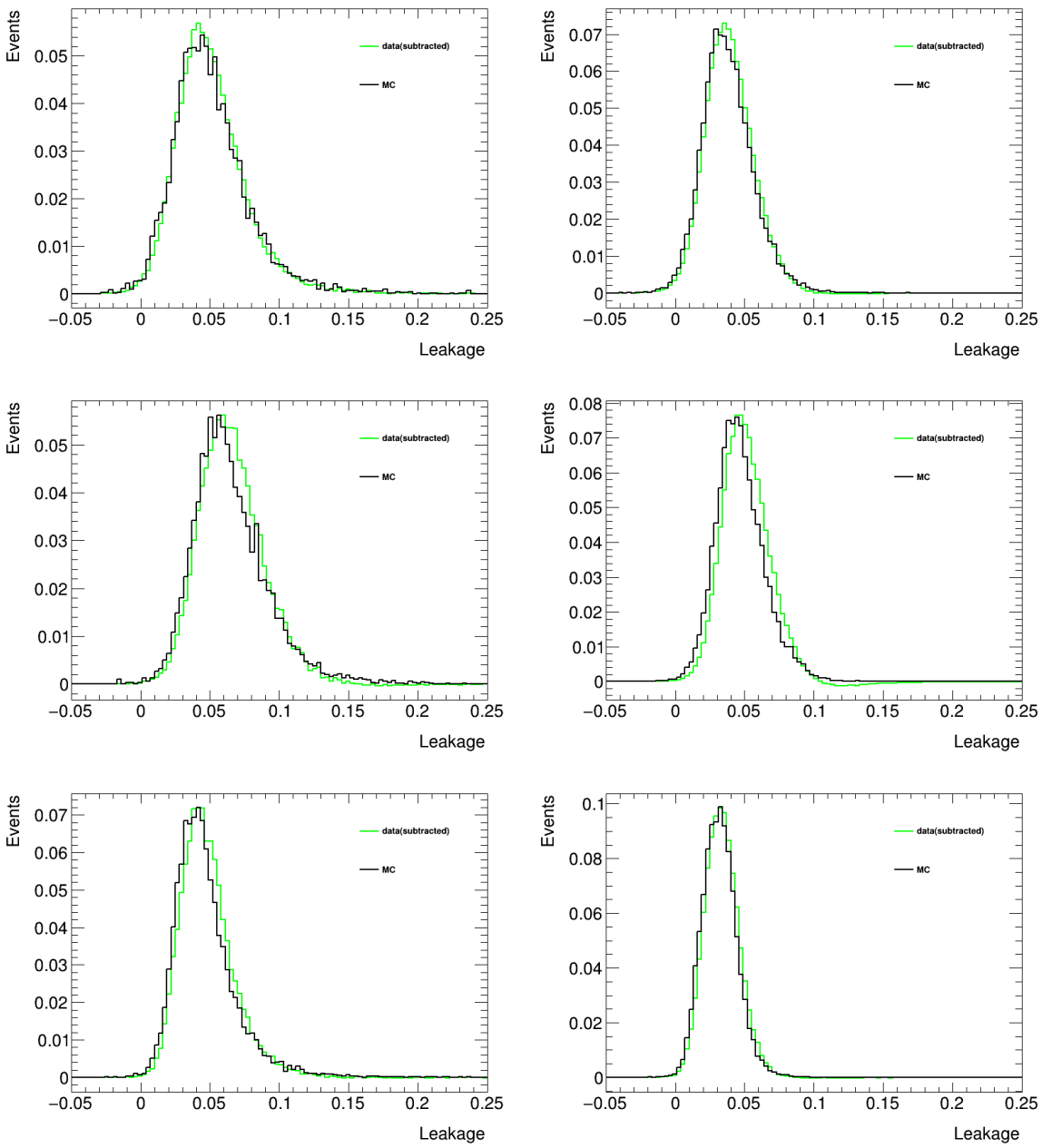

Figure 4.10 – Distributions of the shower leakage for converted (left) and unconverted (right) photons in $|\eta| < 0.8$ (top row), $0.8 < |\eta| < 1.37$ (middle) and $1.52 < |\eta| < 2.37$ (bottom). The black histogram represents MC, and the green represents data after background subtraciton.

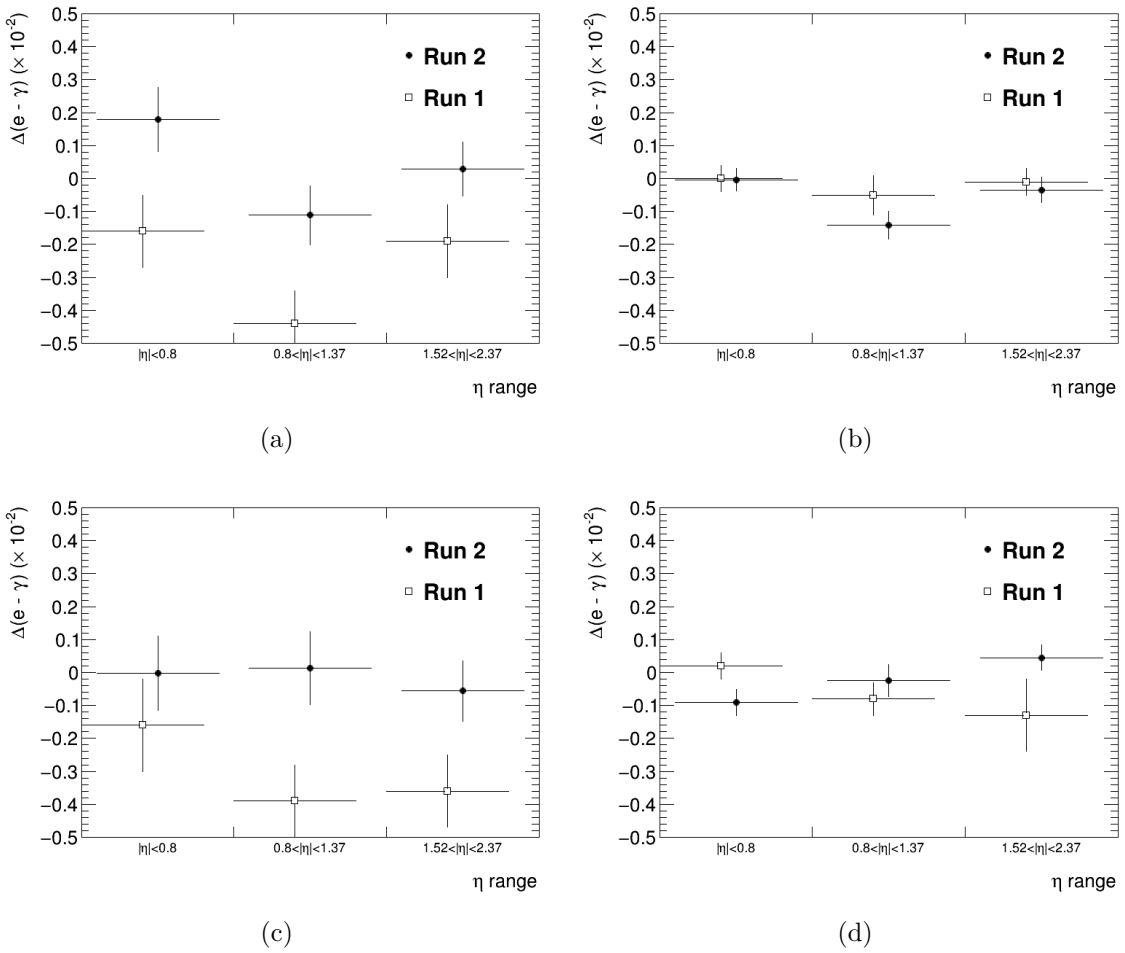

Figure 4.11 – Double difference measured with $Z \to \mu\mu\gamma$ sample in three η regions (x-axis), for converted photons (left) and unconverted photons (right), with $p_T > 25$ GeV (top row) or $15 < p_T < 25$ GeV (bottom row). Electrons have $p_T > 25$ GeV. Open squares represent Run 1 numbers and black dots represent Run 2 results.

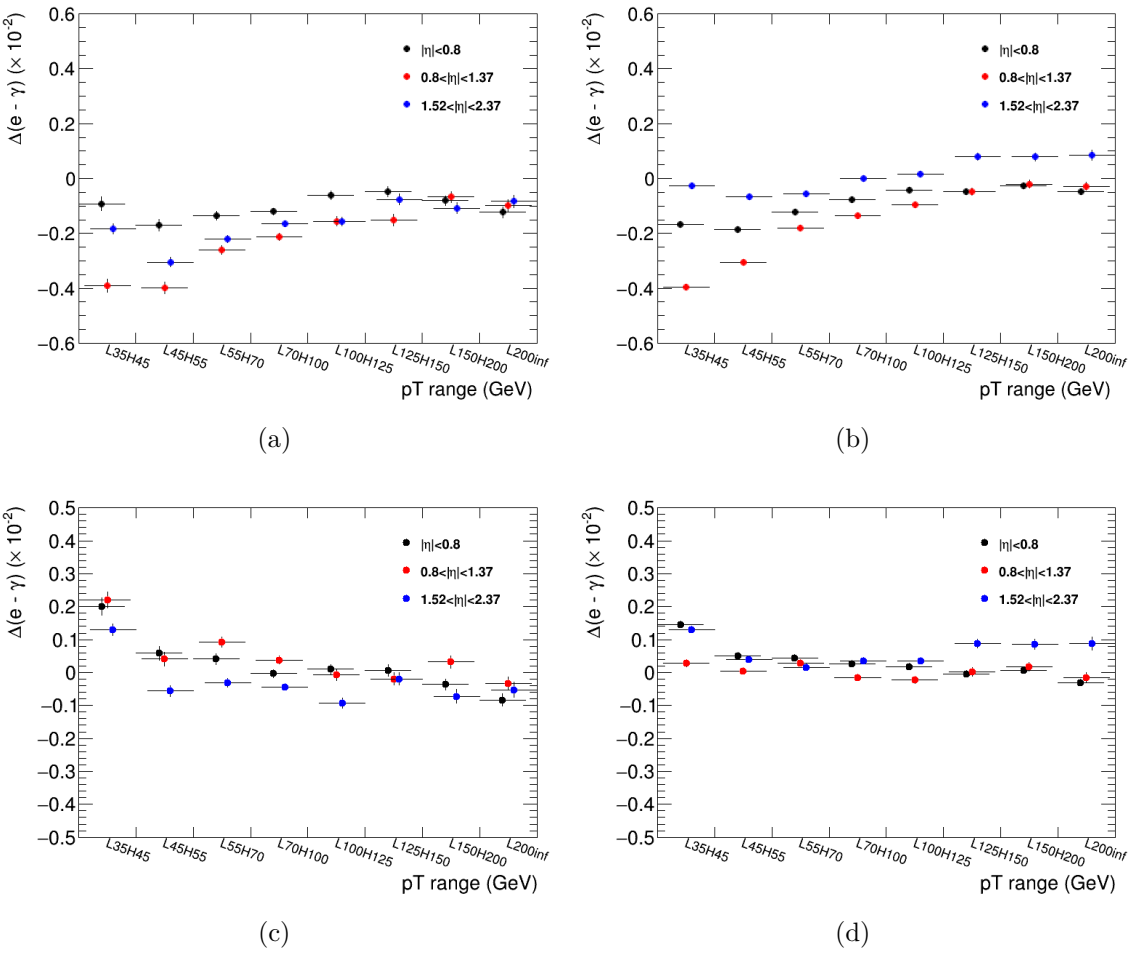

Figure 4.12 – Double difference measured with diphoton sample in eight p_T regions (x-axis), for converted photons (left) and unconverted photons (right). The upper row shows the results before subtracting background. The black dots represent $|\eta| < 0.8$, red corresponds to $0.8 < |\eta| < 1.37$, and blue to $1.52 < |\eta| < 2.37$.

Only photons and electrons from Z decay channels are used in the following checks, the conclusions are therefore limited by the statistical accuracy.

4.3.1 p_T and η dependence

The EM shower shape varies a lot with respect to the transverse momentum of the photon and electron candidates, and this shift is not perfectly modeled by the MC simulation. The dependence on p_T of the data-MC differences of energy leakage is studied in three η bins ($|\eta| < 0.8$, $0.8 < |\eta| < 1.37$ and $1.52 < |\eta| < 2.37$). The requirement on the electron p_T is relaxed to 18 GeV, in order to be better compare to photons. Given the p_T spectra shown in Fig. 4.1, three finer p_T bins are chosen for photons ($10-18, 18-25, > 25$ GeV) and six bins for electrons ($18-25, 25-35, 35-45, 45-50, 50-55, > 55$ GeV).

The data-MC differences are shown in Fig. 4.13 and 4.14 for photons and electrons separately. Generally, the data-MC difference in the outer barrel region ($0.8 < |\eta| < 1.37$) is larger than in the other two bins. Figure 4.14 shows that the data-MC difference is lower when $p_T^e < 25$ GeV. One explanation is that this region suffers from larger fake electron background for which the mismodeling of shower shape is significant.

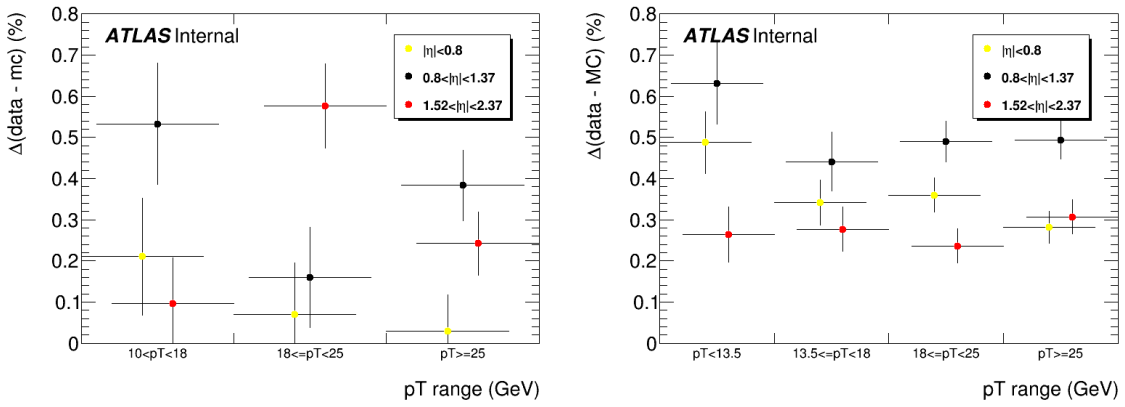

(a) (b)

Figure 4.13 – Data-MC difference of leakage for (a) converted photon and (b) unconverted photon in three p_T bins (x-axis) and three η regions ($|\eta| < 0.8$ in yellow, $0.8 < |\eta| < 1.37$ in black and $1.52 < |\eta| < 2.37$ in red).

There are two p_T bins common to electrons and photons: 18 to 25 and 25 to 35 GeV in which the double difference can be calculated. The results are shown in Fig. 4.15. Except for converted photons in the end-cap region (mainly due to large data-MC difference in leakage for electrons), the double difference is around 0.2% or below. The double differences and their statistical uncertainties are listed in Tab.4.3, and are consistent with the results in Tab. 4.2 within the statistical uncertainties.

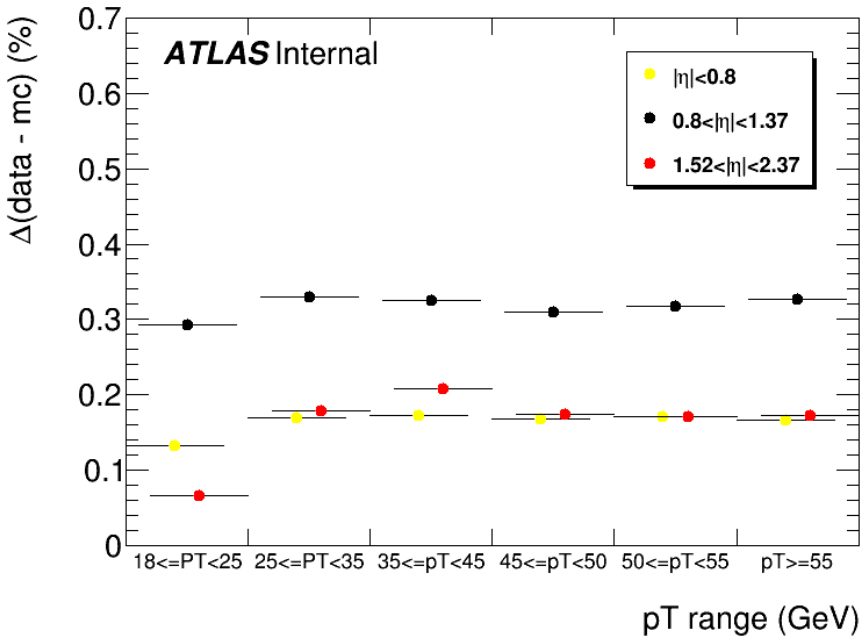

Figure 4.14 – Data-MC difference for electrons in six p_T bins (x-axis) and three η regions ($|\eta| < 0.8$ in yellow, $0.8 < |\eta| < 1.37$ in black and $1.52 < |\eta| < 2.37$ in red).

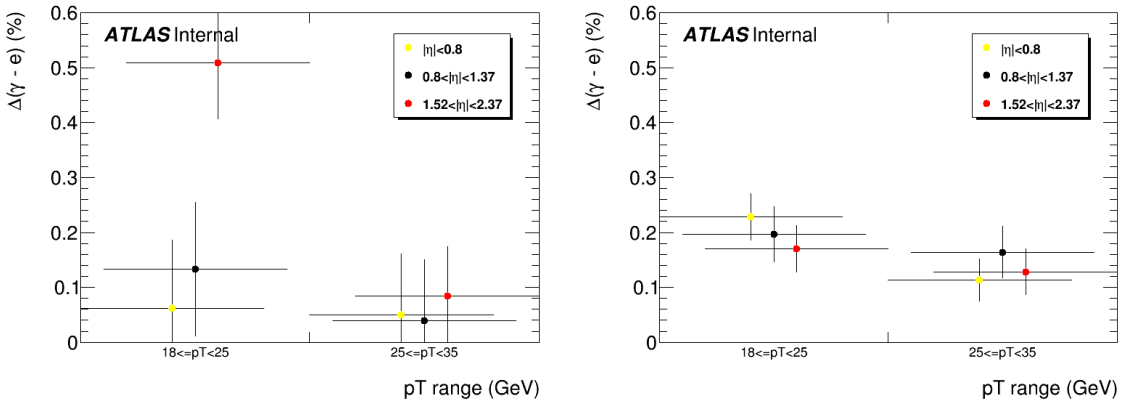

(a) (b)

Figure 4.15 – Double difference for electron and (a) converted photon, (b) unconverted photon in two p_T bins (x-axis) and three η regions ($|\eta| < 0.8$ in yellow, $0.8 < |\eta| < 1.37$ in black and $1.52 < |\eta| < 2.37$ in red).

4.3.2 Leakage along η and ϕ directions

Because of the electromagnetic field provided by the ATLAS magnet system, the energy leakage along ϕ and η directions could be different. Figure 4.17 shows the initial 7×11 ($\eta \times \phi$) window (barrel case) in which the results discussed so far were estimated. The region in yellow corresponds to a 3×7 window, from which the energy

Double difference(%)	$\|\eta\| < 0.8$	$0.8 < \|\eta\| < 1.37$	$1.52 < \|\eta\| < 2.37$
El - Conv, $18 < p_T < 25$ GeV	0.058 ± 0.126	0.138 ± 0.121	0.511 ± 0.102
El - Conv, $25 < p_T < 35$ GeV	0.057 ± 0.112	0.030 ± 0.111	0.079 ± 0.091
El - Unconv, $18 < p_T < 25$ GeV	0.230 ± 0.042	0.203 ± 0.050	0.168 ± 0.042
El - Unconv, $25 < p_T < 35$ GeV	0.112 ± 0.039	0.159 ± 0.047	0.127 ± 0.042

Table 4.3 – Double difference measured for converted and unconverted photons in two p_T regions.

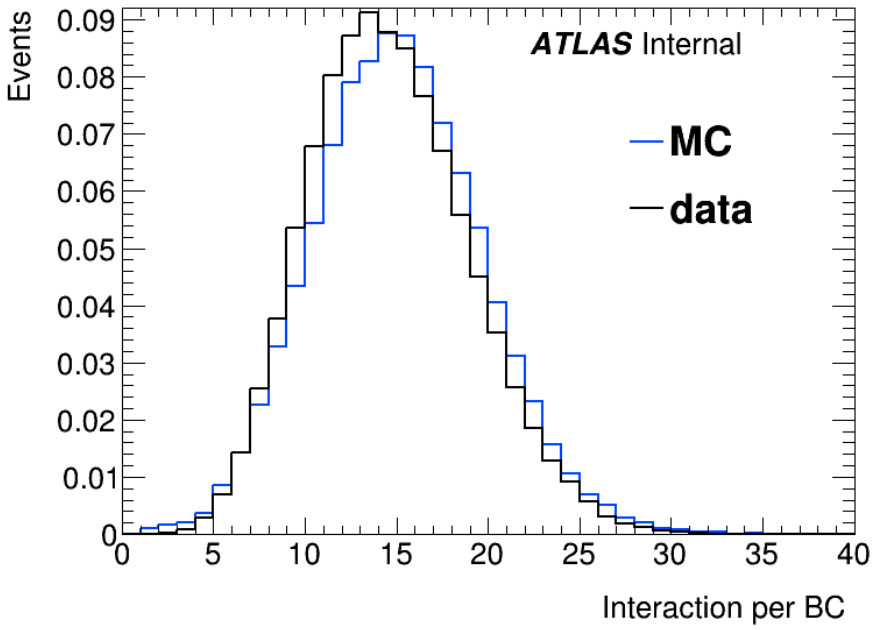

Figure 4.16 – Number of interactions per bunch crossing in data and MC samples.

of the cluster is calculated. Outside of this window, the regions in green and blue correspond to the energy leakage.

For the ϕ direction, the actual square window one want to study is the light blue part in Fig. 4.17. However in the studied samples only the $(7 \times 11) - (7 \times 7)$ window energy is available and therefore is used in the following. The total leakage equals to the η leakage plus ϕ leakage.

For the end-cap region, since the cluster size being used now is 5×5, the actual variables that are used to calculate η and ϕ leakage should be different from that used in the barrel region. However, the correct variables are also not available and the η and ϕ leakage for the end-cap region are calculated assuming the size of the cluster is 3×7.

Fig. 4.18 and 4.19 show the photon η and ϕ leakage respectively, while the total leakage is the same in both figures. The results for electrons are shown in Fig. 4.20.

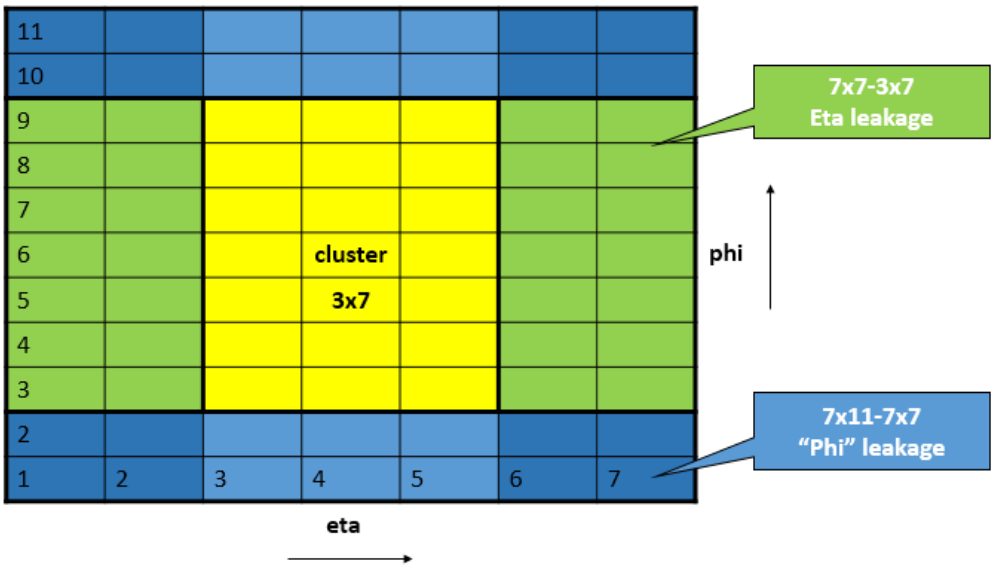

Figure 4.17 – An illustration of the regions used to calculate the energy cluster and leakages in the middle layer of the barrel calorimeter.

The average leakage is very close between data and MC, except for the outer barrel region ($0.8 < |\eta| < 1.37$). For the ϕ leakage the data and MC are even closer. The leakage along η is much larger than leakage along ϕ.

4.3.3 Pile-up dependence

The pile-up rate in Run 2 is larger than in Run 1, which may lead to different performance of the double difference. Figure 4.16 shows the number of interactions per bunch crossing in data and MC samples used in the Run 2 study. Four bins are set accordingly: $(< 12, 12-15, 15-18, > 18)$, and the results are given in three η bins (Fig. 4.21). Electrons have $p_T > 25$ GeV and photons have $p_T > 10$ GeV. Although the measurement is limited by statistics, the double difference is generally stable with respect to the pile-up rate.

4.3.4 Impact of additional material

Another important check is to measure the impact coming from the amount of simulated detector material. The shape of electromagnetic showers changes with respect to the amount of the material that the particle travels through in the detector. Considering the imperfect simulation, this effect is studied by altering the configuration of material upstream of the calorimeter using single particle samples generated by the event generator named ParticleGun. All the particles are selected with $50 < p_T < 150$ GeV, and tight identification requirement for the photons.

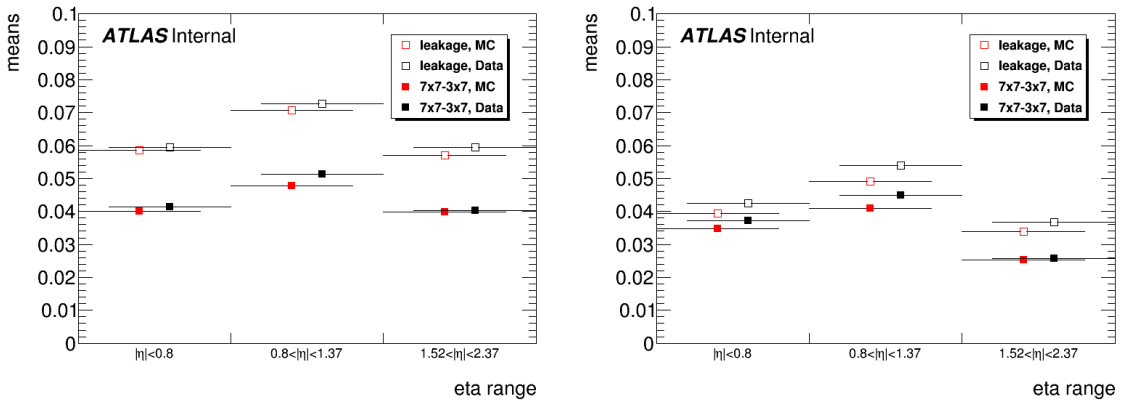

(a)

(b)

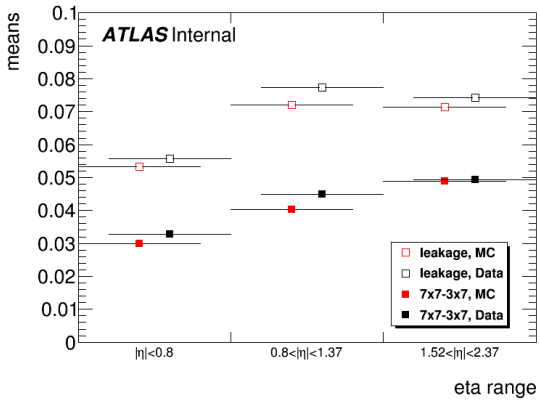

(c)

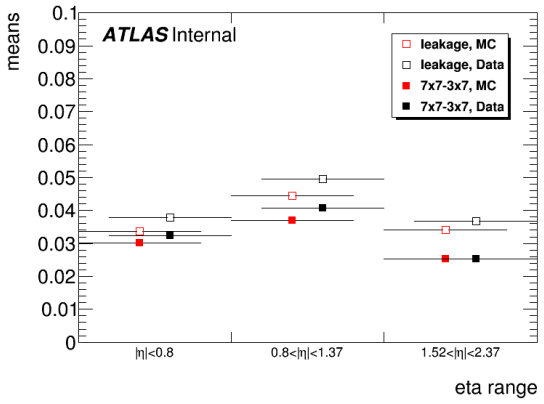

(d)

Figure 4.18 – Average leakage along η (solid squares) for converted photons (left) and unconverted photons(right) in three bins of η (x-axis), with $p_T > 25$ GeV (top row) or $p_T < 25$ GeV (bottom row).The total leakage is shown with open squares for comparison.

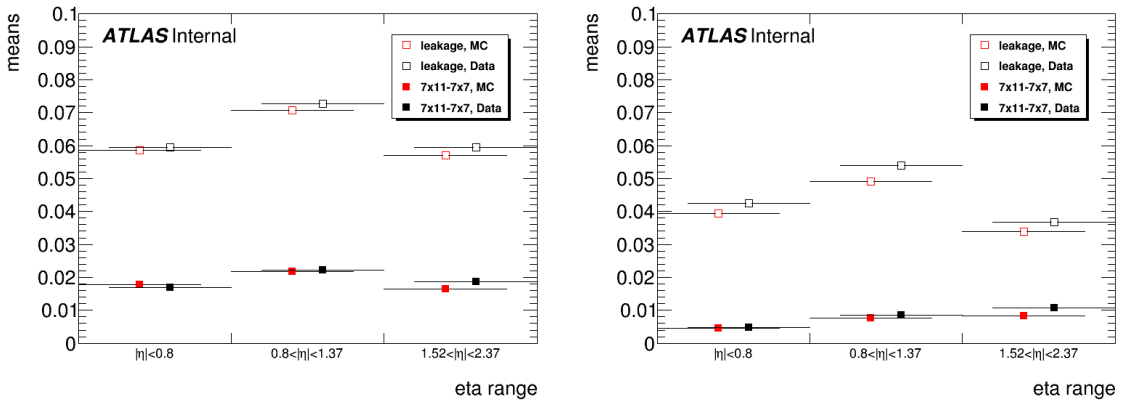

(a) (b)

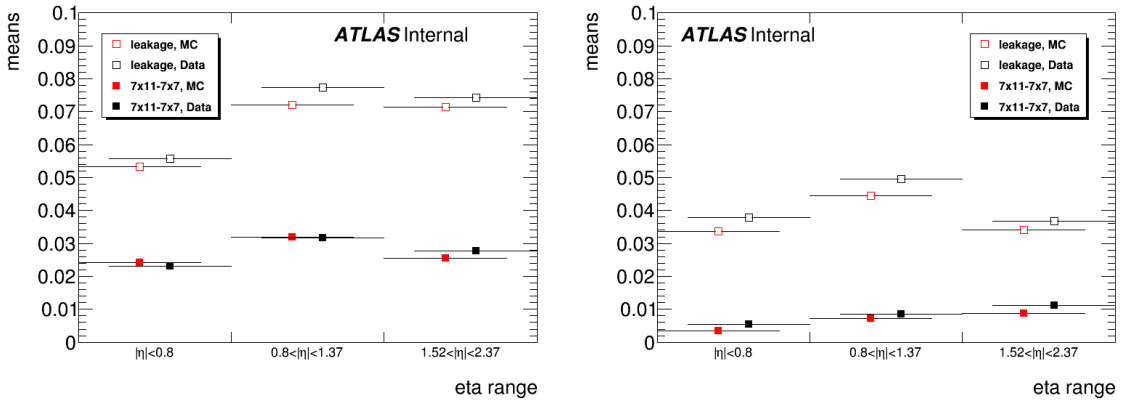

(c) (d)

Figure 4.19 – Average leakage along ϕ (solid squares) for converted photons (left) and unconverted photons(right) in three bins of η (x-axis), with $p_T > 25$ GeV (top row) or $p_T < 25$ GeV (bottom row).The total leakage is shown with open squares for comparison.

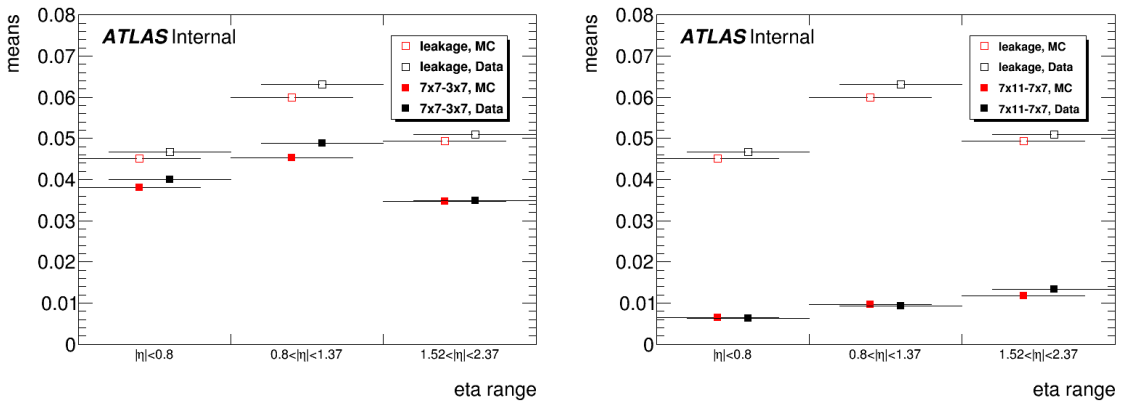

(a) (b)

Figure 4.20 – Average leakage along η (solid squares, a) and along ϕ (solid squares, b) for electrons in three bins of η (x-axis). The total leakage is shown with open squares for comparison.

Six different configurations are considered: Config N[4] (s2764), Config C'+D'[5] (s2765), Config E'+L'[6] (s2766), Config F'+M+X[7] (s2767), Config G'[8] (s2768), Increase PP0 (patch panel 0, containing the optoboards in the detector cryostat) Pixel services (s2889). The difference in energy leakage with respect to the nominal configuration is shown in Fig.4.22 for converted photons, unconverted photons and electrons. To check the overall effect, another double difference between distorted and nominal samples, electrons and photons is defined as:

$$\Delta(e-\gamma) = (l^{distorted} - l^{nominal})^{El} - (l^{distorted} - l^{nominal})^{Conv,Unconv} \tag{4.5}$$

The results are shown in Fig.4.23. It can be seen that the most significant difference in barrel region appears when Config G' is applied. In particular, for the end-cap region, the largest effect arises when increasing the material of the PP0 of pixel services. The largest difference here is below 0.2%, and the double difference is around 0.1%.

Although the discrepancy induced by the additional material is not negligible, it gives smaller electron to photon difference than the difference between MC and data.

[4]Config N in simulation: +5%X_0 PS-layer1 end-cap.

[5]Config C'+D' in simulation: +10% Pixel (including IBL) services and +10% SCT services.

[6]Config E'+L' in simulation: 5% extra material for whole inner detector, +7.5%X_0 at SCT/TRT end-cap, +5%X_0 radial barrel cryostat.

[7]Config F'+M+X in simulation: +7.5%X_0 inner detector endplate, +5%X_0 radial PS-Layer1, +30%X_0 in front of the end-cap calorimeter.

[8]Config G' in simulation: 5% extra material for whole inner detector, 15% relative increase of SCT and Pixel services (ie 10% extra on top of +5% whole ID), +7.5%X_0 at SCT/TRT end-cap, 7.5%X_0 at ID end plate, +5%X_0 radial PS-Layer1 barrel, +5%X_0 PS-layer1 end-cap and Transition distortion.

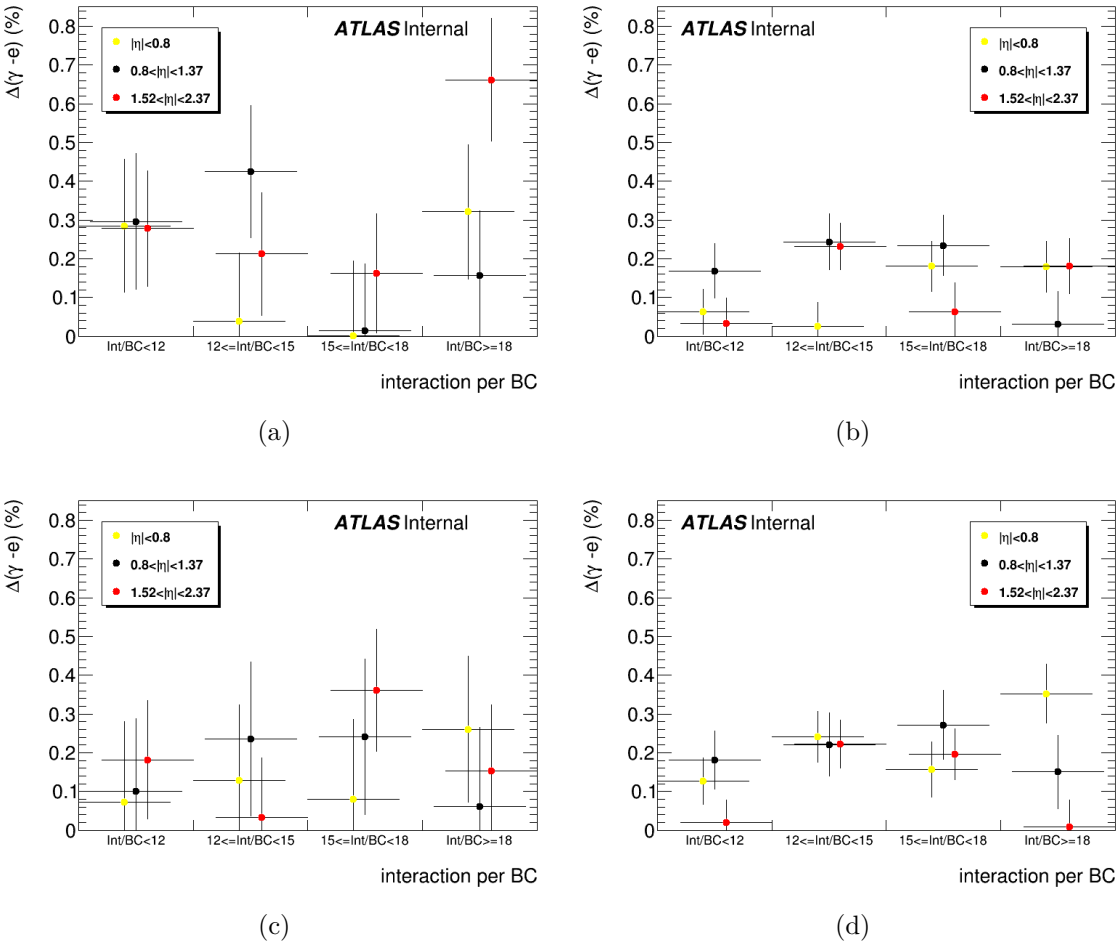

Figure 4.21 – Double difference as a function of the number of interactions per bunch crossing and for three η bins, for converted photons (left) and unconverted photons (right), with $p_T > 25$ GeV (top row) or $p_T < 25$ GeV (bottom row).

Therefore, additional material should not be considered as an important source of lateral leakage as a photon-specific uncertainty.

4.3.5 Other effects

A few more studies are performed to ensure that the strategy of the measurement is reliable. Negligible impact on the double difference is found compared to the statistical uncertainty, as summarized below:

- pile-up reweighting. The pile-up reweighting is not applied when the raw results is obtained (Sec. 4.2). By comparing the results before and after pile-up reweighting, one can see small shifts of double difference which are still within the statistical uncertainty. This reweighting is applied in the final results.

- background in Z decay channel. By altering the invariant mass cuts on M_{ee} for $Z \to ee$ events and $M_{\mu\mu\gamma}$ for $Z \to \mu\mu\gamma$ events, more or less background events are included in the signal sample since no dedicated background removal is applied. To check this effect, the measurement is repeated three times with different invariant mass criteria while keeping other selections unchanged, and no significant effect is observed. The tightest invariant mass selection is applied in the main studies, as introduced earlier.

- shape of energy leakage distribution. The mean value of the energy leakage is used in the measurement. To check if there is any significant impact coming from the different profiles between the distribution of electrons and photons of different conversion type, the median value is taken as an alternative way to calculate the energy leakage. No obvious change in double difference is observed, therefore the median value is not used in the main studies.

- energy leakage in first layer of the EM calorimeter. The energy leakage in layer 1 is much smaller than in layer 2, since the electromagnetic shower is mainly developed in the second layer. The double difference results obtained with leakage in both layer 1 and 2 or layer 2 only are very similar. It is therefore decided to keep the current definition of the energy leakage, i.e. use only the layer 2 value.

- definition of cluster size. To compare the Run 1 and Run 2 results, double difference is also measured by changing the definition of cluster size (3×7 in the barrel, 5×5 in the end-cap region) back to the definition in Run 1 (3×5, only for unconverted photon in barrel region). The change in double difference is negligible within the statistical uncertainty.

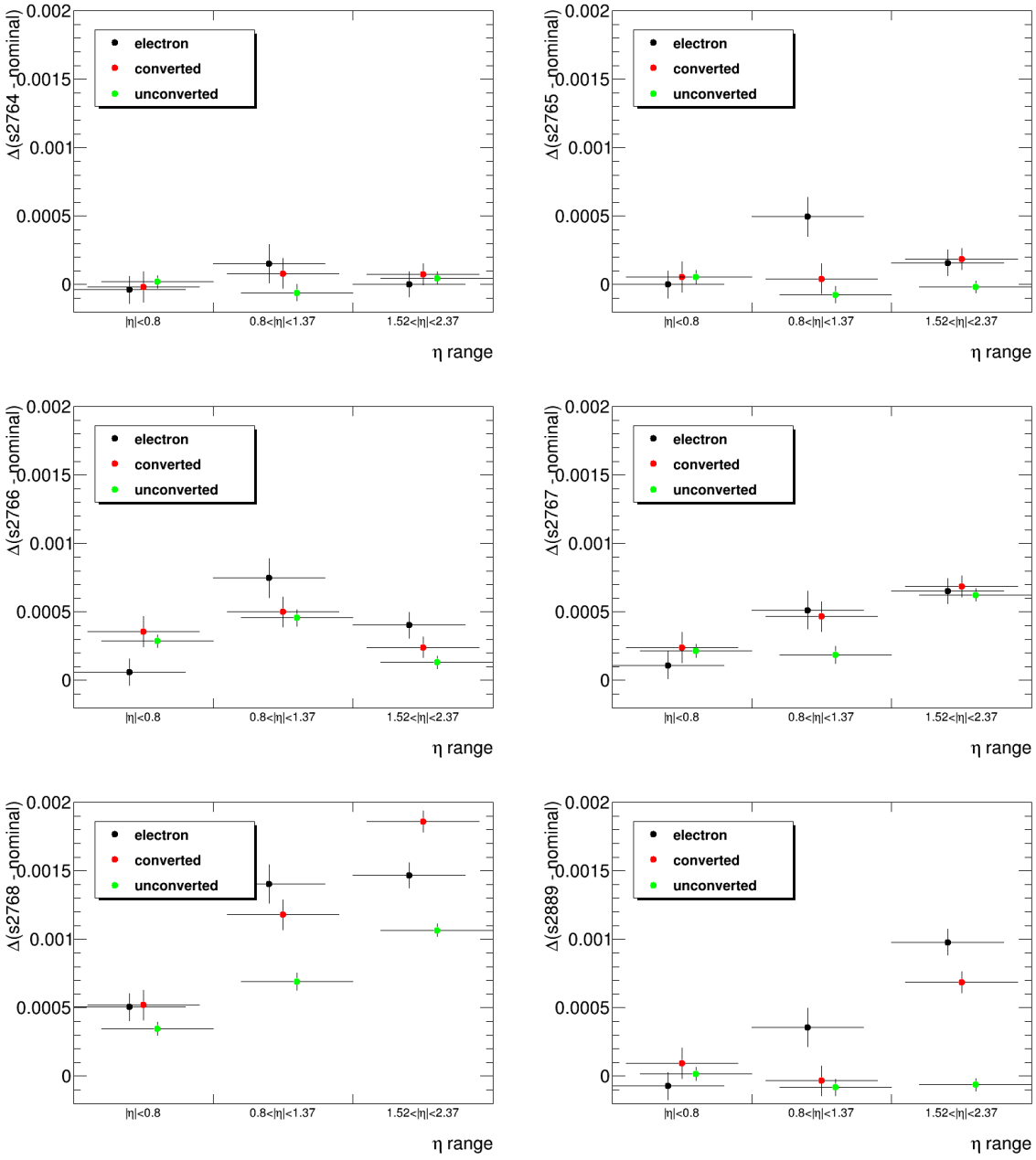

Figure 4.22 – Difference of energy leakage between distorted and nominal samples for electron(black), converted photon(red) and unconverted photon(green). The tags of samples used in left 3 plots are (from top to bottom): Config N (s2764), Config E'+L' (s2766), Config G' (s2768); the tags of samples used in right 3 plots are (from top to bottom): Config C'+D' (s2765), Config F'+M+X (s2767), Increase PP0 pixel services (s2889).

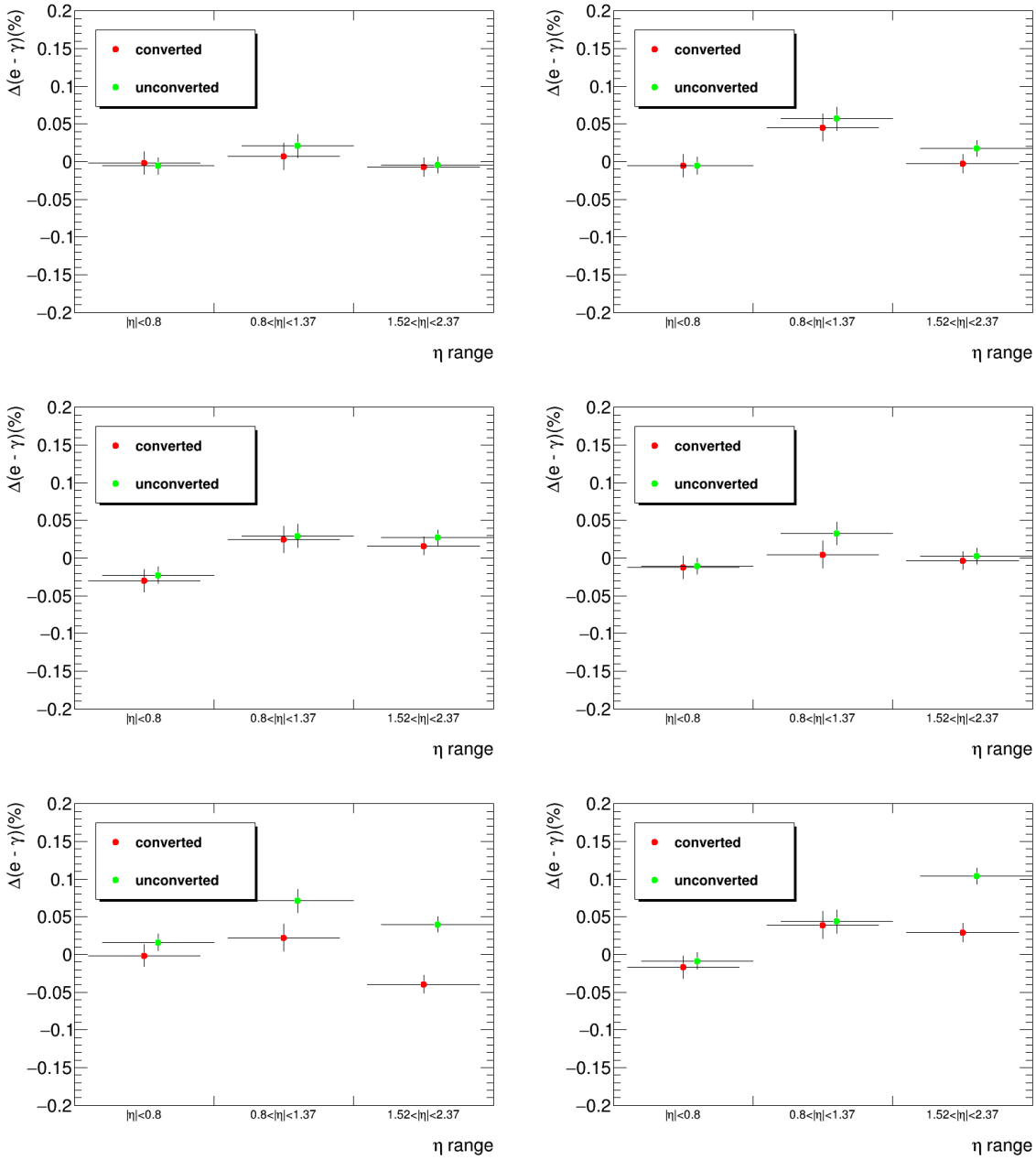

Figure 4.23 – Double difference of energy leakage between distorted and nominal samples, electron and photon (converted photon in red and unconverted photon in green). The tags of samples used in left 3 plots are (from top to bottom): Config N (s2764), Config E'+L' (s2766), Config G' (s2768); the tags of samples used in right 3 plots are (from top to bottom): Config C'+D' (s2765), Config F'+M+X (s2767), Increase PP0 pixel services (s2889).

4.3.6 Conclusion

One can draw the following conclusions about the performance of the measurement of the double difference from the studies described in this section. The total energy leakage is the sum of leakage along η and ϕ directions, and the leakage along η is much larger due to the way of clustering. The EM shower and its energy leakage varies with respect to the transverse momentum, and this effect is different for data and simulated sample. However, the difference between the energy leakage in data and MC is always constant with p_T, therefore the final results of double difference can still be safely given in only two p_T bins. The pile-up rate does not have a significant effect on double difference in the current (2016 data taking) condition. There is a non-negligible discrepancy introduced by additional simulated detector material, however its impact on electron-to photon difference is relatively small and is not considered as an important source of photon-specific uncertainty.

The measurement is limited by the available statistics of the photon samples. Although slight biases of the energy leakage can be introduced by the effects discussed above, they are not considered as sources of systematic uncertainty since the variations in double difference is negligible within the statistical uncertainty.

4.4 Refined double difference measurement and final results

This section describes two important corrections needed to be applied before the double difference result is taken as systematic uncertainty of photon calibration: the pedestal shift correction and the conversion mismodeling correction. In addition, systematic uncertainties from the background subtraction method applied in the diphoton channel are introduced as well. However, as mentioned before, the results obtained with diphoton samples are not included in the final photon-specific systematic uncertainty in order to be consistent with the energy calibration. The final numbers of double difference and the comparison between the Z decay and diphoton results are given at the end of this chapter.

4.4.1 Corrections on the double difference

Pedestal shift

There is a global small but not negligible energy difference between data and MC observed comparing "ZeroBias" triggered events (events triggered randomly in filled bunches proportionally to the luminosity) with empty bunches. The difference can be explained by a global pedestal shift in the simulation. In order to take it into account, a small energy has to be added to the cell energy in MC samples.

With pedestal correction in MC samples, the energy leaking outside a cluster of size $size$ reads:

$$l^{MC} = \frac{E_{\mathrm{s2}}(7\times 11) + E_{\mathrm{shift}}(\eta,\mu) - E_{\mathrm{s2}}(size)}{E_{\mathrm{s2}}(size)} \tag{4.6}$$

where E_{shift} is the pedestal shift, calculated as a small energy (per cell) times the total number of cells. It also depends on the pseudorapity of the particle and on the average number of interactions per bunch crossing μ.

After pedestal correction, the value of double difference slightly increases[9], as can be seen in Tab. 4.4. The statistical uncertainty is not affected and still dominant.

Double difference(%)	$\lvert\eta\rvert < 0.8$	$0.8 < \lvert\eta\rvert < 1.37$	$1.52 < \lvert\eta\rvert < 2.37$
Before pedestal correction			
El - Conv, $p_T^\gamma > 25$GeV	0.273 ± 0.095	-0.056 ± 0.089	-0.014 ± 0.080
El - Unconv, $p_T^\gamma > 25$GeV	-0.072 ± 0.033	-0.164 ± 0.040	-0.092 ± 0.035
El - Conv, $15 < p_T^\gamma < 25$ GeV	0.196 ± 0.114	-0.031 ± 0.112	-0.138 ± 0.093
El - Unconv, $15 < p_T^\gamma < 25$ GeV	-0.158 ± 0.038	-0.087 ± 0.046	-0.026 ± 0.037
After pedestal correction			
El - Conv, $p_T^\gamma > 25$GeV	0.270 ± 0.095	-0.001 ± 0.089	0.037 ± 0.080
El - Unconv, $p_T^\gamma > 25$GeV	-0.082 ± 0.033	-0.128 ± 0.040	-0.060 ± 0.035
El - Conv, $15 < p_T^\gamma < 25$ GeV	0.208 ± 0.114	0.086 ± 0.112	-0.077 ± 0.093
El - Unconv, $15 < p_T^\gamma < 25$ GeV	-0.155 ± 0.038	-0.024 ± 0.046	0.031 ± 0.038

Table 4.4 – Double difference obtained using Z decay photons for converted and unconverted photons, before and after pedestal correction.

Conversion reconstruction mismodeling

The MVA algorithm used for the calibration has been trained separately for converted and unconverted photons, as mentioned in Sec. 3.2. Therefore, if a photon is flagged with the wrong conversion status, its energy will be improperly calibrated. This could happen easily for converted photons where the conversion tracks are not reconstructed, especially if the conversion occurs at large radius. Unconverted photons can also be classified as converted when a track from pile-up is wrongly assigned to the candidate photon.

The reconstruction efficiency and conversion fake rate is measured with the ratio of the deposited energy in layer 1 and layer 2 of the EM calorimeter, $E_{1/2}$. The number of photons reconstructed as converted N_{conv}^{reco} (unconverted N_{unconv}^{reco}) is given by:

[9] This does not mean that the overall difference increases due to the pedestal shift: only the absolute value of double difference is taken as systematic uncertainty.

$$N_{conv}^{reco} = N f_{Conv} \times f_{Reco} + N(1 - f_{Conv}) \times f_{Fake} \tag{4.7}$$

$$N_{unconv}^{reco} = N(1 - f_{Conv}) \times (1 - f_{Fake}) + N f_{Conv} \times (1 - f_{Reco}) \tag{4.8}$$

where N is the total number of photons, and f_{Conv} is the probability of a photon to convert, f_{Reco} is the conversion reconstruction efficiency, i.e. the efficiency of reconstructing a true converted photon as converted. Finally, f_{Fake} is the conversion fake rate, i.e. the probability to reconstruct an unconverted photon as converted. f_{Conv}, f_{Reco} and f_{Fake} are extracted from simulation and data.

In order to correct for the difference between simulation and data, weights that correct for conversion reconstruction mismodeling are applied to the energy leakage in simulation. Four weights are computed depending on the true and reconstruction conversion status of the candidate photon:

- for a true converted photon reconstructed as unconverted: $\frac{f_{\text{Conv}}^{\text{DATA}}(1-f_{\text{Reco}}^{\text{DATA}})}{f_{\text{Conv}}^{\text{MC}}(1-f_{\text{Reco}}^{\text{MC}})}$
- for a true unconverted photon reconstructed as unconverted: $\frac{(1-f_{\text{Conv}}^{\text{DATA}})(1-f_{\text{Fake}}^{\text{DATA}})}{(1-f_{\text{Conv}}^{\text{MC}})(1-f_{\text{Fake}}^{\text{MC}})}$
- for a true converted photon reconstructed as converted: $\frac{f_{\text{Conv}}^{\text{DATA}} f_{\text{Reco}}^{\text{DATA}}}{f_{\text{Conv}}^{\text{MC}} f_{\text{Reco}}^{\text{MC}}}$
- for a true unconverted photon reconstructed as converted: $\frac{(1-f_{\text{Conv}}^{\text{DATA}}) f_{\text{Fake}}^{\text{DATA}}}{(1-f_{\text{Conv}}^{\text{MC}}) f_{\text{Fake}}^{\text{MC}}}$

The weights are given in Tab. 4.5. The uncertainties on f_{Conv}^{Data}, f_{Reco}^{Data} and f_{Fake}^{Data} are propagated as uncertainties on the weights (Tab. 4.6), used to calculate the systematic uncertainty of the double difference after reweighting.

Weight	Reco U/True C	Reco U/True U	Reco C/True C	Reco C/True U
$\lvert\eta\rvert < 0.8$	1.935	0.963	0.920	1.703
$0.8 < \lvert\eta\rvert < 1.37$	1.286	1.001	0.873	1.709
$1.52 < \lvert\eta\rvert < 1.81$	2.460	1.004	0.861	0.765
$1.81 < \lvert\eta\rvert < 2.37$	1.213	0.976	0.910	0.081

Table 4.5 – Weights applied on MC samples to correct for conversion reconstruction mismodeling.

The value of the double difference obtained using Z decay photons after conversion reweighting are given in Tab. 4.7. The pedestal correction detailed in Section 4.4.1 is included. The systematic uncertainties on the double difference are given in Tab. 4.8.

Weight	Reco U/True C	Reco U/True U	Reco C/True C	Reco C/True U
$\|\eta\| < 0.8$	0.228	0.010	0.048	0.053
$0.8 < \|\eta\| < 1.37$	0.082	0.011	0.030	0.185
$1.52 < \|\eta\| < 1.81$	0.120	0.011	0.016	0.118
$1.81 < \|\eta\| < 2.37$	0.021	0.0083	0.014	0.049

Table 4.6 – Uncertainty on the weights applied on MC samples to correct for conversion reconstruction mismodeling.

Conversion reconstruction reweighting generally reduces the mean of the absolute value of double difference in the region $|\eta| < 0.8$. For the other two η bins, the double difference increases slightly.

Since the effect of conversion mismodeling is not negligible, the final number taken as photon-specific uncertainty should consider both the double difference before and after the conversion mismodeling reweighting.

Double difference(%)	$\|\eta\| < 0.8$	$0.8 < \|\eta\| < 1.37$	$1.52 < \|\eta\| < 2.37$
Before conversion reweighting			
El - Conv, $p_T > 25$GeV	0.270 ± 0.095	-0.001 ± 0.089	0.037 ± 0.080
El - Unconv, $p_T > 25$GeV	-0.082 ± 0.033	-0.128 ± 0.040	-0.060 ± 0.035
El - Conv, $15 < p_T < 25$ GeV	0.208 ± 0.114	0.086 ± 0.112	-0.077 ± 0.093
El - Unconv, $15 < p_T < 25$ GeV	-0.155 ± 0.038	-0.024 ± 0.046	0.031 ± 0.038
After conversion reweighting			
El - Conv, $p_T > 25$GeV	0.133 ± 0.096	-0.042 ± 0.089	0.050 ± 0.080
El - Unconv, $p_T > 25$GeV	-0.058 ± 0.033	-0.115 ± 0.040	-0.001 ± 0.036
El - Conv, $15 < p_T < 25$ GeV	-0.021 ± 0.115	0.034 ± 0.113	-0.051 ± 0.093
El - Unconv, $15 < p_T < 25$ GeV	-0.113 ± 0.038	-0.002 ± 0.046	0.060 ± 0.038

Table 4.7 – Double difference obtained using Z decay photons for converted and unconverted photons, before and after conversion reweighting.

4.4.2 Systematic uncertainty of background subtraction method for diphoton sample

During the background subtraction procedure applied in the studies of the diphoton channel, the control region used to estimate the background contribution may have different characteristics from the real jet component, depending on how the control region is built. To cover this difference, two sources of systematical uncertainty are

Systematic uncertainty	$\|\eta\| < 0.8$	$0.8 < \|\eta\| < 1.37$	$1.52 < \|\eta\| < 2.37$
El - Conv, $p_T > 25$GeV	0.014	0.0027	0.00058
El - Unconv, $p_T > 25$GeV	0.0049	0.0032	0.0027
El - Conv, $15 < p_T < 25$ GeV	0.022	0.0033	0.0010
El - Unconv, $15 < p_T < 25$ GeV	0.0088	0.0058	0.00084

Table 4.8 – Systematic uncertainties on the double difference due to the error of the weights.

considered: the uncertainty on the background fraction and the uncertainty on the mean value of the energy leakage of the background. In order to quantify these uncertainties, another control region named "Loose'4" is built. The Loose'4 selection requires the photon candidate to pass loose ID while failing at least one of the four cuts on the following shower shape variables: ΔE, E_{ratio}, F_{side} or w_{eta1}, as illustrated in Fig. 3.12.

In order to estimate the systematic uncertainty due to fraction of background, the passIsolation variable is fitted again with the signal template described in Sec. 4.1.3 and the background template obtained from the Loose'4 sample. The new set of background fractions is used to normalize the background energy leakage from the Loose'2 control region. A new signal leakage distribution is extracted and the difference between the mean values of the distribution and the nominal one is taken as systematic uncertainty. Figure 4.24 shows the double difference with error bands corresponding to the systematic uncertainties.

In order to estimate the systematic uncertainty due to the profile of energy leakage, the background leakage distribution is now built from the Loose'4 control region and subtracted from data while keeping the fractions computed with Loose'2 background unchanged. Again the difference of the mean value of photon energy leakage in data with the nominal one is taken as systematic uncertainty. Figure 4.25 shows the double difference with error bands corresponding to the systematic uncertainties due to the shape of the background energy leakage distribution.

Finally, Fig. 4.26 shows the double difference with error bands corresponding to the total systematic uncertainties due to the fraction of background and energy leakage shape. It can be seen that the systematic uncertainties decrease with p_T. The statistic in control region runs out in high p_T region as the photon purity goes high, and the difference of how the control region is built (with Loose'4 or Loose'2) becomes negligible.

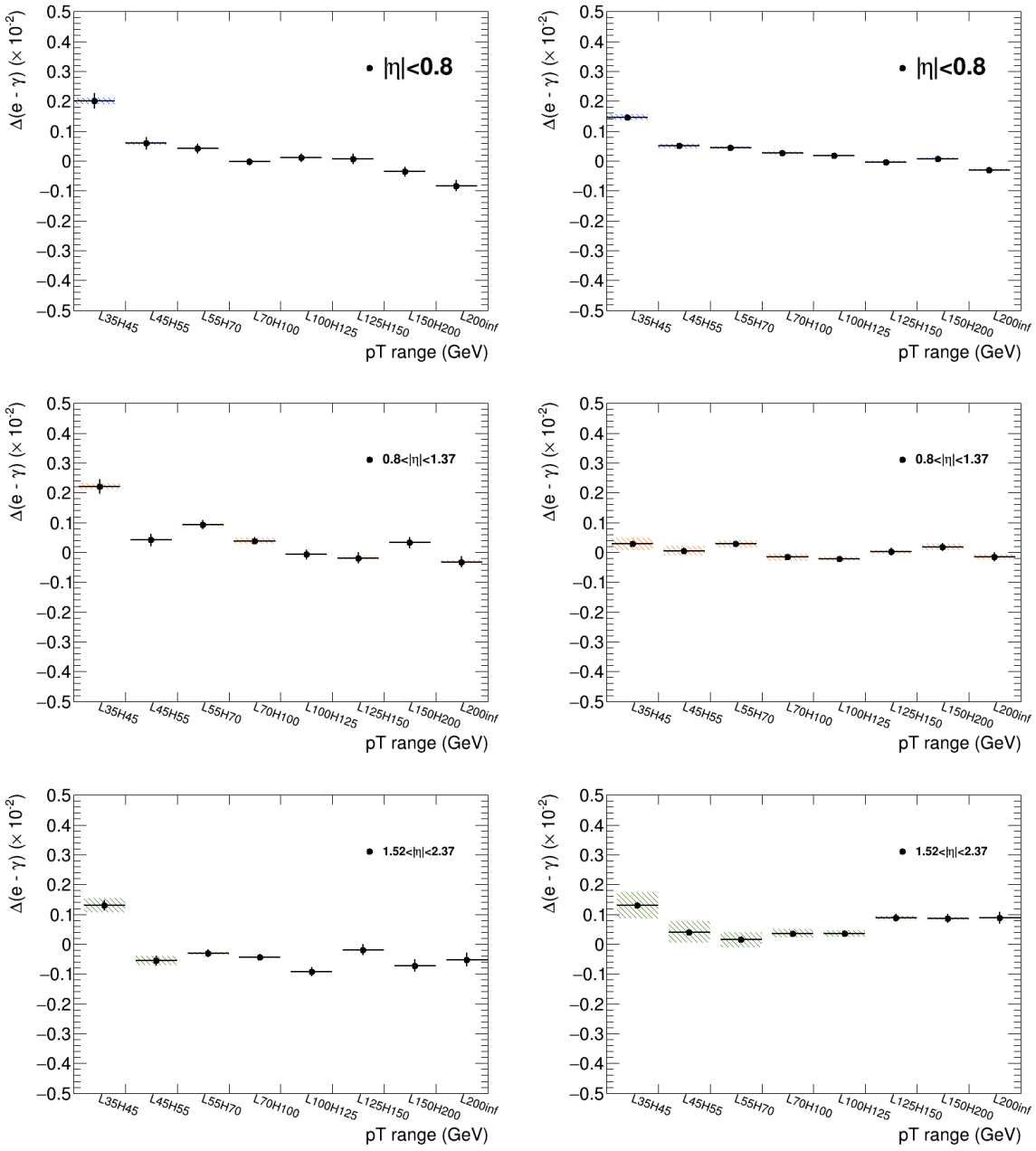

Figure 4.24 – Double difference for leading converted photon (left) and unconverted photon (right) in $|\eta| < 0.8$ (top row), $0.8 < |\eta| < 1.37$ (middle) and $1.52 < |\eta| < 2.37$ (bottom). The error bar corresponding to statistical uncertainty. The error band corresponding to systematic uncertainty due to unknown fraction of background component.

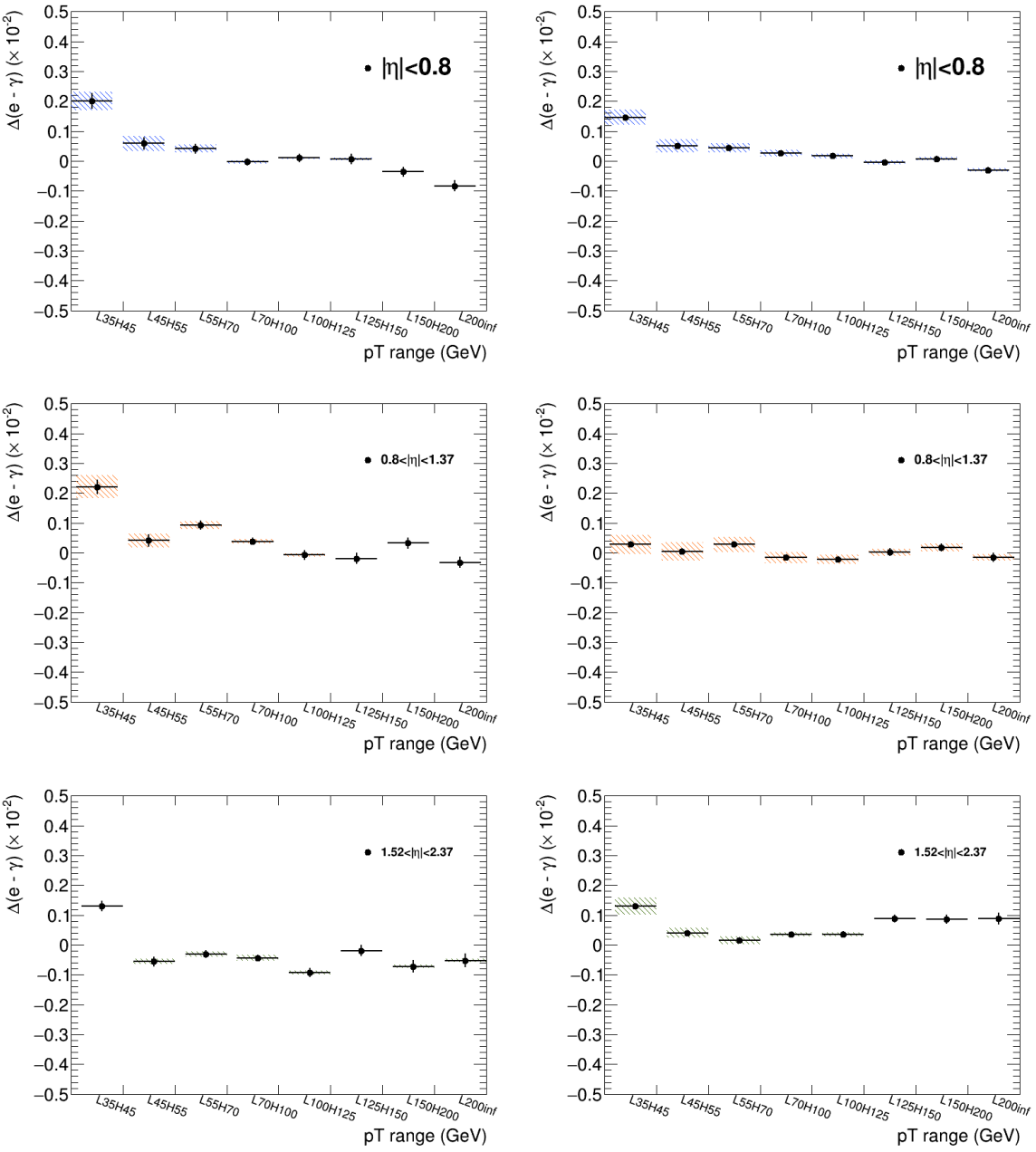

Figure 4.25 – Double difference for leading converted photon (left) and unconverted photon (right) in $|\eta| < 0.8$ (top row), $0.8 < |\eta| < 1.37$ (middle) and $1.52 < |\eta| < 2.37$ (bottom). The error bar corresponding to statistical uncertainty. The error band corresponding to systematic uncertainty due to unknown shape of background component.

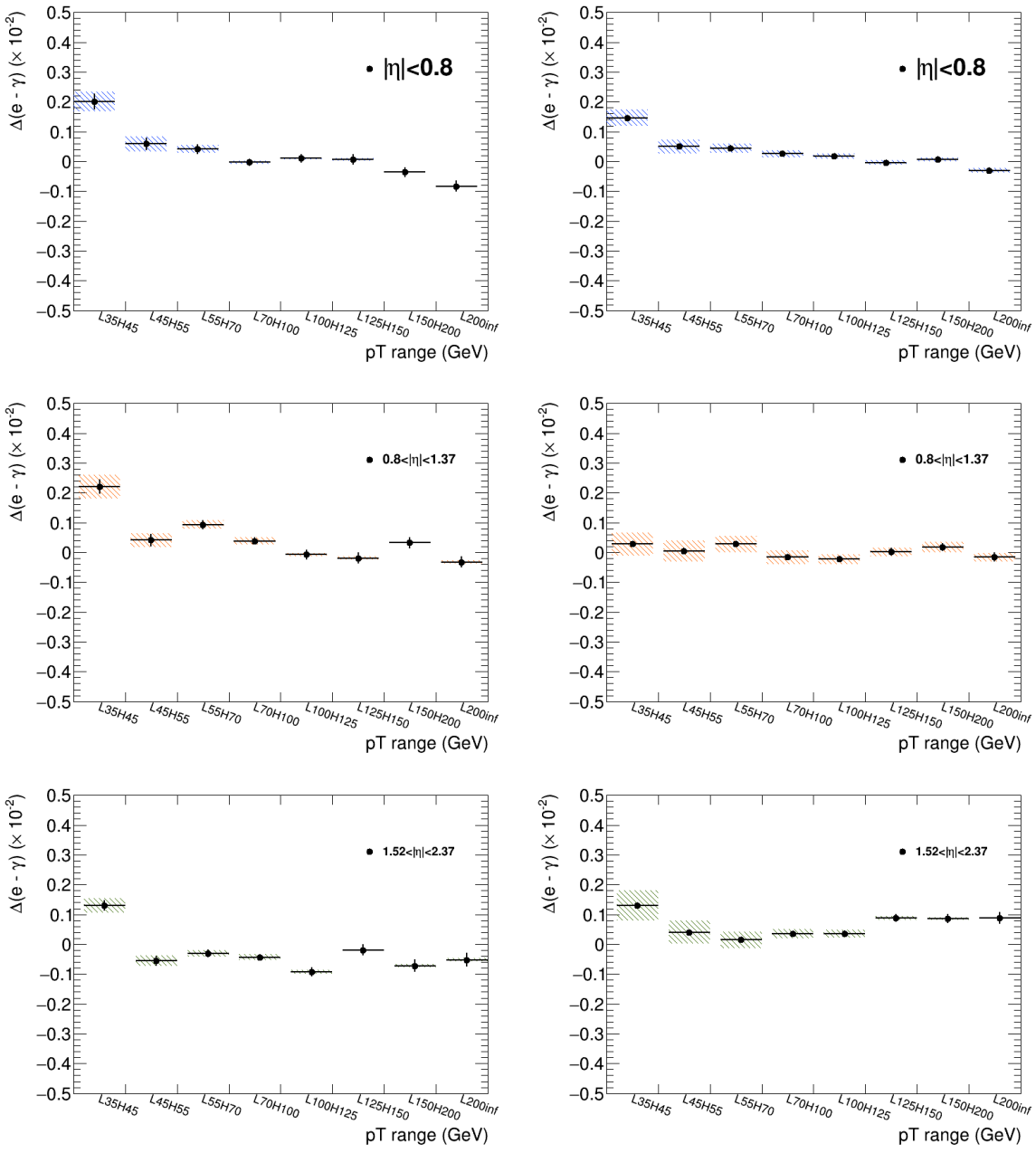

Figure 4.26 – Double difference for leading converted photon (left) and unconverted photon (right) in $|\eta| < 0.8$ (top row), $0.8 < |\eta| < 1.37$ (middle) and $1.52 < |\eta| < 2.37$ (bottom). The error bar corresponding to statistical uncertainty, and the error band corresponding to the total systematic uncertainty.

4.4.3 Final results

The final uncertainty coming from the energy leakage difference between electron and photon is quoted as the maximum between the absolute value of the double difference (after pedestal correction) before conversion mismodeling reweighting, after reweighting, and the statistical uncertainties. Table. 4.9 shows the final outputs of this study. These numbers are assigned as one of the photon-specific systematic uncertainty of photon energy calibration of the ATLAS collaboration. Note that only the numbers obtained with the $Z \to ee$ and the $Z \to \mu\mu\gamma$ events enter the main calibration results.

Systematic uncertainty	$\|\eta\| < 0.8$	$0.8 < \|\eta\| < 1.37$	$1.52 < \|\eta\| < 2.37$
El - Conv, $p_T > 25$GeV	0.270	0.089	0.080
El - Unconv, $p_T > 25$GeV	0.082	0.128	0.060
El - Conv, $15 < p_T < 25$ GeV	0.208	0.113	0.093
El - Unconv, $15 < p_T < 25$ GeV	0.155	0.046	0.060

Table 4.9 – Systematic uncertainty coming from lateral energy leakage measured with photons from $Z \to \mu\mu\gamma$ envents, quoted as the maximum between the absolute value of the double difference before and after conversion reweighting, and the statistical uncertainties.

Studies with diphoton events provide a cross-check of the results above and complete the measurement in higher transverse momentum region. As a summary, Figure 4.27 shows the double difference in three η bins, with p_T of candidates from 10 GeV to above 200 GeV. Error bars represent the statistical uncertainties. The first two bins of the x-axis correspond to photons from $Z \to \mu\mu\gamma$ events, while the rest corresponds to photons from diphoton events. All electrons come from $Z \to ee$ events. Generally, the absolute value of double difference is smaller than 0.2%. No obvious trend with respect to p_T is observed. The uncertainty on the results from the radiative Z sample is dominated by statistics, while the systematic uncertainty due to the limited knowledge of the background leakage distribution shape and fraction dominate the error on the results from diphoton events.

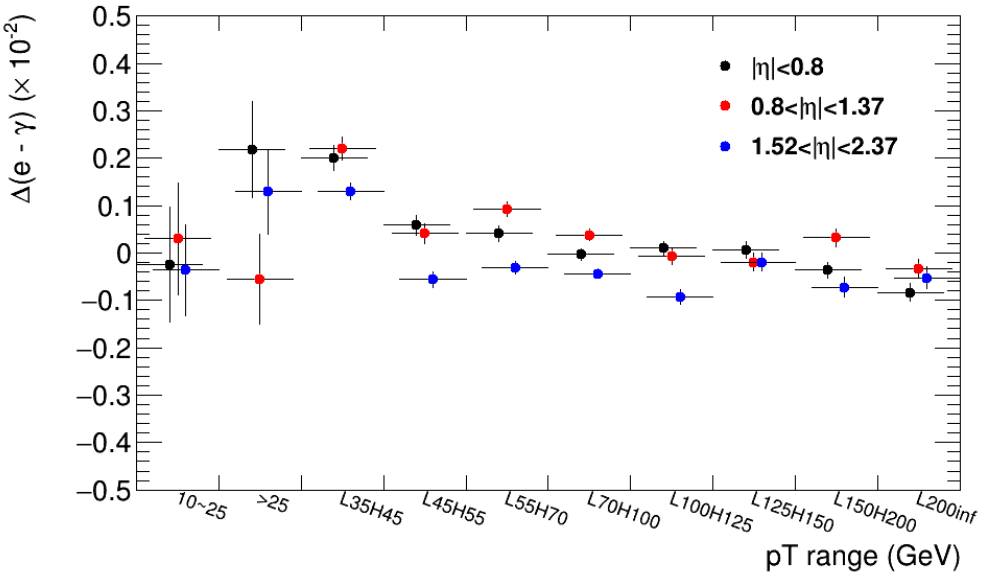

(a)

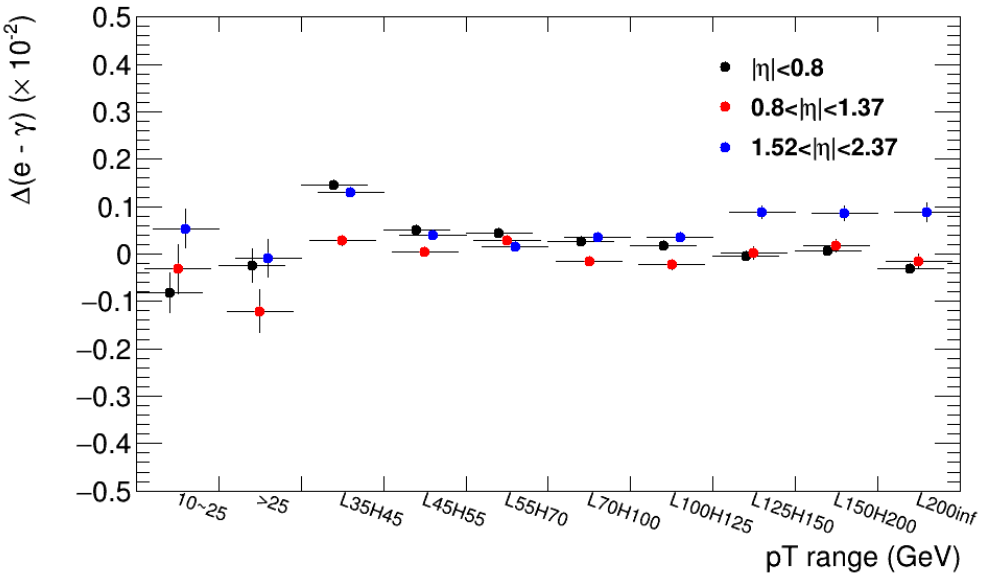

(b)

Figure 4.27 – Double difference in different p_T regions (x-axis), for (a) converted photons and (b) unconverted photons. The black dots represents $|\eta| < 0.8$, red is $0.8 < |\eta| < 1.37$, and blue is $1.52 < |\eta| < 2.37$. Left two bins (on x-axis): results with photon from radioactive Z decay channel. Right eight bins: results with photon from diphoton channel.

Chapter 5

Search for diphoton resonances

This chapter describes two analyses that search for diphoton resonances in different invariant mass ranges: a low-mass range of 60 to 110 GeV using 80 fb^{-1} of pp collision data collected at $\sqrt{s} = 13$ TeV with the ATLAS detector, published as a conference note at ICHEP in 2018[46]; and a high-mass range above 160 GeV using the full Run 2 dataset corresponding to an integrated luminosity of 139 fb^{-1}.

The diphoton final state is very important for searches for physics beyond the Standard Model. This final state is sensitive to new resonances thanks to a smoothly falling background that is relatively easy to model, and an excellent invariant mass resolution that can be used to distinguish the signal from the Standard Model background. Two signal models, a spin-0 resonant state (X) and a spin-2 graviton excitation (G^*) are searched for. As introduced in Sec. 1.2, the spin-0 resonances are predicted in many extensions of the Standard Model[47][48][49][50][51]. They are searched for in a model-independent way in both low and high-mass ranges. The spin-2 graviton resonances are predicted by the Randall-Sundrum model[15][16] with one warped extra dimension (RS1). The lightest Kaluza-Klein (KK) graviton excitation state with mass m_{G^*} and a coupling $k/\bar{M}_{pl}$ is searched for, where k is the curvature of the extra dimension and $\bar{M}_{pl}$ is the reduced Planck scale. The spin-2 resonances are only searched for in the high-mass range using the RS model as a benchmark, as the RS1 model is already excluded with m_{G^*} below 1.7 TeV (with $k/\bar{M}_{pl} = 0.01$) in the previous study[52].

The general strategy is the same for both low-mass and high-mass searches: the invariant mass distribution in data is fitted with analytic functions that model the background and signal shapes. The methods of signal and background modeling are also similar for the two analyses. Besides the separately optimized event selections, one of the main difference between the two analyses is that the low-mass search suffers from one important background component that comes from electron pairs from the decay of Z bosons (Drell-Yan background). Hence, three categories defined according to the conversion status of the two photons are used in order to improve the sensitivity of this analysis. In addition, the high-mass search benefits from the recent developments of

the background-distribution smoothing techniques, which brings a significant reduction of the systematic uncertainty from the determination of the background function.

The details of datasets and simulated samples used in the analyses are presented in Sec. 5.1. The event selections are listed in Sec. 5.2. The signal modeling and the fiducial/total acceptance corrections are introduced in Sec. 5.3 and Sec. 5.5. The determination of the analytical form of the background shape is described in Sec. 5.4. All the systematic uncertainties are discussed in Sec. 5.6. The statistical method and models used in the two analyses are explained in Sec. 5.7. Finally, the results are presented in Sec. 5.8, showing the limits on the production cross section times branching ratio and the p-value as a function of resonance mass and width.

Previously, the low-mass diphoton search results were published by the ATLAS Collaboration with data collected at 8 TeV[53]. A small excess near 95 GeV was observed by the CMS Collaboration when combining data recorded at 8 TeV and 13 TeV[54]. For high-mass region, results of the search using 37 fb^{-1} data collected at 13 TeV in 2015 and 2016 were published by the ATLAS Collaboration[52] in 2017. The CMS Collaboration reported their high-mass search using 35.9 fb^{-1} at 13 TeV in 2018[55].

I joined the analysis team in the middle of the low-mass search effort. I have contributed to almost all areas of the analyses, while I was mostly involved in the high-mass search. My main contributions are the overall background study, the systematic uncertainties and the statistical interpretation in the high-mass search. In the low-mass search, I also contributed to the event selection optimization, signal modeling validation, the studies of the Standard Model Higgs contamination and some the systematic uncertainties from signal and background modeling.

5.1 Data and Monte Carlo samples

The datasets and the simulated MC samples used in the searches are listed in this section. The simulated samples are used to optimize the event selections (Sec. 5.2), compute the correction factors (Sec. 5.5), and model the signal and background shapes (Sec. 5.3 and 5.4). Since the data-taking conditions changed in each year, different sets of independent MC samples are produced and added together, weighted by their luminosity.

5.1.1 Low-mass samples

Data

The low-mass analysis uses 80 fb^{-1} of data collected in 2015, 2016 and 2017 at $\sqrt{s} = 13$ TeV. Diphoton triggers that are run unprescaled are used when recording the pp collisions, requiring both leading and sub-leading photons to have transverse energy

(E_T) above 20 GeV. A tight photon identification is applied in the high-level trigger, and also an isolation requirement in 2017. The recorded events are only used if they pass the data quality (DQ) requirements and are in the Good Run List (GRL).[1] The datasets that are good to use correspond to an integrated luminosity of 3.2 fb^{-1} for 2015, 33.6 fb^{-1} for 2016 and 43.6 fb^{-1} for 2017. The uncertainty of the measurement of the integrated luminosity is 2.1% for the 2015 data, 2.2% for 2016 and 2.4% for 2017[56].

Signal samples

The scalar Higgs-like signal models are simulated for generic spin-0 resonance search using a Higgs boson production process in pp collision at $\sqrt{s} = 13$ TeV, with the scalar particle X decaying to photon pairs. The simulated signal samples are produced for different hypotheses of the resonance mass m_X, in the mass range of 40 to 180 GeV. The default samples are produced via gluon-gluon fusion (ggF) with MadGraph5_aMC@NLO[57] version 2.3.3 at next-to-leading order (NLO) in quantum chromodynamics (QCD), using the NNPDF3.0 NLO PDF set. The MadGraph generator is interfaced to Pythia8[58] for parton showering and hadronization. For all the signal samples, the Narrow Width Approximation (NWA, $\Gamma_X = 4.07$ MeV, the width of the 125 GeV SM Higgs boson) is assumed.

Since the spin-0 search is model-independent, the fiducial corrections (Sec. 5.5) are also studied for other Higgs-like production modes: vector boson fusion (VBF), associated production with a vector boson (WH, ZH), and associated production with a top quark pair ($t\bar{t}H$). The VBF samples are simulated with the Powheg generator using CT10 PDF set, interfaced to Pythia8 for parton showering and hadronization as well, while the other processes are simulated with Pythia8 generator, using NNPDF23 LO PDF set.

The different MC signal samples are listed in Table 5.1.

Background samples

For continuum diphoton ($\gamma\gamma$) background production, two kinds of background events are generated with the Sherpa generator. The simulations are performed in slices of diphoton invariant mass and added together according to their cross section, in order to maximize the statistics over the whole search range.

The leading order diphoton sample ("Sherpa LO") is generated using the Sherpa 2.2.2 generator. The LO sample is produced in the early stages of the analysis, and is used for analysis optimization and some cross-checks. The matrix elements

[1] The dataset used for physics analyses has to satisfy the data quality requirements: the beams are stable, the sub-detectors and magnets are fully operational, not too many noisy cells are observed, etc. On top of the general DQ requirement, GRL is a xml file that specifies the sets of "good" luminosity blocks, i.e. over which data our analysis should run.

Process	Generator	Mass[GeV]
ggF	MG5_AMC@NLO + Pythia8	40-50-60-70-80-90-100-110-120-140-160-180
ggF	Powheg+Pythia8	40-60-80-100-120
VBF	Powheg+Pythia8	40-60-80-100-120
WH	Pythia8	40-60-80-100-120
ZH	Pythia8	40-60-80-100-120
$t\bar{t}H$	Pythia8	40-60-80-100-120

Table 5.1 – Low-mass analysis: signal samples of the five Higgs production modes, generator and available mass points.

are calculated with up to 2 partons at LO, and merged with the Sherpa parton showering[59] using the ME + PS@LO prescription[60]. The CT10 PDF set[61] is used in conjunction with dedicated parton shower tune developed by the Sherpa authors. Three slices of the LO sample are used with the following invariant mass ranges: 0-55, 55-100, 100-160 GeV.

The next-to-leading order diphoton sample ("Sherpa NLO") is generated using a more recent implementation, Sherpa 2.2.4[62]. The NLO sample is more accurate and therefore used for background modeling. Parton-level calculations for different jet multiplicities are combined: matrix elements are calculated at NLO accuracy for up to one real emission of one additional parton, and at LO for two and three additional partons. The NNPDF3.0 NNLO PDFs[63] are used in conjunction with the corresponding Sherpa default tune. Two slices of samples are used with the following invariant mass ranges: 50-90, 90-175 GeV.

To study the Drell-Yan background, MC samples of $Z \to ee$ decays are simulated using POWHEG-BOX V2 interfaced to the Pythia8 version 8.186 parton shower model. The CT10 parton distribution function set is used in the matrix element. Sliced samples generated with Sherpa 2.2.1 are also used for systematic uncertainties.

5.1.2 High-mass samples

Data

The high-mass analysis uses the full Run 2 dataset of 139 fb^{-1}, collected in 2015, 2016, 2017 and 2018, the overall relative uncertainty of integrated luminosity is 1.7%[56]. Similarly to low-mass search, the data are recorded with the lowest-E_T unprescaled diphoton trigger, with additional photon identification and isolation criteria. The E_T thresholds are 35 GeV and 25 GeV for leading and sub-leading photons. A loose identification requirement is applied for 2015-2016 dataset, while a medium identification requirement is applied for 2017-2018 dataset in order to cope

with the increasing pile-up. Only the events in GRL and passing the data quality requirements are used.

Scalar signal samples

Similarly to the samples used in the low-mass spin-0 search, scalar Higgs-like signal samples are produced for different hypotheses of the resonance mass m_X, in the range 200-5000 GeV. The generators and PDF sets used to produce all five production modes are the same as in Sec. 5.1.1. The search covers signal with width from 4 MeV (NWA) up to $\Gamma_X/M_X = 10\%$ (large width case, LW). When modeling the large width signal (Sec. 5.3), the signal shape is described using convolutions of the NWA shape with a Breit-Wigner distributions, since generating signal samples for all values of m_X and Γ_X is impractical and unnecessary. Only samples with $\Gamma_X/m_X = 2\%$, 6% and 10% are produced for signal modeling and validation.

The different MC spin-0 signal samples are listed in Table 5.2.

Process	Generator	Width assumption[Γ_X/m_X]
ggF	MG5_AMC@NLO + Pythia8	NWA
ggF	Powheg+Pythia8	NWA
VBF	Powheg+Pythia8	NWA
WH	Pythia8	NWA
ZH	Pythia8	NWA
$t\bar{t}H$	Pythia8	NWA
ggF	MG5_AMC@NLO + Pythia8	2%, 6%, 10%

Table 5.2 – High-mass analysis: signal samples of the five Higgs production modes, generator and width assumption. The samples are generated for masses 0.2, 0.4, 0.8, 1, 1.2, 1.6, 2, 2.4, 3, 4 and 5 TeV.

Graviton signal samples

The spin-2 graviton signal events are generated using a Randall-Sundrum (RS) graviton production model in pp collision at $\sqrt{s} = 13$ TeV, with the graviton G^* decaying to photon pairs. The implementation of Pythia8 version 8.186 and the NNPDF23LO PDF set are used. The graviton samples are produced for different coupling values $k/\bar{M}_{pl}$ in the range $0.01 < k/\bar{M}_{pl} < 0.3$, and graviton masses m_{G^*} in the range $500 < m_{G^*} < 7000$ GeV. With a small coupling value ($k/\bar{M}_{pl} = 0.01$), the signal is considered as NWA case. LW signal shape is described using convolutions of the NWA shape with the graviton lineshape.

The different MC spin-0 signal samples are listed in Table 5.2.

Generator	Mass[TeV]	$k/\bar{M}_{pl}$
Pythia8	0.5-1-2-3-4	0.01-0.05-0.1
Pythia8	5-6-7	0.01-0.05-0.1-0.2-0.3

Table 5.3 – High-mass analysis: graviton samples of different mass m_{G^*} and coupling $k/\bar{M}_{pl}$ values.

Background samples

Similar to the low-mass analysis, background events from continuum $\gamma\gamma$ production are generated using Sherpa 2.2.4 with the default tune. Matrix elements are calculated at NLO for up to one real emission of one additional parton, and at LO for two and three additional partons. The NNPDF3.0 NNLO PDF sets are used. The simulations are also performed in slices of diphoton invariant mass: 90-175, 175-2000, 1400-2000, $2000 - \infty$ GeV.

5.2 Event selection

Low-mass selection and categorisation

The photon candidates are required to fall within the calorimeter acceptance $|\eta| < 2.37$, excluding the transition region between the barrel and end-cap calorimeters $1.37 < |\eta| < 1.52$. Only diphoton events with invariant mass in the range $60 < m_{\gamma\gamma} < 120$ GeV are selected. Both photons are required to have transverse energies above 22 GeV, which is slightly higher than the trigger threshold to ensure uniform trigger efficiency.

Tight photon identification as well as the photon isolation criteria are required to reject fake photons (jets mis-identified as photons). Among the three isolation working points in Tab. 3.2, the choice is made by comparing the gain in significance relative to the loosest selection FixedCutLoose: $Z_{relative}/Z_{Loose} = \varepsilon_S/\sqrt{\varepsilon_B}$, where ε_S and ε_B are the ratio of isolation efficiencies of signal and background respectively, defined as $N_{relative}/N_{Loose}$. The subscript *relative* stands for an isolation working point under test, namely FixedCutTight or FixedCutTightCaloOnly. The FixedCutLoose working point is selected, since no significant improvement is observed by switching to other working points. The total and relative selection efficiency[2] for signal is summarized in Fig. 5.1.

Events that pass the selections above are split into three categories depending on the conversion reconstruction status of the leading and sub-leading photons: both

[2]relative selection efficiency: cut efficiency with respective to the previous cut in the analysis cutflow.

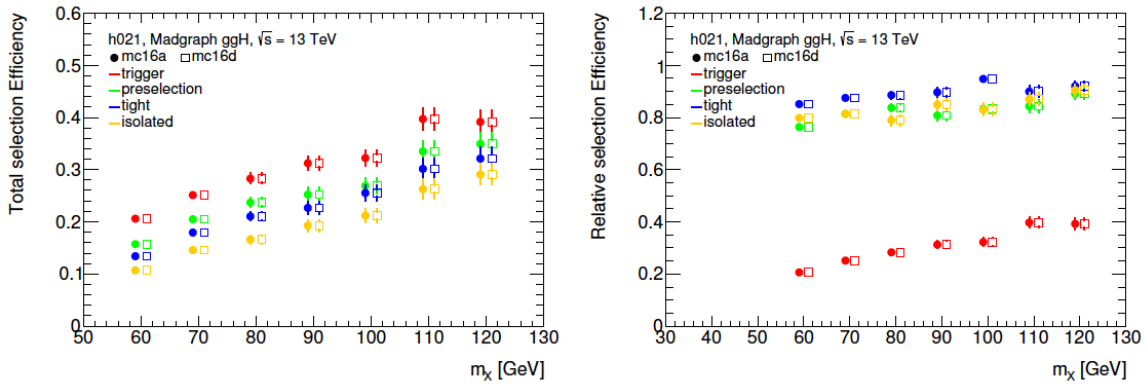

(a) (b)

Figure 5.1 – The (a) total and (b) relative signal selection efficiency for different mass points, measured with mc16a (corresponding to 2015+2016 data) and mc16d (2017 data) samples.

converted (CC), both unconverted (UU), or one converted and one unconverted (CU). Since the fake photons from the Drell-Yan background are reconstructed mainly as converted photons, the categorisation improves the sensitivity. The numbers of data events after selection in each category are summarized in Tab. 5.4.

Year	2015	2016	2017
Preselection	638392	6720477	4101517
Identification	391529	4041009	2838686
Isolation	152850	1564423	1696862
UU	49.9%	52.5%	47.8%
CU	41.0%	39.4%	42.1%
CC	9.1%	8.1%	9.9%

Table 5.4 – The cut flow measured in the invariant mass range from 60 to 120 GeV, for 2015, 2016 and 2017 data respectively. The fractions of events in each conversion category are also presented.

High-mass Selection

The searches for both signal models use a common set of event selection: photon candidates are required to fall within $|\eta| < 2.37$, excluding the transition region $1.37 < |\eta| < 1.52$. Only diphoton events with invariant mass above 150 GeV are selected. Tight photon identification criteria is required. Kinematic cuts on the photon transverse momentum relative to the invariant mass of the diphoton are applied as well. Comparing to previous high-mass search, the isolation working point and the

relative E_T cuts are re-optimized and harmonized between spin-0 and spin-2 selections by checking the gain in relative significance. As a result, the leading (sub-leading) photon is required to satisfy $E_T/m_{\gamma\gamma} > 0.3$ (0.25), and the FixedCutTight isolation working point is selected for this analysis. The numbers of data and signal MC events after selection are summarized in Tab. 5.5.

Selection	Scalar	Graviton	Data (139 fb^{-1})
All events	1./1.	1./1.	364.97M
GRL	-	-	357.42M
Trigger	-	-	304.26M
Detector DQ	-	-	304.26M
2 loose photons	76.7%	67.7%	86.42M
Tight ID	67.7%	59.8%	15.00M
Isolation	61.2%	53.7%	5.93M
$m_{\gamma\gamma} > 150$ GeV	61.2%	53.7%	746896
Rel. E_T cuts	53.5%	41.9%	433655

Table 5.5 – The cut flow measured for (1) the full Run 2 data, (2) a NWA scalar signal sample with $m_X = 1$ TeV, and (3) a graviton sample with $k/\bar{M}_{pl} = 0.01$ rand $m_{G^*} = 1$ TeV. For the MC samples, the efficiency is shown relative to the total event yield after applying event weights ("absolute efficiency"). For data, the absolute yields are shown. The kinematic acceptance cuts are included in the "2 loose photons" selection.

5.3 Signal modeling

The signal modeling strategy introduced in this section is common to both analyses. The spin-0 signal models are used in both low-mass and high-mass searches, while the spin-2 graviton signal model is only used for high-mass search, as graviton with small m_{G^*} is already excluded.

The signal lineshape is obtained by convolving the experimental mass resolution function with the line shape at generator level (namely the true lineshape) of the resonance. In the case of signals under the narrow width approximation (NWA), the natural width of the resonance is negligible and the the signal model can be taken as the resolution function of the detector centered around m_X. In the case of large width signals, the true line shape is described by the product of a relativistic Breit-Wigner (BW) function and mass-dependent factors accounting for the parton luminosity and the matrix elements of the production and decay processes.

5.3.1 Narrow-width signal modeling

The resolution model is described by a double-sided Crystal Ball (DSCB) function. It has a Gaussian core, and asymmetric non-Gaussian tails to take into account the non-linear energy leakage effects and energy loss in inactive material. The DSCB function is defined as:

$$F_{\mathrm{NW}}(m_{\gamma\gamma}; t, n_{\mathrm{high}}, n_{\mathrm{low}}, \alpha_{\mathrm{high}}, \alpha_{\mathrm{low}}) = N \cdot \begin{cases} e^{-t^2/2} & \text{if } -\alpha_{\mathrm{low}} \leq t \leq \alpha_{\mathrm{high}} \\ \dfrac{e^{-0.5\alpha_{\mathrm{low}}^2}}{\left[\frac{\alpha_{\mathrm{low}}}{n_{\mathrm{low}}}\left(\frac{n_{\mathrm{low}}}{\alpha_{\mathrm{low}}} - \alpha_{\mathrm{low}} - t\right)\right]^{n_{\mathrm{low}}}} & \text{if } t < -\alpha_{\mathrm{low}} \\ \dfrac{e^{-0.5\alpha_{\mathrm{high}}^2}}{\left[\frac{\alpha_{\mathrm{high}}}{n_{\mathrm{high}}}\left(\frac{n_{\mathrm{high}}}{\alpha_{\mathrm{high}}} - \alpha_{\mathrm{high}} + t\right)\right]^{n_{\mathrm{high}}}} & \text{if } t > \alpha_{\mathrm{high}}, \end{cases} \tag{5.1}$$

where $t = (m_{\gamma\gamma} - \mu_{\mathrm{CB}})/\sigma_{\mathrm{CB}}$; μ_{CB}[3] and σ_{CB} represent the mean and width of the Gaussian core of the function; N is a normalization parameter; α_{low} (α_{high}) is the position of the junction between the Gaussian and power law on the low (high) mass side; n_{low} (n_{high}) is the exponent of this power law. Figure 5.2 is an illustration of the DSCB function.

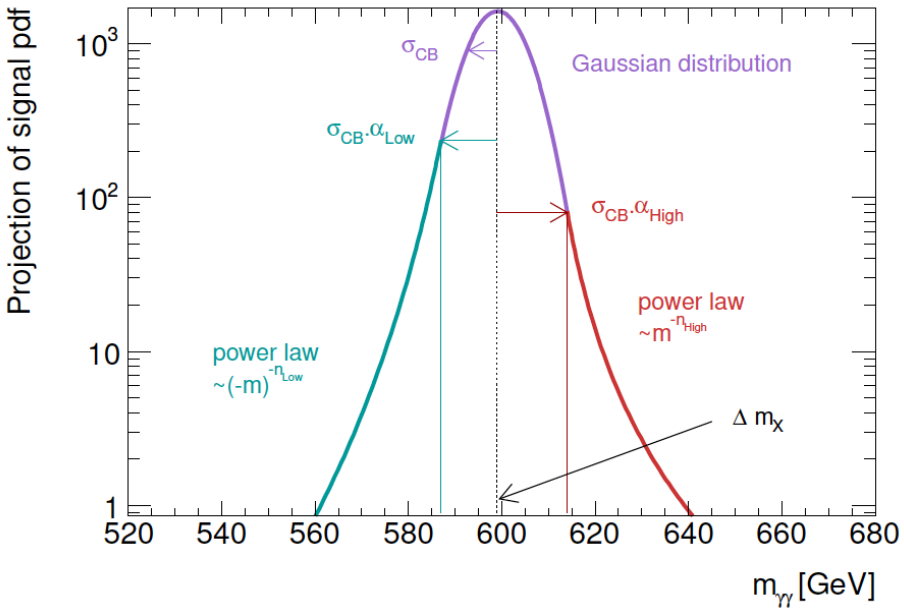

Figure 5.2 – Example of DSCB function and illustrative description of its parameters for a signal mass of $m_X = 600$ GeV. $\Delta m_X = \mu_{CB} - m_X$ in this plot.

The six parameters of the DSCB can be expressed as functions of m_X, in order to describe the narrow-width signal shape across different resonance mass values. As mentioned in Sec. 5.1, the ggF signal samples are used for the signal modeling as

[3] Defining as $\mu_{\mathrm{CB}} = m_X + \Delta m_X$, where Δm_X is the difference between the resonance mass and the Gaussian peak.

default. First, the signal $m_{\gamma\gamma}$ distributions for each mass point are fit with DSCB shape, yielding a set of DSCB parameters at each m_X value. Then, the mass dependent evolution of parameter is described by linear functions. For low-mass analysis, the two steps are done separately in UU, CC and CU categories. A simultaneous fit to signal samples at various mass point is applied to obtain the coefficients of the signal parameterization, followed by individual fits at each mass points as a validation. The obtained parameterization is shown in Fig. 5.3 for UU category as an example. The method is simplified for the high-mass analysis, with the linear functions directly fitted to the results from the individual mass point fits. The extracted parameterizations (separately for spin-0 and spin-2 to accommodate the different kinematics) are later validated against the simulated diphoton mass distribution. Figure 5.4 shows the narrow-width signal parameterization for the high-mass spin-0 analysis.

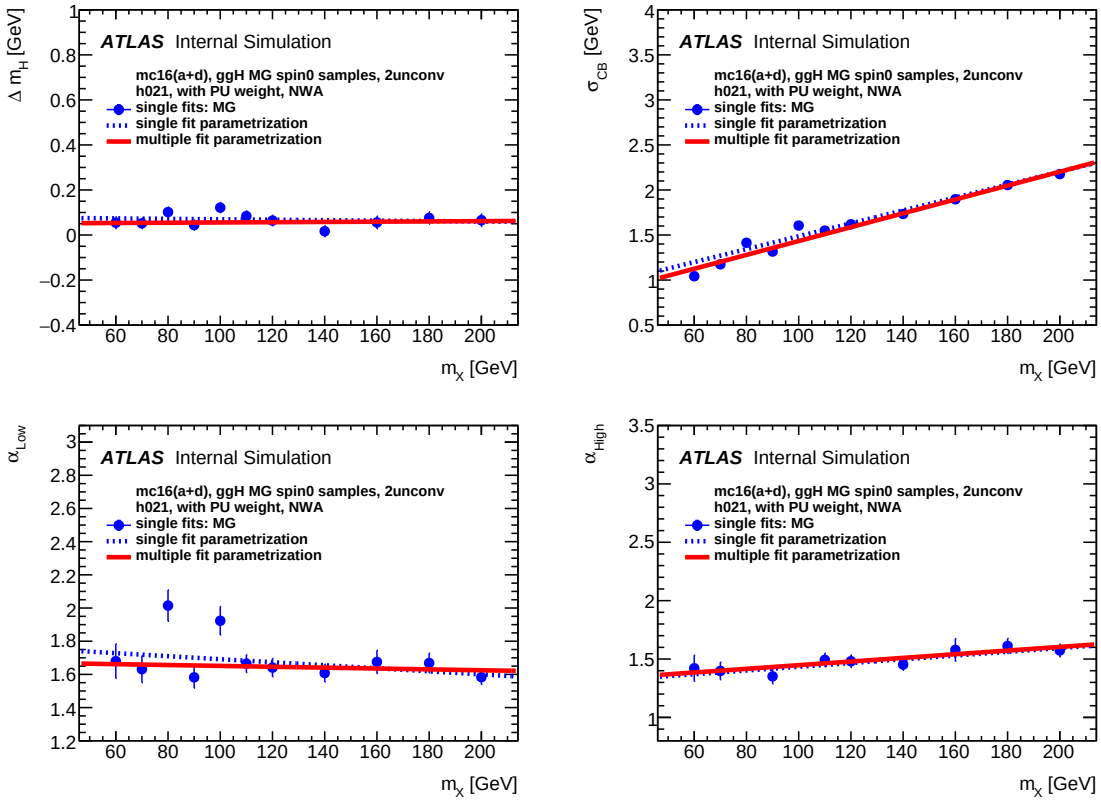

Figure 5.3 – Low-mass analysis: result of the simultaneous fits of the $m_{\gamma\gamma}$ distributions from 40 to 200 GeV for the UU category. The four plots correspond to the parameters $\Delta m_X = \mu_{CB} - m_X$, σ_{CB}, α_{low} and α_{high}. The other two parameters, n_{low} and n_{high}, are set to constants in the fit. The red line corresponds to the result of the multiple fit while the dashed lines correspond to the linear fit of the individual mass point fits.

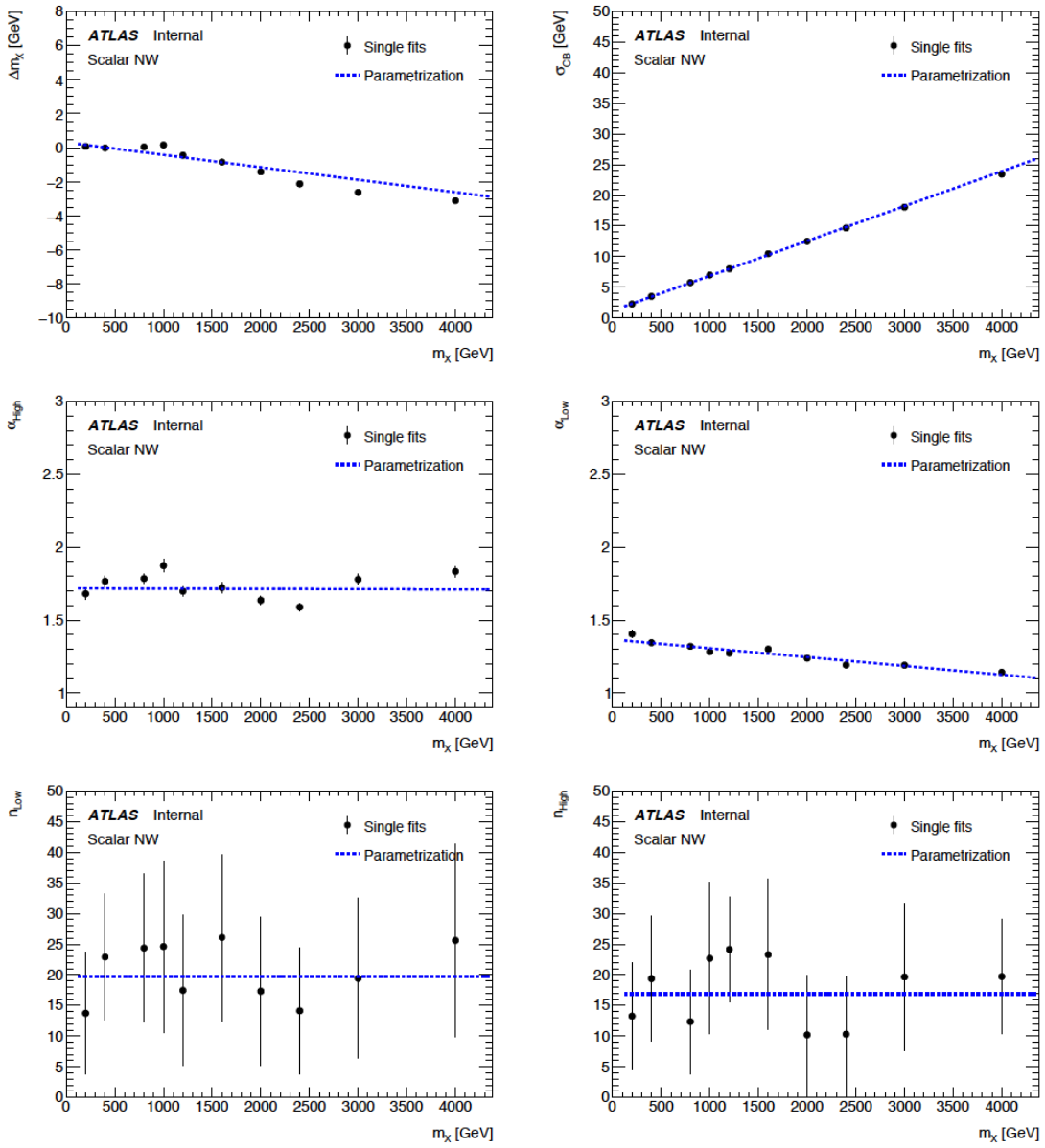

Figure 5.4 – High-mass analysis: DSCB parameters as a function of the resonance mass m_X in the range 200 to 4000 GeV for a spin-0, narrow-width resonance produced by gluon-gluon fusion. The parameters $\Delta m_X = \mu_{CB} - m_X$, σ_{CB}, α_{low}, α_{high}, n_{low} and n_{high} are extracted from fitting the DSCB function on single-mass point MC signal samples. The dependence of each parameter as a function of m_X is parameterized with linear functions (dotted lines) fitted to the results of the single-mass point fits. In the case of the parameter n_{low} and n_{high}, no explicit mass dependence is observed. Those parameters are therefore fixed to constant.

5.3.2 Large-width signal modeling

Large-width signal shapes for spin-0 resonances are described by convolving the DSCB function obtained above with the lineshape describing a large width resonance[64]:

$$F_{\text{LW}} = F_{\text{NW}}(m_{\gamma\gamma}; m_X) * m_{\gamma\gamma}^7 * \mathcal{L}_{gg} * F_{\text{B-W}}(m_{\gamma\gamma}; \Gamma_X) \tag{5.2}$$

$$F_{\text{B-W}} = \left((m_{\gamma\gamma}^2 - m_X^2)^2 + (m_{\gamma\gamma} * \Gamma_X)^2\right)^{-1} \tag{5.3}$$

where F_{NW} is the detector resolution function, $F_{\text{B-W}}$ is the relativistic BW function for a resonance of mass m_X and width Γ_X. $\mathcal{L}_{gg}$ is the gluon-gluon luminosity, which is parametrized as a function of $m_{\gamma\gamma}$ using the functional form:

$$p_1(1-(x/\sqrt{s})^{p_2/3})^{p_3} \cdot (x/\sqrt{s})^{p_4} \tag{5.4}$$

where $\sqrt{s} = 13$ TeV. The four parameters p_i are given in Table 5.6. They were derived from a fit to the gluon-gluon luminosity calculated with the NNPDF3.0 PDF set at NLO.

For a spin-2 resonance with coupling $k/\bar{M}_{pl}$, its width can be determined using the following relation:

$$\Gamma_{G^*}/m_{G^*} = 1.44(k/\bar{M}_{pl})^2 \tag{5.5}$$

which indicates that if $k/\bar{M}_{pl}$ is small enough, the resonance could be considered as a narrow-width signal. The resolution function for spin-2 search is obtained with the graviton samples generated with the coupling of $k/\bar{M}_{pl} = 0.01$, which describes graviton resonance with a negligible signal width. For the resonance with larger $k/\bar{M}_{pl}$, the signal lineshape is constructed using a convolution of the resolution function and the true graviton lineshape. Similarly to the spin-0 LW resonance case, the graviton lineshape is described by the product of a relativistic BW function (Eq. 5.3) and mass-dependent factors, given by[64]:

$$F_{G^*} \propto m_{\gamma\gamma}^7 (\mathcal{L}_{gg} + \alpha\mathcal{L}_{q\bar{q}}) * F_{\text{B-W,grav}}(m_{\gamma\gamma}; k/\bar{M}_{pl}) \tag{5.6}$$

where $F_{B-W,\text{grav}}$ is the relativistic BW function for a resonance mass m_{G^*} and width Γ_{G^*}, $\mathcal{L}_{gg}$ and $\mathcal{L}_{q\bar{q}}$ parameterize the gluon-gluon and quark-antiquark parton luminosities, that follow the same functional form as Eq. 5.4 with parameters given in Table 5.6. α denotes the relative contribution strength of the $q\bar{q}$-initiated processes to the gg-initiated processes. In the fits, the value is set to $\alpha = 3/2$[4].

[4]The value 3/2 is obtained by directly checking the output cross section of the two processes of Pythia. In some literature, this value is 2/3 computed from the relative LO cross section of $gg \to G^*$ and $q\bar{q} \to G^*$ processes. However, since the choice of α barely affects the graviton line shape elsewhere, the value 3/2 is used in the end.[64]

Parton Luminosity Term	p_1	p_2	p_3	p_4
$\mathcal{L}_{gg}$ (spin-0)	$2.093 \cdot 10^{-6}$	1	11.657	-2.557
$\mathcal{L}_{gg}$ (spin-2)	$1.892 \cdot 10^{-6}$	0.983	11.297	-2.581
$\mathcal{L}_{q\bar{q}}$ (graviton)	$8.435 \cdot 10^{-8}$	1	8.092	-2.266

Table 5.6 – The parameters of the functional forms Eq. 5.4 of the gluon-gluon (L_{gg}) and quark-antiquark ($L_{q\bar{q}}$) luminosities, derived for the spin-0 scalar and spin-2 models considered in the analysis. These functional forms are fit on the NNPDF3.0 NLO PDF parton distribution functions, which were used to simulate the MC samples for the LW scalar. Note that the parameters of the gluon-gluon luminosities for spin-0 and spin-2 are from independent fits. The parameter values are slightly different, however the difference is negligible compared with the signal modeling systematic uncertainties.

5.4 Background modeling

The background modeling procedure is discussed in this section. For the high-mass search, there is only one inclusive conversion category while for the low-mass search, all the background components and their normalization are estimated separately in each category. Generally, the most important background is the non-resonant background (continuum background) coming from the QCD production of photon pairs ($\gamma\gamma$), photon-jet pairs (γj) and jet pairs (jj), where one or two jets are mis-identified as a photon. In the low-mass region, the background contamination is a bit more complicated: the resonant background coming from Drell-Yan process is also significant, where the two electrons from radiative Z decays are misidentified as photons. In addition, since the upper limit of the invariant mass window is close to the mass of the Standard Model Higgs boson, the SM Higgs contamination is checked as well.

For the continuum background, the distributions of each background component are combined according to their respective fractions in order to construct the total background. The distribution of $\gamma\gamma$ events is taken directly from MC simulation. The shapes of the other components are modeled using data-driven approaches. Their respective fractions are obtained using a background decomposition method. The total continuum background is fitted on data with an analytical function selected and validated through a so-called *spurious signal* test. The normalization and parameters of the function are determined by the fit. For the Drell-Yan background, the normalization is obtained from the $e \to \gamma$ fake rates measured in data, and the shape is determined by fitting the dielectron data sample, followed by a Smirnov transformation[65] in order to correct for the bremsstrahlung effect.

In this section, the determination of the shape and normalization of the non-resonant background is introduced in Sec. 5.4.1. The Drell-Yan and Standard Model

Higgs backgrounds are introduced in Sec. 5.4.2. The final results of the background modeling are shown in Sec. 5.4.3.

5.4.1 Non-resonant background

The continuum background consists of two components: one is the *irreducible* background coming from the Standard Model production of real prompt photon pairs ($\gamma\gamma$), the other is the *reducible* background, including events with jets faking one or two reconstructed photon candidates (γj and jj). By applying photon identification and isolation criteria, this second source of QCD background can be reduced significantly.

The shape of irreducible background is obtained with the high-statistics Sherpa NLO samples by applying the analysis selection listed in Sec. 5.2. Note that the smoothness of the background MC samples is not naturally guaranteed since the background samples are sliced in $m_{\gamma\gamma}$. The corresponding issue (called "stitching issue") is discussed in Appendix A. The shape of reducible background is obtained from data control regions: background templates are built separately for the two components, and added according to their respective fractions measured in data.

Normalization of the irreducible and reducible backgrounds

The 2x2D sideband decomposition method[67] is implemented to estimate the relative fractions of the $\gamma\gamma$, γj and jj components in the invariant mass spectrum. Considering $\gamma\gamma$ as signal, the procedure to obtain the $\gamma\gamma$ purity in signal region is introduced below.

First, two requirements of the signal selection are loosened in order to construct a new sample (namely L'L') that is enriched in fake-photon background: the photon isolation criteria are dropped, and the tight photon identification criteria are relaxed according to one of the LoosePrime configurations, as listed in Tab. 5.7. In this sample, the observed yield $W_{tot}^{L'L'}$ is given by the sum of the unknown signal yield ($W_{\gamma\gamma}^{L'L'}$) and the background yields ($W_{\gamma j}^{L'L'}$, $W_{j\gamma}^{L'L'}$[5] and $W_{jj}^{L'L'}$):

$$W_{tot}^{L'L'} = W_{\gamma\gamma}^{L'L'} + W_{\gamma j}^{L'L'} + W_{j\gamma}^{L'L'} + W_{jj}^{L'L'} \tag{5.7}$$

Then, depending on whether the leading or sub-leading photons passes or fails the tight identification and isolation criteria, this new sample can be divided into 16 orthogonal subsamples. One of the subsamples is the signal region (namely TITI, where "T" stands for Tight, and "I" stands for Isolated. "TITI" denotes that both photon candidates pass the tight identification and isolation requirements), while the rest ones are control regions of background contaminations. In each of the subsamples,

[5] $j\gamma$ and γj represent the two cases of a photon-jet event, where either the leading or the sub-leading photon is actually a mis-identified jet. The calculated yields of these two components are added together in the end.

ID name	Variables used in the selection
Loose	R_{had1}, R_{had}, R_{η}, $w_{\eta 2}$
Tight	Loose + R_{ϕ}, w_{s3}, F_{side}, ΔE, E_{ratio}, $w_{s1,\text{tot}}$, f_1
LoosePrime-2	Tight – w_{s3}, F_{side}
LoosePrime-3	Tight – w_{s3}, F_{side}, ΔE
LoosePrime-4	Tight – w_{s3}, F_{side}, ΔE, $w_{s1,tot}$
LoosePrime-5	Tight – w_{s3}, F_{side}, ΔE, E_{ratio}, $w_{s1,tot}$

Table 5.7 – Definitions of the Loose, Tight[66], and LoosePrime selections. For Loose and Tight, the variables are those used in the selection. The LoosePrime selections are defined with respect to the Tight selection and the variables for which the Loose criterion is applied instead are listed. For example, in the LoosePrime-2 selection the tight identification criteria are applied to all the shower variables, with the exception of the two shower shape variables mentioned.

the observed yield can be expressed as a function of the signal and background yields in the L'L' sample, the identification and isolation efficiencies for prompt photons passing the LoosePrime selection,[6] background identification and isolation fake rates, and the correlations between the isolation distribution of the two fake photons in jj events. Therefore, one can deduce the signal and background yields given the identification and isolations efficiencies of the signal as inputs. As an example, the observed signal yield in the TITI region is given by:

$$\begin{aligned} N_{\text{TITI}} = & W_{\gamma\gamma}^{L'L'} \varepsilon_{I1}\varepsilon_{T1}\varepsilon_{I2}\varepsilon_{T2} \\ & + W_{\gamma j}^{L'L'} \varepsilon_{I1}\varepsilon_{T1} f_{I2} f_{T2} \\ & + W_{j\gamma}^{L'L'} f_{I1} f_{T1} \varepsilon_{I2}\varepsilon_{T2} \\ & + W_{jj}^{L'L'} f'_{I1} f'_{T1} f'_{I2} f'_{T2} \xi_{Ijj} \end{aligned} \tag{5.8}$$

where

- ε_{I1} and ε_{I2} are the isolation efficiencies for the leading and sub-leading photons respectively;
- ε_{T1} and ε_{T2} are the tight dentification efficiencies for the leading and sub-leading photons respectively;
- f_{I1} and f_{I2} are the isolation fake rates for γj and $j\gamma$ events;

[6] To simplify the method, it is assumed that the efficiencies are identical for leading photons in $\gamma\gamma$ and γj, and for sub-leading photons in $\gamma\gamma$ and $j\gamma$ events.

- f_{T1} and f_{T2} are the tight identification fake rates for γj and $j\gamma$ events;
- f'_{I1} and f'_{I2} are the isolation fake rates for jj events;
- f'_{T1} and f'_{T2} are the tight identification fake rates for jj events;
- ξ_{Ijj} is the isolation correlation factor between the jets in jj events.

In the calculation, the correlation between the isolation and the identification efficiencies for $\gamma\gamma$ and γj events is neglected. Clearly there are 16 equations like Eq. 5.8, and 19 unknowns in total. Six of the unknowns are inputs of the system or fixed to a constant number:

- ε_{I1}, ε_{I2}, ε_{T1} and ε_{T2} are determined directly from the Sherpa diphoton sample;
- ξ_{j1} and ξ_{j2} are fixed to 1, they are the correlation between the identification and the isolation fake rates for the leading and sub-leading jets.

The remaining 13 unknowns are outputs, determined through a minimisation procedure of the decomposition method:

- the four yields $W_{\gamma\gamma}^{L'L'}$, $W_{\gamma j}^{L'L'}$, $W_{j\gamma}^{L'L'}$ and $W_{jj}^{L'L'}$;
- the tight identification fake rates f_{T1}, f_{T2}, f'_{T1} and f'_{T2};
- the isolation fake rates f_{I1}, f_{I2}, f'_{I1} and f'_{I2} ;
- the isolation correlation factorξ_{Ijj} between the jets in jj events.

The extraction of yields, efficiencies and fake rates described above is performed in 6 $m_{\gamma\gamma}$ bins with a fixed bin size of 10 GeV for the low-mass analysis, and in 7 bins for the high-mass analysis with a minimum bin size of 50 GeV. The $m_{\gamma\gamma}$ bins are chosen to be wide enough so that the events in each bin is enough, and more importantly, the mass spectrum in data cannot reveal potential peaks to comply with the blind analysis policy.

For the high-mass analysis, the estimated yields in the mass range [150, 2000] GeV of $\gamma\gamma$, γj and jj components as a function of $m_{\gamma\gamma}$ are shown in Fig. 5.5. The decomposition results are computed with full Run 2 data. The $\gamma\gamma$ purity and the respective fractions are obtained separately for 2015-2016, 2017 and 2018 datasets, since the trigger and the pile-up conditions are different. As shown in Fig. 5.6, the $\gamma\gamma$ purity is $89\% - 97\%$ depending on the diphoton mass, and it does not change significantly between the data-taking periods. The average value of the purity over mass range, 92%, is taken for normalization between the irreducible and reducible components.

For lower mass range [60, 120] GeV, the background decomposition is done separately for the three conversion categories. Figure 5.7 shows the decomposition results

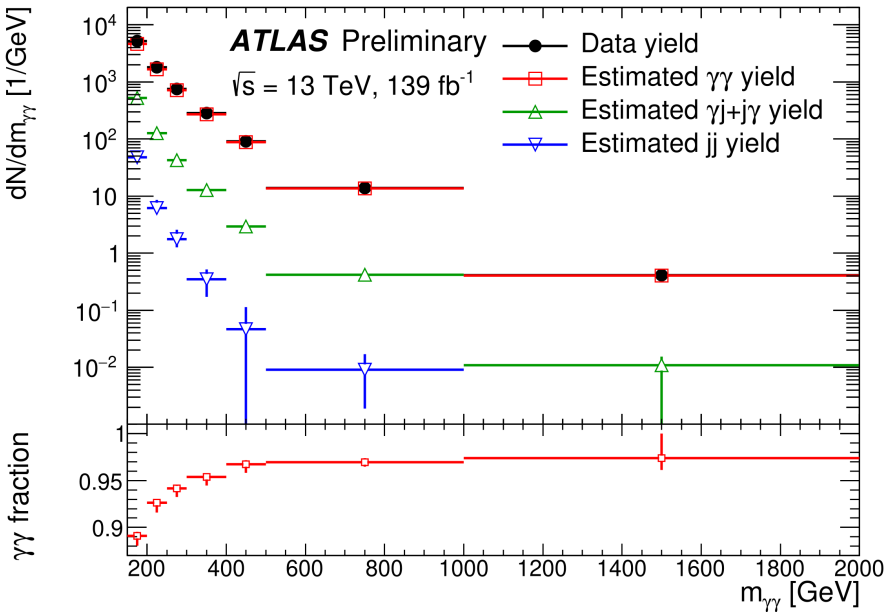

Figure 5.5 – High-mass analysis: the $\gamma\gamma$, γj and jj event yields determined by the 2x2D sideband method as a function of the diphoton mass.

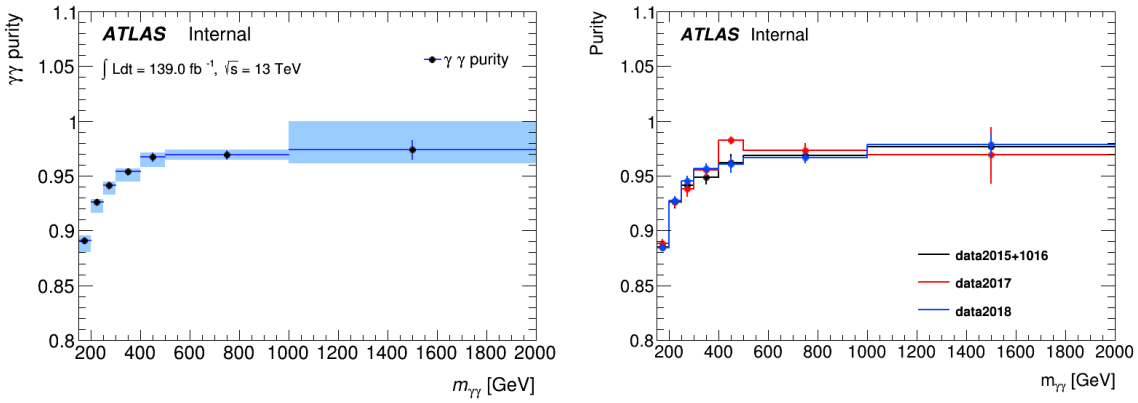

(a) (b)

Figure 5.6 – High-mass analysis: purity of the data sample in prompt isolated diphotons as obtained from the 2x2D sideband decomposition method. Result (a) is shown with statistical errors (error bars) and systematic errors associated with the variation of the LoosePrime definition (error bands). Results (b) is obtained separately for different data-taking periods in order to compare the purity for different pile-up and trigger conditions and good agreement is seen. The errors shown reflect only the statistical uncertainty.

obtained with 2017 data for the UU and CC categories as an example. A bump-like structure can be clearly seen around the Z peak in the CC category, which comes from the Drell-Yan background. In general, the UU category has the highest $\gamma\gamma$ purity while the purity in CC category is about 3% lower. The $\gamma\gamma$ purity also slightly increases with the diphoton mass, from $60\% - 70\%$ in the given mass range. The inclusive numbers to be quoted as $\gamma\gamma$ fractions are 69% for UU, 66% for CU and 65% for CC category.

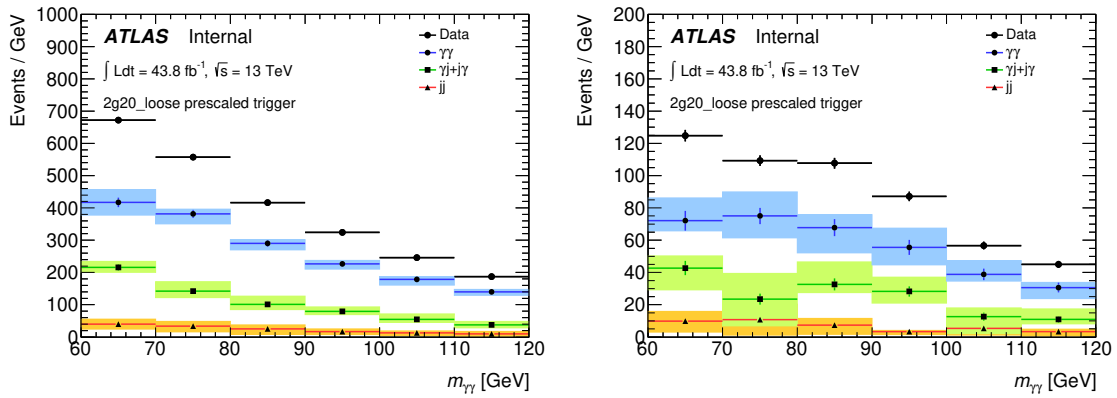

(a) (b)

Figure 5.7 – Result from low-mass analysis: the $\gamma\gamma$, γj and jj event yields determined by the 2x2D sideband method as a function of the diphoton mass with 2017 data, for the UU (left) and CC (right) categories.

The leading systematic uncertainty of this method comes from the choice of the LoosePrime definition. To cover the statistical uncertainty and the systematic uncertainties on the choice of LoosePrime definition, isolation working point and other potential sources, a conservative number of $\pm 3\%$ is assigned as the uncertainty on $\gamma\gamma$ fraction for high-mass search, and $\pm 5\%$ for low-mass search.

Reducible background shape

It is impossible to obtain the reducible background model directly from γj MC sample as mentioned in the previous chapter, since the simulated shape is not accurate enough and only a small fraction of γj events pass the diphoton selection. On the other hand, if the yield estimation described above is performed with fine $m_{\gamma\gamma}$ binning, the decomposition method could be used to provide a reliable shape of reducible background. However, this would effectively unblind the input dataset, and higher granularity would also introduce larger statistic fluctuations. Therefore, the reducible background shape is estimated using the data control samples.

In the signal sample, the prompt photon candidates are required to pass both tight photon identification and isolation criteria. In order to build a control sample enriched in γj and $j\gamma$ events, there are multiple ways to invert these two cuts. In addition, the real $\gamma\gamma$ events may also satisfy the control region requirements and bias the shape

of the jet-enriched sample, therefore they need to be subtracted. Depending on the definition of the control region, the shape and normalization of $\gamma\gamma$ contamination are also different. This bias due to inaccurately simulated $\gamma\gamma$ contribution in control region might be significant if the contamination is high.

In the low-mass analysis, three orthogonal control regions are studied:

- $TIT\bar{I}$: the two photons (leading and sub-leading photons) pass the tight identification cuts, while one photon passes the isolation cuts and the other one fails. This definition of control region is very close to the one of signal region, however it brings large Drell-Yan contamination as well. The $\gamma\gamma$ contamination in this control region is relatively high (about 25%, as estimated on MC from the number of real diphoton events passing the $TIT\bar{I}$ selection) in this case.

- $TI\bar{T}\bar{I}$: one photon passes both tight identification and isolation cuts, while the other passes the loose identification but fail the tight identification and isolation cuts. This definition is far from signal region, with $\gamma\gamma$ contamination less than 10%.

- $TI\bar{T}I$: two photons pass the isolation cuts, one photon passes the tight identification, while the other passes the loose identification but fails the tight identification cuts. As a compromise between the other two control regions, this definition is closer to signal region comparing to $TI\bar{T}\bar{I}$, and the $\gamma\gamma$ contamination is also about 25%.

In general, we want the control regions to be as close to the signal region as possible in order to minimize the bias from inverting the selections. However in the case of $TIT\bar{I}$, this definition introduce a large Drell-Yan contamination that would be complicated to remove, similar to what was found in the background decomposition in the signal region (Fig. 5.7). The $TIT\bar{I}$ control region is therefore discarded.

The other two control regions are tested against γj MC samples, and significant bias coming from the inversion of idenfication and isolation is observed, even for the purest γj sample ($TI\bar{T}\bar{I}$). Figure. 5.8 shows the $m_{\gamma\gamma}$ shapes of the $TI\bar{T}\bar{I}$ and $TI\bar{T}I$ from data control samples, as well as the the shape from diphoton MC samples. $TI\bar{T}I$ is chosen as a baseline, and $TI\bar{T}\bar{I}$ is taken as one systematic variation of the reducible background shape.

The data control region used in high-mass analysis inherits the similar definition as $TI\bar{T}I$. However the loose identification requirement is tightened to medium since the trigger-level identification is already requiring so. The isolation criteria are applied on both leading and sub-leading photons. One photon is required to pass the tight identification cuts, while the other fails the tight identification, but passes certain LoosePrime selection given in Tab. 5.7. Such constructed data control region with LoosePrime-4 selection together with the expected diphoton contribution obtained from MC samples is shown in Fig. 5.9.

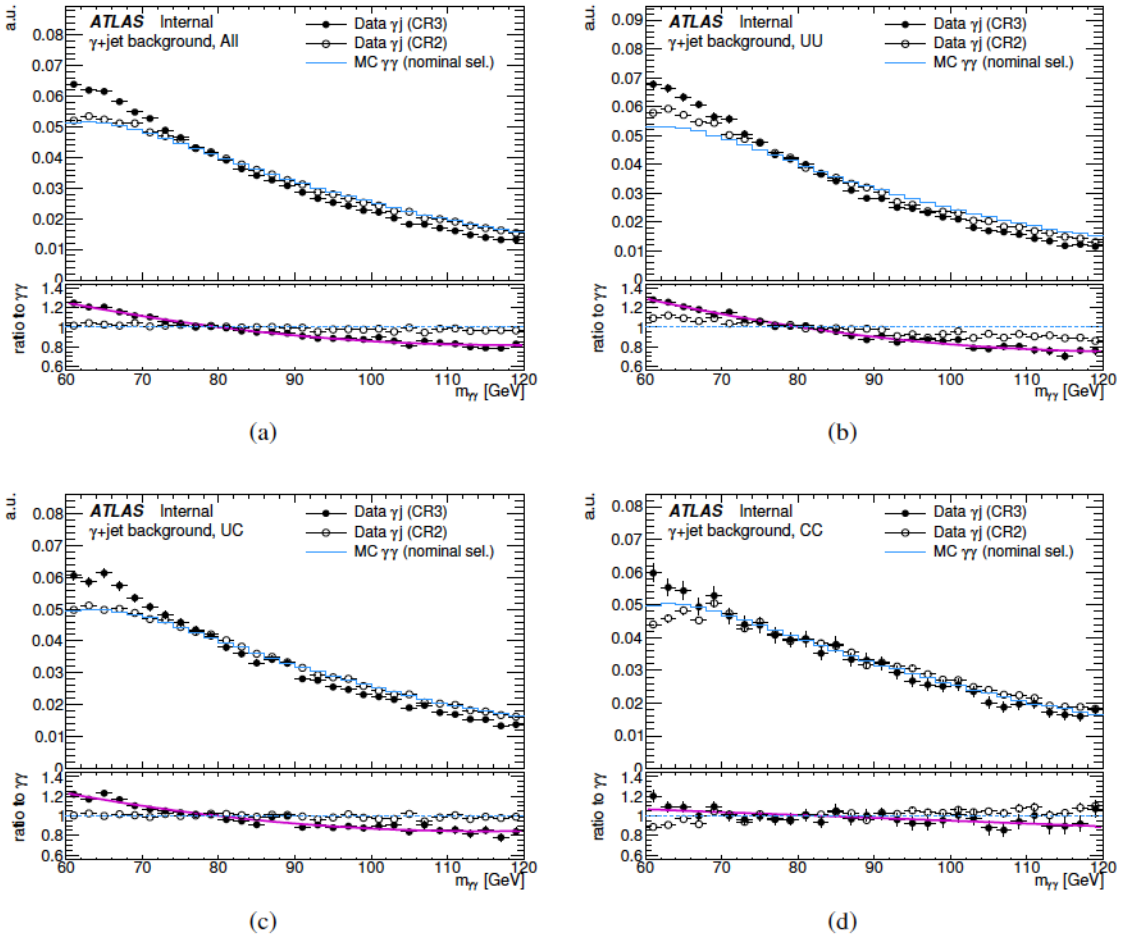

Figure 5.8 – Low-mass analysis: the invariant mass distribution of diphoton candidates in the data-driven $TI\bar{T}\bar{I}$ ("CR2" in plot) and $TI\bar{T}I$ ("CR3") control regions and in the diphoton MC sample for the three categories (UU, UC, CC). All histograms are normalized to the same area. The bottom panels correspond to the ratio to the diphoton MC shape. The pink line corresponds to a polynomial fit to the $TI\bar{T}I/\gamma\gamma$ MC ratio.

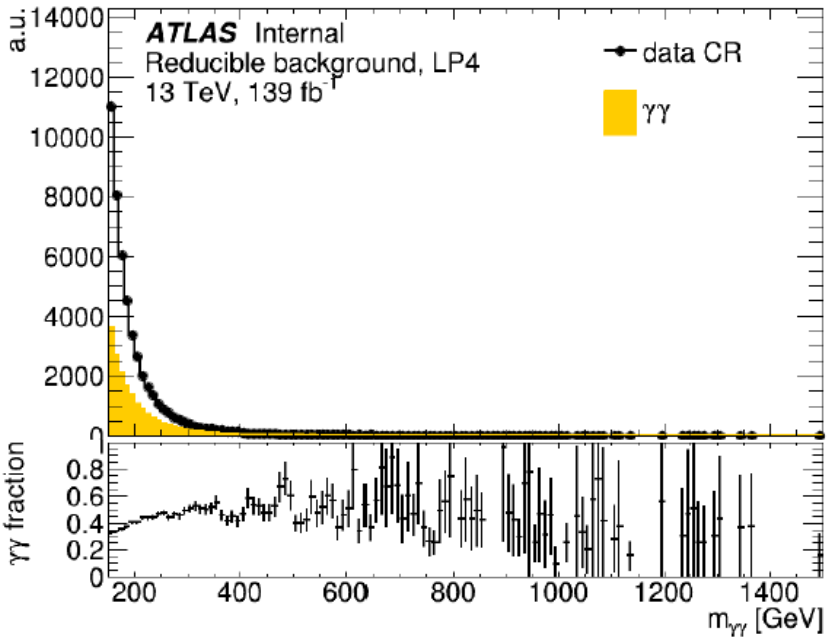

Figure 5.9 – High-mass analysis: invariant mass distribution of events in the data control region LoosePrime-4, shown together with the expected contribution for prompt diphoton events from MC simulation. Although this is a control region enriched in γj events, there is still a large contribution from true $\gamma\gamma$ events of about 40% which is subtracted in order to estimate the $m_{\gamma\gamma}$ shape of the reducible background.

It can be seen that the $\gamma\gamma$ contamination is quite large (about 40%), because the medium identification requirement at trigger-level has already reject a lot of real jets. The accuracy of the simulation of the $\gamma\gamma$ contribution in control region is worse than in the signal region, and the actual shape and normalization of the $\gamma\gamma$ contribution highly depend on the LoosePrime selection. Therefore, data control regions are also constructed with other LoosePrime definitions listed in Tab. 5.7 in order to check the dependence on different definitions with better or worse $\gamma\gamma$ contamination. Figure 5.10 shows the diphoton mass distribution obtained with each of the LoosePrime definitions. Both the purity of γj events and reasonable identification requirements should be considered. For example, the LoosePrime-2 control region requires the tightest identification and is supposed to be the one that is closest to the signal region. However, its statistic is limited, and a large $\gamma\gamma$ contamination leaking from the signal into this control region has to be subtracted. The LoosePrime-5 selection is the loosest one, allowing much higher statistics and larger γj fraction. However the LoosePrime-5 definition is far from the tight photon identification, which means the fake photons selected in this region is less representative of the actual background in the signal region. In the end, the LoosePrime-4 control region is used as the default definition, while the other LoosePrime variations are used to estimate the systematic uncertainty on the reducible background shape. As a cross check, the invariant mass spectrum estimated from LoosePrime-4 control region is rebinned and compared with the decomposition result. Despite the statistical uncertainties especially in the high-mass region, good agreement is found between these two methods.

In principle, one could also build a jj enriched control region by inverting the identification requirement on both leading and sub-leading photons. However, the background decomposition results indicates that the contribution of multi-jet events is insignificant, especially in the high-mass case. Studies show that the impact of adding or not a jj component is fully covered by the systematic uncertainties on the background shape, therefore the total continuum background template is for now simplified with only two components, $\gamma\gamma$ and γj, as introduced in the next subsection.

Total non-resonant background template and associated systematics

The total non-resonant background template is built by summing the irreducible and reducible components, and then normalized to the yield estimated in data. However, the statistics of the data control region is too small to provide a smooth background template with acceptable fluctuations. Therefore the total continuum background template is actually obtained by reweighting the high-statistics diphoton MC samples. In low-mass analysis, the ratio (Fig. 5.8) between the $TI\bar{T}I$ distribution and the MC $\gamma\gamma$ distribution is fitted with a polynomial function, separately for each category. The fitted function is then used to reweight the diphoton MC sample, in order to get a smooth shape of the reducible component thanks to the high statistics of the Sherpa $\gamma\gamma$

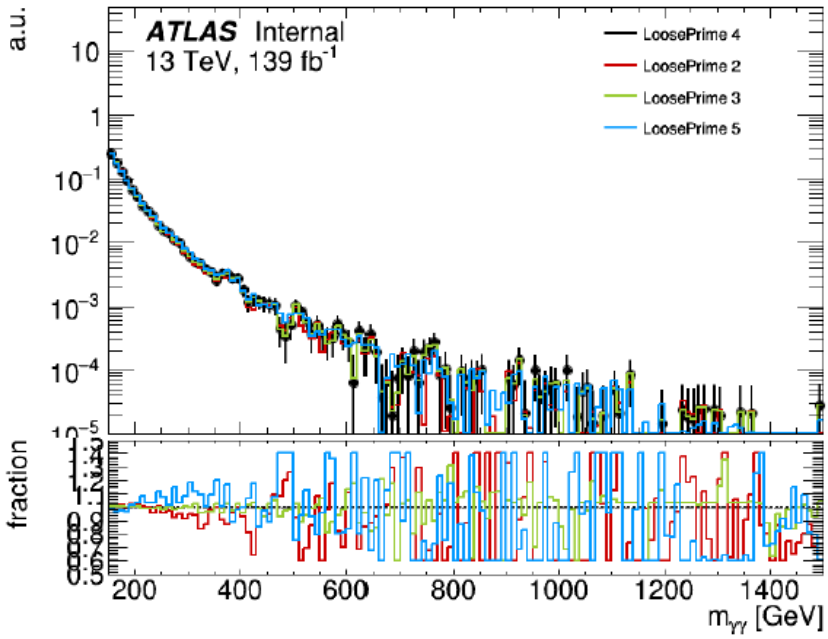

Figure 5.10 – High-mass analysis: reducible background distributions obtained from data control regions. The data markers indicate the normalized event yields and shape from the data of the default LoosePrime selection, LoosePrime-4. The distributions are also obtained using the other LoosePrime selections in order to assess the systematic uncertainty on the shape of the reducible background. All the LoosePrime distributions are normalized to the same area.

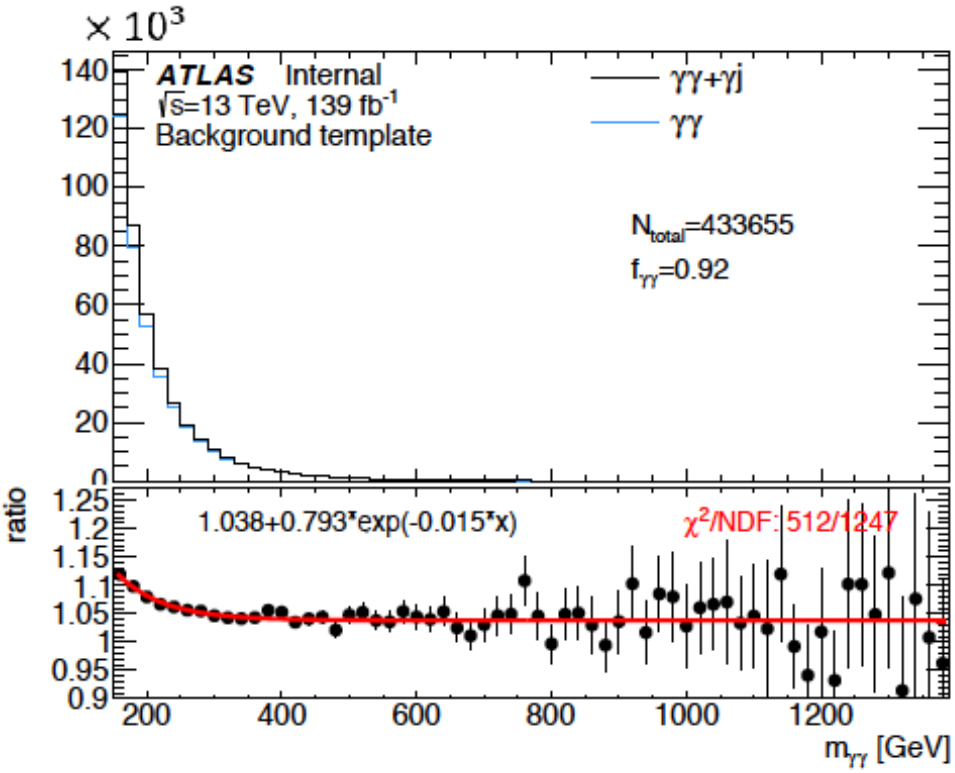

Figure 5.11 – High-mass analysis: an illustration of the total background template constructed from MC simulation for the $\gamma\gamma$ component and a dedicated data control region for the reducible γj component (black marks). The contribution of the $\gamma\gamma$ component is also shown (blue line) to emphasize its contribution to the overall template. The lower panel shows the ratio between the total template and the $\gamma\gamma$ component indicating the contribution of the reducible component; the reducible component fraction ranges from approximately 10% at low diphoton mass to 3% at higher diphoton mass.

samples. The total continuum template is built by adding the $\gamma\gamma$ and γj components according to their measured fractions in data using the 2x2D decomposition method. For the high-mass analysis where the search range is wide, the reducible background contamination is only significant in the lowest part of the mass range since the $\gamma\gamma$ purity increases with the diphoton invariant mass. The smoothing method is therefore adjusted to simplify the fit. As shown in Fig. 5.11, the two components are first added together, and then the ratio of the sum of $\gamma\gamma + \gamma j$ to $\gamma\gamma$ is fitted with a simple exponential function. The fitted function is then used to reweight the diphoton component in order to obtain the total background template.

The total background template is eventually normalized to the data yields, therefore only the sources of systematic uncertainty that affect the shape of the template are to be considered and studied carefully. There are three main sources: the relative fraction between $\gamma\gamma$ and γj components; the reducible background shape that is affected by the control region definition and smoothing procedure; and the irreducible background shape that is affected by the MC simulation and its corrections.

To study the first two sources, alternative background templates are built with different systematic variations:

- change the $\gamma\gamma$ fraction. Increase or decrease the fraction by 5% (for low-mass analysis) or 3% (for high-mass analysis).
- use alternative definition of the control region. Use $TI\bar{T}\bar{I}$ instead of $TI\bar{T}I$ (for the low-mass analysis), or switch from LoosePrime-4 to other LoosePrime selections (for the high-mass analysis).
- change the functional form used for smoothing (negligible for high-mass analysis).

For the low-mass analysis, the nominal template and the templates built with these variations are shown in Fig. 5.12. The largest impact comes from using the alternative control region (up to 5%), as the definition of $TI\bar{T}\bar{I}$ and $TI\bar{T}I$ are quite different.

The systematic uncertainties on the irreducible background shape are only studied for the high-mass analysis. The experimental uncertainties come from the corrections applied to the MC simulation, such as the pile-up modeling, the photon energy scale and energy resolution, and the efficiencies of photon identification and isolation. These corrections change with respect to the diphoton invariant mass in a wide mass range, and are not so significant in the low-mass case. Alternative background templates with variation due to the experimental systematics are built by varying the corrections applied on the $\gamma\gamma$ sample. Figure. 5.13 shows the templates built with all the systematic variations mentioned above for the high-mass analysis. The largest impact comes from the fraction of $\gamma\gamma$ component, as the template is built in a wide mass range. The experimental uncertainties of the $\gamma\gamma$ component is found to be small compared to the one associated with the $\gamma\gamma$ fraction, and the uncertainties on energy resolution and pile-up efficiencies are negligible.

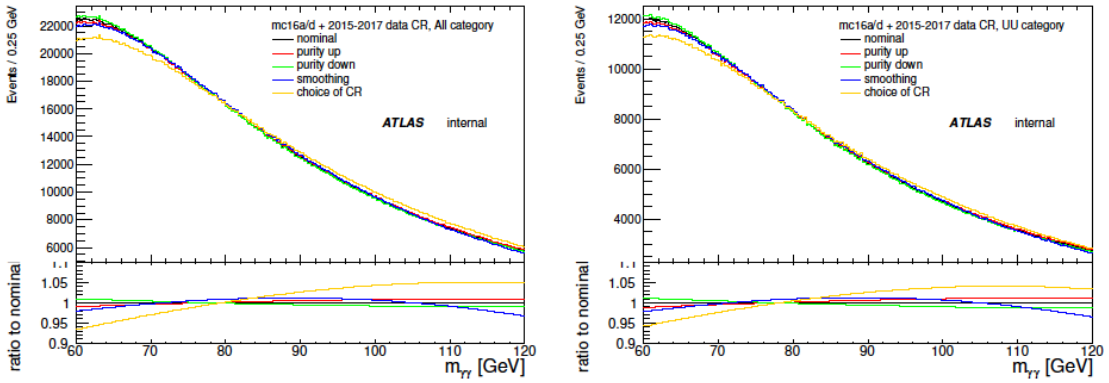

(a) inclusive

(b) UU category

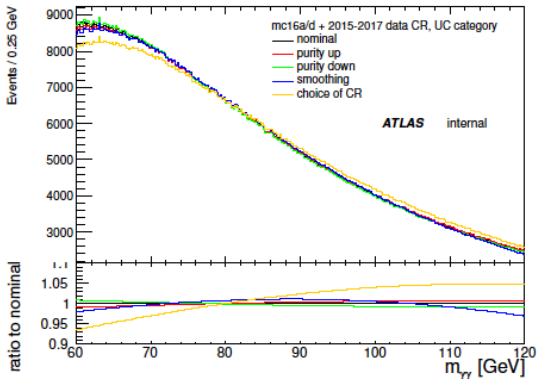

(c) UC category

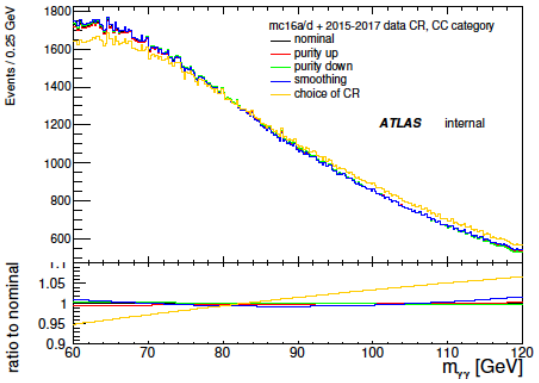

(d) CC category

Figure 5.12 – Low mass analysis: non-resonant background template with systematic variations associated with the reducible component for the inclusive case and the three categories.

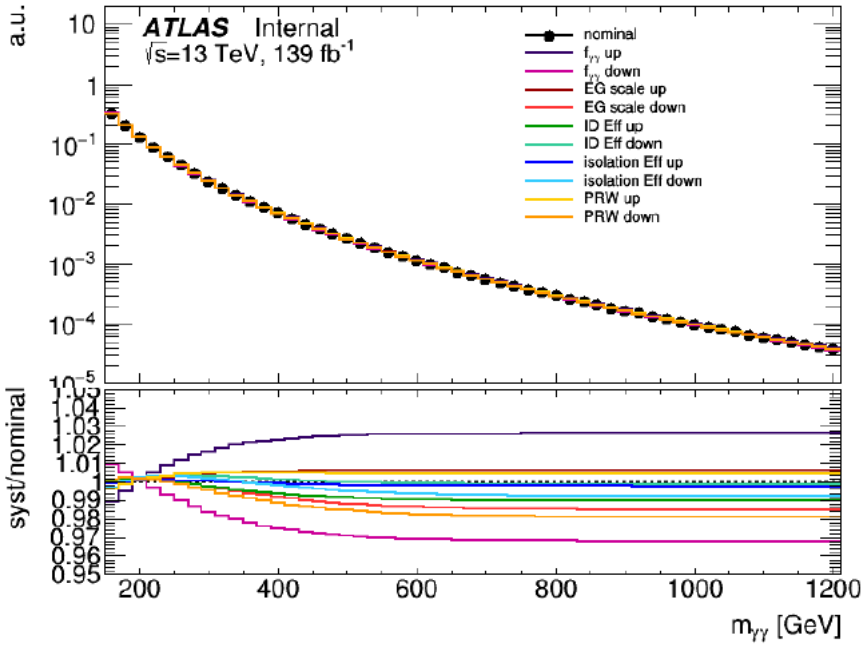

Figure 5.13 – High-mass analysis: total $\gamma\gamma + \gamma j$ background template with systematic variations associated with the experimental uncertainties affecting the shape of the diphoton MC simulation.

The theoretical uncertainties affecting the shape of the $\gamma\gamma$ component are also studied, as they have a significant effect in the high-mass region. Uncertainties on the QCD scales and the PDF set used in the simulation are considered. For the QCD scales, the factorization scale (μ_F) and the renormalization scale (μ_R) are set to alternative values. The two combinations that give the largest shape variation (μ_R=1, μ_F=0.5 and μ_R=0.5, μ_F=1) are used to build the systematic variated template. For the PDF uncertainties, all the 100 eigen-value variations of the nominal (NNPDF3.0 NLO) PDF set as well as some alternative (MMHT2014 NNLO, CT14 NNLO, PDF4LHC15 NNLO, etc.) PDF sets are studied. The ones that give the largest shape variation are picked. Due to the limitation of statistics, a similar smoothing procedure as the one used for the construction of the total background template is applied: the ratio of the distribution of each of the selected variations to the nominal one is fitted, and the extracted function is used to reweight the $\gamma\gamma$ shape in order to obtain the background template for each systematic variation. The templates associated with theory uncertainties are shown in Fig. 5.14. For the overall normalization, it can be seen that the theory uncertainties are quite large especially above 2 TeV, but their actual impact is limited since only the variations on shape matters.

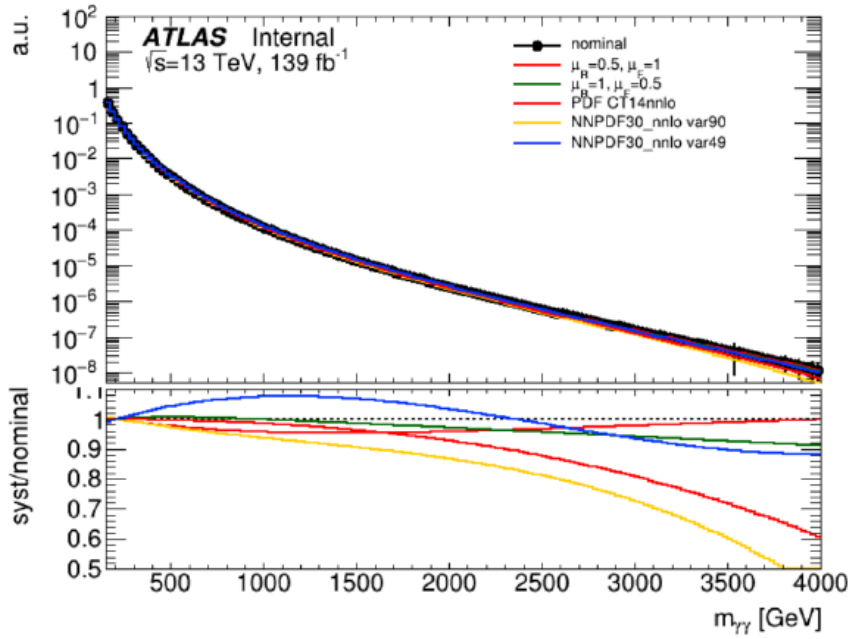

Figure 5.14 – High-mass analysis: total $\gamma\gamma + \gamma j$ background template with systematic variations associated with the theoretical uncertainties affecting the shape of the diphoton MC simulation.

Choice of fit function and spurious signal estimation

The non-resonant background contribution to the overall $m_{\gamma\gamma}$ distribution is modeled by a smooth functional form fitted to the distribution in data. The parameters of the functional form are determined by the fit, along with the signal and background yields. This function has to be capable of describing the background over the whole search range, and to be flexible enough to accommodate different underlying background distributions as well as the systematic variations.

In order to choose the functional form for the continuum background, a signal-plus-background fit is performed on the background-only template described above, for each given mass hypothesis m_X. The potential bias due to the choice of the fit function is estimated by the fitted signal yield $N_{spurious}(m_X)$ (spurious signal), which is considered as a systematic uncertainty associated with the background modeling. The spurious signal reflects how a given function can adapt to the continuum background shape obtained as described above, under the assumption of infinite statistics.

If the fitted number $N_{spurious}$ is significantly smaller than the uncertainty of the signal yield in the full mass range of interest, the function is considered as valid. A criterion is therefore set on $N_{spurious}/\delta S$ and its dependence on m_X, where δS is the statistical uncertainty of the signal. Practically, the statistical uncertainty of background is used instead of δS, as the signal-to-background ratio is quite small and the expected statistical uncertainty from the fluctuations of the background

is dominant compared to the uncertainty of the hypothetical signal. The cut on $N_{spurious}/\delta S$ is chosen based on the limitation of available MC: for the low-mass analysis the cut $N_{spurious}/\delta S < 30\%$ is required, and for the high-mass the requirement is $N_{spurious}/\delta S < 50\%$.

For the low-mass analysis, the nominal gluon-gluon fusion scalar signal model is used in the signal-plus-background fits, separately for each conversion categories. The following functional forms are tested:

- a Fermi distribution: $f(x) = 1/(e^{(x-\mu)/k}+1)$;
- Bernstein polynomials: $f(x) = \sum_{i=0}^{n} c_i \cdot x^i (1-x)^{n-i}$, with $n = 5$ to $n = 7$;
- a Landau distribution;
- the sum of a Landau distribution and an exponential distribution.

The fits are performed in the mass range [60,120] GeV, and the spurious signal is tested between 65 and 110 GeV. The relative spurious signal $N_{spurious}/\delta S$ results are shown in Fig. 5.15 for the three categories respectively. The functions with the smallest relative spurious signal and less degrees of freedom are chosen: the Landau+exponential function for the UU and UC categories, and a fifth order Bernstein polynomial for the CC category. The highest value of $N_{spurious}$ over the search range is included as a systematic uncertainty on background modeling.

The spurious signal study is more complicated for the high-mass analysis. The value of $N_{spurious}$ decreases rapidly with m_X, and the extraction of spurious signal suffers a lot from the statistical fluctuations of the background template. Therefore a dedicated smoothing technique is applied. All the scalar (nominal gluon-gluon fusion) and graviton signal models with different signal width are used in the signal-plus-background fits. The following primary functional form, referred as PowLog-n function, is tested:

$$f(x; a, a_i) = (1 - x^{1/3})^a \cdot x^{\sum_{i=0}^{n} a_i (log x)^i} \tag{5.9}$$

where $x = \frac{m_{\gamma\gamma}}{\sqrt{s}}$ is a transformation that improves the numerical stability, n denotes the highest power of the logarithm present in the exponent of the expression. For example, when $n = 0$, the simplest function form PowLog-0 is given as:

$$f(x; a, a_0) = (1 - x^{1/3})^a \cdot x^{a_0} \tag{5.10}$$

The fits are performed in the mass range [150,4000] GeV, and the spurious signal is tested in a smaller range depending on the signal width. With only two degrees of freedom, the PowLog-0 function is already capable of describing the background sufficiently. Figure 5.16 shows the estimation of the spurious signal for the narrow width scalar signal model. In the low $m_{\gamma\gamma}$ region where the local statistical fluctuations

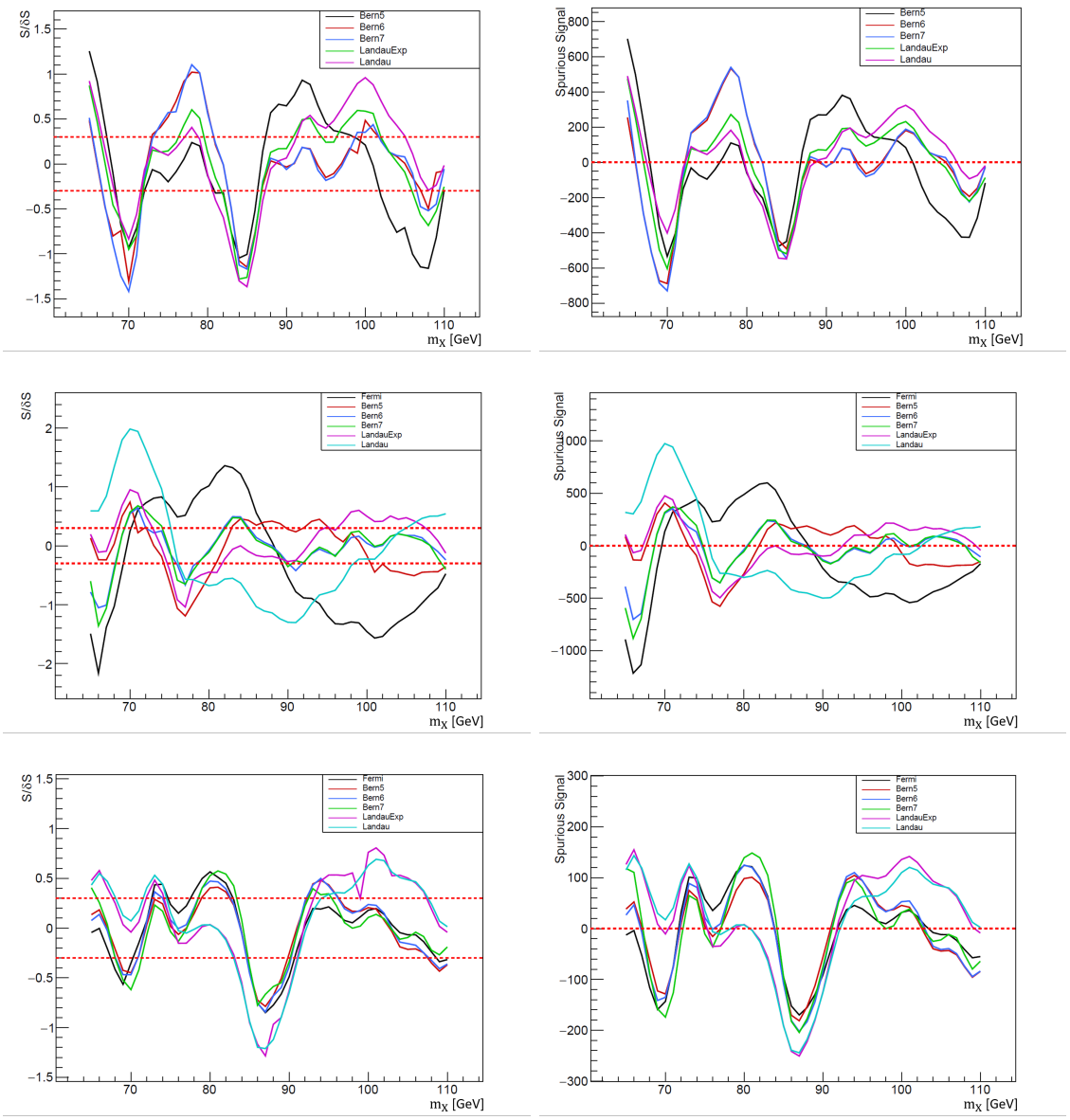

Figure 5.15 – Low-mass analysis: results of the spurious signal scan over m_X in the UU (top row), UC (middle) and CC (bottom) categories. The spurious signal is illustrated in terms of the number $N_{spurious}$ relative to the statistical uncertainty of the background (left) and in term of the absolute value of $N_{spurious}$ (right).

are large, lots of spurious signal events can be observed. In the region above 2 TeV, the number of spurious signal is much smaller due to the significantly larger statistics of diphoton MC. At 1.3 - 1.4 TeV, a large under-fluctuation occursin the background template that comes from the slicing of the MC samples, as the statistics runs out in the high mass tail of the $m_{\gamma\gamma}$ distribution of the [175, 1400] GeV slice. A particularly large spike of spurious signal is therefore seen in that region. Despite these local features, the spurious signal for most mass points is within the 50% envelope.

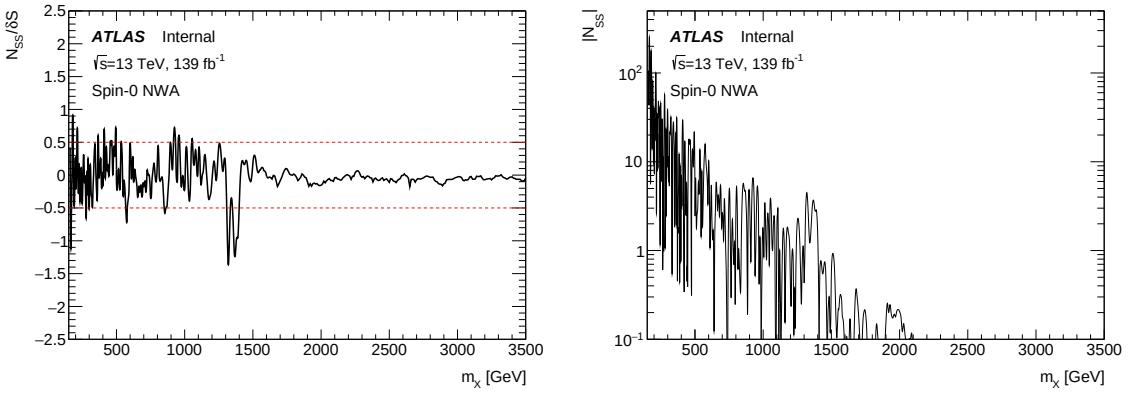

(a) (b)

Figure 5.16 – High-mass analysis: result of the spurious signal scan over m_X assuming the NW signal model and using a background template derived solely from the Sherpa $\gamma\gamma$ MC sample. The spurious signal is illustrated in terms of the $N_{spurious}$ relative to the statistical uncertainty of the background (a) and in term of the absolute value of $N_{spurious}$ (b).

The local features of the spurious signal results, especially the spike around 1.4 TeV, are caused by the statistical fluctuations of the background template. To suppress this impact, the background template is smoothed using the Functional Decomposition (FD) method[68], as briefly introduced in Appendix B. The basic idea of FD is to model the given dataset (in this case, the background template) as a truncated series expansion in a complete set of orthonormal basis functions, using a process analogous to Fourier analysis. Figure 5.17 shows the comparison between the raw background template and the FD-smoothed one. No significant bias is seen on the determination of the spurious signal. The spurious signal tests are then performed on the FD-smoothed template, as shown in Fig. 5.18. Comparing to the spurious signal results with raw background template in Fig. 5.16, the spike at 1.4 TeV has been removed and a remarkable reduction in the number of spurious signal is achieved. This is considered as a more precise estimation of the background mismodeling, especially for the regions that initially suffer from large local statistical fluctuations.

Although the PowLog-0 function is already capable of describing the background shape, PowLog-n functions with more degrees of freedom are also tested to see if they

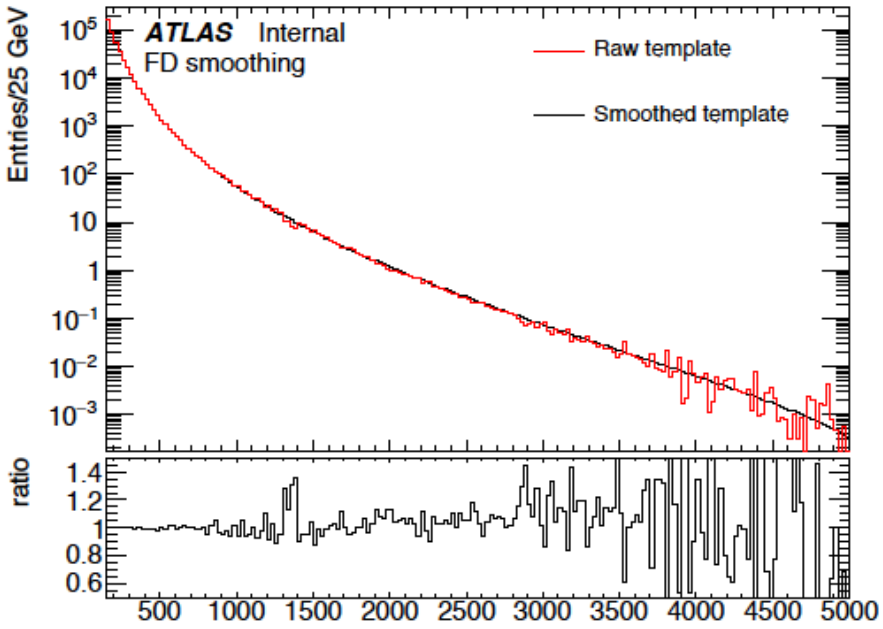

Figure 5.17 – High-mass analysis: comparison of the background template taken from the Sherpa $\gamma\gamma$ MC sample (red) and the template obtained by smoothing using FD (black) in the $m_{\gamma\gamma}$ range [150,4000] GeV. The ratio plot illustrates the relative deviation between the two templates.

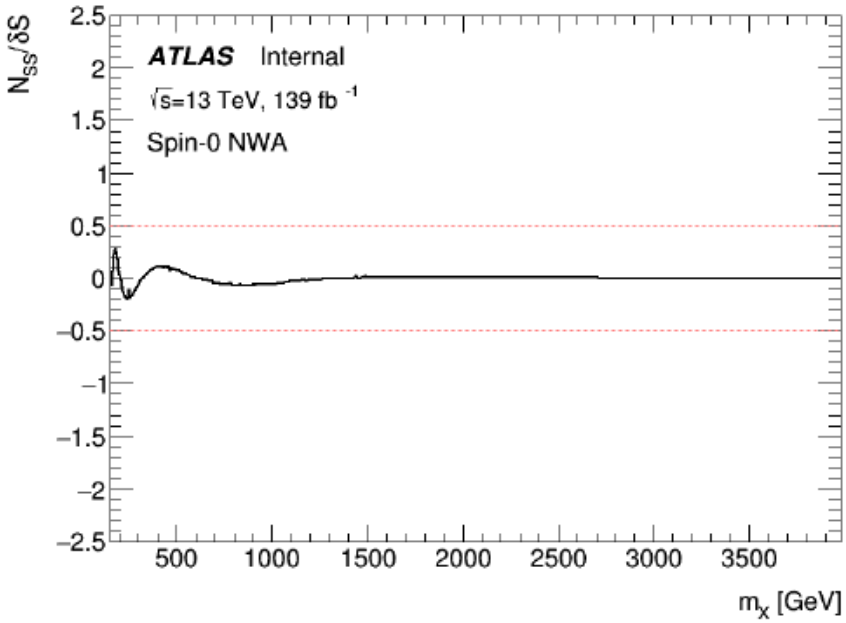

Figure 5.18 – High-mass analysis: spurious signal relative to the statistical uncertainty of the background determined using the NW signal model and the FD-smoothed distribution as the background template. The overall modeling systematic is found to be smaller than 30%, which compares favorably to the more than 50% effect seen in Fig. 5.16.

have the flexibility to capture the systematic variations of the background template. By doing so, a robust estimation of background mismodeling is ensured as the constructed template cannot describe the shape in data perfectly. The PowLog-1 function with three free parameters is chosen as the baseline function after being checked against systematic variations of the background template. It can better adapt to the small changes of the background shape comparing to PowLog-0, and has smallest number of free parameters.

A constant number (the maximum $N_{spurious}$) is taken as the spurious signal systematic uncertainty in the low mass analysis, since the search range is quite limited and the number of spurious signal does not vary much with respect to the diphoton mass. In the high-mass analysis, the spurious signal is parameterized as a function of the diphoton mass in order to estimate the background mismodeling more accurately. The idea is to identify the local maxima in the $|N_{spurious}|$ distribution, and then fit them with a functional form similar to Eq. 5.9 describing an envelope that covers all the possible systematic variations. Parameterization of the spurious signal is performed for all the signal models. As an example, Fig. 5.19 shows the spurious signal estimations for narrow spin-0 resonance with the largest variations: the fraction of $\gamma\gamma$ component, the QCD scales and the PDF variations. The envelope shown in green filled area is the parameterization of the spurious signal uncertainty as a function of diphoton mass. The extracted functions for spin-0 and spin-2 cases are given in Tab. 5.8 and Tab. 5.9. Spurious signal results obtained with all possible variations of the background template are found to be within the envelope. These parameterized functions of the maximum value of the spurious signal at each m_X enter the statistical model as a nuisance parameter.

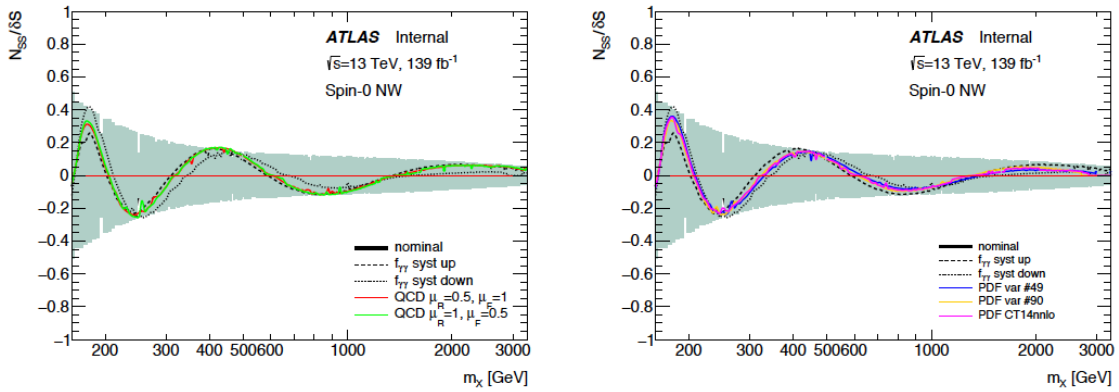

Figure 5.19 – High-mass analysis: spurious signal relative to the statistical uncertainty for the narrow spin-0 resonance, shown for nominal against the $f_{\gamma\gamma}$, QCD scales and PDF systematic variations. The green filled area is the envelope that contains the local maxima of the variations.

Γ_X/m_X	$N_{spurious}(m_X)$
NW	$0.276 \times (1-x^{0.5})^{7.202} \times x^{-2.524-0.808\times log(x)-0.134\times log^2(x)}$
2%	$66.952 \times (1-x^{0.1})^{4.149} \times x^{-1.267} + 24775.411 \times exp(-0.015x)$
6%	$x^{-119.720+51.979\times log(x)-7.681\times log^2(x)+0.381\times log^3(x)}$
10%	$3.718 \times x^{-63.155+27.603\times log(x)-4.215\times log^2(x)+0.222\times log^3(x)}$

Table 5.8 – High-mass analysis: parameterization of the spurious signal in the spin-0 search, $N_{spurious}$, as a function of m_X, obtained for a signal of variable width expressed for the luminosity of the data (139 fb^{-1}). In the functions, $x = \frac{m_X}{\sqrt{s}}$.

$k/\bar{M}_{pl}$	$N_{spurious}(m_X)$
0.01	$7.486 \times (1-x^{1/30})^{2.781} \times x^{-2.014-0.066\times log(x)}$
0.05	$41.487 \times (1-x^{1/30})^{2.819} \times x^{-0.57-0.103\times log^2(x)} + 8.244 \times exp(-0.002x)$
0.1	$76.532 \times (1-x^{1/30})^{2.127} \times x^{0.127-0.120\times log^2(x)} + 16.712 \times exp(-0.002x)$

Table 5.9 – High-mass analysis: parameterization of the spurious signal in the spin-2 search, $N_{spurious}$, as a function of m_X, obtained for a signal of variable width expressed for the luminosity of the data (139 fb^{-1}). In the functions, $x = \frac{m_X}{\sqrt{s}}$.

5.4.2 Resonant background

The following two backgrounds, Drell-Yan background and Standard Model Higgs background are only considered in the low-mass analysis.

Drell-Yan background

Similarly to the method used for the signal shape modeling, the Drell-Yan (DY) background where both electrons are misidentified as photons is modeled using a double-sided Crystal Ball function fitted on a DY background template. In order to estimate the DY background properly, a precise description of the Z peak from the electron background and a correct estimation of the electron fake rate are both important.

The shape of DY background is determined by fitting a dielectron data sample, since the statistic of simulated $Z/\gamma^* \to ee$ sample where both electrons are reconstructed as photons is limited. Both candidates in the dielectron sample are reconstructed and calibrated as electrons, and must pass the same E_T cuts as required in the diphoton analyses. The Tight electron identification is also required. To avoid double counting, electrons overlapping with a photon within a cone $\Delta R = 0.1$ are not selected.

Fake photons in the DY background are generally originated from electrons that lose a non-negligible amount of energy due to bremsstrahlung, leading to a slight shift of the invariant mass distributions between the dielectrons, selected as mentioned

above, and fake photon pairs in the diphoton signal sample. To correct for this effect, a Smirnov transformation is used to represent the difference in kinematics between electrons and fake photons.

Next, the electron template is normalized to the amount of dielectron events faking diphoton events using the electron to photon fake rates[53]. The $e \to \gamma$ fake rate is measured in data using ee and $e\gamma$ events, independently for leading and sub-leading candidates in both converted and unconverted categories. The Smirnov transformation is also applied. The fake rates are measured within a window around the Z peak, and the non-resonant background is subtracted from the transformed ee invariant mass distributions. The fake rate is also measured in $Z \to ee$ simulation as a closure test. Different material variations of the MC sample are also used to estimate the systematic uncertainty on the energy loss due to bremsstrahlung, correlated with the detector material.

Figure 5.20 shows the comparison of the transformation of the simulated ee template with two candidates reconstructed as ee, $\gamma\gamma$ and ee after applying the Smirnov transformation. Good agreement between $\gamma\gamma$ and electron pairs faking photon pairs is observed. The largest uncertainty of the DY background model comes from the normalization ($\pm$9 to 21%), affected by the choice of mass window, the statistic limitation of the available MC sample, the statistical uncertainty from the fits, the background subtraction during fake rate estimation and the generator used for the simulated samples. The uncertainties on the DY shape ($\pm$2 to 3%) and peak position ($\pm$0.1 to 0.2%) are also considered.

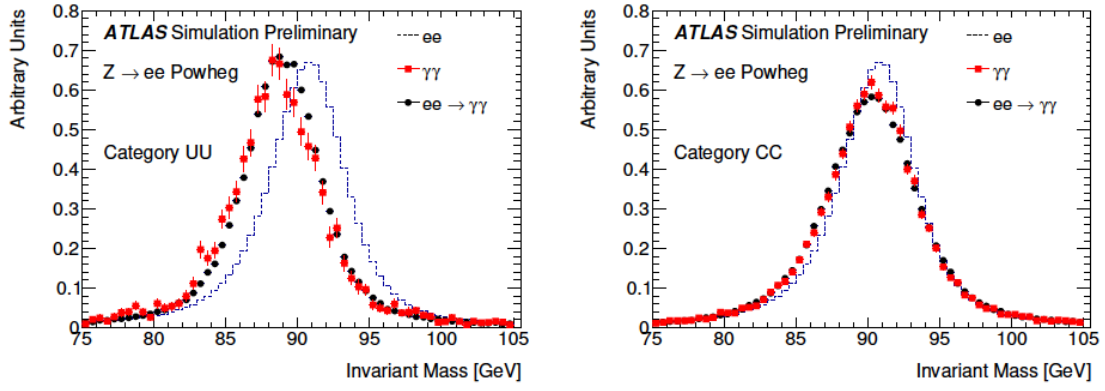

(a) Category UU (b) Category CC

Figure 5.20 – Low-mass analysis: invariant mass distribution in the (a) UU and (b) CC categories for fully simulated $Z \to ee$ events reconstructed as ee (black dotted-lines), $\gamma\gamma$ (red squares) and reconstructed as ee after applying the Smirnov transform (black circles).

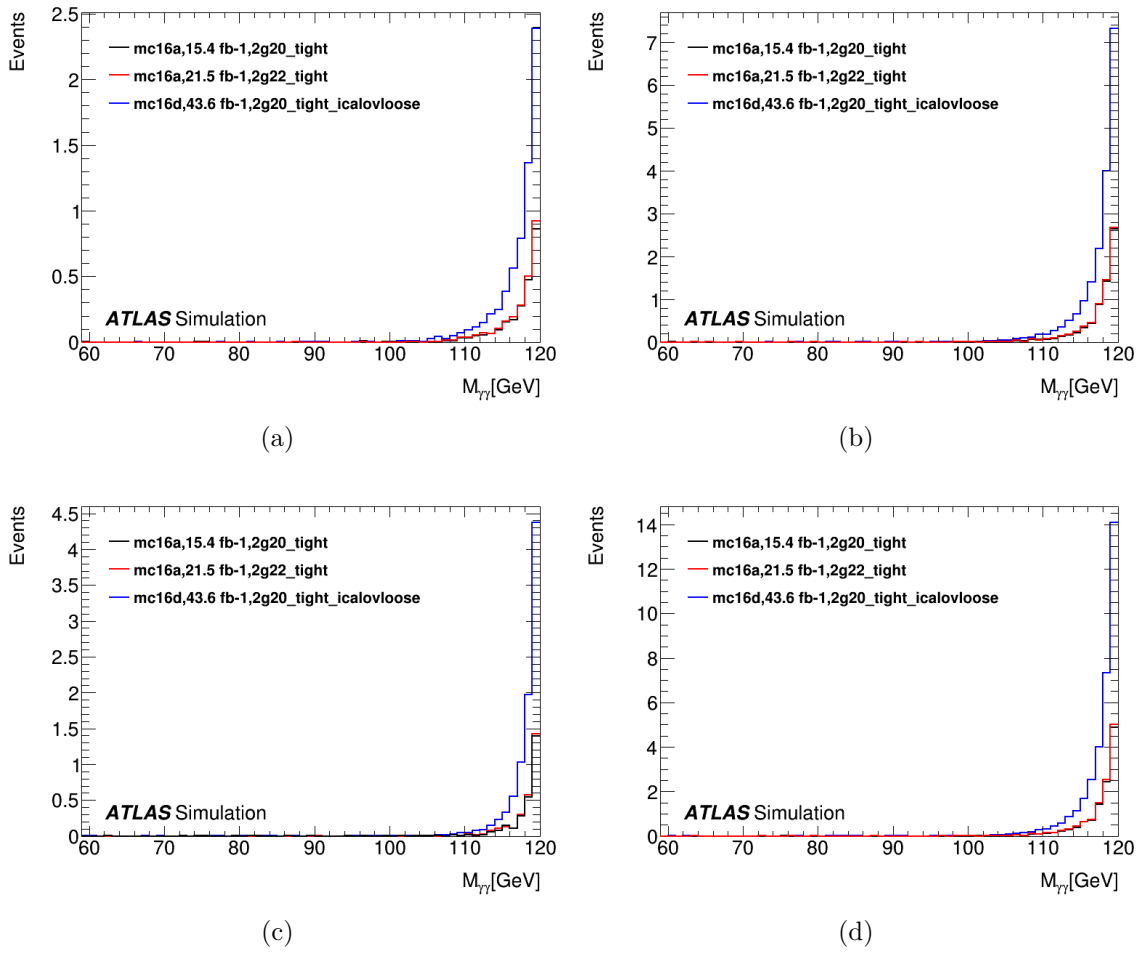

Figure 5.21 – Low-mass analysis: the invariant mass distribution of three Standard Model Higgs MC samples with $60 < M_{\gamma\gamma} < 120$ GeV for the (a) CC. (b) CU. (c) UU. (d) Sum of three categories.

Standard Model Higgs background

The Standard Model Higgs at $m_{\gamma\gamma} = 125$ GeV is a small but peaking background to the low-mass analysis. The $m_{\gamma\gamma}$ distribution of the Standard Model Higgs MC sample in the range 60 to 120 GeV is shown in Fig. 5.21. Its contribution to the total background is estimated from a SM Higgs sample of gluon-gluon fusion production, while other production modes are neglected. After the analysis selection described in Sec. 5.2 is applied, the Standard Model Higgs component is added to the predicted reducible background for each conversion category. Two variables, the bias on background yield due to SM Higgs ($N_{Higgs}/\sqrt{N_{bkg}}$) and the fraction of SM Higgs background ($N_{Higgs}/(N_{Higgs}+N_{bkg})$) are calculated to estimate the impact of the additional resonant background, where N_{Higgs} and N_{bkg} are the numbers of the SM Higgs and the $\gamma\gamma+\gamma j$ background events ($Z \to ee$ background is not considered). The results are shown in Fig. 5.22 and Fig. 5.23. From the study, one can see that the SM Higgs

amounts to less than 0.35% of the total background in all bins. Therefore, this SM Higgs contamination is neglected when the final background template is built.

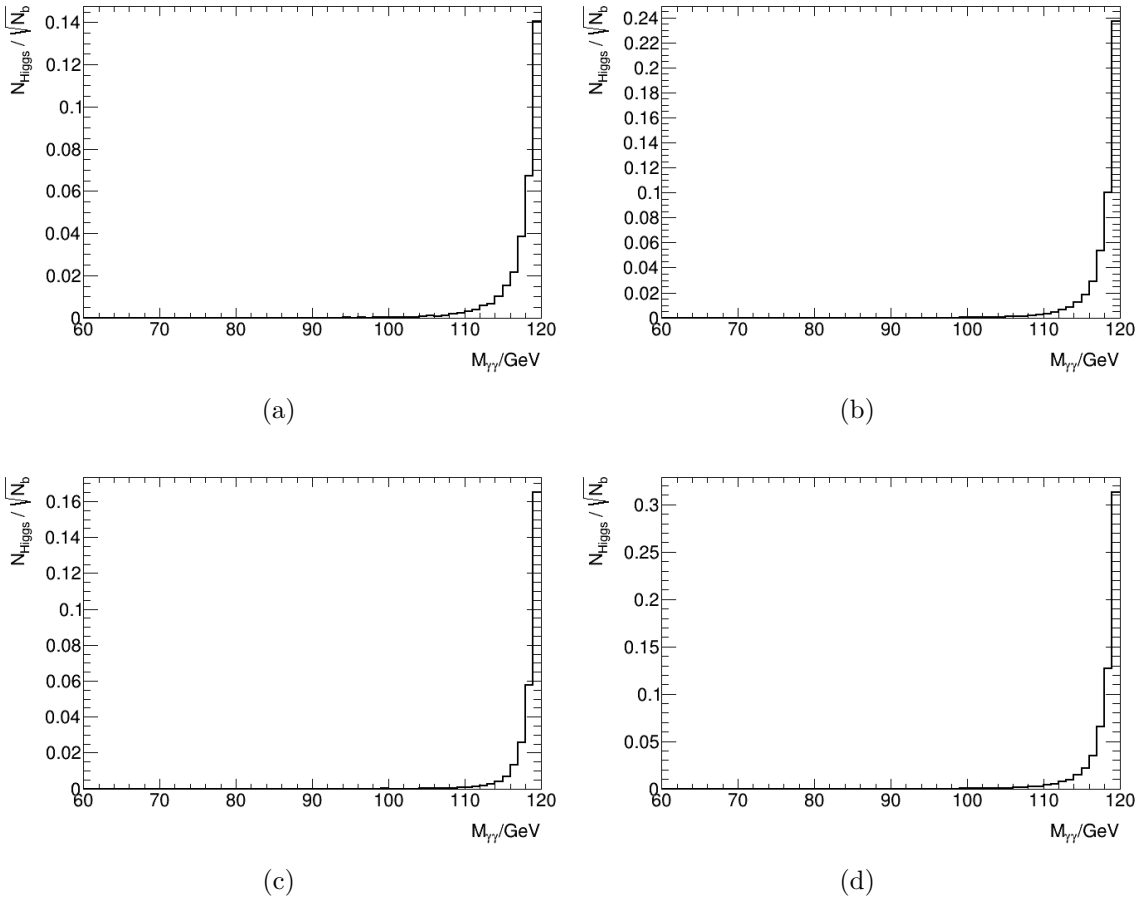

Figure 5.22 – Low-mass analysis: the backgrounds bias due to Standard Model Higgs for the (a) CC. (b) CU. (c) UU. (d) Sum of three categories.

5.4.3 Background modeling results

The background-only fit of the data for the low-mass analysis is shown in Fig. 5.24, the three conversion categories are shown in different colors. As expected, the Drell-Yan contribution is significant in the CC category. No abnormal structure is seen in the residuals.

The background-only fit of the data for the high-mass analysis is shown in Fig. 5.25 in both log and linear y-axis. The fit quality is check excluding the mass region above 1.4 TeV due to the limitation of statistics (bins with too few entries tend to bias the estimation), $\chi^2/N_{dof} = 37.2/54$ is found.

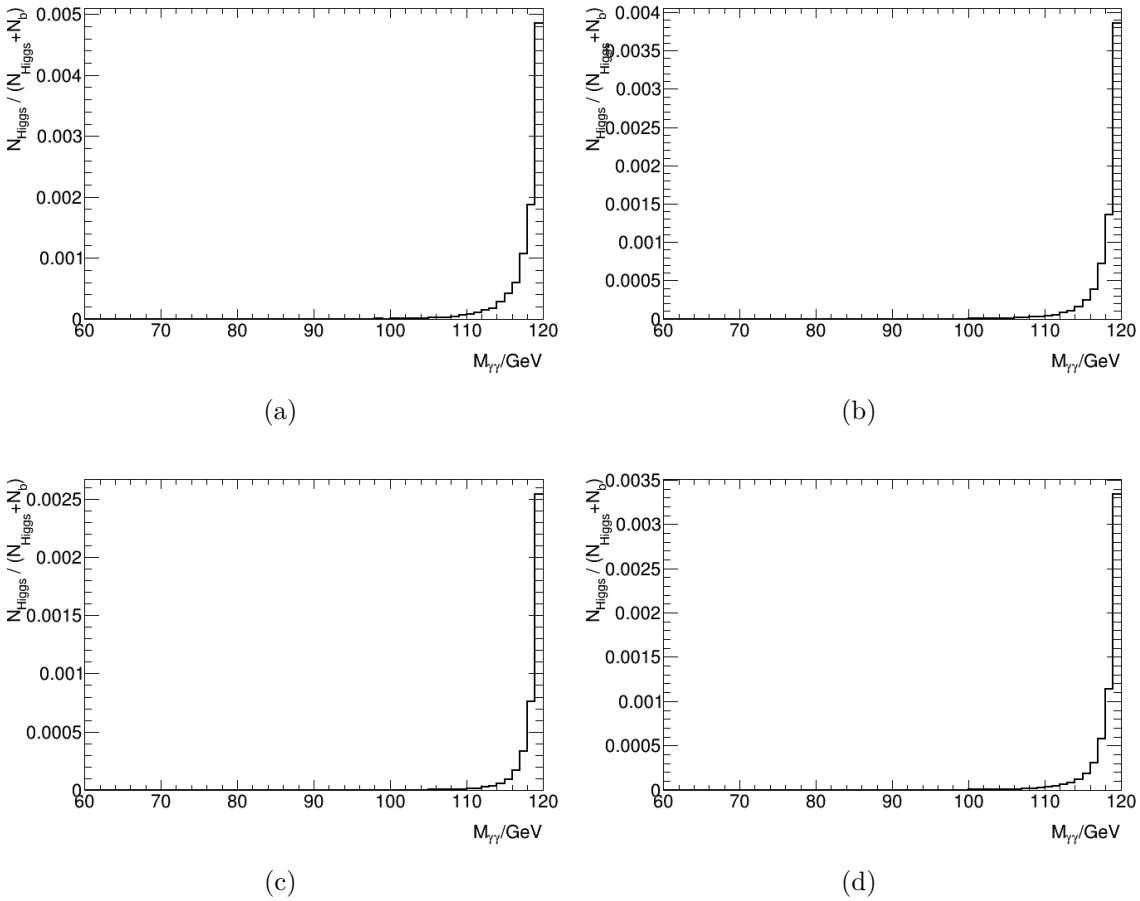

Figure 5.23 – Low-mass analysis: Fraction of Standard Model Higgs in the total background. (a) CC. (b) CU. (c) UU. (d) Sum of three categories.

5.5 Fiducial and total acceptance corrections

The analysis strategy goes as following: for the spin-0 search, the aim is to provide model-independent results by setting limits on the fiducial cross section. For the spin-2 search in the high-mass analysis where a warped extra-dimension model is taken as a benchmark model, the aim is to set limits on total cross section, which can be directly compared with theory. In general, the total cross section for process $pp \to X \to \gamma\gamma$ can be expressed as:

$$\sigma_X \cdot \mathscr{B}(X \to \gamma\gamma) = \frac{N_{sig}^{reco}}{C_X \cdot A_X \cdot L_{int}} \tag{5.11}$$

where $\mathscr{B}$ is the branching ratio, N_{sig}^{reco} is the measured reconstruction level signal yield, L_{int} is the integrated luminosity. A_X and C_X are correction factors obtained from simulation samples, which are needed to translate the measured yields in terms of cross section. A_X is the acceptance of the fiducial volume, which is used to extrapolate measurements that are performed in a restricted kinematic phase space (limited by the acceptance of the detector) to the full phase space. C_X is the correction factor

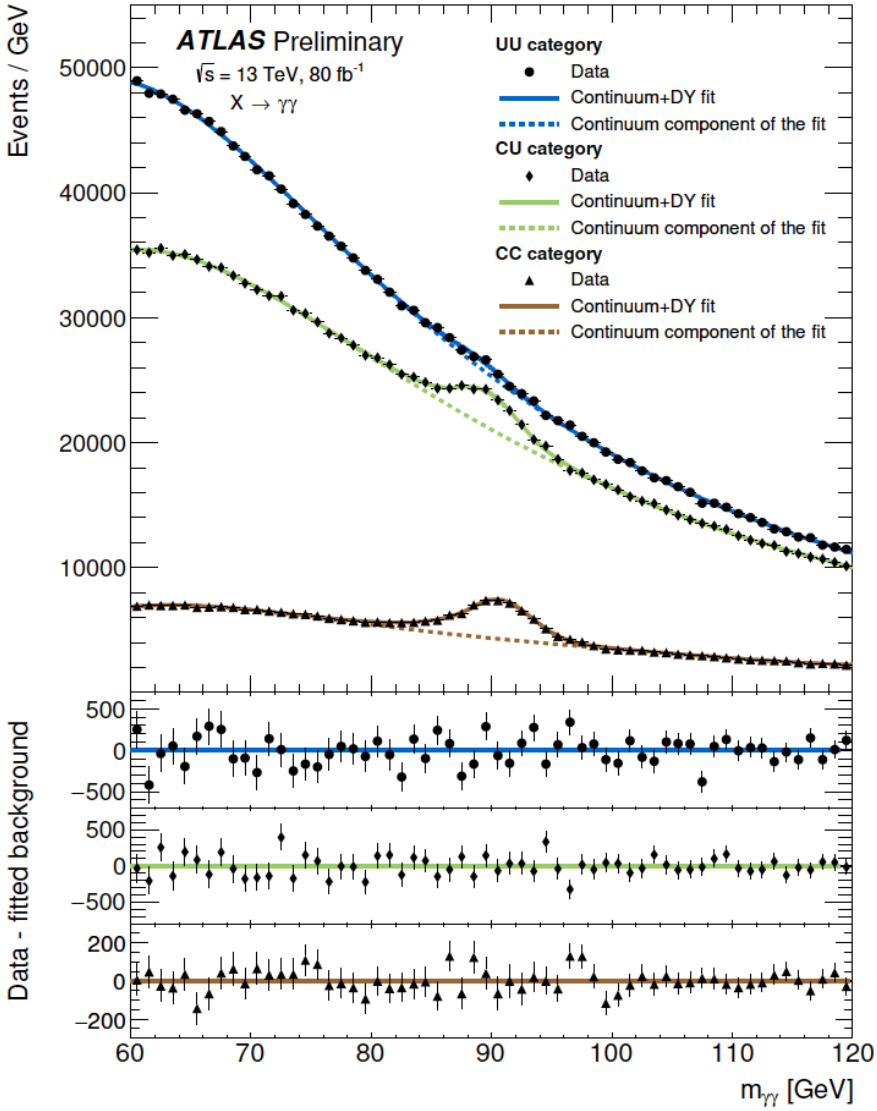

Figure 5.24 – Low-mass analysis: background-only fit to the data (black markers) as a function of the diphoton invariant mass $m_{\gamma\gamma}$ for the three conversion categories. The solid lines show the sum of the Drell-Yan and the continuum background components, the dashed lines show only the continuum background components. The difference between the data and the total background component is shown at the bottom separately for each category.

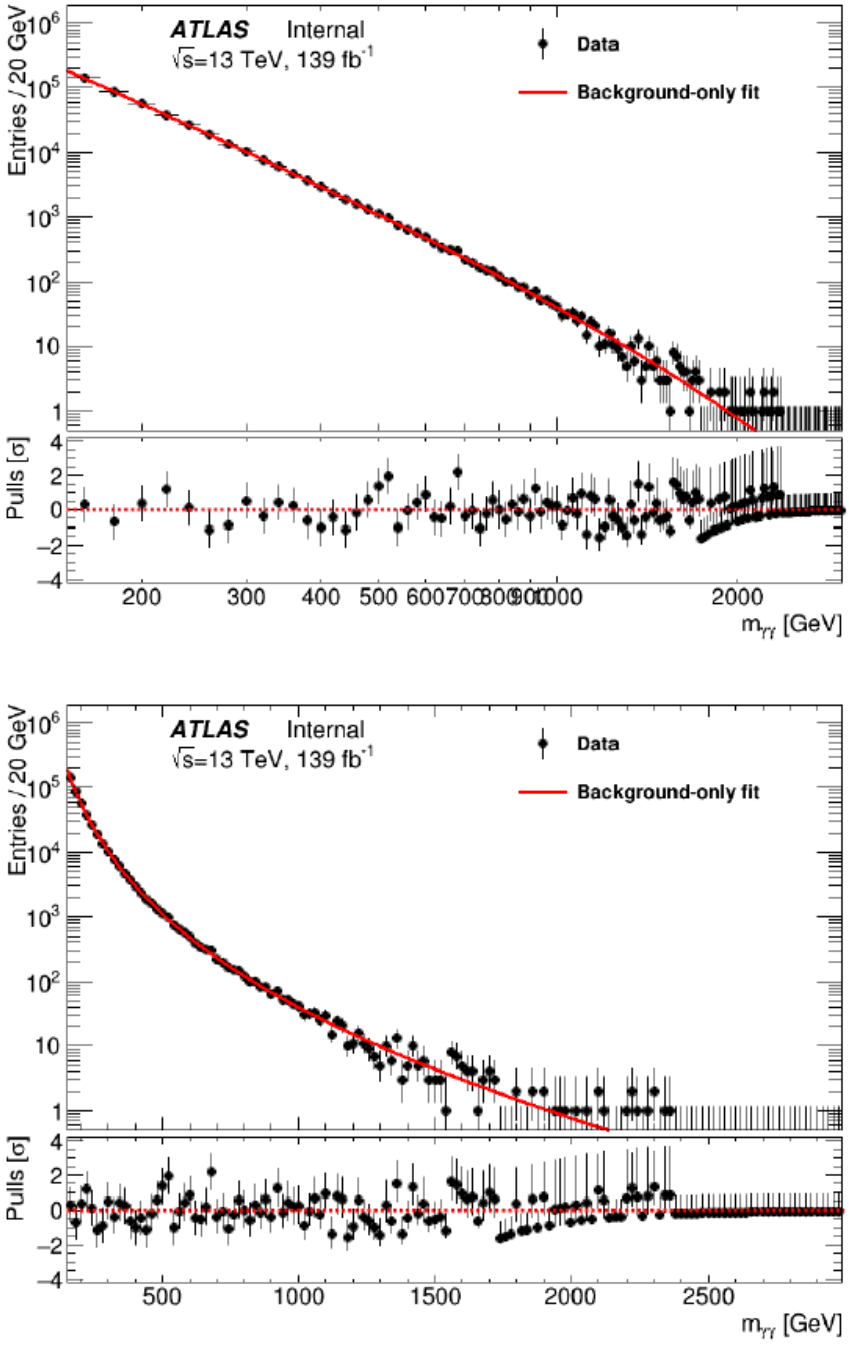

Figure 5.25 – High-mass analysis: background-only fit to the data (black markers) as a function of the diphoton invariant mass $m_{\gamma\gamma}$. The normalized residuals between the data and the fit is shown in the bottom panel. There is no data event with $m_{\gamma\gamma} > 2400$ GeV.

for detector effects on events that fall into the fiducial volume of the analysis, defined by the geometrical acceptance of the detector and the accessible kinematic phase space. The C_X factor is used to correct for reconstruction, identification and selection efficiencies, as well as the migrations in and out of the fiducial volume.

The acceptance is highly model-dependent, since the kinematics of the hypothetical signal can change dramatically with respect to various theory assumptions. For the spin-0 analysis, to reduce the dependence on specific models, the fiducial cross section is measured, which is given by:

$$\sigma_{X,fid} \cdot \mathscr{B}(X \to \gamma\gamma) = \frac{N_{sig}^{reco}}{C_X \cdot L_{int}} \tag{5.12}$$

The results are determined only with respect to the phase space which is accessible by the detector. In this case, only the C_X factor is included. The model dependence of C_X factor is rather small, since the detector efficiencies are rather stable with respect to the photon kinematics. The remaining model dependency that might affect the signal yield is included in systematic uncertainty, which will be introduced later.

5.5.1 Fiducial volume and correction factor

In order to minimize the model dependence, the fiducial volume defined at truth level is designed to closely match the experimental acceptance of the measurement, given by the geometrical acceptance of the detector, the reconstruction conditions and any other kinematic analysis selections. Therefore, the fiducial volume is defined by kinematic cuts applied on the truth level photon variables that mimic the selections applied at the reconstruction level.

The kinematic cuts applied on truth photon variables are basically the same as in Sec. 5.2. For low-mass search, both photons should be within $|\eta| < 2.37$, excluding the transition region $1.37 < |\eta| < 1.52$ between the barrel and the end-cap calorimeters. Both photons are required to have transverse energies above 22 GeV. For high-mass search, both photons should be within $|\eta| < 2.37$ but including the transition region for simplicity. The relative E_T cuts for leading and sub-leading photons, $E_T/m_{\gamma\gamma} > 0.3$ and $E_T/m_{\gamma\gamma} > 0.25$, are also applied.

In addition, the reconstructed photons tend to have larger calorimeter isolation energy (leading to lower selection efficiency) if the resonance is produced in association with many high E_T jets. Therefore, truth-level isolation requirement is also applied to further reduce the production dependence. For low-mass search, the truth-level isolation is defined as the scalar sum of the transverse energy of all the stable particles (except neutrinos and muons) found within a $\Delta R = 0.2$ cone around the true photon, namely *etcone*20. The truth-level isolation requirement is $etcone20 < 0.065 E_T$ (GeV), which is the loose calorimeter-only isolation requirement. A similar variable *etcone*40

is used for high-mass search with a cone size $\Delta R = 0.4$. The isolation requirement is $etcone40 < 0.05(E_T + 120)$ GeV.

The C_X factor is defined as:

$$C_X = \frac{N_{selection}}{N_{fiducial}} \tag{5.13}$$

where $N_{selection}$ is the number of reconstructed signal events that pass the analysis selection, $N_{fiducial}$ is the number of signal events generated within the fiducial volume. The compution of C_X factor is performed for all available production modes and values of resonance mass. A function is then fitted to the results in order to provide the interpolation between mass points, as shown in Figs. 5.26 and 5.27 for low-mass and high-mass results respectively. In a wide mass range, the difference of the computed C_X factor between the different production modes is relatively small. The C_X factor drops above 1 TeV, which is mainly caused by the decrease in the photon identification efficiency at very high transverse energy.

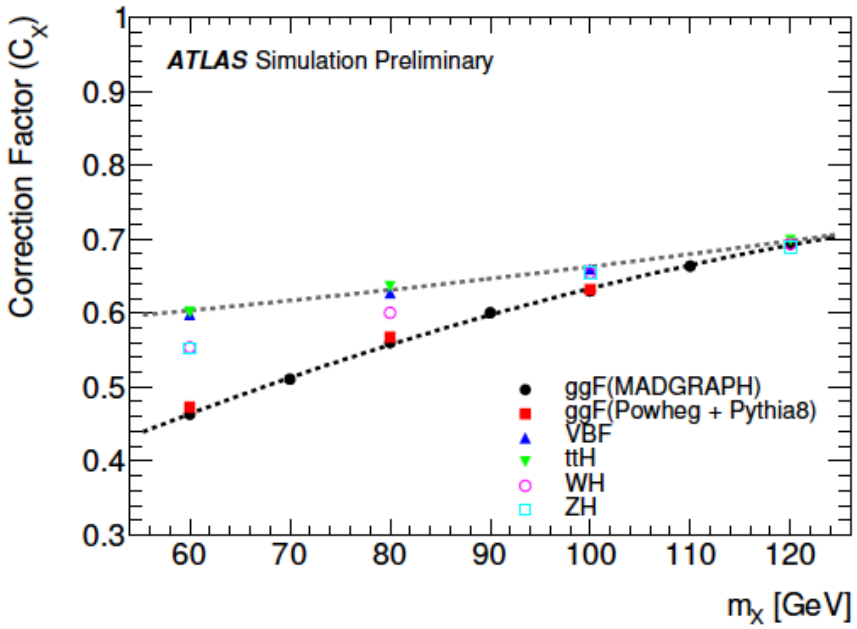

Figure 5.26 – Low-mass analysis: the C_X factor as a function of m_X for different production modes in the low-mass range. The dashed black line represents the parameterization of the nominal ggF mode and the dashed gray line represents the parameterization of the maximal deviation from the nominal values.

5.5.2 Acceptance factor

The A_X factor is defined as:

$$A_X = \frac{N_{fiducial}}{N_{total}} \tag{5.14}$$

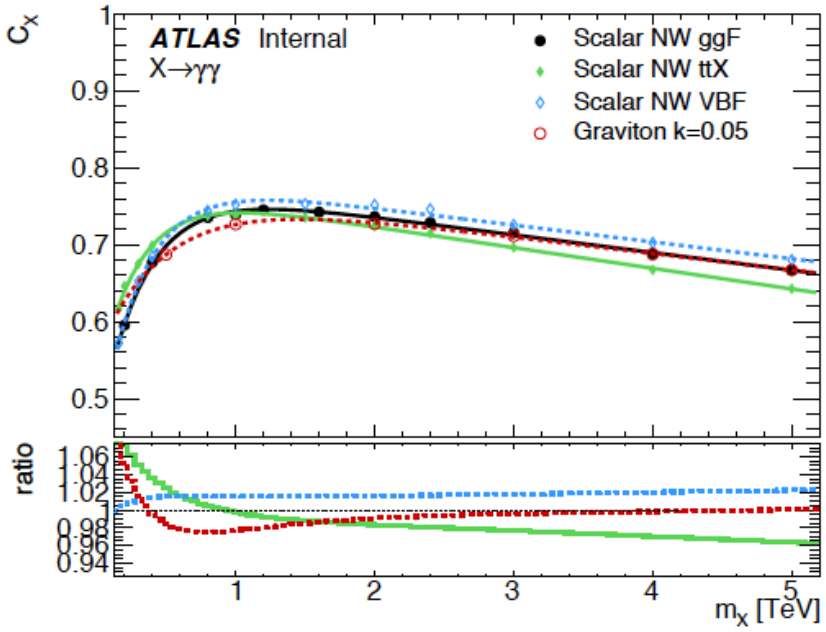

Figure 5.27 – High-mass analysis, spin-0 search: the C_X factor as a function of m_X for different production modes in the high-mass range. The lines illustrate the interpolation fits for each production mode, while the bottom panel illustrates the ratio of the C_X factor determined in a given production mode to the baseline prediction from the ggF production mode.

where N_{total} is the total number of the generated signal events, $N_{fiducial}$ is the number of events that pass the fiducial selection. The A_X factor is used for the calculation of total cross section in spin-2 search, and is also provided in spin-0 search so that the results determined with respect to a restricted phase space can be reinterpreted to the total phase space. Figures 5.28 and 5.29 show the determination of A_X for the different production modes, as a function of m_X for the two analyses. The acceptance correction can vary by up to 30% between the different production modes.

Finally, the total acceptance-times-efficiency-correction factor, $C_X \cdot A_X$, is actually used in the spin-2 graviton search for the projection to the total cross section. It is defined as:

$$C_X \cdot A_X = \frac{N_{selection}}{N_{total}} \tag{5.15}$$

The results as a function of m_{G*} for different coupling hypotheses are given in Fig. 5.30. Parameterization of the $C_X \cdot A_X$ factor is given by a simple exponential function.

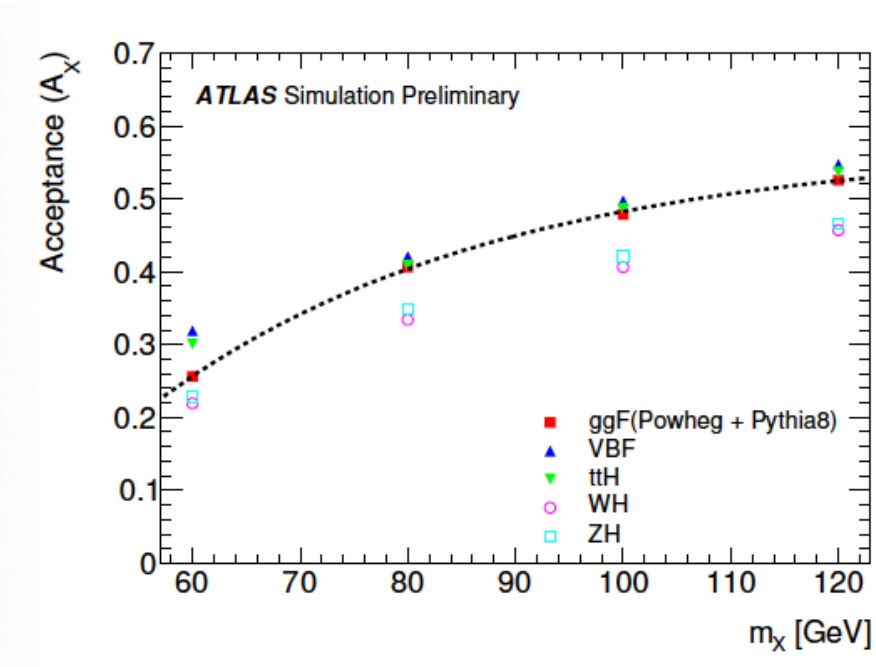

Figure 5.28 – Low-mass analysis: the A_X factor as a function of m_X for different production modes. The dashed black line represents the parameterization of the nominal ggF mode.

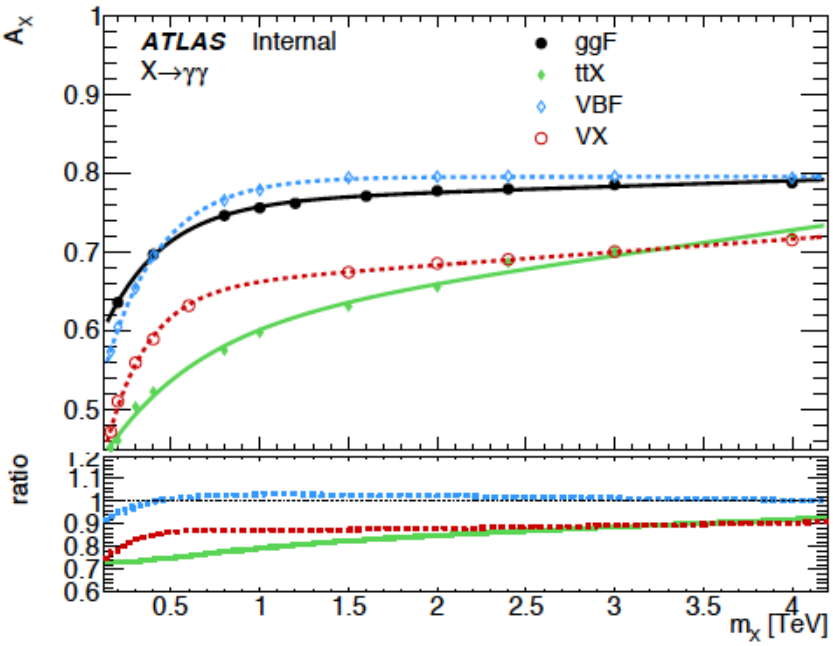

Figure 5.29 – High-mass analysis, spin-0 search: acceptance correction factor for different production modes of the scalar narrow width signal. The lines illustrate the interpolation for each production mode. The bottom panel illustrates the ratio of the A_X factor for a given production mode to the corresponding one from ggF production mode.

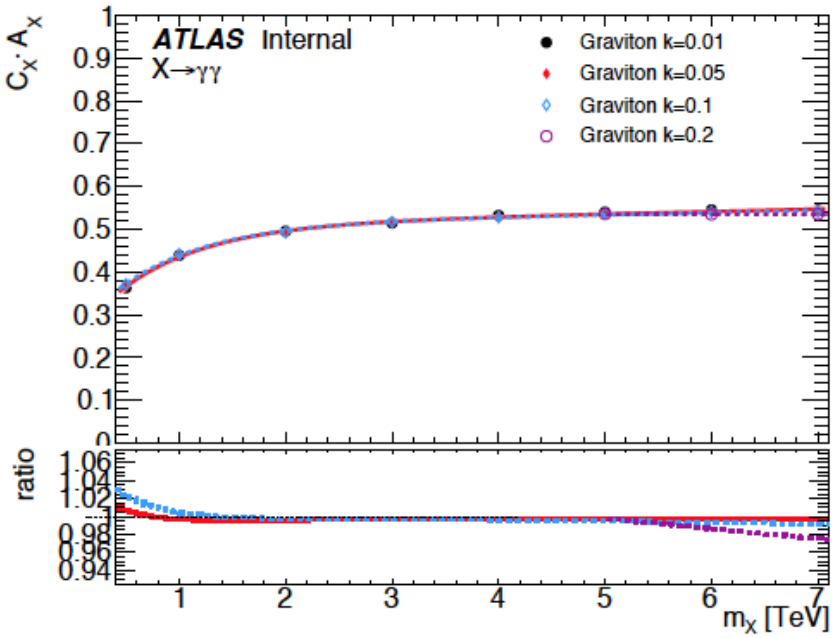

Figure 5.30 – High-mass analysis, spin-2 search: total efficiency-times-acceptance, $C_X \cdot A_X$, computed using the MC simulation samples for various graviton signals assuming different k/M_{pl} hypotheses. The $C_X \cdot A_X$ factors for the different width hypotheses considered in the simulation are all found to follow a similar trend as a function of m_{G*}.

5.6 Systematic uncertainties

The relevant sources of systematic uncertainty are discussed and summarized in this section, including experimental and fit uncertainties from both signal and background modeling. The sources affecting the signal yields (Sec. 5.6.1) and the modeled signal shape (Sec. 5.6.2) are the same for the low-mass and high-mass analyses. The uncertainties on background modeling is summarized in Sec. 5.6.3. Specially, the migration between the three conversion categories in low-mass analysis is quantified in Sec. 5.6.4. Summary tables of the different sources of the systematic uncertainty for the two analyses are given in Sec. 5.6.5.

5.6.1 Signal modeling uncertainties

The energy resolution and energy scale are the most relevant sources of the systematic uncertainty in signal modeling. The uncertainty on the photon energy scale shifts the peak position of the modeled signal (Δm_X). The uncertainty on the energy resolution mainly impacts the width of the distribution (σ_{CB}). In order to determine the effects of the photon energy scale and resolution, the signal MC events are reprocessed using the photon energy scale and energy resolution smearing, and the shift in Δm_X and the variation on σ_{CB} are estimated. The estimation of the uncertainties on signal modeling is done separately in each conversion categories.

For the energy scale, the relative difference of the mean value of the modified and nominal $m_{\gamma\gamma}$ distributions at given m_X is parameterized, and taken as the energy scale uncertainty. The value is found to be about 0.6% for the high-mass analysis, and between 0.3% to 0.5% for the low-mass analysis.

The energy scale variation also affects the resolution, but it is proved to be quite small and can be safely neglected. Similarly, the difference of the width of the modified and nominal distributions at given m_X is taken as the energy resolution uncertainty. This value is highly correlated to the photon mass. It varies from $^{+17\%}_{-12\%}$ to $^{+51\%}_{-29\%}$ as a function of m_X, in the mass range from 200 GeV to 2 TeV. For low-mass analysis below 110 GeV, it is found to be between 2% to 8%.

The narrow-width signal models are extracted using gluon-gluon fusion MC samples. Therefore, a closure test is used to check the impact of the unknown production mode. Pseudo-datasets are used for this test, with a background component generated from the background function (parameters fixed to the result of a background-only fit to the background template), and a signal component from the $m_{\gamma\gamma}$ distribution in signal MC sample of the tested production mode. The background is normalized to the data yield, and the signal is normalized to the expected 2σ upper limit on the fiducial cross section. Two production modes, gluon-gluon fusion and associated production with top quark pair (ttH) are compared, since they have the most different kinematic distributions. The nominal gluon-gluon fusion signal model is used to fit the pseudo-datasets, and

the bias on the signal yield is taken as the systematic uncertainty associated to the production mode. This bias is mass-dependent: it is found to be up to 6% at low mass, and reduced to about 0.5% at 800 GeV. By repeating the fit with nuisance parameters for the uncertainties on the energy resolution and scale, the bias becomes even smaller. It means that any potential bias on the signal yields due to the hypothetical signal production mode is sufficiently covered by the experimental systematic uncertainties on the signal modeling (especially energy resolution), therefore no additional uncertainty is needed.

5.6.2 Signal yield uncertainties

The uncertainties on signal yields are derived from different sources that are associated with the experimental conditions and the hypothetical signal production process. The details of these sources are given below, and the size of each uncertainty is summarized in the next section.

Production process

As the spin-0 analysis has no assumption on the production modes (of the hypothetical scalar signal), the correction factor can be changed significantly according to the given production mode with different kinematics, as mentioned in Sec. 5.5. Therefore, a systematic uncertainty is assign to account for this effect by taking the envelope of the difference in the correction factor obtained from different production modes.

Photon identification

Data-driven methods are used to measure the photon identification efficiency, which is used to compute the scale factors (data-to-MC ratios). The up and down uncertainty of the scale factors are propagated to the analysis by applying the corresponding variation.

Photon isolation

The uncertainty from the photon isolation efficiency comes from the contribution of both calorimeter-based isolation and track-based isolation. The associated uncertainty on the signal yield is obtained by applying a data-driven shift to the calorimeter isolation, and a p_T dependent shift to the track isolation[69]. The shifts on the correction factor from these two parts are calculated separately and combined in quadrature.

Photon trigger

A bootstrap method[70] is used to estimate the diphoton trigger efficiency. The uncertainty of this estimation is taken to be the systematic uncertainty associated with photon trigger.

Pile-up reweighting

Pile-up reweighting is applied to the simulated samples in order to cover the difference between the predicted and actually measured distributions of the average number of pp interactions per bunch crossing ($<\mu>$). The uncertainty associated with the pile-up reweighting is obtained by shifting the distribution of $<\mu>$ before is was used to reweight the MC sample.

Photon energy scale and resolution

The photon energy resolution and energy scale uncertainties could also impact the correction factor, as they may cause migrations in and out of the fiducial volume of the detector. These effects are estimated using the up and down variations of energy scale and resolution similarly as in Sec. 5.6.1, and are found to be insignificant comparing to other sources.

Luminosity

As mentioned in Sec. 5.1, the uncertainty of the integrated luminosity is propagated to the analyses.

5.6.3 Background modeling

As mentioned in Sec. 5.4.1, the parameterized number of the spurious signal enters the statistical model as a nuisance parameter. It is added as a variation of the signal yield that is described by a Gaussian distribution of mean equal to zero, and width equal to the parameterized value at given m_X. This is the dominant source of systematic uncertainty in the low-mass analysis, while its impact is much smaller in the high-mass analysis thanks to the Functional Decomposition process. In addition, the uncertainty coming from the imperfect modeling of the Drell-Yan background in the low-mass analysis is described in Sec. 5.4.2.

5.6.4 Migration between categories

In the low-mass analysis, an additional systematic uncertainty is assigned to take into account the migration between the three conversion categories. Since the conversion of photons is related to the amount of material upstream of the calorimeter,

this uncertainty is estimated by comparing the number of recorded events in each category in simulated single photon samples with alternative detector geometries. The fraction of converted photons f_{conv} is measured in the distorted samples and used to compute the fraction of each category (f_{UU}, f_{CC} and f_{UC}). The number of events in each category computed with nominal and alternative samples are compared and the slightly mass-dependent difference is taken as systematic uncertainty.

5.6.5 Systematics uncertainties summary

The main sources of the systematic uncertainties are summarized in Tab. 5.10 for the low-mass analysis, and in Tab. 5.11 for the high-mass analysis. The dominant impact comes from the imperfectly estimated spurious signal (background modeling) systematics for the low-mass analysis, making this analysis systematics-limited. For the high-mass analysis, thanks to the Functional decomposition method, the size of spurious signal is much smaller. The largest systematic uncertainty comes from the photon energy resolution during signal modeling.

5.7 Statistical method

5.7.1 Profile log-likelihood ratio method

In the resonance searches, the numbers of signal and background events in the selected data sample are estimated from maximum-likelihood fits, using an extended profile likelihood to incorporate the systematic uncertainties. For a set of measured quantities $x = (x_1, x_2, ..., x_n)$, the extended likelihood of the given dataset is:

$$L(\mu, \theta|x) = e^{-n} \prod_{i=1}^{n} [s(\mu) \cdot f_s(x_i;\theta) + b \cdot f_b(x_i;\theta)] \tag{5.16}$$

where f_s and f_b are the probability density functions (pdf) of the signal and background, $s(\mu)$ and b are the number of signal and background events respectively. μ is the parameter of interest, in this case is the cross section.

To test a hypothetical value of μ, the profile likelihood ratio (PLR) is constructed as:

$$\lambda(\mu) = \frac{L(\mu, \hat{\hat{\theta}}(\mu))}{L(\hat{\mu}, \hat{\theta})} \tag{5.17}$$

where $\hat{\mu}$ and $\hat{\theta}$ are the values of the parameters that maximize the likelihood function ("best fit" values), and $\hat{\hat{\theta}}(\mu)$ is the value of θ that maximizes the likelihood

Table 5.10 – Low-mass analysis: summary of the main sources of systematic uncertainty on the limit on the fiducial cross seciton.

Source	Uncertainty
Signal yield	
Luminosity (2015-2017)	$\pm 2.0\%$
Trigger	$\pm 1.4 \sim 1.7\%$, mass dependent
Photon identification	$\pm 1.5 \sim 2.3\%$, mass dependent
Isolation efficiency	$\pm 4\%$, mass dependent
Pile-up reweighting	$\pm 1.8 \sim 4.1\%$, mass dependent
Scalar production process	$\pm 2.4 \sim 25\%$, mass dependent
Photon energy scale	$\pm 0.13 \sim 0.49\%$, mass dependent
Photon energy resolution	$\pm 0.053 \sim 0.28\%$, mass dependent
Signal modeling	
Photon energy resolution	$\pm 2 \sim 8\%$, mass and category dependent
Photon energy scale	$\pm 0.3 \sim 0.5\%$, mass and category dependent
Migration between categories	
Material	$-2.0/+1.0/+4.1\%$, category dependent
Non-resonant background modeling	
Maximum spurious signal	604/496/181 events, mass and category dependent
DY background modeling	
Peak position	$\pm 0.1 \sim 0.2\%$, category dependent
Template shape	$\pm 2 \sim 3\%$, category dependent
Normalization	$\pm 9 \sim 21\%$, category dependent

Table 5.11 – High-mass analysis: summary of the main sources of systematic uncertainty on the limit on the fiducial and total cross seciton. The spurious signal (background modeling uncertainty) is obtained from a mass parametrization (Tab. 5.8 and 5.9). The number of spurious signal for a narrow- (large-) width resonance at given mass point are quoted here.

Source	Uncertainty
Signal yield	
Luminosity (2015-2018)	$\pm 1.7\%$
Trigger	$\pm 0.5\%$
Photon identification	$\pm 0.5\%$
Isolation efficiency	$\pm 1.5\%$
Pile-up reweighting	$\pm(2 \sim 0.2)\%$, mass dependent
Scalar production process	$\pm(7 \sim 3)\%$, mass dependent
Photon energy scale/resolution	negligible
Signal modeling	
Photon energy resolution	$^{+17\%}_{-12\%}$ (at $m_X = 200$ GeV) $\sim$ $^{+51\%}_{-29\%}$ (at $m_X = 2$ TeV)
Photon energy scale	$\pm 0.5\% \sim \pm 0.6\%$, mass dependent
Pile-up reweighting	negligible
Background modeling, spin-0	
NWA	114–0.04 events (m_X =160-2800 GeV)
$\Gamma_X/m_X = 2\%$	107–0.14 events (m_X =400-2800 GeV)
$\Gamma_X/m_X = 6\%$	223–0.38 events (m_X =400-2800 GeV)
$\Gamma_X/m_X = 10\%$	437–0.50 events (m_X =400-2800 GeV)
Background modeling, spin-2	
$k/\bar{M}_{pl} = 0.01$	4.71–0.04 events (m_{G^*} =500-2800 GeV)
$k/\bar{M}_{pl} = 0.05$	19.00–0.09 events (m_{G^*} =500-2800 GeV)
$k/\bar{M}_{pl} = 0.1$	31.20–0.20 events (m_{G^*} =500-2800 GeV)

function when μ is fixed (conditional maximum likelihood estimator). The test statistic is given as:

$$t_\mu = -2\ln\lambda(\mu) \tag{5.18}$$

The likelihood ratio is always between 0 to 1,[7] while 1 indicates that the data and the hypothetical μ are in good agreement. By definition, t_μ is always positive.

5.7.2 Discovery p-value

The compatibility of the given dataset with the background-only hypothesis (or null hypothesis, $\mu = 0$) is quantified by the p-value. The probability, under the null hypothesis assuming that no signal is present, of obtaining a signal yield at least as large as the observed one is denoted as p_0. Large value of p_0 suggests that the datasets agrees more with the background-only hypothesis, while small p_0 suggests a significant positive signal.

The one-sided test statistic is defined as:

$$t_0^{uncap} = \begin{cases} -2\ln\dfrac{L(0,\hat{\hat{\theta}}(0))}{L(\hat{\mu},\hat{\theta})}, \hat{\mu} \geq 0, \\ +2\ln\dfrac{L(0,\hat{\hat{\theta}}(0))}{L(\hat{\mu},\hat{\theta})}, \hat{\mu} < 0. \end{cases} \tag{5.19}$$

and the p-value of the null hypothesis is computed as:

$$p_0 = \int_{t_{0,obs}}^{\infty} f(t_0|0)dt_0 \tag{5.20}$$

where $t_{0,obs}$ is the test statistic observed in data, and $f(t_0|0)dt_0$ is its pdf. The observed value of t_0 will be large in the presence of a signal.

In the asymptotic regime[71], one can directly compute p_0 from the test statistic using asymptotic formulae. Otherwise, p_0 should be computed by sampling the distribution of the test statistic in the null hypothesis using pseudo-experiments, which is the case for the high-mass end of the search region (above 2.3 TeV).

The discovery p-value can also be expressed as a Gaussian significance Z, defined as:

$$Z = \Phi^{-1}(1 - p_0(t_0^{uncap})) \tag{5.21}$$

where Φ is the cumulative distribution function of a standard Gaussian, of which the upper tail integral equals to the p-value. Usually, one can claim a discovery only with 5σ significance.

[7] Usually, only $\mu \geq 0$ is considered as a valid "physical" signal. However, as long as the pdf is positive, $\mu < 0$ is also allowed. $\hat{\mu} < 0$ corresponds to negative fluctuations in data with respect to the background-only hypothesis.

5.7.3 Look-elsewhere effect

In the high-mass analysis, as the search is performed in a quite large mass range, one needs to consider what is the probability to have a fluctuation as (or bigger than) the observed one anywhere in the search range, namely the "look-elsewhere effect"[72].

When scanning the wide range in search for resonances, the p-value obtained at a given m_X and width is called the local p-value, corresponding to local significance Z_0^{local}. Instead, the global p-value and significance are more relevant as they take into account the possibility of background fluctuation occurring anywhere in the test. There are multiple ways to compute the global significance. For a simple 1D p-value scan, once a reference level of p-value is given (usually $p = 0.5$, "0σ level"), the asymptotic formula[73] is given as:

$$p_{global} = p_{local} + N_{up} e^{-1/2(Z_{local}^2 - Z_{ref}^2)} \tag{5.22}$$

where N_{up} is the number of upcrossings of the p-value curve that crosses the reference level p-value, and Z_{ref} is the significance corresponding to the chosen reference level of p-value. The statistical uncertainty on the global p-value is obtained by varying N_{up} by $\pm\sqrt{N_{up}}$. Eq. 5.22 also has multidimensional form.

However, a more straightforward and reliable way is to run background-only pseudo-experiments generated from the signal and background function fitted on the observed data and the profiled values of the nuisance parameters. For the generation of each pseudo-experiment, the global observables (e.g. background function parameters) are randomized according to a Gaussian constraint pdf with a mean value equal to the profiled value of the corresponding nuisance parameter. Values of the experimental observables (e.g. $m_{\gamma\gamma}$ and N) are generated randomly from the background-only pdf and the Poisson probability distribution.

In order to determine the maximum Z_0^{local}, one could perform fits for every possible mass and width hypothesis, determine the Z_0^{local} value at each point, and find the maximum value. As this approach is computationally intensive, alternatively, a number of maximum-likelihood fits are performed on each pseudo-dataset. The initial values of the parameters of the interest (e.g. signal mass, width and cross section) are randomized within the signal search range. The fit giving the minimum negative log-likelihood value is assumed to correspond to the maximum Z_0^{local}.

From the distribution of Z_0^{local} ($H(Z_0^{local})$), the Z_0^{global} for a given $Z_0^{local,obs}$ is computed by integrateing the observed Z_0^{local} to infinity:

$$Z_0^{global,obs} = \int_{Z_0^{local,obs}}^{\infty} H(Z_0^{local}) dZ_0^{local} \tag{5.23}$$

In this way, a functional relation $Z_0^{global}(Z_0^{local})$ is determined. Uncertainties coming from the number of pseudo-experiments and the $p_0^{local,obs}$ are provided when reporting the global significance.

5.7.4 Upper limits

In the case that no discovery can be claimed, upper limits are set on μ in order to exclude certain models. The upper limit can be computed using the one-sided test statistic, which defined as:

$$\tilde{q_\mu} = \begin{cases} -2ln\dfrac{L(\mu,\hat{\hat{\theta}}(\mu))}{L(0,\hat{\hat{\theta}}(0))}, \hat{\mu} < 0, \\ 0, \hat{\mu} > \mu, \\ -2ln\dfrac{L(\mu,\hat{\hat{\theta}}(\mu))}{L(\hat{\mu},\hat{\theta})}, 0 \leq \hat{\mu} \leq \mu. \end{cases} \tag{5.24}$$

where L is the likelihood function; $\hat{\mu}$ and $\hat{\theta}$ are the best fit values of μ and θ, $\hat{\hat{\theta}}(\mu)$ is the best fit value of θ for a fixed μ. Specially, in the case $\hat{\mu} < 0$, the likelihood value at $\mu = 0$ is used instead to avoid negative pdfs.

A 95% confidence level (C.L.) on the parameter of interest is computed using a modified frequentist approach[74][75]. The modified CL_s p-value is given as:

$$p_{\mu_{up}}^{CL_s} = \frac{p_{\mu_{up}}}{p_b} = \frac{\int_{\tilde{q_{\mu,obs}}}^{\infty} f(\tilde{q_\mu}|s+b)d\tilde{q_\mu}}{\int_{\tilde{q_{\mu,obs}}}^{\infty} f(\tilde{q_\mu}|b)d\tilde{q_\mu}} \tag{5.25}$$

Limits at 95% C.L. set on μ are then computed

5.7.5 Statistical models

The statistical models used for the two analyses are basically following the same form, as detailed below.

Low-mass analysis

The numbers of signal and background events are estimated with an extended maximum-likelihood fit to the binned $m_{\gamma\gamma}$ distribution, separately in the three conversion categories.

The parameterized signal and background models are described in Sec. 5.3 and Sec. 5.4. The signal pdf is a DSCB function with parameters computed as a function of m_X. The background pdf is either a Landau+exponential function (UU and UC categories) or a fifth order Bernstein polynomial function (CC category), as discussed in Sec. 5.4.1; the function parameters are all free in the fit. The systematics summarized in Tab. 5.10 are included in the fits via nuisance parameters constrained by Gaussian terms.

The extended pdf is given by:

$$\mathcal{L} = \prod_{c=1}^{n_c} e^{-N_c^{total}} \prod_{i=1}^{n_c^{data}} \mathcal{L}_c(m_{\gamma\gamma}(i,c)) \tag{5.26}$$

where $n_c = 3$ is the number of categories; n_c^{data} and N_c^{total} are the number of data events and the sum of the fitted numbers of events in each component in category c; $m_{\gamma\gamma}(i,c)$ is the $m_{\gamma\gamma}$ value for event i of category c. The per-event term of the signal-plus-background model is:

$$\begin{aligned}
&\mathcal{L}_c(m_{\gamma\gamma};\sigma_{fid},m_X,N_{uu,c},N_{uc,c},N_{cu,c},N_{cc,c},N_{bkg,c},a_c,\theta) = \\
&N_{X.c}(\sigma_{fid},m_X,\theta_{N_X},\theta_{SS})f_X(m_{\gamma\gamma},m_X,x_X(m_X),\theta_\sigma) \\
&+N_{uu,c}(\theta_{N_{uu,c}})f_{uu,c}(m_{\gamma\gamma},x_{uu,c},\theta_{uu,c}) \\
&+N_{uc,c}(\theta_{N_{uc,c}})f_{uc,c}(m_{\gamma\gamma},x_{uc,c},\theta_{uc,c}) \\
&+N_{cu,c}(\theta_{N_{cu,c}})f_{cu,c}(m_{\gamma\gamma},x_{cu,c},\theta_{cu,c}) \\
&+N_{cc,c}(\theta_{N_{cc,c}})f_{cc,c}(m_{\gamma\gamma},x_{cc,c},\theta_{cc,c}) \\
&+N_{bkg,c}f_{bkg,c}(m_{\gamma\gamma},a_c)
\end{aligned} \tag{5.27}$$

where σ_{fid} is the fiducial production cross section of the new resonance of mass m_X; $N_{uu,c}$, $N_{uc,c}$, $N_{cu,c}$, and $N_{cc,c}$ are the number of Drell-Yan background events identified respectively as unconverted-unconverted (contributing to the UU category), unconverted-converted, converted-unconverted (both contributing to the UC category) and converted-converted (contributing to the CC category); $N_{bkg,c}$ is the fitted number of background events; a are the parameters of the function that describe the non-resonant background shape; θ denotes the nuisance parameters used to describe the systematic uncertainties.

The nuisance parameters are listed below:

- θ_{lumi}: uncertainty on the integrated luminosity of the data sample.
- θ_{trig}, θ_{ID}, θ_{isol}, θ_{CX}, θ_{PU}: experimental uncertainties on the signal yield.
- θ_{ES}: photon energy scale systematic uncertainty;
- θ_{ER}: photon energy resolution systematic uncertainty;
- θ_{mig}^{mat}: migration uncertainty between categories.
- $\theta_{SS,uu}$,$\theta_{SS,cu}$,$\theta_{SS,cc}$: spurious signal systematics for each category. In low-mass analysis, the maximum value of spurious signal is taken as systematic uncertainty.
- $\theta_{norm,uu}^{stat}$,$\theta_{norm,uc}^{stat}$, $\theta_{norm,cu}^{stat}$,$\theta_{norm,cc}^{stat}$: uncertainty on the normalisation of each Drell-Yan component due to limited statistics in the computation of the template. The uncertainties are assumed to be uncorrelated as they are computed independently for each category.
- $\theta_{norm,uu}^{mat}$,$\theta_{norm,uc}^{mat}$, $\theta_{norm,cu}^{mat}$,$\theta_{norm,cc}^{mat}$: uncertainty on the normalisation of each Drell-Yan component due to systematic effects of the material, also considered as uncorrelated.

- $\theta^{gen}_{norm,uu}$,$\theta^{gen}_{norm,uc}$, $\theta^{gen}_{norm,cu}$,$\theta^{gen}_{norm,cc}$: uncertainty on the normalisation of each Drell-Yan component due to systematic effects of using the Sherpa generator instead of Powheg, also assumed to be uncorrelated.

- $\theta^{BS}_{peak,uu}$,$\theta^{BS}_{peak,uc}$, $\theta^{BS}_{peak,cu}$,$\theta^{BS}_{peak,cc}$, $\theta^{BS}_{sigma,uu}$,$\theta^{BS}_{sigma,uu}$, $\theta^{BS}_{sigma,uc}$, $\theta^{BS}_{sigma,cu}$,$\theta^{BS}_{sigma,cc}$, $\theta^{BS}_{ALo,uu}$,$\theta^{BS}_{sigma,uc}$, $\theta^{BS}_{ALo,cu}$,$\theta^{BS}_{ALo,cc}$, $\theta^{BS}_{AHi,uu}$,$\theta^{BS}_{AHi,uc}$, $\theta^{BS}_{AHi,cu}$: uncertainty on the parameters of the Double-sided Crystal-Ball used as model of each Drell-Yan component. The uncertainties are assumed to be uncorrelated as they are computed independently for each category.

- $\theta^{mat}_{peak,DY}$, $\theta^{mat}_{sigma,DY}$: uncertainty on the peak position and width of each Drell-Yan component due to systematic effects of the material description. These effects are assumed to be correlated between Drell-Yan components, so are described as a function of a single nuisance parameters.

- $\theta^{gen}_{peak,DY}$, $\theta^{gen}_{sigma,DY}$: systematic uncertainty on the shape of the Drell-Yan components of using the Sherpa generator instead of Powheg, also assumed to be correlated.

$N_{bkg,c}$ is a free parameter in the fit. $N_{X,c}$ represents the number of events for the searched resonance, described as the product of the total number of events (proportional to σ_{fid}) and the category fractions. This allows σ_{fid} to be directly extracted from the fit. In a given conversion category c, the number of events for the searched resonance N_X is given as:

$$N_X(\sigma_{\rm fid}, m_X, \theta_{N_X}, \theta_{SS}) = \sigma_{\rm fid} \cdot L_{\rm int} \cdot C_X(m_X) \cdot \prod_{k}^{\dim \theta_{N_x}} K_k(\theta_k) + \delta_{SS} \cdot \theta_{SS} \qquad (5.28)$$

where $L_{\rm int}$ is the integrated luminosity; $C_X(m_X)$ is the value of the C_X factor for the considered mass m_X; δ_{SS} (=$|N_{SS}|$) and θ_{SS} are the values of the background modeling uncertainty and its associated nuisance parameter; K_k denotes a function describing the effect of the k-th normalization systematic, and the index k runs over the set of systematic uncertainties affecting N_X. The expression $K_k(\theta_k) = [r_k(m_X)]^{\theta_k}$ is used, where $r_k(m_X)$ is approximately given by $N_{X,+k}(m_X)/N_X(m_X)$ for $\theta_k > 0$ and $N_X(m_X)/N_{X,-k}(m_X)$ for $\theta_k < 0$. This expression means that the modifications to the signal event yield for $\theta_k = \pm 1$ correspond to the $\pm 1\sigma$ variations used to define the uncertainties.

In addition, the number of Drell-Yan events in each category should also be taken into account. The systematic uncertainties on the normalization of the DY background template are described by nuisance parameters introduced above.

High-mass analysis

The numbers of signal and background events are estimated with an extended maximum-likelihood fit to the binned $m_{\gamma\gamma}$ distribution. In the high-mass analysis, there is only one inclusive conversion category. The statistical models for the spin-0 and spin-2 searches are identical, except for using the C_X or $C_X \cdot A_X$ factor.

The parameterized signal and background models are described in Sec. 5.3 and Sec. 5.4. The signal pdf is a DSCB function with parameters computed as a function of m_X. The background pdf $f_b(m_{\gamma\gamma}; a)$ is using the function from Eq. 5.9 in Sec. 5.4.1; the parameters of this function are all treated as free parameters in the fit. The systematics summarized in Tab. 5.11 are included in the fits via nuisance parameters constrained by Gaussian terms.

The signal-plus-background model used to describe the data can be written as:

$$\begin{aligned}\mathcal{L}(m_{\gamma\gamma}; \sigma, m_X, \alpha_X, N_b, a, \theta) &= f_X(m_{\gamma\gamma}; x_X(m_X, \alpha_X), \theta_\sigma) \cdot N_X(\sigma; m_X, \theta_{N_X}, \theta_{SS}) \\ &+ f_b(m_{\gamma\gamma}; a) \cdot N_b\end{aligned} \tag{5.29}$$

where f_X, f_b and N_X, N_b denote the probability density function (pdf) and corresponding yield for a given signal X and the background components; N_b is a free parameter in the fit, N_X is given as in Eq. 5.28 (In the high-mass case, δ_{SS} is a mass-dependent number); σ is the fiducial (total) cross section times branching ratio of the hypothetical resonance of mass m_X decaying to two photons; a are the parameters of the function that describe the background shape, and θ_{N_X} is the set of nuisance parameters for systematic uncertainties affecting N_X, as listed below:

- θ_{lumi} : uncertainty on the integrated luminosity of the data sample.
- θ_{trig}, θ_{ID}, θ_{isol}, θ_{CX}, θ_{PU} : experimental uncertainties on the signal yield.
- θ_{SS}: spurious signal systematic uncertainty;
- θ_{ES}: photon energy scale systematic uncertainty;
- θ_{ER}: photon energy resolution systematic uncertainty;
- θ_{C_X}: production-mode uncertainty on the C_X factor (spin-0 search).

The overall likelihood including extended and constraint terms is given by:

$$\begin{aligned}&\mathcal{L}(\sigma_{\text{fid}}, m_X, \alpha_X, N_b, a, \theta) = \\ &e^{-(N_X+N_b)} \left[\prod_{i=1}^{n} \mathcal{L}(m_{\gamma\gamma_i}; \sigma_{\text{fid}}, m_X, \alpha_X, N_b, a, \theta)\right] \left[\prod_{k=1}^{\dim\theta} \exp\left(-\tfrac{1}{2}\left(\theta_k - \theta_k^{\text{aux}}\right)^2\right)\right]\end{aligned} \tag{5.30}$$

where n is the total number of events in the data, $m_{\gamma\gamma_i}$ is the diphoton mass for a given event, and θ^{aux} denotes the set of constants obtained from auxiliary measurements and are used to constrain the nuisance parameters for the systematic uncertainties.

5.8 Results

5.8.1 Low-mass search results

The p-value scan in range [65, 110] GeV with the 80 fb^{-1} dataset is shown in Fig. 5.31. No significant excess above 1σ with respect to the background-only hypothesis is observed. As introduced in Sec. 5.7.3, a global significance of 2.4σ is computed using the approximate formula given in Eq. 5.22.

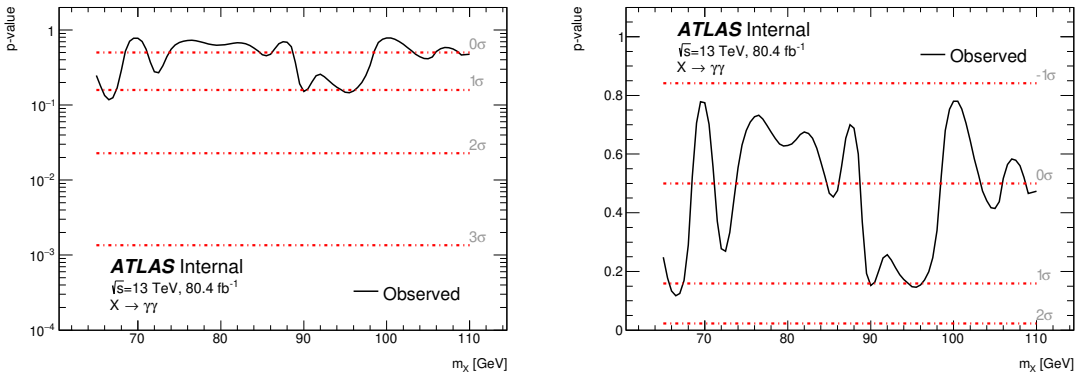

(a) (b)

Figure 5.31 – Low-mass: observed p-value for the background-only hypothesis, p_0, in (a) logarithmic and (b) linear scale, as a function of the resonance mass m_X.

The expected and observed limits are shown in Fig. 5.32. An upper limit at the 95% $C.L.$ is set on the fiducial cross section times branching ratio ($\sigma_{fid} \cdot B$) from 30 to 101 fb in the mass range [65, 110] GeV, which is consistent with the absence of a signal. This limit is slightly improved in the lower mass part compared to the 2014 result[53] (30 to 90 fb in the same mass range) obtained with 20.3 fb^{-1} data, thanks to the increased luminosity and optimized analysis selection. However, the sensitivity loss is significant due to the overall spurious signal. Figure 5.33 shows the impact of the systematic uncertainties on the upper limit on the fiducial cross section. It can be found that the spurious signal (non-resonant background modeling) systematic uncertainty is dominant. In addition, the imperfect modeling of the Drell-Yan background leads to the sensitivity loss around 90 GeV.

5.8.2 High-mass search results

Scalar results

The one-dimensional local p-value scans as a function of the resonance mass m_X are shown in Fig. 5.34 for the narrow-width approximation, and for several different values of Γ_X/m_X. The two-dimensional (scanning over both m_X and the relative

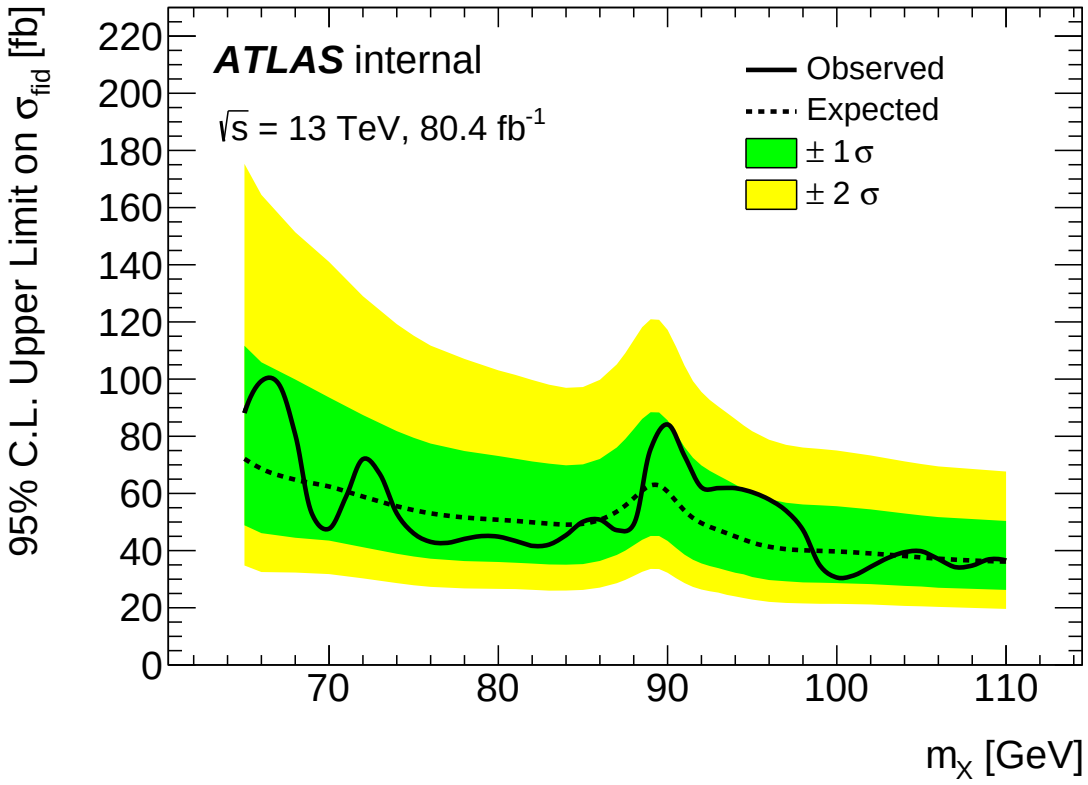

Figure 5.32 – Low-mass analysis: expected and observed limits on the fiducial cross section times branching ratio $\sigma_{fid} \cdot B$ of a narrow resonance as a function of the resonance mass m_X in the 65-110 GeV mass range. The green and yellow bands show the $\pm 1\sigma$ and $\pm 2\sigma$ uncertainties on the expected limit.

width Γ_X/m_X) scans are shown in Fig. 5.35. The 2D p value is scanned in 2 GeV steps in m_X in the mass range [400, 2800] GeV and steps of 0.5% in Γ_X/m_X in the relative width range [0, 10%].

The most significant excess is observed for m_X around 684 GeV for the NWA model, corresponding to a 3.29σ local significance. One can also check the deviation of the parameters after the fits ("pulls") at this mass point as the evidence for the various biases from the systematic uncertainties. The pulls of the fit parameters for $m_X = 684$ GeV are shown in Fig. 5.36. Only the signal mass resolution nuisance parameter is pulled a little bit (still within the uncertainty on the signal mass resolution), as the data prefer a slightly wider resonance.

The global significances corresponding to the maximum local significances observed (at 684 GeV) in the analyses are calculated using 1000 pseudo-experiments, following the method described in Sec. 5.7.3. For a local significance of 3.29σ in the scalar analysis, the global significance is found to be $(1.3 \pm 0.06)\sigma$. The uncertainties quoted here on the global significance value come from the generated toy sample sizes. The global significance is also computed with the asymptotic formula, and the results are found to be the same.

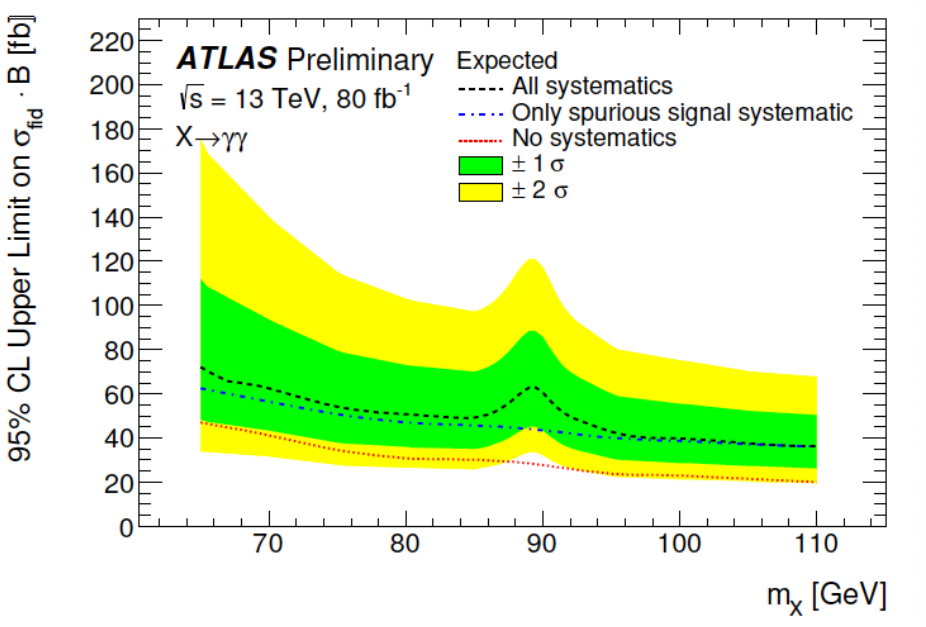

Figure 5.33 – Low-mass analysis: expected upper limits on the fiducial cross section times branching ratio $\sigma_{fid} \cdot B$ as a function of the resonance mass m_X in the 65-110 GeV mass range. The black curve represents all the systematic uncertainties are considered; the blue curve represents that only the spurious signal uncertainty in considered; the red curve represents that no systematic uncertainties are considered.

Both expected and observed limits are produced based on the asymptotic formulas[71] to determine the fiducial cross section value corresponding to 95% $C.L.$ exclusion. One-dimensional fiducial limit scans as function of m_X limit are shown for different relative width Γ_X/m_X in Fig. 5.37. In addition, the 2D expected and observed limits are given in Fig. 5.38 in the mass range [400,2800] GeV.

While limits in Figs. 5.37 and 5.38 are computed using the asymptotic approximation, one must consider the case where the statistics in the data begin to run out (usually called "deep Poisson" regime). When the expected number of data events is too small, the asymptotic approximation does not reflect the true distribution anymore and usually leads to unphysical results[71]. In this regime (above $m_X = 2400$ GeV for the high-mass analysis), the limits should be set using pseudo-experiments instead. As an example, Fig. 5.39 shows the upper limits (black) for a NWA spin-0 resonance as a function of m_X, obtained with asymptotic approximation and toys (blue). It can be seen clearly that in the high-mass tail and some other low event count regions, the limits obtained with asymptotic approximation tend to be over-optimistic. Similar studies are also done for the spin-2 search. However, limit calculations for each resonance mass and for different signal width are extremely CPU consuming.[8] The toy-based expected and observed limit computation is not fully completed yet.

[8]With the application of the fast distribution sampling technique using linearized likelihood[76], the computation time has been significantly reduced.

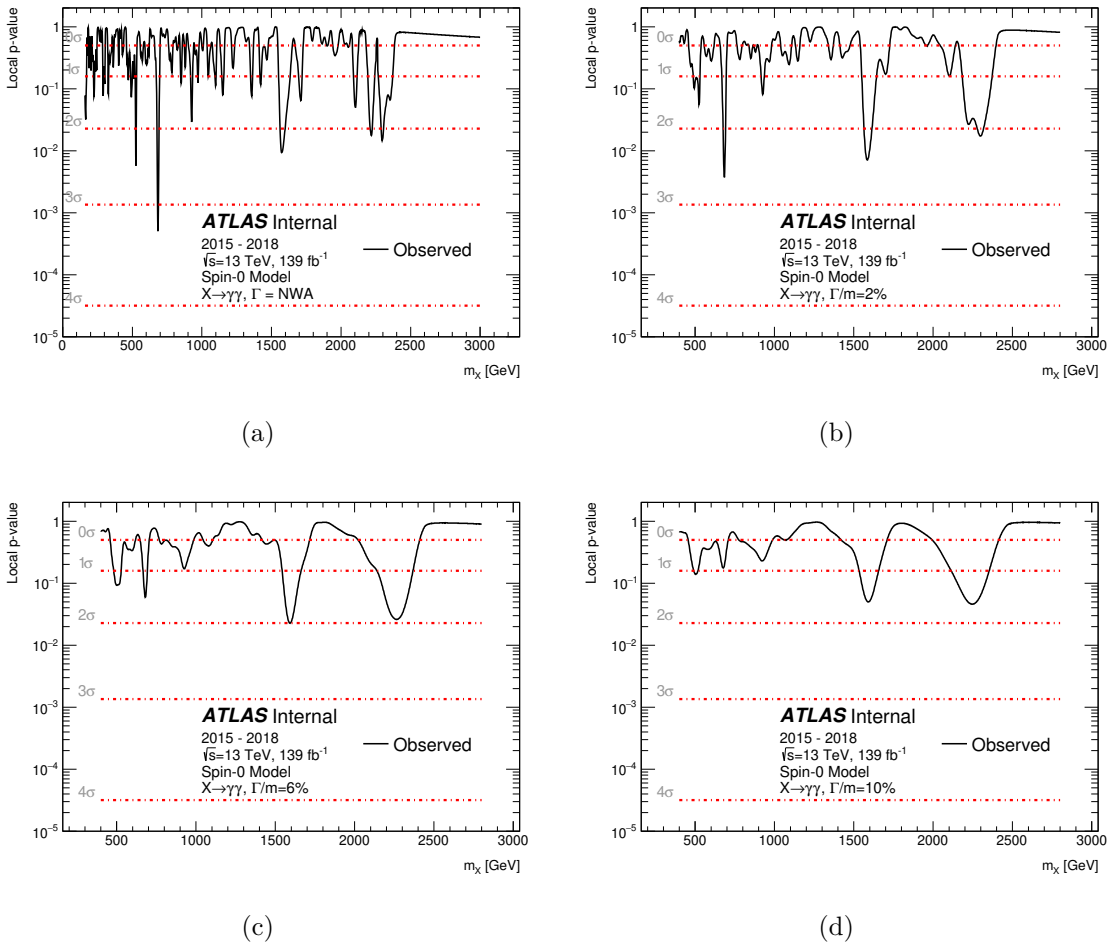

Figure 5.34 – High-mass analysis, spin-0 search: observed scan of the p-value for the background-only hypothesis as a function of the assumed mass, for various values of Γ_X/m_X for the full 139 fb^{-1} dataset.

Graviton results

The 2D p-value scans (with respect to m_{G^*} and the coupling $k/\bar{M}_{pl}$) for the background-only hypothesis are shown in Fig. 5.40, in the mass range [500, 2800] GeV and in the coupling range [0.01, 0.1]. In addition, one-dimensional p-value scans as a function of graviton mass are shown for different values of coupling in Fig. 5.41.

The most significant excess is also observed for m_{G^*} around 684 GeV and a coupling of 0.01, corresponding to 3.29 σ local significance. This corresponds to a global significance of $(1.36 \pm 0.06)\sigma$, which is evaluated for a search region defined as $500 < m_G < 2800$ GeV, $0.01 < k/\bar{M}_{pl} < 0.1$, based on an ensemble of 1000 pseudo-experiments.

The expected and observed limits are computed for the range [500, 2800] GeV $0.01 < k/\bar{M}_{pl} < 0.10$. The two-dimensional scan results are shown in Fig. 5.42. In addition, one-dimensional limit scans are shown for certain three coupling values

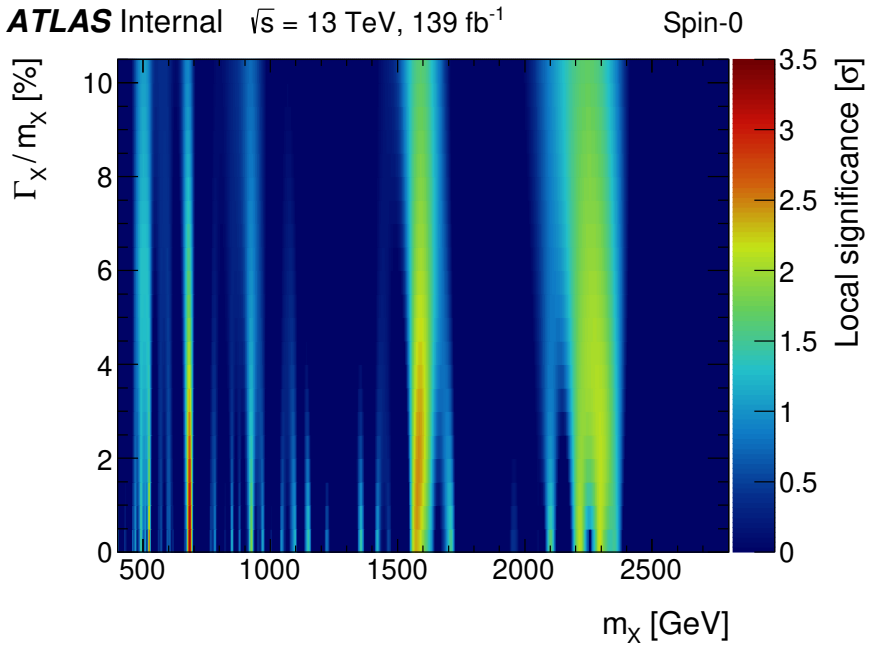

Figure 5.35 – High-mass analysis, spin-0 search: observed two-dimensional scan of the p-value, converted to significance, for the background-only hypothesis, as a function of the probed resonance mass m_X and relative natural width Γ_X/m_X for the full 139 fb^{-1} data.

in Fig. 5.43. Above $m_X = 2400$ GeV where the data runs out, the expected and observed limits are obtained with pseudo-experiments, as shown in the blue curves. The theoretical predictions for an RS1 graviton are also shown in the one-dimensional scan plots, with a theoretical systematic uncertainty computed using all the 100 eigenvalue variations of the nominal PDF set. Compared with the theoretical predictions, The RS1 graviton model is excluded for m_{G^*} below 2.2, 3.9 and 4.5 TeV for coupling values of 0.01, 0.05 and 0.1 respectively.

5.9 Conclusion

Conclusions of the low-mass and high-mass analyses are summarized in this section. Previous results published by the ATLAS and the CMS experiments are also discussed, in order to provide an overall picture of the search for a new resonance in the diphoton final state.

5.9.1 Low-mass analysis

A search for a spin-0 narrow-width resonance decaying to a pair of photons in the invariant mass range [65, 110] GeV is presented, using 80.4 fb^{-1} of pp collision data collected at $\sqrt{s} = 13$ TeV. This search is limited by systematic uncertainties, with the

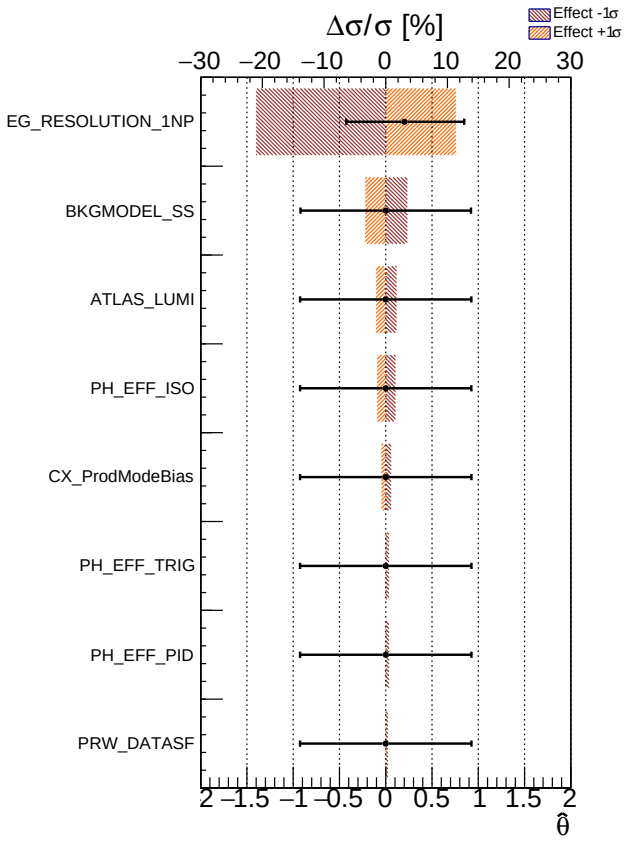

Figure 5.36 – High-mass analysis, spin-0 search: pulls of fit to data for $m_X = 684$ GeV, where the largest local significance is observed. The post-fit effect of each systematic source considered in the fit is also shown.

dominant uncertainty arising from the choice of functions modeling the continuum background. No significant excess above the Standard Model expectation is found, the global significance is estimated to be 2.4σ. The observed 95% $C.L.$ upper limits are set on the fiducial cross section times branching ratio, between 30 to 101 fb depending on the diphoton invariant mass.

This search is an update to the search in 2014 with 20.3 fb^{-1} of Run 1 data recorded with the ATLAS detector at $\sqrt{s} = 8$ TeV[53]. The limits are improved a little compared to the previous result, however the expected improvement coming from the increased luminosity is not reached. A similar search for a low-mass diphoton resonance in the mass range [70, 110] GeV was carried out by the CMS collaboration in 2017 as well[54], using 19.7 fb^{-1} data collected at $\sqrt{s} = 8$ TeV and 35.9 fb^{-1} data collected at $\sqrt{s} = 13$ TeV. A small excess was observed at a mass of 95 GeV, with a global significance of 1.3σ. Our result could not exclude this excess, however the p-value as a function of m_X is also checked with the spurious signal systematic uncertainty removed, and proves that we would still be sensitive to the CMS excess if the analysis were not systematic-limited. This motivated us to treat the systematic uncertainty on the choice of background function more carefully, and both the high-mass analysis and the ongoing low-mass analysis with full Run 2 data use the functional decomposition method to improve our estimation on this systematic uncertainty.

5.9.2 High-mass analysis

Searches for new resonances are also presented in the high-mass range, using the full Run 2 data that corresponding to an integrated luminosity of 139 fb^{-1}, collected at $\sqrt{s} = 13$ TeV. The analyses are optimized to search for a spin-0 scalar resonance with mass above 200 GeV, and a spin-2 graviton predicted by the Randall-Sundrum (RS) model with mass above 500 GeV. Thanks to the optimization of the analysis selection and the background smoothing technique, a better sensitivity for resonances above 1 TeV is achieved and the systematic uncertainty on the choice of the analytic function to model the background is no longer a limitation. No significant excess above the Standard Model expectation is found, while the most significant excess is observed at $m_X = 684$ GeV for the spin-0 narrow-width model and for the spin-2 graviton model ($k/\bar{M}_{pl}$), corresponding to 3.29σ local significance. The global significance corresponding the the maximum local significance is found to be 1.30σ and 1.36σ respectively for the two models. In the spin-0 search, the upper limits are set on the fiducial cross section times branching ratio for a narrow-width resonance, between 12.5 fb to 0.03 fb in the mass range from 160 to 2800 GeV. In the spin-2 search, the upper limits are set on the total cross section times branching ratio for different assumptions on the graviton coupling and mass. For $k/\bar{M}_{pl} = 0.1$, the observed upper limits are set between 3.2 fb to 0.04 fb in the graviton mass range from 500 to 5000 GeV.

Previously the search for high-mass spin-0 and spin-2 RS graviton resonances was performed with the 2015 data corresponding to 3.2 fb^{-1}[77]. Near a mass of 750 GeV, an excess of 3.9σ and 3.8σ was found for the spin-0 and spin-2 models respectively. In a similar search with 19.7 and 3.3 fb^{-1} data collected at $\sqrt{s}$=8 and 13 TeV respectively, the CMS collaboration also claimed an 3.4σ excess compatible with a narrow-width resonance with a mass of about 750 GeV[78]. However, this excess was not seen again by the ATLAS collaboration in the updated search in 2016 data or in the present analysis, and was probably just a statistical fluctuation in data. In the combined 2015 and 2016 dataset corresponding to 37 fb^{-1}[52], the largest local derivation from the Standard Model expectation is 2.6σ for a spin-0 narrow-width signal near 730 GeV, and 3.0σ for a spin-2 $k/\bar{M}_{pl} = 0.3$ graviton signal near 708 GeV. Nevertheless, much better limits were obtained in the present analysis compared to 37 fb^{-1} analysis thanks to the optimization and the increased luminosity.

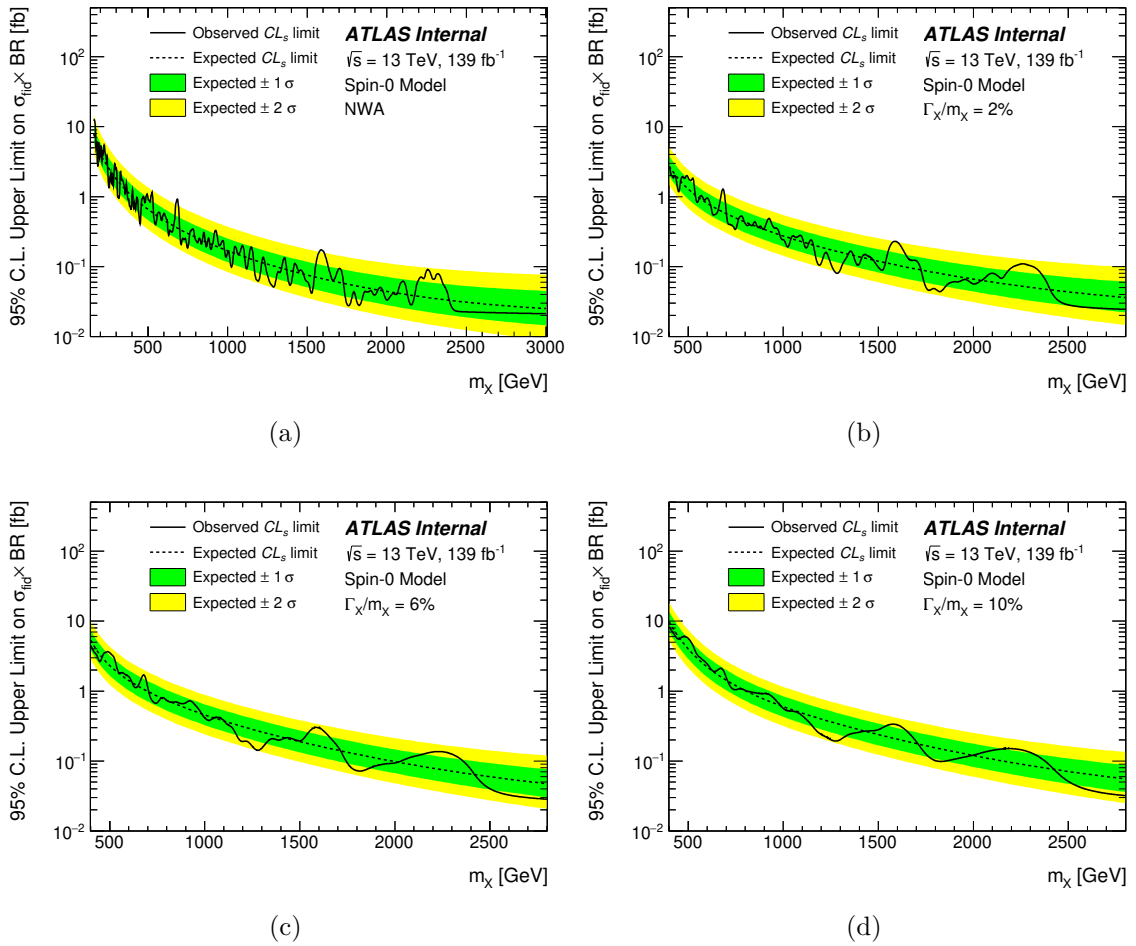

Figure 5.37 – High-mass analysis, spin-0 search: expected and observed limit on the fiducial production cross section limit σ_{fid} as a function of the resonance mass m_X, for various values of the relative signal width Γ_X/m_X for the combined 139 fb^{-1} dataset. Results shown in these plots are obtained with asymptotic formulas.

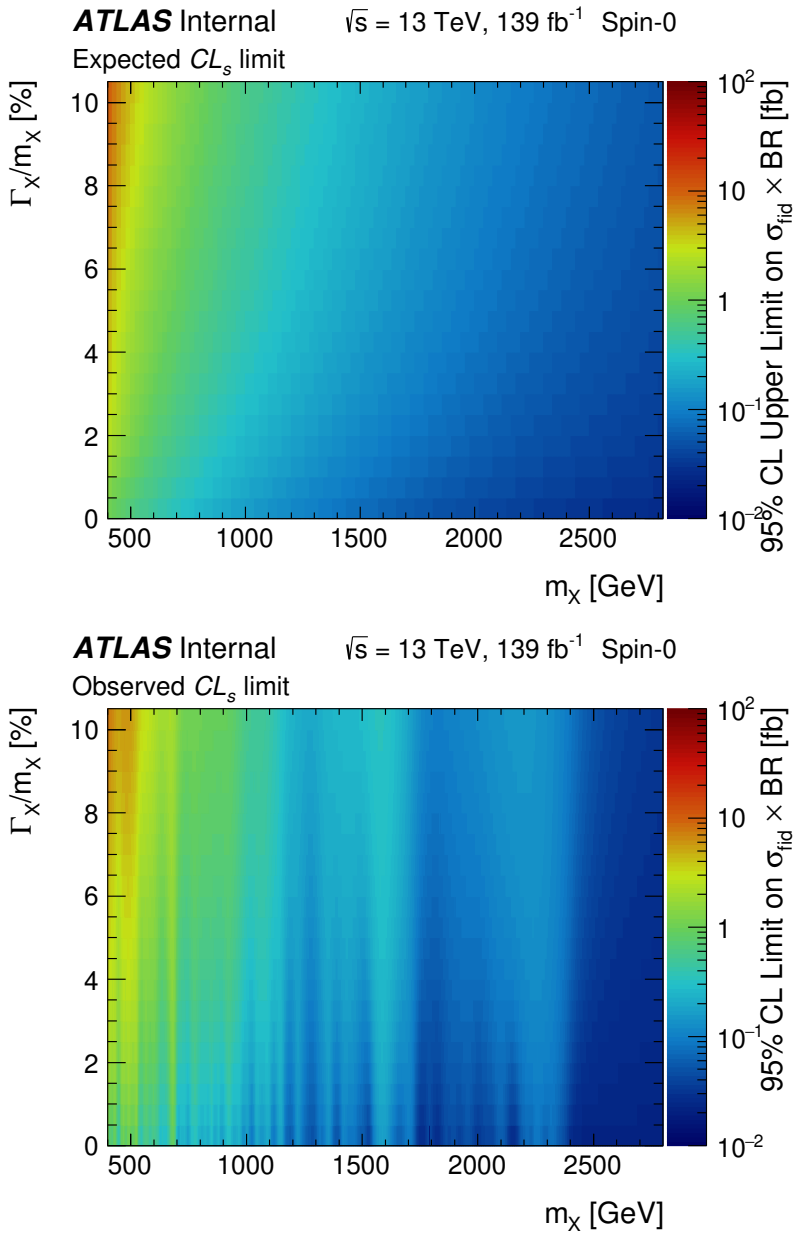

Figure 5.38 – High-mass analysis, spin-0 search: expected and observed two-dimensional limit on the fiducial production cross section σ_{fid} as a function of the resonance mass m_X and relative natural width Γ_X/m_X.

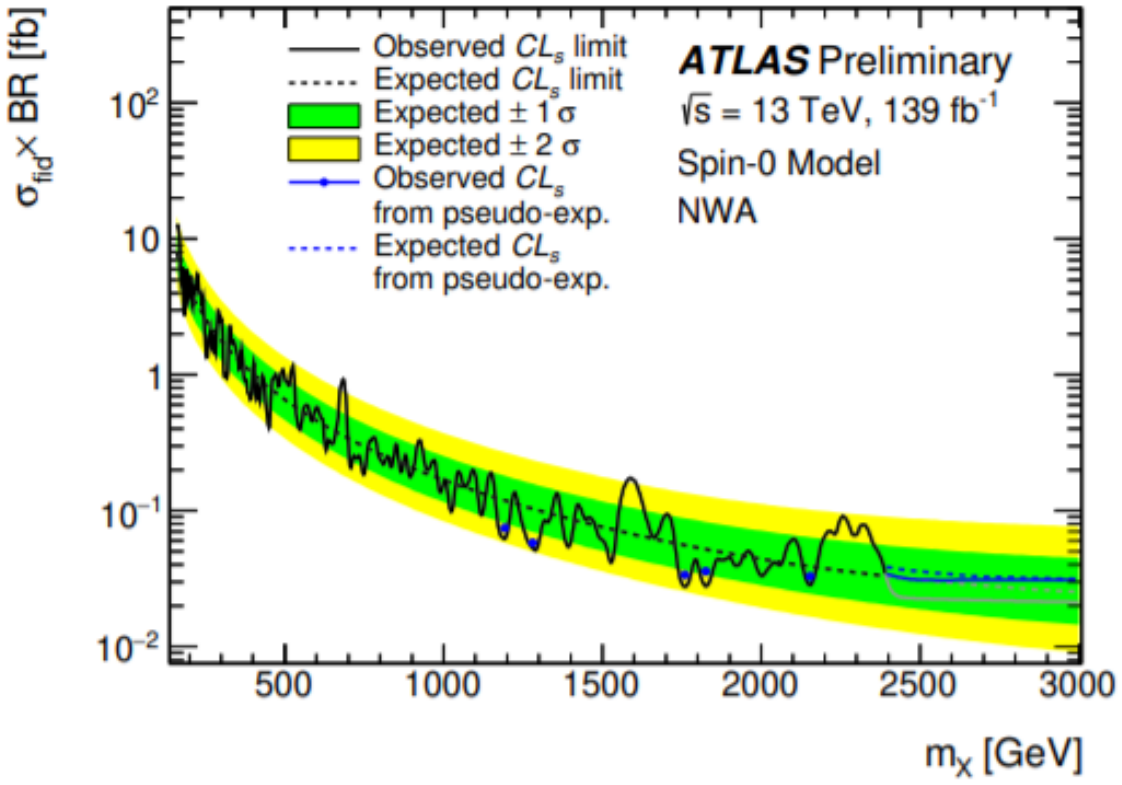

(a)

Figure 5.39 – High-mass analysis, spin-0 search: expected and observed limit on the fiducial production cross section limit σ_{fid} as a function of the resonance mass m_X, for a NWA resonance. For masses greater than 2400 GeV, pseudo-experiments are used to derive the expected (blue dashed line) and observed (blue line) limits. In addition, pseudo-experiments are also used to compute a limit at several lower masses (blue dots) to shwo the deviation of the asymptotic approximation in these low event count regions.

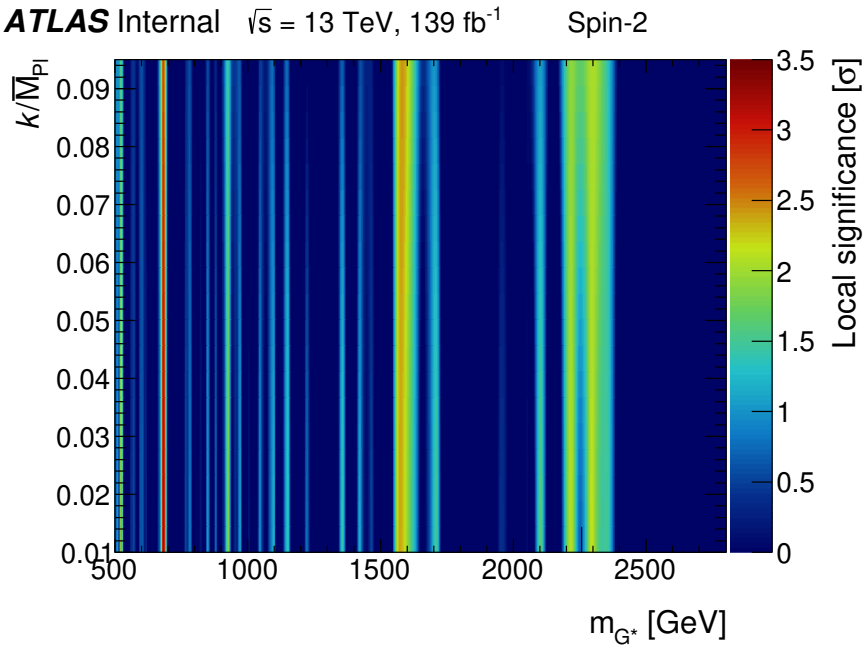

Figure 5.40 – High-mass analysis, spin-2 search: observed two-dimensional scan of the p-value for the background-only hypothesis, as a function of the probed resonance mass m_{G^*} and coupling $k/\bar{M}_{pl}$ for the full Run-2 dataset.

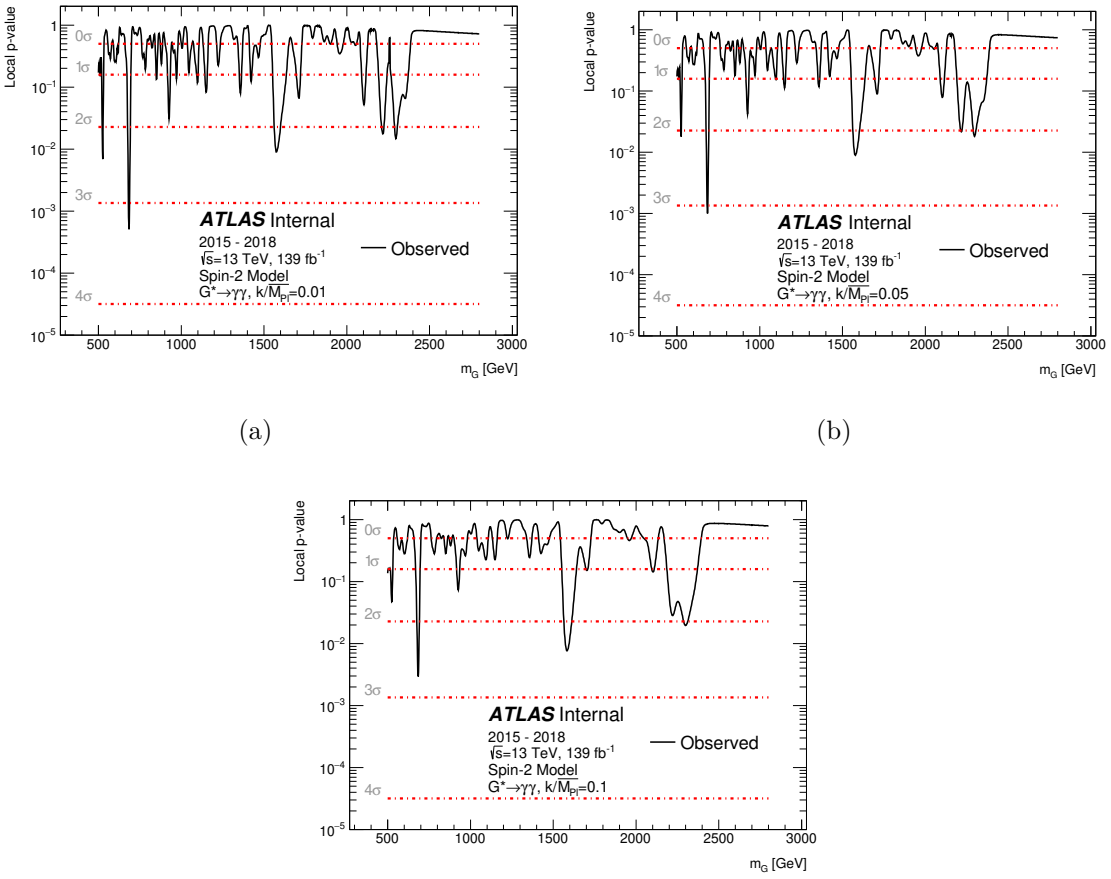

Figure 5.41 – High-mass analysis, spin-2 search: observed scan of the p-value for the background-only hypothesis as a function of the assumed mass, for various values of $k/\bar{M}_{pl}$. The p-value results are derived only for the full Run-2 dataset.

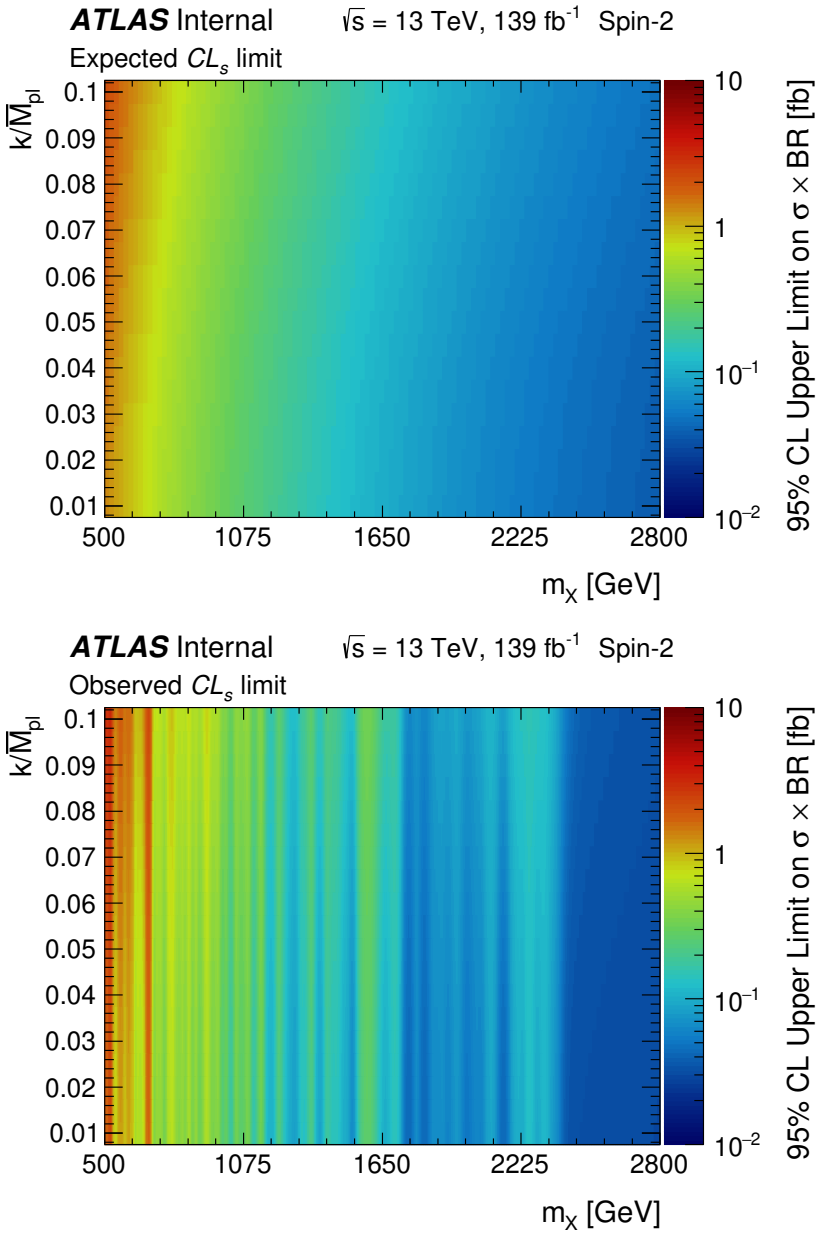

Figure 5.42 – High-mass analysis, spin-2 search: expected and observed two-dimensional limit on the total production cross section times branching ratio to two photons $\sigma \times BR(G^* \to \gamma\gamma)$ for the RS1 graviton as a function of the resonance mass m_{G^*} and relative coupling $k/\bar{M}_{pl}$.

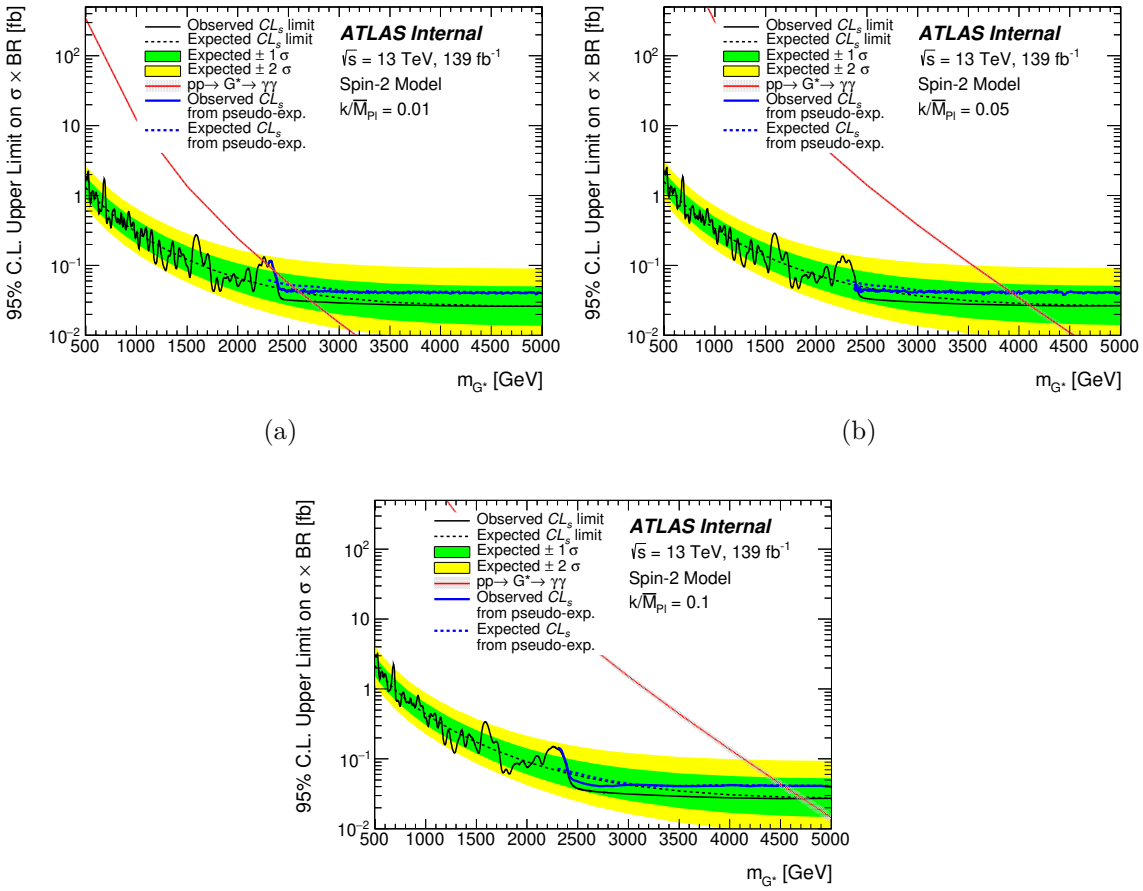

Figure 5.43 – High-mass analysis, spin-2 search: expected and observed limit on the total production cross section times branching ratio to two photons $\sigma \times BR(G^* \to \gamma\gamma)$ for the RS graviton as a function of the resonance mass m_{G^*}, for various values of the signal coupling $k/\bar{M}_{pl}$ for the full Run 2 dataset. The theoretical predictions for an RS1 graviton are shown (red) along with the expected and observed limits using pseudo-experiments (blue).

Conclusion

It has been a long journey for the elementary particle physics since the first thoughts of peeking inside the atoms and the nucleus. Our largest and most powerful tool nowadays for particle physics researches, the Large Hadron Collider, started to deliver proton-proton collision data since 2009. Over the years, about 26 fb^{-1} of pp collisions at $\sqrt{s} = 7$ and 8 TeV were delivered to both ATLAS and CMS during the first run of the LHC, and 147 fb^{-1} of pp collisions were collected at $\sqrt{s} = 13$ TeV by the ATLAS detector during the whole Run 2. The long shutdown for the purpose of maintaining and upgrading of the LHC began in December 2018, aiming for higher centre-of-mass energy and luminosity. In 2012, the discovery of the Higgs Boson filled in the last missing piece of the Standard Model, while the Standard Model is still incomplete as an ultimate answer and experimentalists are keep searching for signs of new physics beyond the Standard Model. The journey is far from end.

All the exciting discoveries and reliable measurements own to the precise reconstruction and calibration of the physics objects in the ATLAS detector. In this thesis, one of the systematic uncertainty of the energy calibration of photons is focused on. While the electron-to-photon extrapolation is performed smartly assuming the energy scale obtained from electron samples are also valid for photons, this photon-specific uncertainty arises from the difference of an energy-dependent mismodeling of the lateral shower shape between electron and photon. To quantity this effect, the lateral energy leakage outside a given cluster in the electromagnetic calorimeter is studied, and its difference between data and MC, electrons and photons ("double difference") is taken as an additional systematic uncertainty in the photon energy calibration. The double difference is measured in different η and E_T regions using $Z \to \mu\mu\gamma$ sample, and photons from diphoton sample are also used for the first time as an extension and cross-check of the study.

In parallel, searches for new resonances decaying to photons pairs are also performed. The two presented analyses share a common strategy: one searches for a spin-0 resonant state in the low-mass region using 80 fb^{-1} of data collected in 2015-2017, the other searches for a spin-0 resonance and a spin-2 graviton excitation predicted by the Randall-Sundrum model with one warped extra dimension, using 139 fb^{-1} of full Run 2 dataset. Both analyses are updates to previous ATLAS and CMS results. Although no significant excess with respect to the Standard Model expectation is observed

considering the look elsewhere effect, better upper limits are set thanks to the analysis optimization and increased luminosity. It is also worth mentioning that the Functional Decomposition method is introduced for the first time in the high-mass background modeling procedure, and the corresponding systematic uncertainty on the choice of the analytical function describing the non-resonant background. The search will carry on with the benefit of larger statistics as well as the challenge of much higher pile-up condition in the coming Run 3.

Bibliography

[1] R.P. Feynman. *Feynman lectures on gravitation*. Ed. by F.B. Morinigo, W.G. Wagner, and B. Hatfield. Dec. 1996 (cit. on p. 15).

[2] Charles W. Misner, K.S. Thorne, and J.A. Wheeler. *Gravitation*. San Francisco: W. H. Freeman, 1973. ISBN: 978-0-7167-0344-0, 978-0-691-17779-3 (cit. on p. 15).

[3] Paul A.M. Dirac. "The quantum theory of the electron". In: *Proc. Roy. Soc. Lond. A* 117 (1928), pp. 610–624. DOI: 10.1098/rspa.1928.0023 (cit. on p. 17).

[4] Abdelhak Djouadi. "The anatomy of electroweak symmetry breaking". In: *Physics Reports* 457.1-4 (Feb. 2008), pp. 1–216. ISSN: 0370-1573. DOI: 10.1016/j.physrep.2007.10.004. URL: http://dx.doi.org/10.1016/j.physrep.2007.10.004 (cit. on p. 22).

[5] Sarthak Satapathy et al. "Higgs in Quark Gluon Plasma". In: Jan. 2020 (cit. on p. 23).

[6] G. Rajasekaran. "Fermi and the theory of weak interactions". In: *Resonance* 19.1 (Jan. 2014), pp. 18–44. ISSN: 0973-712X. DOI: 10.1007/s12045-014-0005-2. URL: http://dx.doi.org/10.1007/s12045-014-0005-2 (cit. on p. 24).

[7] D. B. Chitwood et al. "Improved Measurement of the Positive-Muon Lifetime and Determination of the Fermi Constant". In: *Physical Review Letters* 99.3 (July 2007). ISSN: 1079-7114. DOI: 10.1103/physrevlett.99.032001. URL: http://dx.doi.org/10.1103/PhysRevLett.99.032001 (cit. on p. 25).

[8] James Saxon. "Discovery of the Higgs Boson, Measurements of its Production, and a Search for Higgs Boson Pair Production". Presented 13 06 2014. July 2014. URL: https://cds.cern.ch/record/1746004 (cit. on pp. 25, 67).

[9] D. de Florian et al. "Handbook of LHC Higgs Cross Sections: 4. Deciphering the Nature of the Higgs Sector". In: 2/2017 (Oct. 2016). DOI: 10.23731/CYRM-2017-002. arXiv: 1610.07922 [hep-ph] (cit. on p. 30).

[10] G.C. Branco et al. "Theory and phenomenology of two-Higgs-doublet models". In: *Physics Reports* 516.1-2 (July 2012), pp. 1–102. ISSN: 0370-1573. DOI: 10.1016/j.physrep.2012.02.002. URL: http://dx.doi.org/10.1016/j.physrep.2012.02.002 (cit. on pp. 32, 33).

[11] Mark Trodden. "Electroweak baryogenesis: A Brief review". In: *33rd Rencontres de Moriond: Electroweak Interactions and Unified Theories*. 1998, pp. 471–480. arXiv: hep-ph/9805252 (cit. on p. 32).

[12] "LHC Machine". In: *JINST* 3 (2008). Ed. by Lyndon Evans and Philip Bryant, S08001. DOI: 10.1088/1748-0221/3/08/S08001 (cit. on pp. 32, 37).

[13] Jihn E. Kim. "Light Pseudoscalars, Particle Physics and Cosmology". In: *Phys. Rept.* 150 (1987), pp. 1–177. DOI: 10.1016/0370-1573(87)90017-2 (cit. on p. 32).

[14] R.D. Peccei and Helen R. Quinn. "CP Conservation in the Presence of Instantons". In: *Phys. Rev. Lett.* 38 (1977), pp. 1440–1443. DOI: 10.1103/PhysRevLett.38.1440 (cit. on p. 32).

[15] Lisa Randall and Raman Sundrum. "Large Mass Hierarchy from a Small Extra Dimension". In: *Phys. Rev. Lett.* 83 (17 Oct. 1999), pp. 3370–3373. DOI: 10.1103/PhysRevLett.83.3370. URL: https://link.aps.org/doi/10.1103/PhysRevLett.83.3370 (cit. on pp. 33, 113).

[16] Lisa Randall and Raman Sundrum. "An Alternative to Compactification". In: *Phys. Rev. Lett.* 83 (23 Dec. 1999), pp. 4690–4693. DOI: 10.1103/PhysRevLett.83.4690. URL: https://link.aps.org/doi/10.1103/PhysRevLett.83.4690 (cit. on pp. 33, 113).

[17] Ignatios Antoniadis et al. "New dimensions at a millimeter to a fermi and superstrings at a TeV". In: *Physics Letters B* 436.3-4 (Sept. 1998), pp. 257–263. ISSN: 0370-2693. DOI: 10.1016/s0370-2693(98)00860-0. URL: http://dx.doi.org/10.1016/S0370-2693(98)00860-0 (cit. on p. 33).

[18] GARY FELDER. "WARPED GEOMETRY OF BRANE WORLDS". In: *International Journal of Modern Physics A* 17.29 (Nov. 2002), pp. 4297–4305. ISSN: 1793-656X. DOI: 10.1142/s0217751x02013344. URL: http://dx.doi.org/10.1142/S0217751X02013344 (cit. on p. 33).

[19] Fernand Grard and Jean Nuyts. "Elementary Kaluza-Klein towers revisited". In: *Phys. Rev. D* 74 (2006), p. 124013. DOI: 10.1103/PhysRevD.74.124013. arXiv: hep-th/0607246 (cit. on p. 35).

[20] *LEP design report*. By the LEP Injector Study Group. Geneva: CERN, 1983. URL: https://cds.cern.ch/record/98881 (cit. on p. 37).

[21] *LEP design report*. Copies shelved as reports in LEP, PS and SPS libraries. Geneva: CERN, 1984. URL: https://cds.cern.ch/record/102083 (cit. on p. 37).

[22] G. Aad et al. "The ATLAS Experiment at the CERN Large Hadron Collider". In: *JINST* 3 (2008), S08003. DOI: 10.1088/1748-0221/3/08/S08003 (cit. on p. 37).

[23] S. Chatrchyan et al. “The CMS Experiment at the CERN LHC”. In: *JINST* 3 (2008), S08004. DOI: 10.1088/1748-0221/3/08/S08004 (cit. on p. 37).

[24] Jr. Alves A.Augusto et al. “The LHCb Detector at the LHC”. In: *JINST* 3 (2008), S08005. DOI: 10.1088/1748-0221/3/08/S08005 (cit. on p. 37).

[25] K. Aamodt et al. “The ALICE experiment at the CERN LHC”. In: *JINST* 3 (2008), S08002. DOI: 10.1088/1748-0221/3/08/S08002 (cit. on p. 37).

[26] “High-Luminosity Large Hadron Collider (HL-LHC): Technical Design Report V. 0.1”. In: 4/2017 (Nov. 2017). Ed. by G. Apollinari et al. DOI: 10.23731/CYRM-2017-004 (cit. on p. 38).

[27] M Capeans et al. *ATLAS Insertable B-Layer Technical Design Report*. Tech. rep. CERN-LHCC-2010-013. ATLAS-TDR-19. Sept. 2010. URL: https://cds.cern.ch/record/1291633 (cit. on p. 45).

[28] ATLAS Collaboration. *Technical Design Report for the ATLAS Inner Tracker Pixel Detector*. Tech. rep. CERN-LHCC-2017-021. ATLAS-TDR-030. Geneva: CERN, Sept. 2017. URL: https://cds.cern.ch/record/2285585 (cit. on p. 45).

[29] ATLAS Collaboration. *Technical Design Report for the ATLAS Inner Tracker Strip Detector*. Tech. rep. CERN-LHCC-2017-005. ATLAS-TDR-025. Geneva: CERN, Apr. 2017. URL: https://cds.cern.ch/record/2257755 (cit. on p. 46).

[30] *Particle Identification Performance of the ATLAS Transition Radiation Tracker*. Tech. rep. ATLAS-CONF-2011-128. Geneva: CERN, Sept. 2011. URL: https://cds.cern.ch/record/1383793 (cit. on p. 46).

[31] U. Amaldi et al. “The Real Part of the Forward Proton Proton Scattering Amplitude Measured at the CERN Intersecting Storage Rings”. In: *Phys. Lett. B* 66 (1977), pp. 390–394. DOI: 10.1016/0370-2693(77)90022-3 (cit. on p. 51).

[32] William Panduro Vazquez and ATLAS Collaboration. *The ATLAS Data Acquisition system in LHC Run 2*. Tech. rep. ATL-DAQ-PROC-2017-007. 3. Geneva: CERN, Feb. 2017. DOI: 10.1088/1742-6596/898/3/032017. URL: https://cds.cern.ch/record/2244345 (cit. on p. 52).

[33] ATLAS Collaboration. “Performance of the electronic readout of the ATLAS liquid argon calorimeters”. In: *Journal of Instrumentation* 5.09 (Sept. 2010), P09003–P09003. DOI: 10.1088/1748-0221/5/09/p09003. URL: https://doi.org/10.1088%2F1748-0221%2F5%2F09%2Fp09003 (cit. on p. 54).

[34] W Lampl et al. *Calorimeter Clustering Algorithms: Description and Performance*. Tech. rep. ATL-LARG-PUB-2008-002. ATL-COM-LARG-2008-003. Geneva: CERN, Apr. 2008. URL: https://cds.cern.ch/record/1099735 (cit. on p. 55).

[35] *Electron and photon reconstruction and performance in ATLAS using a dynamical, topological cell clustering-based approach*. Tech. rep. ATL-PHYS-PUB-2017-022. Geneva: CERN, Dec. 2017. URL: https://cds.cern.ch/record/2298955 (cit. on p. 55).

[36] Morad Aaboud et al. "Electron reconstruction and identification in the ATLAS experiment using the 2015 and 2016 LHC proton-proton collision data at $\sqrt{s} =$ 13 TeV". In: *Eur. Phys. J. C* 79.8 (2019), p. 639. DOI: 10.1140/epjc/s10052-019-7140-6. arXiv: 1902.04655 [physics.ins-det] (cit. on p. 57).

[37] T Cornelissen et al. *Concepts, Design and Implementation of the ATLAS New Tracking (NEWT)*. Tech. rep. ATL-SOFT-PUB-2007-007. ATL-COM-SOFT-2007-002. Geneva: CERN, Mar. 2007. URL: http://cds.cern.ch/record/1020106 (cit. on p. 57).

[38] R. Frühwirth. "Application of Kalman filtering to track and vertex fitting". In: *Nuclear Instruments and Methods in Physics Research Section A: Accelerators, Spectrometers, Detectors and Associated Equipment* 262.2 (1987), pp. 444–450. ISSN: 0168-9002. DOI: https://doi.org/10.1016/0168-9002(87)90887-4. URL: http://www.sciencedirect.com/science/article/pii/0168900287908874 (cit. on p. 57).

[39] T G Cornelissen et al. "The global χ^2 track fitter in ATLAS". In: *Journal of Physics: Conference Series* 119.3 (July 2008), p. 032013. DOI: 10.1088/1742-6596/119/3/032013. URL: https://doi.org/10.1088%2F1742-6596%2F119%2F3%2F032013 (cit. on p. 57).

[40] *Improved electron reconstruction in ATLAS using the Gaussian Sum Filter-based model for bremsstrahlung*. Tech. rep. ATLAS-CONF-2012-047. Geneva: CERN, May 2012. URL: http://cds.cern.ch/record/1449796 (cit. on p. 57).

[41] Georges Aad et al. "Electron and photon energy calibration with the ATLAS detector using LHC Run 1 data". In: *Eur. Phys. J. C* 74.10 (2014), p. 3071. DOI: 10.1140/epjc/s10052-014-3071-4. arXiv: 1407.5063 [hep-ex] (cit. on p. 59).

[42] ATLAS Collaboration. "Electron and photon energy calibration with the ATLAS detector using 2015-2016 LHC proton-proton collision data". In: *JINST* 14.arXiv:1812.03848. 03 (Dec. 2018). Submitted to JINST, P03017. 61 p. DOI: 10.1088/1748-0221/14/03/P03017. URL: https://cds.cern.ch/record/2650720 (cit. on pp. 61, 62).

[43] ATLAS Collaboration. "Electron and photon performance measurements with the ATLAS detector using the 2015–2017 LHC proton-proton collision data". In: *Journal of Instrumentation* 14.12 (Dec. 2019), P12006–P12006. DOI: 10.

1088/1748-0221/14/12/p12006. URL: https://doi.org/10.1088%2F1748-0221%2F14%2F12%2Fp12006 (cit. on pp. 65–67).

[44] Georges Aad et al. "Electron and photon performance measurements with the ATLAS detector using the 2015–2017 LHC proton-proton collision data". In: *JINST* 14.12 (2019), P12006. DOI: 10.1088/1748-0221/14/12/P12006. arXiv: 1908.00005 [hep-ex] (cit. on pp. 68, 71, 72, 78).

[45] Cyril Pascal Becot. "Diphoton lineshape of the BEH boson using the ATLAS detector at the LHC: calibration, mass, width and interferences". PhD thesis. Diderot U., Paris, Sept. 2015 (cit. on p. 75).

[46] "Search for resonances in the 65 to 110 GeV diphoton invariant mass range using 80 fb^{-1} of pp collisions collected at $\sqrt{s} = 13$ TeV with the ATLAS detector". In: (July 2018) (cit. on p. 113).

[47] M.J.G. Veltman and F.J. Ynduráin. "Radiative corrections to WW scattering". In: *Nuclear Physics B* 325.1 (1989), pp. 1–17. ISSN: 0550-3213. DOI: https://doi.org/10.1016/0550-3213(89)90369-6. URL: http://www.sciencedirect.com/science/article/pii/0550321389903696 (cit. on p. 113).

[48] A. Bolanos Carrera et al. "Minimal spontaneously broken hidden sector and its impact on Higgs boson physics at the Large Hadron Collider". In: *4th CERN-CLAF School of High-Energy Physics*. 2008, pp. 313–316 (cit. on p. 113).

[49] Brian Patt and Frank Wilczek. "Higgs-field portal into hidden sectors". In: (May 2006). arXiv: hep-ph/0605188 (cit. on p. 113).

[50] T. D. Lee. "A Theory of Spontaneous T Violation". In: *Phys. Rev. D* 8 (4 Aug. 1973), pp. 1226–1239. DOI: 10.1103/PhysRevD.8.1226. URL: https://link.aps.org/doi/10.1103/PhysRevD.8.1226 (cit. on p. 113).

[51] Alberto Mariotti et al. "New LHC bound on low-mass diphoton resonances". In: *Phys. Lett. B* 783 (2018), pp. 13–18. DOI: 10.1016/j.physletb.2018.06.039. arXiv: 1710.01743 [hep-ph] (cit. on p. 113).

[52] Morad Aaboud et al. "Search for new phenomena in high-mass diphoton final states using 37 fb^{-1} of proton–proton collisions collected at $\sqrt{s} = 13$ TeV with the ATLAS detector". In: *Phys. Lett. B* 775 (2017), pp. 105–125. DOI: 10.1016/j.physletb.2017.10.039. arXiv: 1707.04147 [hep-ex] (cit. on pp. 113, 114, 177).

[53] Georges Aad et al. "Search for Scalar Diphoton Resonances in the Mass Range $65-600$ GeV with the ATLAS Detector in pp Collision Data at $\sqrt{s} = 8\ TeV$". In: *Phys. Rev. Lett.* 113.17 (2014), p. 171801. DOI: 10.1103/PhysRevLett.113.171801. arXiv: 1407.6583 [hep-ex] (cit. on pp. 114, 147, 170, 176).

[54] "Search for new resonances in the diphoton final state in the mass range between 70 and 110 GeV in pp collisions at $\sqrt{s} = 8$ and 13 TeV". In: (Sept. 2017) (cit. on pp. 114, 176).

[55] A. M. Sirunyan et al. "Search for physics beyond the standard model in high-mass diphoton events from proton-proton collisions at $\sqrt{s} = 13$ TeV". In: *Phys. Rev. D* 98.9 (2018), p. 092001. DOI: 10.1103/PhysRevD.98.092001. arXiv: 1809.00327 [hep-ex] (cit. on p. 114).

[56] "Luminosity determination in *pp* collisions at $\sqrt{s} = 13$ TeV using the ATLAS detector at the LHC". In: (June 2019) (cit. on pp. 115, 116).

[57] J. Alwall et al. "The automated computation of tree-level and next-to-leading order differential cross sections, and their matching to parton shower simulations". In: *JHEP* 07 (2014), p. 079. DOI: 10.1007/JHEP07(2014)079. arXiv: 1405.0301 [hep-ph] (cit. on p. 115).

[58] Torbjörn Sjöstrand, Stephen Mrenna, and Peter Skands. "A brief introduction to PYTHIA 8.1". In: *Computer Physics Communications* 178.11 (June 2008), pp. 852–867. ISSN: 0010-4655. DOI: 10.1016/j.cpc.2008.01.036. URL: http://dx.doi.org/10.1016/j.cpc.2008.01.036 (cit. on p. 115).

[59] S Schumann and F Krauss. "A parton shower algorithm based on Catani-Seymour dipole factorisation". In: *Journal of High Energy Physics* 2008.03 (Mar. 2008), pp. 038–038. ISSN: 1029-8479. DOI: 10.1088/1126-6708/2008/03/038. URL: http://dx.doi.org/10.1088/1126-6708/2008/03/038 (cit. on p. 116).

[60] Stefan Höche et al. "QCD matrix elements and truncated showers". In: *Journal of High Energy Physics* 2009.05 (May 2009), pp. 053–053. ISSN: 1029-8479. DOI: 10.1088/1126-6708/2009/05/053. URL: http://dx.doi.org/10.1088/1126-6708/2009/05/053 (cit. on p. 116).

[61] Hung-Liang Lai et al. "New parton distributions for collider physics". In: *Phys. Rev. D* 82 (7 Oct. 2010), p. 074024. DOI: 10.1103/PhysRevD.82.074024. URL: https://link.aps.org/doi/10.1103/PhysRevD.82.074024 (cit. on p. 116).

[62] Frank Siegert. "A practical guide to event generation for prompt photon production with Sherpa". In: *Journal of Physics G: Nuclear and Particle Physics* 44.4 (Mar. 2017), p. 044007. DOI: 10.1088/1361-6471/aa5f29. URL: https://doi.org/10.1088%2F1361-6471%2Faa5f29 (cit. on p. 116).

[63] Richard D. Ball et al. "Parton distributions for the LHC Run II". In: *JHEP* 04 (2015), p. 040. DOI: 10.1007/JHEP04(2015)040. arXiv: 1410.8849 [hep-ph] (cit. on p. 116).

[64] Yee Chinn Yap. "PhD thesis: Search for New Physics with Two Photons in the Final State with the ATLAS Detector". Presented 23 Jan 2017. Feb. 2017. URL: http://cds.cern.ch/record/2252531 (cit. on p. 124).

[65] Luc Devroye. “Sample-based Non-uniform Random Variate Generation”. In: (1986), pp. 260–265. URL: http://doi.acm.org/10.1145/318242.318443 (cit. on p. 125).

[66] *Measurements of Photon efficiencies in pp collision data collected in 2015, 2016 and 2017 at* $\sqrt{s} = 13$ *TeV with the ATLAS detector*. Tech. rep. ATL-COM-PHYS-2018-1604. Geneva: CERN, Nov. 2018. URL: https://cds.cern.ch/record/2647979 (cit. on p. 127).

[67] Georges Aad et al. “Measurement of isolated-photon pair production in *pp* collisions at $\sqrt{s} = 7$ TeV with the ATLAS detector”. In: *JHEP* 01 (2013), p. 086. DOI: 10.1007/JHEP01(2013)086. arXiv: 1211.1913 [hep-ex] (cit. on p. 126).

[68] Ryan Edgar et al. *Functional Decomposition: A new method for search and limit setting*. 2018. arXiv: 1805.04536 [physics.data-an] (cit. on pp. 143, 199).

[69] Jean-Baptiste De Vivie De Regie et al. *ATLAS electron, photon and muon isolation in Run 2*. Tech. rep. ATL-COM-PHYS-2017-290. This note contains the Moriond 2017 recommendations. It will be updated when new recommendations become available. Geneva: CERN, Mar. 2017. URL: https://cds.cern.ch/record/2256658 (cit. on p. 159).

[70] Tianjue Min et al. *Selection and performance for the* $H \to \gamma\gamma$ *2018 analyses using 2015+16+17 pp collision data at* $\sqrt{s} = 13$ *TeV with the ATLAS detector*. Tech. rep. ATL-COM-PHYS-2018-250. Geneva: CERN, Mar. 2018. URL: https://cds.cern.ch/record/2309522 (cit. on p. 160).

[71] Glen Cowan et al. “Asymptotic formulae for likelihood-based tests of new physics”. In: *The European Physical Journal C* 71.2 (Feb. 2011). ISSN: 1434-6052. DOI: 10.1140/epjc/s10052-011-1554-0. URL: http://dx.doi.org/10.1140/epjc/s10052-011-1554-0 (cit. on pp. 164, 172).

[72] Eilam Gross and Ofer Vitells. “Trial factors for the look elsewhere effect in high energy physics”. In: *Eur. Phys. J. C* 70 (2010), pp. 525–530. DOI: 10.1140/epjc/s10052-010-1470-8. arXiv: 1005.1891 [physics.data-an] (cit. on p. 165).

[73] Glen Cowan et al. “Asymptotic formulae for likelihood-based tests of new physics”. In: *Eur. Phys. J. C* 71 (2011). [Erratum: Eur.Phys.J.C 73, 2501 (2013)], p. 1554. DOI: 10.1140/epjc/s10052-011-1554-0. arXiv: 1007.1727 [physics.data-an] (cit. on p. 165).

[74] A L Read. “Presentation of search results: theCLstechnique”. In: *Journal of Physics G: Nuclear and Particle Physics* 28.10 (Sept. 2002), pp. 2693–2704. DOI: 10.1088/0954-3899/28/10/313. URL: https://doi.org/10.1088%2F0954-3899%2F28%2F10%2F313 (cit. on p. 166).

[75] Thomas Junk. "Confidence level computation for combining searches with small statistics". In: *Nuclear Instruments and Methods in Physics Research Section A: Accelerators, Spectrometers, Detectors and Associated Equipment* 434.2-3 (Sept. 1999), pp. 435–443. ISSN: 0168-9002. DOI: 10.1016/s0168-9002(99)00498-2. URL: http://dx.doi.org/10.1016/S0168-9002(99)00498-2 (cit. on p. 166).

[76] Nicolas Berger and Chris Hayes. *Fast distribution sampling using Linearized likelihood*. 2020. URL: https://indico.cern.ch/event/955947/contributions/4017181/attachments/2104245/3575040/StatForum-20200917.pdf (cit. on p. 172).

[77] Morad Aaboud et al. "Search for resonances in diphoton events at $\sqrt{s}$=13 TeV with the ATLAS detector". In: *JHEP* 09 (2016), p. 001. DOI: 10.1007/JHEP09(2016)001. arXiv: 1606.03833 [hep-ex] (cit. on p. 177).

[78] Vardan Khachatryan et al. "Search for Resonant Production of High-Mass Photon Pairs in Proton-Proton Collisions at $\sqrt{s}$ =8 and 13 TeV". In: *Phys. Rev. Lett.* 117.5 (2016), p. 051802. DOI: 10.1103/PhysRevLett.117.051802. arXiv: 1606.04093 [hep-ex] (cit. on p. 177).

Appendices

Appendix A

Stitching of the sliced MC background samples

As introduced in Sec. 5.1, the background MC samples are sliced in $m_{\gamma\gamma}$ for both low-mass and high-mass analyses, in order to maximize the statistics over the whole search range. However, the smoothness of the template is no longer guaranteed, because the statistical precision of the generated event yields exceeds the precision of the cross section corresponding to each MC slice, which is only accurate to percent-level. At a consequence, significant discontinuities appear at each of the $m_{\gamma\gamma}$ edges where two sample slices meet, and lead to large spurious signals. Taking the high-mass analysis as an example: Fig A.1 shows the background only fit in the low-mass range with the PowLog-0 function using two MC slices. A discontinuity can be clearly seen around the connecting point of the two slices at 175 GeV.

In order to mitigate this effect, for each connecting point of two MC slices, an ad-hoc scaling correction is applied to one of the two slices. Since the background modeling is irrelevant to the overall normalization of the background template, the choice of the MC slice to be corrected is not important. This scaling correction is determined based

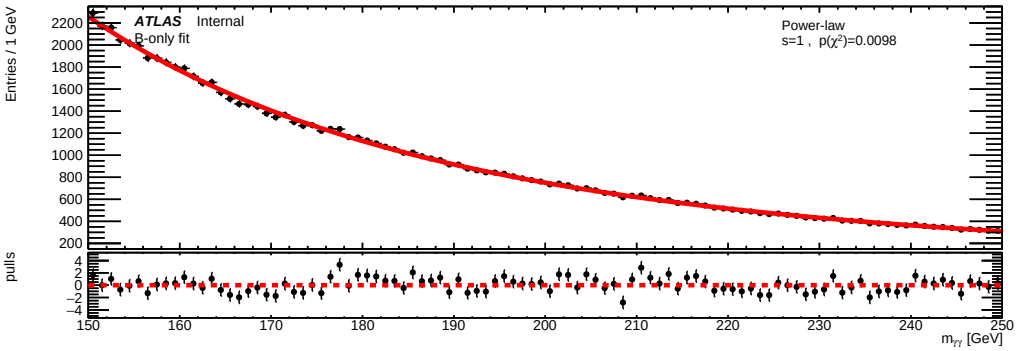

Figure A.1 – High-mass analysis: fit to the $m_{\gamma\gamma}$ distribution of the diphoton background MC template in the range [150, 250] GeV, obtained from the 90-175 GeV and 175-200 GeV MC slices. PowLog-0 (Eq. 5.10) is used in the fit.

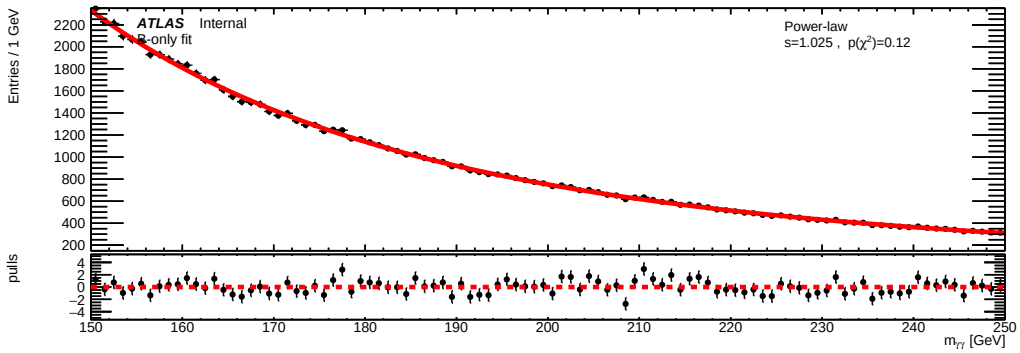

Figure A.2 – High-mass analysis: fit to the $m_{\gamma\gamma}$ distribution of the diphoton background MC template in the range [150, 250] GeV, obtained from the 90-175 GeV and 175-200 GeV MC slices. PowLog-0 (Eq. 5.10) is used in the fit.

on the quality of the background-only fit after applying the correction.[1] Figure A.2 shows the backgroun-only fit to the background template after applying a scaling of 1.025 to the 90-175 GeV slice. Comparing to the result with raw background template (Fig. A.1), the discontinuity around 175 GeV improves a lot. The overall fit quality also improves dramatically from $p(\chi^2) < 0.01$ to $p(\chi^2) = 0.12$.

Note that the scaling correction that gives the best fit quality might not be the "correct" one. In order to estimate the potential systematic uncertainty due to the stitching procedure described above, one mass slice (1400-2000 GeV) is scaled incrementally, and the fit quality $p(\chi^2)$ is found to follow a gaussian distribution with the scaling. The standard deviation σ of this gaussian distribution is therefore taken as the "uncertainty" of the scaling. Alternative background templates are built with σ up and down, and all the variations of template are checked with spurious signal test. In the end, the systematic uncertainty due to stitching procedure only has minor effect on the final FD smoothed background template.

[1] The spurious signal is not checked until the background stitching is finished, in order to minimize any potential bias due to the choice of the scaling correction.

Appendix B

Functional Decomposition smoothing

As discussed in Sec. 5.4.1, the raw background template should be smoothed before the spurious signal test in order to suppress the overall effect of the statistical fluctuations. The basic steps of Functional Decomposition (FD) technique are introduced as following.

First, the input dataset (background template) is modeled by a set of orthonormal functions built from powers of exponential functions. The set of non-orthognal functions function $\{F_n\}$ is orthogonalized to generate the orthogonal function set $\{E_n\}$, where:

$$F_n(z) = \sqrt{2}e^{-nz} \tag{B.1}$$

$$E_n(z) = \sum_{m=0}^{n} d_{nm} F_n(z) \tag{B.2}$$

$$d_{nm} = \sqrt{n}(-1)^{n+m}\left(\frac{2m}{n+m}\right)\prod_{i=1}^{m-1}\frac{m+i}{m-i}\prod_{i=m+1}^{n}\frac{i+m}{i-m} \tag{B.3}$$

the d_{nm} can be calculated recursively[68]. The variable z denotes a transformation of the variable of interest, $m_{\gamma\gamma}$:

$$z = \left(\frac{m_{\gamma\gamma} - m^0_{\gamma\gamma}}{\lambda}\right)^{\alpha} \tag{B.4}$$

where $m^0_{\gamma\gamma}$ is the lower mass cutoff of the spectrum. In the high-mass analysis, $m^0_{\gamma\gamma}$ is set to be 150 GeV. The hyperparameters λ and α are undefined yet, they are determined through optimization during a log-likelihood fit to the background template.

In our case, the signal is absent and FD can model a non-resonant background shape by introducing another hyperparameter N_{bkg}, denoting the upper limits of the number of exponential functions allowed in the smoothing fit. It means that the function series is truncated after N_{bkg} terms, and the background model $B(z)$ is given by:

$$B(z) = \sum_{n=0}^{N_{bkg}-1} b_n E_n(z), \quad b_n = \begin{cases} c_n, & n < N_{bkg} \\ 0, & n \geq N_{bkg} \end{cases} \tag{B.5}$$

Note that if the allowed maximum number of exponential functions is too high, the FD would try to fit all the fluctuations and fail to provide a smoothed template.

Finally, a log-likelihood is constructed and minimized by scanning over the three hyperparameters λ, α and N_{bkg}. The resulting function with optimized hyperparameters are used to model the input background spectrum, in a similar way to a Fourier analysis. The smoothed background model is shown in Fig. 5.17.